



**UNIVERSITY OF THESSALY**  
School of Engineering  
Department of Civil Engineering

## **Water Resources Management in Agricultural Watersheds using Remote Sensing**

**Marios Spiliotopoulos**

**PhD thesis submitted for the Degree of Doctor of Philosophy at the Department of  
Civil Engineering, University of Thessaly.**

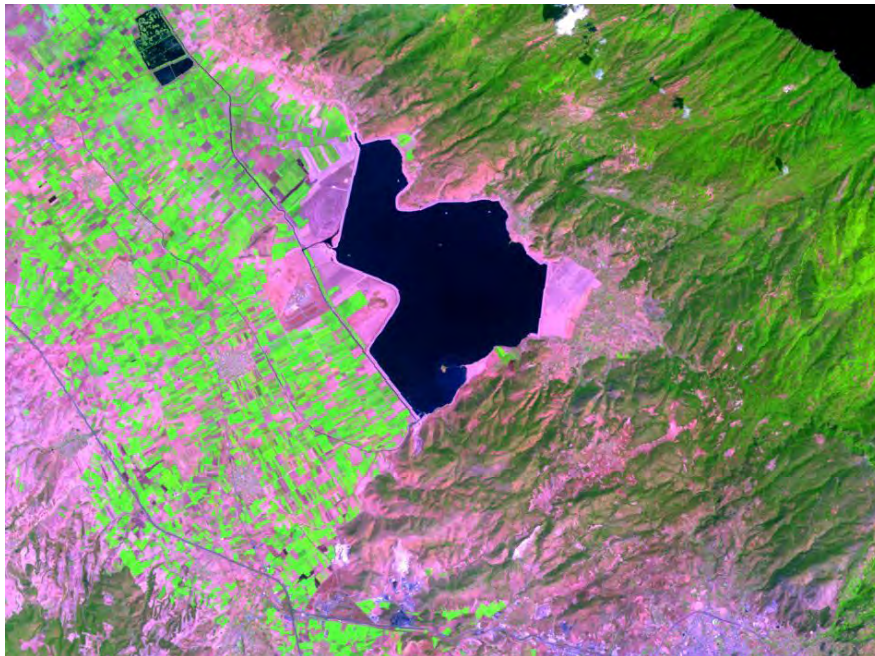
**Volos, December 2014**





**UNIVERSITY OF THESSALY**  
School of Engineering  
Department of Civil Engineering

## **Water Resources Management in Agricultural Watersheds using Remote Sensing**



**Marios Spiliotopoulos**

**PhD thesis submitted for the Degree of Doctor of Philosophy at the Department of  
Civil Engineering, University of Thessaly.**

**Volos, December 2014**





## PREFACE

### Preface

The present thesis “Water Resources Management in Agricultural Watersheds using Remote Sensing” has been submitted as a requirement for the Ph.D. degree at the University of Thessaly (UTH). The main supervisor was Professor Athanasios Loukas (UTH), and co-supervisors were Associate Professor Nikitas Mylopoulos (UTH) and Assistant Professor Hara Michalopoulou (UOA).

The thesis is organized as the main part and the annexes. The main part contains an introduction with the objectives, review of existing work, methodology, results and discussion, and finally conclusions and perspectives. The Annexes encompasses external tables and methodologies closely related with the main part of this thesis. The study has taken place at the Department of Civil Engineering from October 2007 to September 2014. An external research stay of one month was spent at School of Biosystems Engineering, University College Dublin, Ireland (UCD) with Professor Nick Holden as the Host (supervisor). The research was supported by STSM COST ES1106: “Assessment of EUROpean AGRiculture WATER use and trade under climate change (EURO-AGRIWAT)”.

A part of this thesis is a contribution to the projects: “Sustainable Use of Irrigation Water in the Mediterranean Region (SIRRIMED)” – FP7-KBBE-2009-3 – Proposal Reference Number: FP7-245159, and “Development of an integrated system for monitoring and managing the quantity and quality of water resources in rural catchments under climate change. Application in the basin of Lake Karla (YdroMentor)” – Greek Ministry of Education – NSRF 2007-2013 (09ΣΥΝ-31-992).

Volos, December 2014

Marios Spiliotopoulos

**Declaration**

The material contained in this thesis has not been previously submitted by the candidate for a degree in this or any other University.

## Acknowledgments

First of all I would like to thank my supervisor, Prof. Athanasios Loukas, as well as Assoc. Prof. Nikitas Mylopoulos, and Ass. Prof. Hara Michalopoulou for their endless guidance and advice. I would also like to thank Prof. N.R. Dalezios for all these years of cooperation, as well as Dr. L. Toullos, Prof. K.Kittas, and Prof. D. Hadjimitsis for their kind support and participation in my dissertation examination committee. Many thanks also go to Dr. Lampros Vasilliades and Ass. Prof. Chrysi Laspidou for their support and valuable friendship.

The author would like to cordially acknowledge the valuable assistance provided by Prof. D. Hadjimitsis and the personnel of the Laboratory of Remote Sensing and Geo-Environment Research of Technological University of Cyprus. Prof. D. Hadjimitsis provided the GER 1500 spectroradiometer which has been used in the field measurements of this dissertation. The personnel of the Laboratory provided assistance on the processing of the data.

This dissertation was partly financially supported by EFP7's "Sustainable use of irrigation water in the Mediterranean Region" (SIRRIMED), and General Secretariat's of Research and Technology (G.S.R.T.) "An integrated system development for monitoring and managing the quantity and quality of water resources in agricultural water basins under climate change conditions. Application in Karla watershed – HYDROMENTOR". This valuable financial support is highly acknowledged.

Many thanks go, also, to my colleagues and friends George Papaioannou, Pantelis Sidiropoulos, Giannis Tzampiras, Popi Michailidou, Chrisostomos Fafoutis, Katerina Karioti, Kostas Kokkinos and George Tziantzios, on providing me significant reports, documents and files as well as for their friendship and the "brain storming" coffee breaks.

Finally, I would like to thank my family for all the great influence in my life and their support throughout the course of this research.



*To my family*



## Symbols and definitions

Symbol	Unit	Definition
ET	mm	Evapotranspiration
ET <sub>a</sub>	mm	Actual evapotranspiration
ET <sub>o</sub>	mm	Reference evapotranspiration
ET <sub>inst</sub>	mm	Instantaneous evapotranspiration
ET <sub>24</sub>	mm	24h evapotranspiration
G	W/m <sup>2</sup>	Soil heat flux
H	W/m <sup>2</sup>	Sensible heat flux
R <sub>n</sub>	W/m <sup>2</sup>	Net radiation
λE	W/m <sup>2</sup>	Latent heat flux
NDVI	-	Normalized Difference Vegetation Index
LAI	m <sup>2</sup> /m <sup>2</sup>	Leaf Area Index
SAVI	-	-
L	-	Constant* (for the computation of SAVI)
Λ	-	Evaporative fraction
P	mm	Precipitation
T <sub>s</sub>	°C	Land surface temperature
T <sub>a</sub>	°C	Air temperature
LST	°C	Land surface temperature
ΔT	°C	Temperature difference
VIS	μm	Visible band
NIR	μm	Near-infrared band
TIR	μm	Thermal infrared band
R <sub>s</sub> ↓	W/m <sup>2</sup>	Incident shortwave radiation
R <sub>L</sub> ↓	W/m <sup>2</sup>	Incident longwave radiation
R <sub>L</sub> ↑	(W/m <sup>2</sup> ) sr <sup>-1</sup> μm <sup>-1</sup>	Outgoing longwave

$\sigma$	$\text{W/m}^2 (\text{K}^{-4})$	radiation Stefan-Boltzmann constant ( $5.67 \times 10^{-8}$ )
$c_p$	$\text{JKg}^{-1} \text{K}^{-1}$	Air specific heat capacity (1004)
$k$	-	Von Karman constant (0.41)
$G_{sc}$	$\text{W/m}^2$	Global solar constant (1367)
$r_p$	-	Planetary reflectance
$r_a$	-	Atmospheric reflectance
$\alpha$	-	Albedo
$\rho_\lambda$	-	Reflectivity
$d_s$	m	Earth-sun distance
$d_r$	m	Inverse Earth-sun distance
$\lambda$	$\mu\text{m}$	Band wavelength
$\theta$	Rad	Sun zenith angle
JD	days	Julian day (Day of the year)
$\epsilon_o$	-	Surface emissivity
$\epsilon_a$	-	Atmospheric emissivity
$T_B$	K	Brightness temperature
$\delta$	Rad	Solar declination
Lat	Degrees	Latitude
Lon	Degrees	Longitude
$\tau$	-	Transmissivity
$e_s$	kPa	Saturated vapour pressure
$e_a$	kPa	Actual vapour pressure
$e_d$	kPa	Vapour pressure deficit
$\Delta$	kPa	Slope of vapour pressure curve
$\gamma$	kPa $^{\circ}\text{C}$	Psychometric constant
$z$		Vertical height
$z_{om}$	m	Roughness length of heat transfer
$u^*$	m/sec	Friction velocity



$\rho$	$\text{kg/m}^3$	Density of the air
$g$	$\text{m/sec}^2$	gravitational constant (9.81)
$L$	-	Monin-Obukhov length
$K_c$	-	Crop coefficient
$L_\lambda$	Watts/meter squared * ster * $\mu\text{m}$	Spectral Radiance at the sensor's aperture in watts
"gain"	watts/(meter squared * ster * $\mu\text{m}$ )	
"bias"	$(\text{W/m}^2) \text{sr}^{-1} \mu\text{m}^{-1}$	
QCAL	DN (digital number)	The quantized calibrated pixel value
$\text{LMIN}_\lambda$	$(\text{W/m}^2) \text{sr}^{-1} \mu\text{m}^{-1}$	The spectral radiance that is scaled to QCALMIN
$\text{LMAX}_\lambda$	$(\text{W/m}^2) \text{sr}^{-1} \mu\text{m}^{-1}$	The spectral radiance that is scaled to QCALMAX
QCALMIN	DN (digital number)	the minimum quantized calibrated pixel value (corresponding to $\text{LMIN}_\lambda$ ) (0)
QCALMAX	DN (digital number)	the maximum quantized calibrated pixel value (corresponding to $\text{LMAX}_\lambda$ ) (255)

\* $L$  for the computation of SAVI is totally different than the other  $L$  (Monin-Obukhov length).



# TABLE OF CONTENTS

## Table of contents

Preface	iii
Declaration	iv
Acknowledgments	v
Symbols and definitions	ix
1 INTRODUCTION	1
1.1 Water Resources Management	1
1.2 Using Water Resources Effectively in Agriculture Water Use	3
1.3 Use of Remote Sensing for water resources management	9
1.4 Aim of Dissertation-Key Questions-Research Objectives	10
The detailed research objectives of the dissertation are:	10
1.5 Dissertation Structure	11
2 BACKGROUND INFORMATION	13
2.1 Remote Sensing: Active and Passive sensors	13
2.1.1 Landsat Satellites.	17
2.1.2 Terra and Aqua Satellites	21
2.1.3 Moderate Resolution Imaging Spectroradiometer (MODIS)	22
2.1.4 MODIS data products	24
2.2 The estimation of ET (Review of Methods)	26
2.3 Non Remote Sensing based methodologies	26
2.4 The computation of potential evapotranspiration	28
2.4.1 Penman method	28
2.4.2 Penman-Monteith method (1965)	28
2.4.3 FAO Penman Monteith method (Allen et al., 1998)	29
2.4.4 Priestley-Taylor method (1972)	29
2.4.5 Partial equations for the computation of reference evapotranspiration	30
2.5 The computation of actual evapotranspiration	32
2.5.1 Using the complementary relationship	32
2.6 Remote Sensing based Methodologies of ET Estimation	33
2.6.1 Surface Energy Balance Algorithm for Land (SEBAL)	36
2.6.2 METRIC	38
2.6.3 SEBI	39
2.6.4 SEBS	40
2.6.5 S-SEBI	40
2.6.6 TSM	41
2.6.7 TRIANGLE METHOD	41
2.6.8 TRAPEZOID METHOD	43
2.7 Definition and Use of Crop Coefficients	45
2.7.1 Pan evaporation	46
2.7.2 Reference ET	46
2.7.3 Stages of growth – Phenological stages	47
2.7.4 Satellite based $K_c$ estimations	50

2.8	The Use of CropWat Model	55
2.8.1	Requirements	55
2.8.2	Soil parameters calculation	56
2.8.3	ClimWat 2.0 software (used for accessing climatic data):	57
2.8.4	Software Environment	57
2.8.5	Improvements	58
3	Study Area – Land Use Classification	61
3.1	Lake Karla Basin	61
3.2	History: Drain of the Lake Karla	63
3.3	The Lake Karla Restoration	64
3.4	The technical works	65
3.5	The present and future	66
3.6	Agriculture	68
3.7	Land Use Mapping	69
3.7.1	Methodology	70
3.7.2	Greek Geodetic Reference System 1987 (GGRS87)	71
3.7.3	GGRS87 projection	71
3.7.4	GGRS87 datum	72
3.7.5	Supervised Classification	73
3.7.6	Maximum likelihood vs minimum and mahalanobis distance	74
3.7.7	Land use classes	77
3.7.8	Accuracy assessment	82
3.7.9	Classification after the filling of the reservoir	82
4	Methodology	85
4.1	Preprocessing of data	87
4.1.1	Radiometric correction	88
4.1.2	Geometric correction	90
4.1.3	Assessing Geometric Accuracy	93
4.2	Surface Energy Balance Algorithms for Land (SEBAL) – Detailed Methodology	94
4.2.1	Model Requirements	97
4.2.2	Satellite Image Information	97
4.2.3	Meteorological Data	99
4.2.4	Land Use Map	100
4.2.5	Computation of $ET_r$	100
4.2.6	Steps and sub-models.	101
4.2.7	PART 1 : Net Surface Radiation ( $R_n$ )	103
4.2.8	Choosing the “Hot” and “Cold” Pixels	116
4.2.9	Incoming Longwave Radiation ( $R_{L\downarrow}$ )	117
4.2.10	Running the Surface Radiation Balance Equation model for $R_n$	117
4.2.11	PART 2 : Soil Heat Flux ( $G$ )	118
4.2.12	PART 3 : Sensible Heat Flux ( $G$ )	121
4.2.13	Iterative process - Monin-Obukhov length	130
4.2.14	Computation of Latent Heat Flux ( $\lambda ET$ ), Instantaneous ET ( $ET_{inst}$ ), and Reference ET Fraction ( $ET_r F$ )	135
4.2.15	ET computations for longer periods	138
4.2.16	Limitations.	140
4.2.17	Differences between SEBAL and METRIC.	140
4.2.18	METRIC flow chart	143
4.2.19	METRIC using MODIS imagery.	144
4.3	Field spectroscopy	147

4.3.1	Phenological stages of the crops	150
4.3.2	Procedure	151
4.4	Downscaling	157
4.5	Application of CropWat model	164
4.6	Methodological Framework	166
4.6.1	Background application of the “classical” METRIC method	166
4.6.2	Proposed Integrated methodology	167
5	Results	171
5.1	Background methodology	171
5.1.1	Application of classical METRIC methodology	171
5.1.2	ET <sub>a</sub> mapping	172
5.1.3	ET <sub>r</sub> F mapping	173
5.1.4	Zoning of the area.	175
5.1.5	Crop zoning	176
5.1.6	Irrigation requirements.	180
5.2	Validation of ET <sub>a</sub> using METRIC	199
5.2.1	P.M. ET <sub>ref</sub> vs METRIC ET <sub>a</sub> values	199
5.2.2	METRIC ET <sub>a</sub> values vs P.M. ET <sub>a</sub> values	203
5.3	Proposed integrated methodology	209
5.3.1	Field measurements – Vegetation indices	209
5.3.2	MODIS based NDVI – Downscaling	214
5.3.3	Estimation of crop coefficients using the ET <sub>r</sub> F =f(NDVI) relationship	216
5.4	Validation of the proposed methodology	220
5.4.1	Landsat 8 imagery	220
5.4.2	Landsat 7 imagery	222
5.4.3	Estimation of daily crop water requirements using CropWat	223
5.4.4	CropWat sensitivity	226
6	Conclusions and perspectives	229
6.1	Summary of methodology and results	229
6.2	Dissertation Innovative Elements	234
6.3	Limitations	235
6.4	Future Recommendations	236
7	Publications related with this dissertation	239
	References	243
	ANNEX 1	279
	The CLC classification categories	279
	ANNEX 2	287
	Julian Day Calendar	287
	ANNEX 3	295
	The selection of hot and cold pixels	295
	ANNEX 4	303
	Instability	303



## LIST OF TABLES

Table 2.1. Current satellite missions and applications .....	14
Table 2.2. European Sentinel Satellites.....	16
Table 2.1. Landsat Specifications.....	17
Table 2.2. Sensors on-board Landsat.....	18
Table 2.3. Aqua and Terra instruments. ....	21
Table 2.4. MODIS bands. ....	22
Table 2.5. MODIS specifications. ....	23
Table 2.6. MODIS products. ....	24
Table 2.7. Calculation of evapotranspiration: Categories. ....	27
Table 2.8. Prevailed Energy Balance Methodologies.....	35
Table 2.8. Phenological stages of the main crops .....	47
Table 2.9. Stages of Crop Development – British Columbia, Canada . ....	49
Table 2.10. Most widely used Vegetation Indices. ....	51
Table 2.11. CROPWAT requirements. ....	55
Table 3.1. Hellenic Geodetic Reference System Characteristics (HGRS87). ....	72
Table 3.2. Land use classes. ....	77
Table 3.3. Class classification. ....	78
Table 3.4. Land use class statistics .....	81
Table 3.5. Classification statistics-Error Matrix. ....	83
Table 3.6. Land Use class classification. ....	83
Table 4.1. Required data for the application of SEBAL model. ....	98
Table 4.2. Steps needed for the application of METRIC. ....	101
Table 4.3. $ESUN_{\lambda}$ values for Landsat 5 and Landsat 7. ....	105
Table 4.4. Weighting coefficients $\omega_{\lambda}$ values for Landsat 5 and Landsat 7. ....	106
Table 4.5. Filters for the computation of narrow band emissivity. ....	112
Table 4.6. Filters for the computation of broad band emissivity. ....	112
Table 4.7. Constants for the computation of surface temperature. ....	115
Table 4.8. $G/R_n$ values for some selected surfaces. ....	119
Table 4.9. Filters for the computation of $G/R_n$ . ....	120
Table 4.10. $z_{om}$ values for some selected surfaces. ....	124
Table 4.11. Boundary conditions for hot and cold pixels. ....	129
Table 4.12. MODIS Weighting Coefficients for each band for the computation of albedo .....	146
Table 5.1. Landsat 5 TM images used for Lake Karla Watershed.....	171
Table 5.2. New Surface Network irrigation requirements. ....	184
Table 5.3. Pinios LALR Network irrigation requirements .....	187
Table 5.4. South groundwater Network irrigation requirements .....	189
Table 5.5. Central groundwater Network irrigation requirements.....	192
Table 5.6. North groundwater Network irrigation requirements .....	195
Table 5.7. Total irrigation requirements per zone .....	198
Table 5.8. $ET_{ref}$ vs METRIC $ET_a$ values: Independent period 2012 .....	200
Table 5.9. $ET_{ref}$ vs METRIC $ET_a$ values: Dependent period 2007. ....	201
Table 5.10. $K_c$ values according to each phenological stage for crops at Lake Karla watershed. ....	204
Table 5.11. 2012 METRIC based $ET_a$ vs P.M. based $ET_a$ values.....	205
Table 5.12. 2007 METRIC based $ET_a$ vs P.M. based $ET_a$ values.....	208
Table 5.13. GER1500 experimental days for Lake Karla Watershed .....	210
Table 5.14. Landsat 7 images used for Lake Karla Watershed.....	212
Table 5.15. Linear relationships between $ET_F$ and $VI$ . ....	213
Table 5.16. $ET_F$ ( $K_c$ ) and crop irrigation requirement outputs. ....	224
Table 5.17. Average Crop Irrigation Requirement values (mm). ....	225
Table 5.18. CropWat irrigation requirements sensitivity to $K_c$ errors .....	227





## LIST OF FIGURES

Figure 1.1. Hydrologic Cycle (Source: U.S. Army Corps of Engineers .....	1
Figure 1.2. World Water Use .....	4
Figure 1.3. Water use in European Countries .....	4
Figure 1.4. Average Irrigation requirement (mm/year) in EU .....	5
Figure 1.5. Water use in Greece . ....	6
Figure 1.6. Irrigation per region in Greece .....	6
Figure 1.7. Administrative Regions of Greece .....	7
Figure 1.8. Computation of agricultural water use .....	8
Figure 2.1. The electromagnetic spectrum .....	13
Figure 2.2. History of Landsat missions .....	17
Figure 2.3. Landsats: (a) L5, (b) L7.....	20
Figure 2.4. Landsat 8: (a) Launch, (b) On the air .....	20
Figure 2.5. OLI and TIRS sensors mounting .....	20
Figure 2.6. MODIS instrument (taken from modis.gsfc.nasa.gov).....	26
Figure 2.7. Complementary Relationship .....	33
Figure 2.8. Schematic diagram of triangular $T_s$ versus VI relationship .....	42
Figure 2.9. The hypothetical trapezoidal space between $T_s$ - $T_a$ and $F_r$ .....	44
Figure 2.10. Crop coefficients during the growing season .....	48
Figure 2.11. Soil Texture Triangle: Hydraulic Properties Calculator. ....	56
Figure 2.12. CLIMWAT: example. ....	57
Figure 2.13. CROPWAT : example.....	58
Figure 3.1. Lake Karla Basin.....	61
Figure 3.2. Mean monthly values of precipitation and potential evapotranspiration for Lake Karla .....	62
Figure 3.3. Mean monthly values of temperature for Lake Karla basin . ....	62
Figure 3.4. Zoning of areas served by the aquifer. ....	67
Figure 3.5. Zoning of areas irrigated by groundwater pumping. ....	67
Figure 3.6. Zoning of future irrigation network. ....	68
Figure 3.7. The prevailing crops in the study area . ....	69
Figure 3.8. Field observations with a GPS device.....	71
Figure 3.9. Corine Land Cover: Thessaly, Greece .....	74
Figure 3.10. Corine Land Cover Classes. ....	75
Figure 3.11. Maximum likelihood feature space illustration assuming two-dimensions .....	76
Figure 3.12. Supervised classification of the initial a) Landsat TM 15-8-2011. Green is water surface and red is land surface: b) Minimum distance classification, c) maximum likelihood classification. ....	77
Figure 3.13. Supervised classification: Stage 1 .....	78
Figure 3.14. Fields recording using GPS. ....	79
Figure 3.15. Mixed land use.....	80
Figure 3.16. Recognition of thematic classes. ....	80
Figure 3.17. Supervised classification: Stage 2 .....	81
Figure 3.18. Supervised classification: Stage 2, 2012. ....	84
Figure 4.1. Flow chart of the “classical” methodology for the estimation of irrigation requirements .....	85
Figure 4.2. Flow chart of the proposed integrated methodology for the estimation of irrigation requirements. ....	86
Figure 4.3. 2012-10-03, Magnesia region: Initial Landsat 7 ETM+ before and after gapfill.....	88
Figure 4.4. Magnesia region: Landsat 7 ETM+ at-satellite radiance on 03/10/2012 .....	90
Figure 4.5. Landsat TM image to image registration for 27/7/2007. ....	92
Figure 4.6 Image Histogram Equalization (Left: Before, Right: After). ....	93
Figure 4.7 RMSE errors for the first 10 control points tested for a geometric correction procedure. ....	94
Figure 4.8. Surface Energy Balance. ....	95
Figure 4.9. Net radiation = gain – losses. ....	95
Figure 4.10. Header file for the 1-9-2012 Landsat 7 ETM+ image.....	98
Figure 4.11. Computation of $ET_r$ using “ref ET” package.....	100
Figure 4.12. Computation of $ET_r$ manually using Penman – Monteith methodology.....	101
Figure 4.13. Computation of (a) radiance on the left side - Model 1 and (b) reflectivity on the right side – Model 2.....	105

Figure 4.14. Computation of albedo at the top of atmosphere (model 03).	107
Figure 4.15. Computation of surface albedo at the top of atmosphere (model 04).	108
Figure 4.16. Computation of NDVI, SAVI and LAI (model 05).	111
Figure 4.17. Computation of surface emissivity (model 06).	113
Figure 4.18. Computation of surface temperature (merged model 07-08).	115
Figure 4.19. Computation of outgoing longwave radiation (model 09).	116
Figure 4.20. Computation of net surface radiation flux (model 10).	118
Figure 4.21. Computation of Soil Heat Flux (G) (model 11).	120
Figure 4.22. Computation of roughness length ( $z_{om}$ ) (model 12).	125
Figure 4.23. Wind speed direction over vegetation canopy, aerodynamic roughness length ( $z_{om}$ ) and zero plane displacement height	126
Figure 4.24. Computation of aerodynamic resistance to heat transport ( $rah$ ) (Model 13).	127
Figure 4.25. Deriving a and b constants from dT vs. $T_s$ relationship (METRIC).	129
Figure 4.26. Computation of sensible heat flux (H) for Neutral Conditions (Model 14-15).	130
Figure 4.27. Computation of corrected $u^*$ and $rah$ for the first iteration (Model 16).	134
Figure 4.28. Overview of model 16.	135
Figure 4.29. Monin-Obukhov based iteration flow chart.	136
Figure 4.30. Computation of Instantaneous ET ( $ET_{inst}$ ), and Reference ET Fraction ( $ET_rF$ ).	138
Figure 4.31. Flow chart of the METRIC model	143
Figure 4.32. MYD13 NIR Reflectance 26-7-2007.	145
Figure 4.33. GER1500 field spectro-radiometer.	148
Figure 4.34. Spectralon.	148
Figure 4.35. A Lambertian surface where scatter of light is governed by a cosine intensity relationship.	149
Figure 4.36. Reflectance of crops as a status of vegetation health.	149
Figure 4.37. Relative spectral response for LANDSAT TM	150
Figure 4.38. Cotton phenological stages (a) heading 15/6, (b) flowering 31/7, (c) flowering 1/9, (d) maturing 21/9, (e) before harvesting 12/10, (f) harvesting (19/10)	151
Figure 4.39. Multiple GER1500 measurements across the fields.	152
Figure 4.40. Landsat in - Band Average RSR: band 3 (retrieved from USGS Spectral Viewer).	153
Figure 4.41. Landsat in - Band Average RSR: band 4 (retrieved from USGS Spectral Viewer).	153
Figure 4.42. Initial GER1500 reflectance values for selected alfalfa fields.	154
Figure 4.43. Interpolation of the average initial reflectance values.	154
Figure 4.44. Alfalfa spectral measurements for 21/9/2012.	155
Figure 4.45. Cotton spectral measurements for 13/7/2012.	155
Figure 4.46. Maize spectral measurements for 29/6/2012.	156
Figure 4.47. Sugar beet spectral measurements for 13/7/2012.	156
Figure 4.48. Temporal evolution of spectral signatures for cotton.	157
Figure 4.49. Regression based downscaling.	160
Figure 4.50. Subtraction based downscaling.	160
Figure 4.51. METRIC $ET_o$ maps: (a) 26/7/2007 MODIS, (b) 27/8/2007 MODIS, (c) 26/7/2007 Landsat TM, (d) 27/8/2007 Landsat TM	161
Figure 4.52. Predicted $ET_o$ maps and difference between predicted and original maps: (a) regression, (b) subtraction.	162
Figure 4.53. 2D Scatterplots for predicted-original 27/7/2007 Landsat $ET_a$ for (a) regression downscaling method and (b) subtraction downscaling method. The red line is the 1:1 line of perfect agreement.	163
Figure 4.54. CropWat irrigation requirements output.	165
Figure 4.55. "Background" methodology detailed flow chart.	167
Figure 4.56. Proposed integrated methodology detailed flow chart.	169
Figure 5.1. $ET_o$ map for 7/5/2007 (left) and 24/6/2007 (right)	172
Figure 5.2. $ET_o$ map for 10/7/2007 (left) and 26/7/2007 (right)	172
Figure 5.3. $ET_o$ map for 27/8/2007 (left) and 28/9/2007 (right)	173
Figure 5.4. $ET_rF$ map for 7/5/2007 (left) and 24/6/2007 (right)	174
Figure 5.5. $ET_rF$ map for 10/7/2007 (left) and 24/7/2007 (right).	174
Figure 5.6. $ET_rF$ map for 7/5/2007 (left) and 26/7/2007 (right)	174
Figure 5.7. Spatial variation of ET values (right) across a specific cotton field (left)	175
Figure 5.8. The surface network of Lake Karla Watershed.	176

Figure 5.9. The groundwater network of Lake Karla Watershed.....	177
Figure 5.10. Classification of the south groundwater network of Lake Karla Watershed. ....	178
Figure 5.11. Classification of the central groundwater network of Lake Karla Watershed. ....	178
Figure 5.12. Classification of the north groundwater network of Lake Karla Watershed. ....	179
Figure 5.13. Classification of the new surface network of Lake Karla Watershed.....	179
Figure 5.14. Classification of Pinios LALR surface network of Lake Karla Watershed. ....	180
Figure 5.15. Meteorological data input for 2007. ....	181
Figure 5.16. Rainfall data input for 2007 (Larissa). ....	181
Figure 5.17. Crop file input for 2007.....	183
Figure 5.18. Soil file input for 2007.....	183
Figure 5.19. Crop water requirements output for 2007.....	184
Figure 5.20. Crop water requirements per zone. ....	198
Figure 5.21. Location of the meteorological stations of the study area. ....	200
Figure 5.22. $ET_a$ METRIC vs $ET_{ref}$ P.M. values: 2012. ....	201
Figure 5.23. $ET_a$ METRIC vs $ET_{ref}$ P.M. values: 2007. ....	202
Figure 5.24. $ET_a$ METRIC vs $ET_{ref}$ P.M. values: 2012 + 2007. ....	203
Figure 5.25. $K_c$ values during the growing season: a) Cotton, b) Sugar beet, c) Maize .....	204
Figure 5.26. METRIC based $ET_a$ values vs P.M. based $ET_a$ values: 2012.....	207
Figure 5.27. METRIC based $ET_a$ values vs P.M. based $ET_a$ values: 2012 + 2007.....	209
Figure 5.28. Standard deviation of SAVI vs coefficient L. ....	211
Figure 5.29. $ET_rF$ vs NDVI general equation.....	214
Figure 5.30. (a) MODIS based NDVI 13 <sup>th</sup> of June 2012, (b) MODIS based NDVI 29 <sup>th</sup> of June 2012, (c) LANDSAT based NDVI 13 <sup>th</sup> of June 2012 (d) LANDSAT based NDVI 29 <sup>th</sup> of June 2012, (e) Downscaled NDVI map (29 <sup>th</sup> of June 2012). ....	216
Figure 5.31. $ET_rF$ computed, 29 <sup>th</sup> of June 2012. ....	218
Figure 5.32. $ET_rF$ difference, 29 <sup>th</sup> of June 2012. ....	218
Figure 5.33. A “crop mask” applied in the study (in red). ....	219
Figure 5.34. Lake Karla watershed classification map 2012.....	219
Figure 5.35. Landsat 8: 184/032 and 184/033 (path/row) scenes (24-6-2013)/.....	221
Figure 5.36. 24-6-2013: a) $ET_rF$ METRIC map, b) $ET_rF$ new proposed map, c) difference map. ....	222
Figure 5.37. 3-10-2012: a) $ET_rF$ METRIC map, b) $ET_rF$ new proposed map, c) difference map. ....	223



**ABSTRACT**

The goal of this study is a contribution to the water resources management through the detailed study of evapotranspiration estimated by calculating the surface energy balance. The surface energy balance is examined in a new way with the use of satellite remote sensing techniques deriving, finally, crop coefficients values ( $K_c$ ) giving much emphasis to the prevailing local conditions. During this thesis satellite-based energy balance for Mapping EvapoTRanspiration with Internalized Calibration (METRIC) methodology is successfully modified for the region of Thessaly, Greece. At the same time, a new land use map is produced, necessary for the next steps of the described water balance methodologies. Furthermore, field measurements (spectral measurements) for the year 2012 for selected crops at the Lake Karla basin were recorded. Hundreds of surface reflectivity values are filtered and then converted according to the specific wavelengths of Landsat 7 bands. This is achieved by applying the method of interpolation in order to yield values in steps of 1 nm. These values are then filtered according to the relative spectral profiles provided by the satellite manufacturer. Finally, using the Relative Spectral Response (RSR) of Landsat TM/ETM+, and applying interpolation, surface reflectivity values equivalent to channels 1, 2, 3 and 4 of Landsat TM/ETM+ for selected crops of Lake Karla basin, namely cotton, wheat, maize, alfalfa and sugar beet are generated. As a result, vegetation indices can be estimated with high accuracy without the need for atmospheric correction. It is therefore possible now to incorporate accurate values of vegetation indices into METRIC methodology to Lake Karla watershed and finally get separate  $K_c$  values for each crop with a spatial resolution of 30 m x 30 m.  $K_c$  values can be finally introduced into FAO CROPWAT model computing water needs for each crop.

The next step is the application of specialized downscaling techniques, where fine spatial resolution from Landsat imagery, is combined with fine temporal resolution from AQUA/MODIS sensors, resulting to an "artificial"  $ET_a$  and/or  $K_c$  image map with improved spatiotemporal characteristics. This methodology can be applied again for every crop as previously. The reason for doing this procedure is the need for

improvement of Landsat's temporal resolution which is sixteen (16) days. The processing results show that it is possible to predict a 30 m x 30 m  $ET_a$  Landsat image map for Lake Karla watershed simply applying a linear model (linear regression) derived from MODIS images with a 250 m x 250 m spatial resolution. The basic assumption of this methodology is that the fine-scale variability inside a MODIS pixel (250 m x 250 m) is assumed to be fixed between the times of the first and the second Landsat image acquisition. After that, an estimation of the required amount of irrigation water requirements using CROPWAT (FAO) model is generated, using specific land use. At last, a new model incorporating all the previous applied methodologies is established. The new model uses field measurements, downscaling techniques between Landsat and MODIS derived NDVI values and linear regression in order to finally produce daily crop coefficient values with 30 m x 30 m spatial resolution.

Validation of the proposed methodologies which have been developed and applied at this study is not possible through reliable measurements. This happens both to evapotranspiration and crop water requirement measurements. The reason is the absence of lysimeters and/or a water consumption measurement system respectively. For this reason, an internal validation is performed instead. Initially, values of actual evapotranspiration produced by METRIC methodology are checked against the theoretical Penman-Monteith methodology. The procedure is performed at the regions close to the available meteorological stations of the study area. Then, the proposed methodology is validated independently utilizing new Landsat 7 and Landsat 8 images not used initially at the proposed methodology, by comparing the predicted values when applying the proposed methodology with the computed values of evapotranspiration based on METRIC methodology. Validation is satisfactory for both cases. Finally, a sensitivity analysis of the assessment of crop irrigation requirements is performed. CROPWAT outputs are checked against the possible error of crop coefficients derived from the proposed methodology. The results are again encouraging.

## ΠΕΡΙΛΗΨΗ

Στην παρούσα διδακτορική διατριβή επιχειρείται η συμβολή στη διαχείριση υδατικών πόρων μέσω της λεπτομερούς μελέτης της εξατμισοδιαπνοής που εκτιμάται από τον υπολογισμό του επιφανειακού ενεργειακού ισοζυγίου. Το επιφανειακό ενεργειακό ισοζύγιο μελετάται με τη βοήθεια της δορυφορικής Τηλεπισκόπησης και παράγονται με νέο τρόπο, λεπτομερείς τιμές των φυτικών συντελεστών  $K_c$  με έμφαση στην περιοχικότητα. Κατά τη διάρκεια της διατριβής αναπτύχθηκε η μεθοδολογία Satellite-based energy balance for Mapping EvapoTRanspiration with Internalized Calibration (METRIC) και εφαρμόστηκε με επιτυχία στη λεκάνη απορροής της Λίμνης Κάρλας στην Θεσσαλία. Παράλληλα, παράχθηκε ένας νέος χάρτης χρήσεων γης, ο οποίος είναι απαραίτητος για τη μετέπειτα επεξεργασία του υδατικού ισοζυγίου. Επιπλέον πραγματοποιήθηκαν και μετρήσεις ανακλαστικότητας στο πεδίο. Συγκεκριμένα, κατά το έτος 2012 έγιναν 12 ημερήσιες ραδιομετρικές μετρήσεις σε επιλεγμένες καλλιέργειες της υδρολογικής λεκάνης Κάρλας. Καταβλήθηκε προσπάθεια οι μετρήσεις να γίνουν κατά τις περιόδους όπου θα υπήρχε και κάλυψη από το δορυφόρο Landsat 7 κατά την καλλιεργητική περίοδο. Εξαιτίας των καιρικών συνθηκών δεν ήταν δυνατό να αξιοποιηθούν όλες οι εικόνες που λήφθηκαν κατά τις προαναφερθείσες ημέρες, αλλά με τη μέθοδο παρεμβολής των splines επιτυγχάνεται η αντιστοίχιση ημερών πειράματος και δορυφορικών εικόνων. Εκατοντάδες επίγειες μετρήσεις ανακλαστικότητας φιλτράρονται και μετατρέπονται στη συνέχεια σύμφωνα με τα μήκη κύματος των αντίστοιχων καναλιών του δορυφόρου Landsat 7. Αυτό γίνεται με την εφαρμογή της μεθόδου παρεμβολής έτσι ώστε να παραχθούν τιμές ανά 1 nm, ενώ στη συνέχεια οι τιμές αυτές ανάγονται σύμφωνα με τα μήκη κύματος που αντιστοιχούν σε κάθε κανάλι του δορυφόρου Landsat χρησιμοποιώντας τα σχετικά φασματικά προφίλ (relative spectral profiles) που δίνονται από τον κατασκευαστή του δορυφόρου (φιλτράρισμα). Γίνεται δηλαδή εκτίμηση της επιφανειακής ανακλαστικότητας σύμφωνα και ισοδύναμα με τα κανάλια 1, 2, 3 και 4 των οργάνων TM/ETM+ των δορυφόρων Landsat με τη συσκευή GER 1500. Το φασματοραδιόμετρο Geophysical Environmental Research (GER) 1500 είναι ένα

ελαφρύ, υψηλής ακρίβειας φασματοραδιόμετρο, το οποίο καλύπτει το υπεριώδες, το ορατό και το εγγύς υπέρυθρο φάσμα, από τα 350 έως τα 1050 nm. Συνολικά η συσκευή καταγράφει δεδομένα σε 512 κανάλια. Με τη χρήση όμως των Relative Spectral Response (RSR) των Landsat TM/ETM+, και με παρεμβολή, μπορούν κατόπιν να συγκριθούν οι τιμές ανακλαστικότητας του δορυφόρου Landsat 7 με τις τιμές που προέκυψαν από τις επιτόπιες μετρήσεις σε επιλεγμένες καλλιέργειες βαμβακιού, σιταριού, καλαμποκιού, μηδικής και ζαχαροτεύτλων στην περιοχή της Κάρλας. Εκτιμάται επομένως η εκπεμπόμενη και ανακλώμενη ακτινοβολία στο ορατό και στο υπέρυθρο φάσμα της Ηλεκτρομαγνητικής Ακτινοβολίας στις παραπάνω καλλιέργειες, κι έτσι οι δείκτες βλάστησης μπορούν πλέον να εκτιμηθούν με ακρίβεια και χωρίς την ανάγκη διενέργειας ατμοσφαιρικής διόρθωσης. Περαιτέρω διερεύνηση των δεικτών οδηγεί στην εξαγωγή μέσω παλινδρόμησης ξεχωριστών σχέσεων για κάθε καλλιέργεια και για κάθε φαινολογικό στάδιο των καλλιεργειών. Οι σχέσεις οι οποίες εκτιμούν τον φυτικό συντελεστή σε συνάρτηση με τον εκάστοτε δείκτη βλάστησης στις περισσότερες των περιπτώσεων προκύπτει ότι είναι γραμμικές. Είναι επομένως πλέον εφικτή η με λεπτομέρεια εξαγωγή δεικτών βλάστησης και η ενσωμάτωσή τους μέσα στη μεθοδολογία METRIC έτσι ώστε να υπάρχει ακριβής χαρτογραφική απεικόνιση του μεγέθους της πραγματικής εξατμισοδιαπνοής αλλά και του φυτικού συντελεστή σύμφωνα με τις ειδικές τοπικές συνθήκες που επικρατούν στα εδάφη της λεκάνης απορροής της Λίμνης Κάρλας. Έτσι, παράγεται πλέον μια ξεχωριστή τιμή, για κάθε καλλιέργεια, του ειδικού φυτικού συντελεστή  $K_c$  με χωρική ανάλυση 30 m x 30 m. Ο συντελεστής  $K_c$  μπορεί τώρα να εισαχθεί σε μια μέθοδο υπολογισμού υδατικών απαιτήσεων όπως το μοντέλο CROPWAT και να δώσει τιμές αρδευτικών απαιτήσεων ανά καλλιέργεια σε mm ύψους βροχής.

Στη συνέχεια προσομοιώνεται η δημιουργία επιμέρους σχέσεων από τη μεθοδολογία καταβιβασμού (downscaling) η οποία οδηγεί από την επεξεργασία εικόνων MODIS σε μία αναλογική, «τεχνητή» εικόνα  $ET_a$  σύμφωνα με τη χωρική ανάλυση του δορυφόρου LANDSAT. Αυτό μπορεί να γίνει και πάλι αναλογικά για κάθε καλλιέργεια σύμφωνα με την προηγούμενη μεθοδολογία. Η ανάγκη του παραπάνω στόχου προκύπτει από τη χαμηλή χρονική ανάλυση του δορυφόρου Landsat, η οποία είναι δεκαέξι (16) ημέρες, όσο και από την πιθανότητα λόγω αυξημένης νέφωσης να μην



υπάρχει δυνατότητα λήψης της εικόνας αυτής για διαδοχικά 16-ήμερα. Αντιθέτως η λήψη των δορυφόρων MODIS είναι καθημερινή με ότι αυτό συνεπάγεται. Τα αποτελέσματα της επεξεργασίας δείχνουν ότι είναι εφικτή η πρόβλεψη μιας 30 m x 30 m ET<sub>a</sub> Landsat απεικόνισης για την περιοχή της λίμνης Κάρλας εφαρμόζοντας ένα απλό γραμμικό μοντέλο (linear regression) παραγόμενο από εικόνες MODIS χωρικής ανάλυσης 250 m x 250 m με την προϋπόθεση φυσικά ότι η μεταβλητότητα μέσα σε ένα εικονοστοιχείο MODIS (250 m x 250 m) θεωρείται αναλογικά σταθερή μεταξύ του χρόνου από την ανάκτηση της πρώτης έως την ανάκτηση της δεύτερης εικόνας Landsat. Μετά την ολοκλήρωση των σχέσεων που ορίζουν τους φυτικούς συντελεστές ανά εικονοστοιχείο και ανά χρονική περίοδο, γίνεται εκτίμηση του απαιτούμενου ποσού αρδευτικού νερού με τη χρήση του μοντέλου CropWat (FAO). Χωρίζονται υποπεριοχές της λεκάνης απορροής Κάρλας και με τη βοήθεια των γνωστών χρήσεων γης και της χαρτογράφησης του εδάφους που έχει πραγματοποιηθεί μπορεί να γίνει χωρική κατανομή απαιτήσεων και απολήξεων του νερού.

Τέλος, επιχειρείται η ανάπτυξη ενός νέου συνδυαστικού μοντέλου το οποίο ενσωματώνει τη μεθοδολογία της ανάκτησης δεικτών βλάστησης από επίγεια δεδομένα, και τον καταβιβασμό τιμών του δείκτη βλάστησης NDVI μεταξύ Landsat και MODIS προς όφελος της δημιουργίας γραμμικών εξισώσεων που δίνουν απευθείας καθημερινές τιμές του φυτικού συντελεστή  $K_c$  με χωρική ανάλυση 30 m x 30 m.

Η πιστοποίηση των μεθοδολογιών, οι οποίες έχουν αναπτυχθεί και εφαρμοστεί στη διατριβή, δε μπορεί να γίνει μέσω μετρημένων/παρατηρημένων επίγειων ποσοτήτων (π.χ. πραγματικής εξατμισοδιαπνοής και κατανάλωσης νερού για άρδευση), γιατί όσον αφορά την εξατμισοδιαπνοή και την αρδευτική κατανάλωση νερού δεν υπάρχει ένα αξιόπιστο μετρητικό δίκτυο (π.χ. λυσίμετρα ή μετρητές κατανάλωσης νερού) . Για το λόγο αυτό, γίνεται μια εσωτερική επαλήθευση. Αρχικά οι τιμές της πραγματικής εξατμισοδιαπνοής από τη μεθοδολογία METRIC επαληθεύονται βάσει της θεωρητικής μεθόδου Penman-Monteith. Η πιστοποίηση γίνεται σε περιοχές που γειτνιάζουν με τους διαθέσιμους μετεωρολογικούς σταθμούς της περιοχής. Σε δεύτερο στάδιο, η προτεινόμενη μεθολογία πιστοποιείται, ανεξάρτητα, με νέες εικόνες Landsat 7 και Landsat 8, οι οποίες δεν έχουν χρησιμοποιηθεί στην ανάπτυξη της μεθοδολογίας.

Συγκρίνονται οι προβλεπόμενες με τις υπολογισμένες τιμές των φυτικών συντελεστών κατά περίπτωση. Και στα δύο στάδια η πιστοποίηση κρίνεται αρκετά ικανοποιητική. Τέλος, γίνεται μια ανάλυση ευαισθησίας της εκτίμησης των αρδευτικών αναγκών σε συνάρτηση με το πιθανό σφάλμα που προέρχεται από την εκτίμηση των φυτικών συντελεστών. Τα αποτελέσματα και σε αυτή την περίπτωση είναι ενθαρρυντικά.

## CHAPTER 1° INTRODUCTION

### 1 INTRODUCTION

#### 1.1 *Water Resources Management*

The Ancient Greek philosopher Empedocles held that water is one of the four classical elements along with fire, earth and air, and was regarded as the ylem, or basic substance of the universe. Water is an essential resource for all life on the planet covering more of the 2/3 of the Earth's surface. The larger percentage (96.5%) of the planet's water is found in seas and oceans, 1.7% in groundwater, 1.7% in glaciers and the ice caps of Antarctica and Greenland, a small fraction in other large water bodies, and 0.001% in the air as vapour, and precipitation (Gleick, 1993). Only 2.5% of the Earth's water is freshwater, and 98.8% of that water is in ice and groundwater. Less than 0.3% of all freshwater is in rivers, lakes, and the atmosphere, and an even smaller amount of the Earth's freshwater (0.003%) is contained within biological bodies and manufactured products (Gleick, 1993). A very simple illustration of the hydrologic cycle is shown in Figure 1.1.

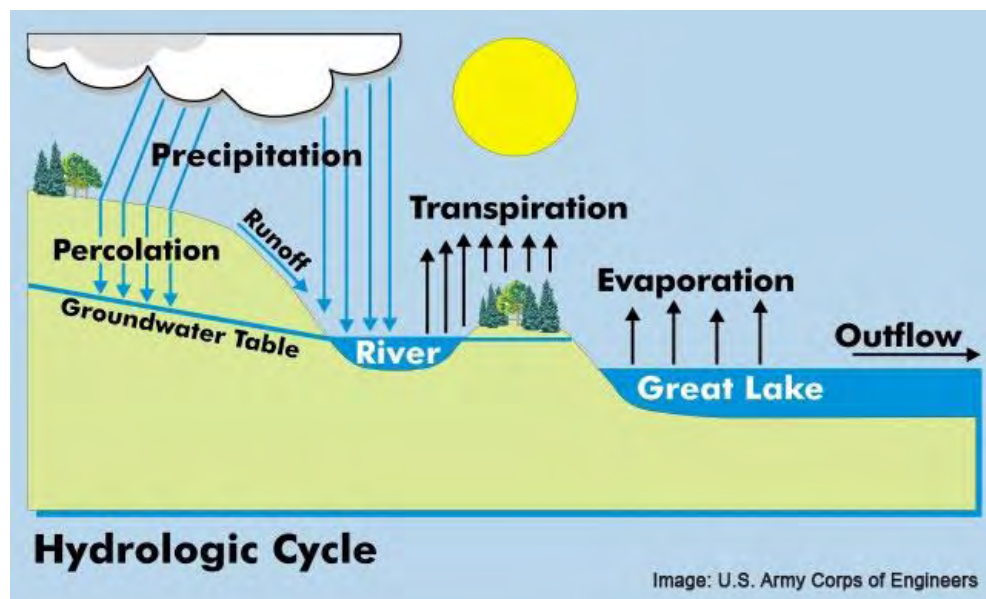


Figure 1.1. Hydrologic Cycle (Source: U.S. Army Corps of Engineers - <http://www.watershedcouncil.org/>)

Water resource management (WRM) can be defined as the man's activity of planning, developing, distributing and managing the optimum use of water resources. WRM is a sub-set of water cycle management, and, ideally, it deals with all the competing demands for water seeking to allocate water on an equitable basis to satisfy all uses and demands. Improved water governance can be achieved through the integrated management of water resources.

The Global Water Partnership (2000) defines Integrated Water resource management (IWRM) as: "A process that promotes the coordinated development and management of water, land, and related resources in order to maximize the resultant economic and social welfare in an equitable manner without compromising the sustainability of vital ecosystems". IWRM is a complex task involving engineering, economy, ecology, sociology, law, and politics.

The main goal of IWRM is to secure (Swiss Federal Institute of Technology, 2014):

- water use efficiency
- ecological integrity and/or restoration of aquatic ecosystems
- clean water bodies
- equity and participation in decision making
- respect of institutional and legal frameworks

The main problems which IWRM has to solve are the planning, the design and operation of the water infrastructures such as reservoirs, pipelines, and channels, the distribution of water resources in space and time, the water scarcity, the competitive use, the water conservation, the aquatic ecosystems preservation, the pollution preservation and finally the access to the water. IWRM also deals with water engineering problems, such as planning, design and operation in water as well as ecology of aquatic ecosystems, decision making and financial management. Finally, interaction with authorities, politicians and stakeholders are also necessary for the achievement of the expected results.

The concept of IWRM has been already recognized in Agenda 21 (the UN Conference on Environment and Development, which took place in Rio in 1992). That was to a large extent based on the UN Conference on Water and Development, which was held in Dublin in January 1992, produced the four Dublin Principles:

- (1) The holistic principle,
- (2) The participatory principle,
- (3) The gender principle, and
- (4) The economic principle.

These principles provided an important mindset for water resources development and management (Jonch-Clausen and Fugl, 2001). The World Bank's 1993 Policy Paper redefined these principles to three: the ecological, the institutional and the instrument principles. Ten year later, in 2002, the Plan of Implementation adopted at the World Summit on Sustainable Development in Johannesburg (WSSD) called for countries to "develop Integrated Water Resources Management and Water Efficiency Plans by 2005." These plans were to be milestones to national water strategy processes until our days (Korsgaard *et al.*, 2007).

## *1.2 Using Water Resources Effectively in Agriculture Water Use*

According to United Nations' UN Water (Feb. 2014), about 70% of world freshwater is consumed by irrigation and it is assigned as agricultural water. From the rest 30%, two thirds are consumed by industry and one third by domestic use (Figure 1.2).

In Europe there is a big variation of agricultural water percentage according to the character of each country. As it seems from Figure 1.3 Germany consumes most of its water to industry, while Malta consumes most of its water to households.

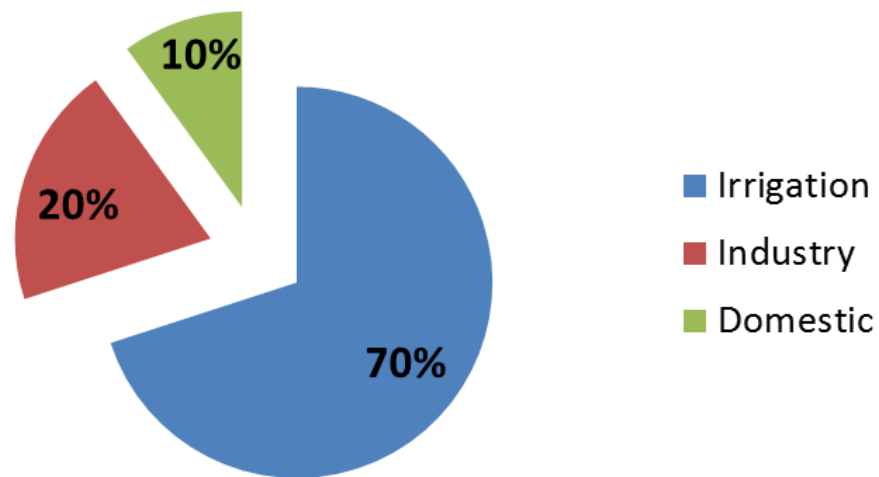


Figure 1.2. World Water Use (Source: U.N. Water- <http://www.fao.org/nr/water/>)

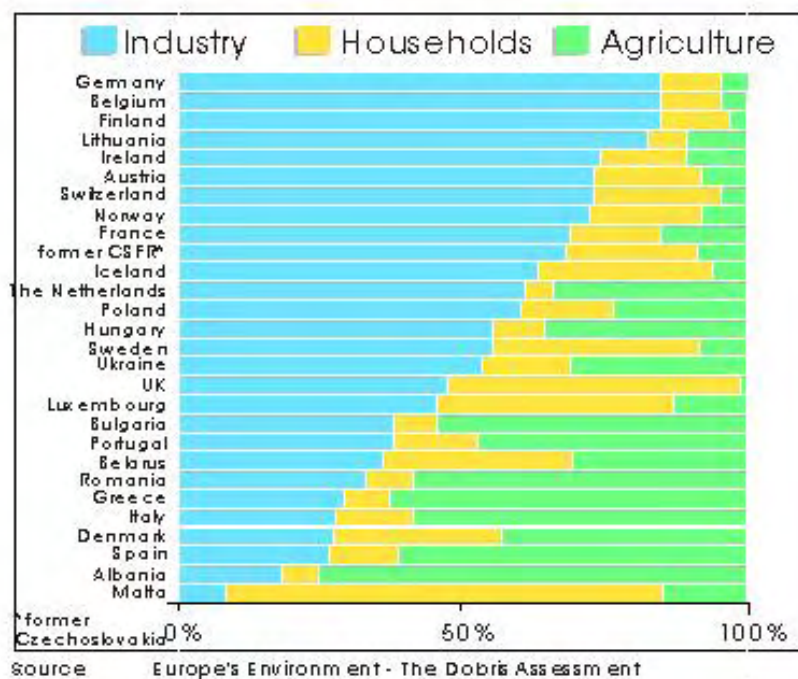


Figure 1.3. Water use in European Countries (Source: Europe's environment- The Dobris assessment- <http://www.eea.europa.eu/>)

Wriedt *et al.*, (2008) applied a soil water and crop growth model to estimate irrigation water requirements with a 10x10 km raster cells spatial resolution. The result (Figure 1.4) illustrates that large amounts of irrigated water are actually needed especially for Southern Europe.

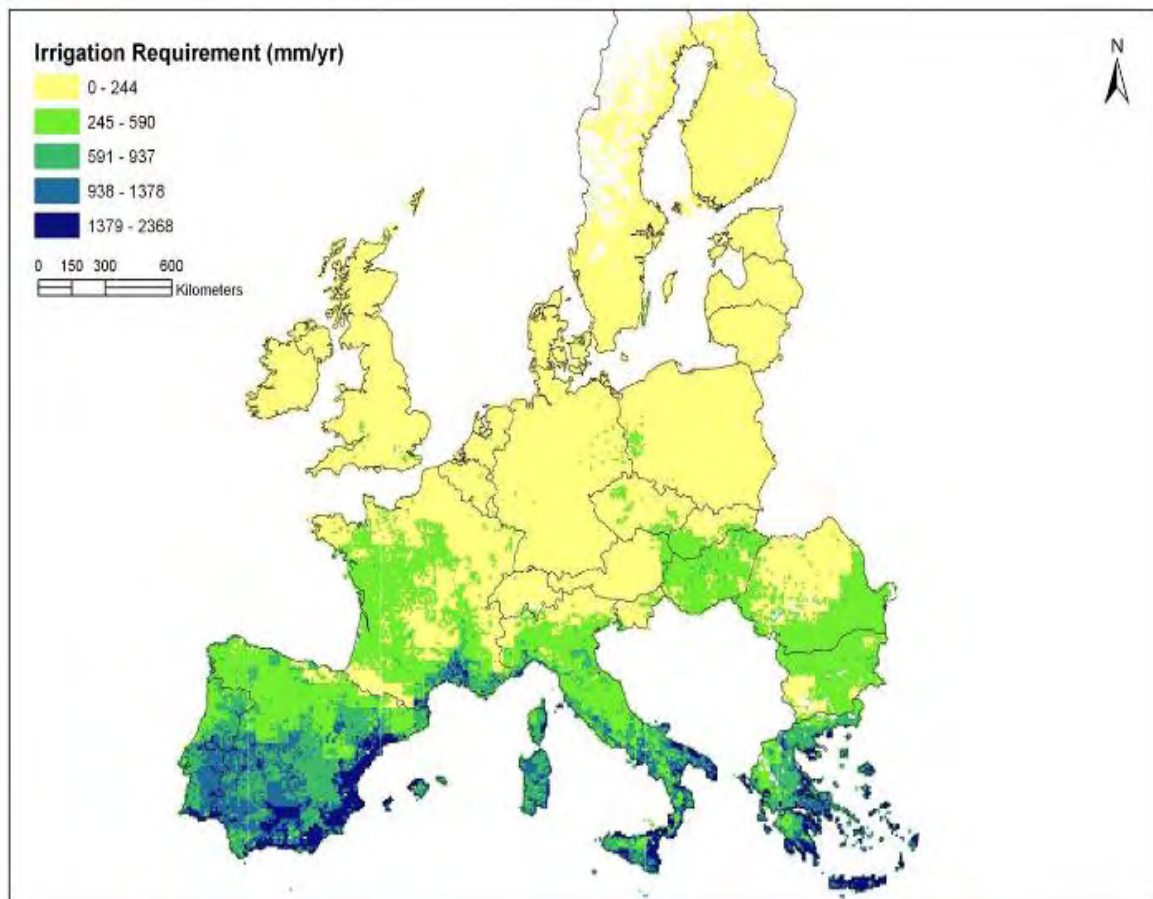


Figure 1.4. Average Irrigation requirement (mm/year) in EU (Source: Wriedt *et al.*, 2008)

Mimikou (2005) made a more thorough study of water resources in Greece showing that almost 86% of the total water in Greece is rural (Figure 1.5).

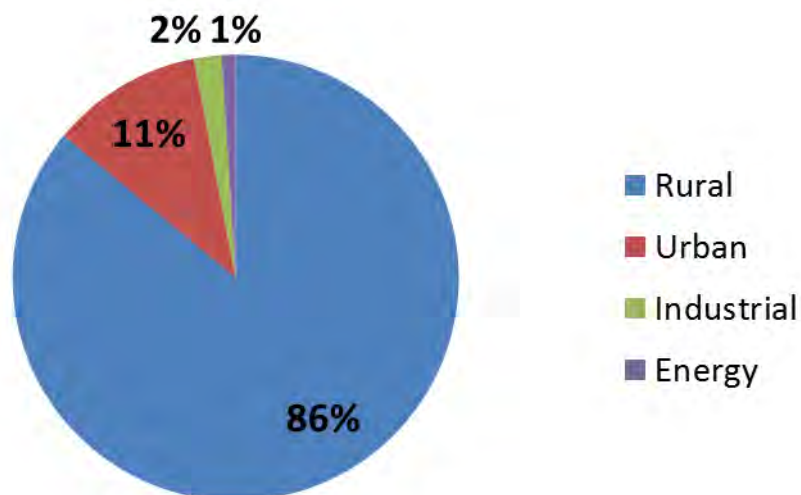


Figure 1.5. Water use in Greece (reproduced from Mimikou, 2005).

Giving a focus in Greece and after dividing the country into 13 administrative regions the following results are indicative (Figure 1.6). It is very significant that Thessaly region, which is the region where the study region is situated, is a very large water consumer even if it is relatively small in area (Figure 1.7).

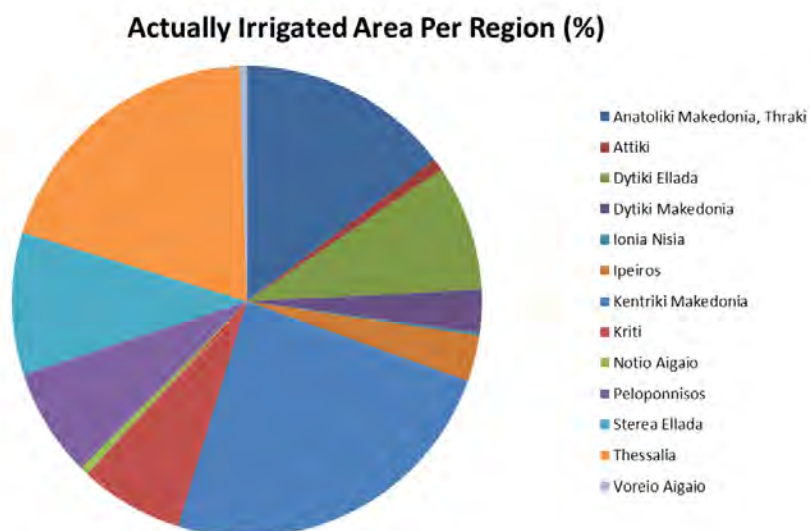


Figure 1.6. Irrigation per region in Greece (reproduced from Mimikou, 2005).





Figure 1.7. Administrative Regions of Greece (reproduced from Greek Ministry of Interior- <http://www.ypes.gr/>)).

In any case, it is obvious that, agriculture consumes a very large amount of the total water supply. How to use this supply effectively is, perhaps, the largest problem of the water resources. Dealing with agriculture, evapotranspiration can be closely related to water demand, meaning that losses due to evapotranspiration can be handled in a way allowing assuring the best conditions for agricultural needs, if water resources management is correctly planned and implemented (Irmak, 2012). Computation of water use based on FAOSTAT methodology is illustrated in Figure 1.8.

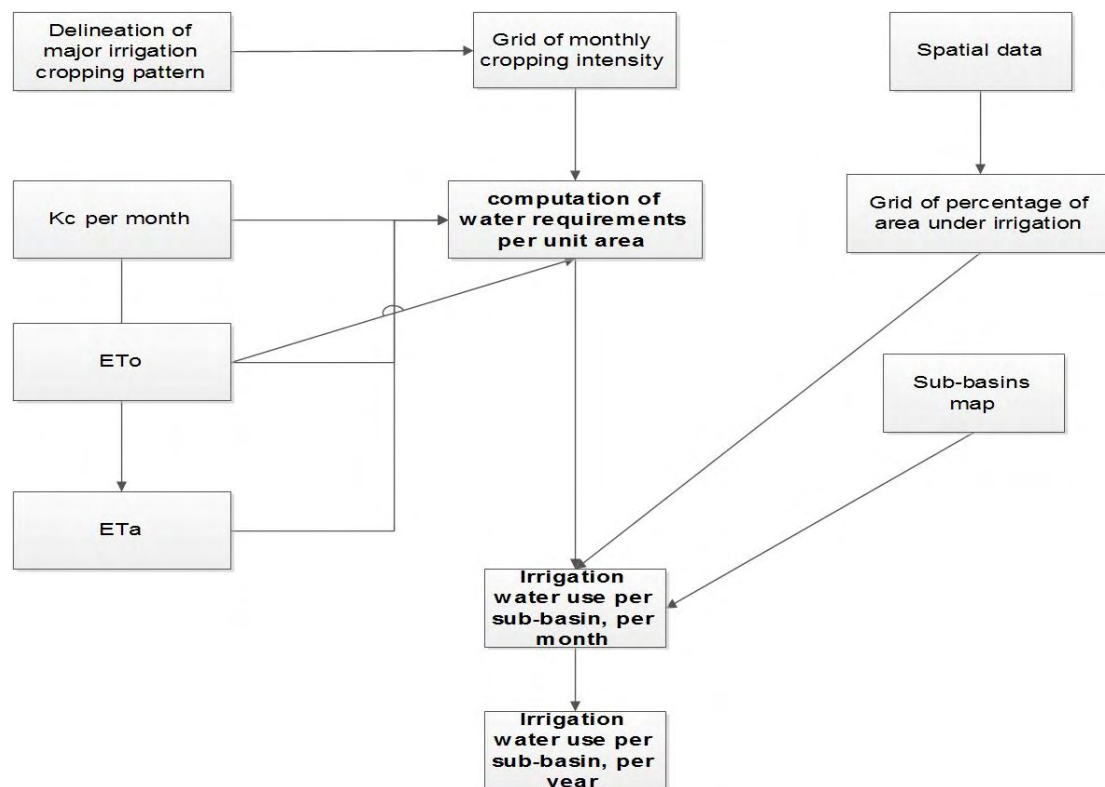


Figure 1.8. Computation of agricultural water use (Reproduced from FAOSTAT-  
<http://faostat.fao.org/>).

It is obvious that evapotranspiration assessment is of outstanding importance both for planning and monitoring purposes, playing a very crucial role to the hydrological balance and the differences between water requirements and availability. The magnitude of evapotranspiration can be compared to the main forcing parameter of the water balance which is the precipitation, and for this reason several climatic classifications are based on comparisons between these two quantities, with the aim of determining specific climate conditions for different areas (Rivas-Martinez, 1995). In this framework, evapotranspiration is the only component of the water balance having a central role also in the energy and carbon balance, since it directly accounts for hydrological, agricultural and ecological effects of drought events (Mendicino and Senatore, 2012).

Most of the water resources in the study region, described later, are overused beyond their sustainable potential. There is already a serious concern because of groundwater over-pumping in the study area. Persistence to the old habits and water policies may

cause permanent damage to water quality and sustainable yield. Thus, opposed to the current conditions, sustainable management of water resources must be an important policy based on a reasonable allocation and the principles of environmental protection.

### *1.3 Use of Remote Sensing for water resources management*

Remote sensing is particularly useful in the field of hydrological modelling where the information can be used for both the estimation of hydrological model parameters and as an input to hydrological models. It is very popular for example to estimate the variability of rainfall in space and time with the aid of ground-based weather radars. But it is very important that, despite the fact that remote sensing gained wide acceptance in the fields of hydrology and water resources management, it is still underdeveloped (Schultz, 1997). Remote Sensing information is most useful in combination with other types of information. It is very useful to transform the given information into other types of information which is often called as “indirect” methodologies. Some tricks are very often used in order to achieve the desirable data set. For example, in order to compute the required long time series of runoff values at an ungauged site, where the dam has to be constructed, the following procedure is followed: At the beginning of the design period of the water project, an hydrological network is installed, collecting ground truth information during a short period (planning period), and then a mathematical model is developed connecting ground truth data with satellite imagery. After this procedure it is possible to reconstruct historical river flows based on satellite data for the whole period of time for which satellite information is available (Schultz, 1997). Another example could be the change detection of an area. It is possible to monitor erosion and silting up with high resolution imagery and indirectly make decisions about the installations. Menenti *et al.* (1996) describe how water demand of crops can be assessed in real time, introducing crop water stress indices derived from thermal infrared measurements. Evapotranspiration of crops under stress is then compared with that of crops under normal conditions.

#### *1.4 Aim of Dissertation-Key Questions-Research Objectives*

The aim of this dissertation is to use remote sensing data sets to help improve agricultural water use as a part of water resources management around the region of Lake Karla Watershed, Greece. For this reason, a new developed methodology for the estimation of crop coefficients is applied and tested throughout the study region and the crop water requirements are estimated.

To meet the scope of the dissertation a number of key questions should be answered:

1. Is it possible to manage actual evapotranspiration as a consumer, and to what extent?
2. Can satellite measurements, combined with meteorological data, be used for the determination of the regional distribution of evapotranspiration?
3. Can the estimates derived from METRIC algorithm used as an input to the models needed to assess water resources?
4. How does land cover/land use change impact water demand?
5. Are there any other factors which impact water demand in the area?

The detailed research objectives of the dissertation are:

1. Estimate evapotranspiration and understand its spatial and temporal variation over Lake Karla Watershed.
  - Assess the importance of actual evapotranspiration to water resources management as a consumer.
  - Understand the computation difficulties of actual evapotranspiration.
  - Assess the advantages of the satellite-based Energy Surface Balance models (SEBAL and METRIC).
  - Compare Landsat TM (or ETM+) estimations with NASA's MODIS products.
  - Derive a new methodology for the combined exploitation of MODIS and Landsat imagery (downscaling).
2. Use multispectral satellite data to derive high quality land use/land cover maps.

- Assess agricultural areas and crop fields for the first time in the study area, with a 30 m x 30 m spatial resolution.
  - Validate land cover maps with field observations.
3. Precisely estimate values of crop coefficient  $K_c$  for the main crops of the study region.
    - Estimate  $K_c$  for each pixel of the study region with a spatial resolution of 30 m x 30 m.
    - Investigate the appearance of  $K_c$  in time and space.
  4. Use field spectroscopy yielding reflectance information and products.
    - Assess the spectral responses of crops through the time and correlate them with the related phenological periods.
    - Estimate Vegetation Indices (VI) without the need of Remote Sensing Imagery.
    - Correlate Vegetation Indices with  $K_c$  values.
  5. Application of FAO's irrigation and planning "CropWat" model.
    - Incorporate local crop and weather conditions to the model.
    - Estimate irrigation needs for the main crops of the study area.
  6. Develop a new methodology to derive daily  $K_c$  values with a 30 m x 30 m spatial resolution and incorporate them to CropWat model (integration).

### 1.5 Dissertation Structure

This first (present) chapter of the dissertation describes how water needs can be estimated using remote sensing, together with a brief definition of water resources management. The second chapter describes well established conventional and Remote Sensing based methods for the estimation of evapotranspiration. A detailed scientific

review is presented. Remote sensing data sets used are described, giving focus to some technical characteristics of the sensors. Crop coefficient theory is presented and CropWat model is described.

The third chapter gives a detailed description of the study area (geography, climate, and geomorphology) together with information about land use classification achieved for this thesis. The fourth chapter describes the methodology used for the processing of images (images calibration, processing, and geo-referencing), the application of surface energy balance, and the field spectroscopy methodology as well as the downscaling technique and CropWat model used. An integration building the new proposed methodology is finally described.

The fifth chapter gives the results of the application of the surface energy balance to the study area. Crop coefficients values are validated using Penman-Monteith methodology. The results then are combined with CropWat model application improving its performance. Crop water requirements are presented. Results of the new integrated proposed methodology are described. Vegetation indices derived from field measurements produce new relationships with crop coefficients. Downscaling NDVI values are inserted into the model producing the final crop coefficient product which is presented and tested. Crop irrigation estimations using CropWat are generated and validated.

The sixth chapter presents the conclusions of the thesis. The chapter evaluates the research objectives, provides conclusions and recommendations, and suggests further research. The seventh chapter presents scientific publications which have been produced through the research towards this dissertation. Finally, scientific publications used and cited in the development of this research and dissertation are listed at the end. Appendices containing tables and information used in the dissertation are also attached separately.

## CHAPTER 2°

### BACKGROUND INFORMATION AND LITERATURE REVIEW

## 2 BACKGROUND INFORMATION

### 2.1 Remote Sensing: Active and Passive sensors

Remote Sensing (RS) as a science is dedicated to everything that has to do with the acquisition of information about an object or phenomenon without making physical contact with the object. RS takes advantage of the power of the sun as a source of energy or radiation. The energy of the sun can be reflected, absorbed or re-emitted. The direct sunlight as well as the reflected one is well known as the visible part of the electromagnetic spectrum, while the absorbed and re-emitted stands for the infrared wavelengths (Figure 2.1). The entire reflected energy takes place only during daytime, when the sun is illuminating the earth. This is when passive sensors are in operation. Passive sensors can only be used to detect energy when the naturally occurring energy is available. But energy is also emitted from the earth. This is happening to the thermal infrared part of the spectrum, and as a consequence, infrared radiation can be detected day or night, as long a sufficient amount of energy can be recorded.

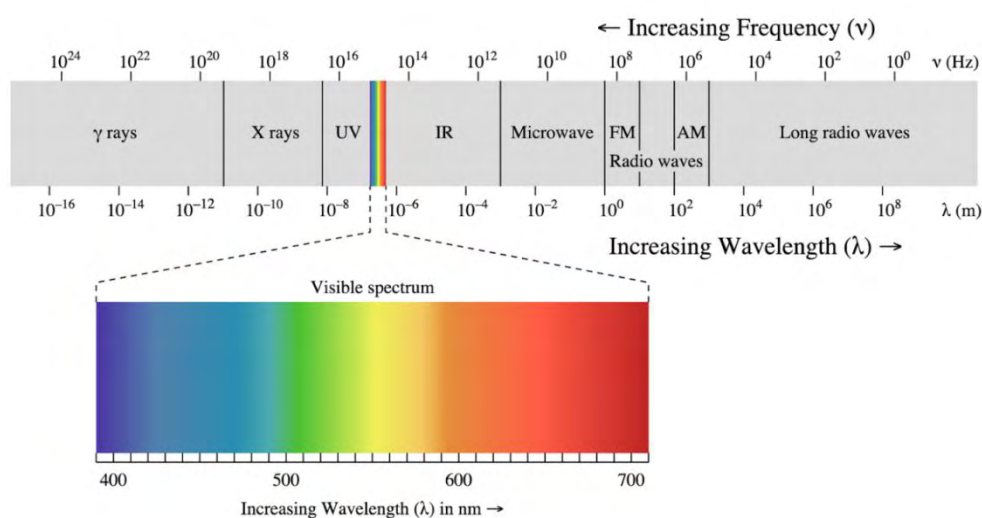


Figure 2.1. The electromagnetic spectrum (This file is shared by Philip Ronan under the Creative Commons Attribution-Share Alike 3.0 Unported license)

As opposite to the passive sensors, active sensors provide their own energy source for illumination. One of the examples of active sensors is traffic radar (Radio Detection and Ranging), or a laser fluorosensor synthetic aperture radar (SAR). The sensor emits radiation by its own, the radiation is directed to the target to be measured and then the radiation is reflected back from the target to the sensor. It is obvious that active sensors can be used anytime of the day or any season, which is something that the passive sensors cannot do. Another advantage is that the active sensors can be used for examining wavelengths that are not sufficiently provided actually by the sun. Microwaves are a good reason for using passive sensors. One more advantage is that using active sensors is easier to control the way that the target is illuminated. However, active systems require the generation of a fairly large amount of energy to adequately illuminate targets. A good example of use both active and passive sensors is a camera. While in bright light conditions a camera acts as a passive sensor, in dark light conditions uses a flash to illuminate the targets and record the reflected radiation.

As a conclusion it can be said that, even if active sensors have many advantages such as they are weather or sunlight independent, and they can adequately penetrate vegetation and soil, are absolutely cost-intensive, and this is a very important disadvantage. It can also be mentioned that radar signals do not contain spectral characteristics, which is very important when the monitoring of environment is the goal. This is why passive sensors are used at this study. Passive sensors usually make use of a scanner equipped with spectrometers. These devices measure signals at several spectral bands simultaneously, and that is why the final image product is called “multispectral”. Multispectral images allow numerous interpretations, and this is one of the subjects which this thesis is dealing with. Current satellite missions and their related applications are shown on Table 2.1 (Dalezios and Spyropoulos, 2015).

Table 2.1. Current satellite missions and applications

Satellite	Type of sensor carrying on	Applications
LANDSAT	Optical, medium spatial resolution, multispectral	General land-cover, land-use mapping, agriculture, environmental monitoring



TERRA	Optical moderate spatial resolution, multispectral, microwave sensors for land and atmosphere	General land-cover, land-use mapping, quality of atmosphere, environmental monitoring, agriculture
AQUA	Optical moderate spatial resolution, multispectral, microwave sensors for atmosphere, land and sea	General land-cover, land-use mapping, quality of atmosphere, environmental monitoring, ocean monitoring
NOAA-AVHRR	Optical low resolution imaging sensors	Atmosphere-Meteorology small scale land-cover mapping sea environment monitoring,
Meteosat Third Generation satellites	Optical and microwave low resolution sensors	Atmosphere - Meteorology small scale land-cover mapping, ocean environment monitoring,
GeoEye-1	Optical, very-high spatial resolution, multispectral	Mapping, environmental monitoring security, precision farming
IKONOS	Optical, very-high spatial resolution, multispectral	Mapping, environmental monitoring security, precision farming
Pleiades	Optical, very-high spatial resolution, multispectral	Mapping, environmental monitoring security, precision farming
RapidEye	Optical, high spatial resolution, multispectral	Mapping, environmental monitoring, precision farming
SPOT 6,7	Optical, very-high spatial resolution, multispectral	Mapping, environmental monitoring security, precision farming
WorldView-1	Optical, very-high spatial resolution, panchromatic	Mapping
WorldView-2	Optical, very-high spatial resolution, multispectral	Mapping, environmental monitoring security, precision farming
TanDEM-X	Radar, high spatial resolution,	Land and Sea: environmental monitoring security, precision farming, sea monitoring
TerraSAR-X	Radar, high spatial resolution,	Land and Sea: environmental monitoring security, precision farming, sea monitoring
COSMO-SkyMed	Radar, very-high spatial resolution,	Land and Sea Mapping, environmental monitoring

Radarsat-2	Radar, high spatial resolution,	security, precision farming, sea monitoring Land and Sea: environmental monitoring security, precision farming, sea monitoring
------------	---------------------------------	---

European Space Agency (ESA) ESA is currently developing a new family of missions called Sentinels. Each Sentinel mission is based on a constellation of two satellites providing a range of technologies, such as radar and multi-spectral imaging instruments for land, ocean and atmospheric monitoring which will be very useful in the near future ([http://www.esa.int/Our\\_Activities/Observing\\_the\\_Earth/Copernicus/Overview4](http://www.esa.int/Our_Activities/Observing_the_Earth/Copernicus/Overview4)).

Specifications of the Sentinels are shown on Table 2.2 (Dalezios and Spyropoulos, 2015).

Table 2.2. European Sentinel Satellites.

Satellite	Type of sensor carrying on	Applications
Sentinel-1A Sentinel-1B	C-band radar medium spatial resolution	Land, ocean monitoring, ice detection, oil spill monitoring, ship detection tracking, flood mapping, monitoring of land-surface motion risks, mapping land-surface, forest, water and soil, agriculture
Sentinel-2A Sentinel-2B	Optical multispectral medium to moderate spatial resolution instruments	Land-cover, usage and change detection maps, geophysical variable maps (leaf chlorophyll content, leaf water content, leaf area index etc.), risk mapping, disaster relief
Sentinel-3A Sentinel-3B	Optical ocean and land colour moderate spatial resolution instrument, sea and land temperature radiometer, altimeter and microwave radiometer	Sea and land applications, sea and land temp, sea-surface and land-ice topography, coastal zones, in land-water and sea ice topography
Sentinel-4A Sentinel-4B	Optical and microwave low resolution sensors	Geostationary atmospheric chemistry missions

Sentinel-5A	UV-VIS-NIR-SWIR push broom	Low earth orbit
Sentinel-5B	grating spectrometer - TROPOMI	atmospheric chemistry
Sentinel-6A	moderate resolution sensor	missions
Sentinel-6A	Altimetry sensors	Altimetry mission
Sentinel-6B		

### 2.1.1 Landsat Satellites.

One of the most prevailing satellite data sets nowadays is the one from the Landsat satellites, which is also used in this thesis extensively. Landsat is the result of an idea of an establishment of a remote sensing satellite program to gather facts about the natural resources of our planet (Figure 2.2). Landsat gave a new option for terrain data, which weather satellites couldn't do it. Table 2.3 gives briefly some of the main specifications of the main Landsat platforms used today, while Table 2.4 gives specifications of the sensors used (<http://landsat.gsfc.nasa.gov>).

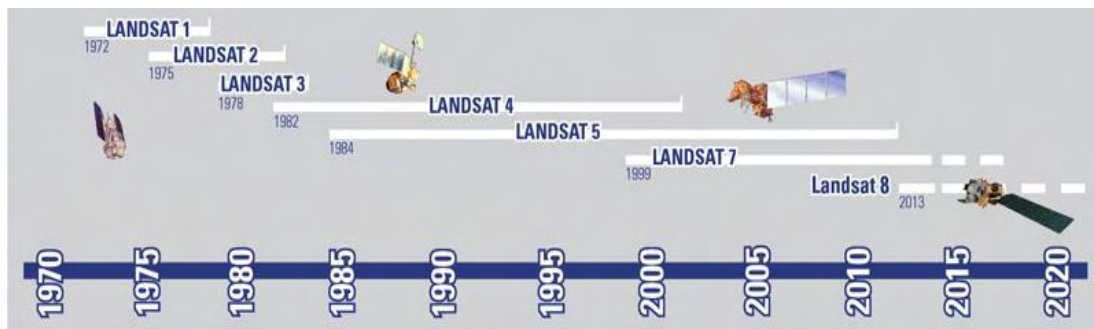


Figure 2.2. History of Landsat missions (<http://landsat.gsfc.nasa.gov>)

Table 2.3. Landsat Specifications

	Landsat 5		Landsat 7		Landsat 8	
Launch History	March 1, 1984-	January 2013	April 15, 1999 -	now	February 11, 2013-	now
Vehicle	Delta 3920		Delta II		Atlas-V rocket	
Site	Vandenberg	Air Force Base, California	Vandenberg	Air Force Base, California	Vandenberg	Air Force Base, California
Orbit	Worldwide Reference System-2 (WRS-2) path/row system					

Sun-synchronous orbit at an altitude of 705 km (438 mi)

Repeat cycle: 16 days

Inclined 98.2° Circles the Earth every 98.9 minutes

	Equatorial crossing time: 9:45 a.m. +/- 15 minutes	Equatorial crossing time: 10:00 a.m. +/- 15 minutes	Equatorial crossing time: 10:00 a.m. +/- 15 minutes
Sensors	Multispectral Scanner (MSS) & Thematic Mapper (TM)	Enhanced Thematic Mapper Plus (ETM+)	Operational Land Imager (OLI) & Thermal Infrared Sensor (TIRS)
Scene Size	170 km x 185 km	170 km x 185 km	170 km x 185 km
Design Life	Min. 3 years	Min. 5 years	Min. 5 years

Table 2.4. Sensors on-board Landsat.

Sensor	Band Wavelengths	Pixel Size (m)
Multispectral	Band 4 Visible green (0.5 - 0.6 $\mu\text{m}$ )	60
Scanner (MSS)	Band 5 Visible red (0.6 - 0.7 $\mu\text{m}$ )	60
	Band 6 Near-Infrared (0.7 - 0.8 $\mu\text{m}$ )	60
	Band 7 Near-Infrared (0.8 - 1.1 $\mu\text{m}$ )	60
Thematic Mapper (TM)	Band 1 Visible (0.45 - 0.52 $\mu\text{m}$ )	30
	Band 2 Visible (0.52 - 0.60 $\mu\text{m}$ )	30
	Band 3 Visible (0.63 - 0.69 $\mu\text{m}$ )	30
	Band 4 Near-Infrared (0.76 - 0.90 $\mu\text{m}$ )	30
	Band 5 Near-Infrared (1.55 - 1.75 $\mu\text{m}$ )	30
	Band 6 Thermal (10.40 - 12.50 $\mu\text{m}$ )	120
	Band 7 Mid-Infrared (2.08 - 2.35 $\mu\text{m}$ )	30

Enhanced Thematic Mapper Plus (ETM+)	Band 1 Visible (0.45 - 0.52 $\mu\text{m}$ )	30
	Band 2 Visible (0.52 - 0.60 $\mu\text{m}$ )	30
	Band 3 Visible (0.63 - 0.69 $\mu\text{m}$ )	30
	Band 4 Near-Infrared (0.77 - 0.90 $\mu\text{m}$ )	30
	Band 5 Near-Infrared (1.55 - 1.75 $\mu\text{m}$ )	30
	Band 6 Thermal (10.40 - 12.50 $\mu\text{m}$ )	60
	Band 7 Mid-Infrared (2.08 - 2.35 $\mu\text{m}$ )	30
	Band 8 Panchromatic (PAN) (0.52 - 0.90 $\mu\text{m}$ )	15
Operational Land Imager (OLI)	Band 1 Visible (0.43 - 0.45 $\mu\text{m}$ )	30
	Band 2 Visible (0.450 - 0.51 $\mu\text{m}$ )	30
	Band 3 Visible (0.53 - 0.59 $\mu\text{m}$ )	30
	Band 4 Red (0.64 - 0.67 $\mu\text{m}$ )	30
	Band 5 Near-Infrared (0.85 - 0.88 $\mu\text{m}$ )	30
	Band 6 SWIR 1 (1.57 - 1.65 $\mu\text{m}$ )	30
	Band 7 SWIR 2 (2.11 - 2.29 $\mu\text{m}$ )	30
	Band 8 Panchromatic (0.50 - 0.68 $\mu\text{m}$ )	15
	Band 9 Cirrus (1.36 - 1.38 $\mu\text{m}$ )	30
Thermal Infrared Sensor (TIRS)	Band 10 TIRS 1 (10.6 - 11.19 $\mu\text{m}$ )	100
	Band 11 TIRS 2 (11.5 - 12.51 $\mu\text{m}$ )	100

From Table 2.4 it is obvious that, the spectral bands of the Operational Land Imager (OLI) sensor provide some enhancement from prior Landsat instruments. There is an addition of two new spectral bands: a deep blue visible channel (band 1) specifically designed for water resources and coastal zone investigation, and a new infrared channel (band 9) for the detection of cirrus clouds. The TIRS instrument collects two spectral bands for the wavelength covered by a single band on the previous TM and ETM+ sensors. More information can be found at: [http://landsat.usgs.gov/band\\_designations\\_landsat\\_satellites.php](http://landsat.usgs.gov/band_designations_landsat_satellites.php). Landsat 8 used in this thesis only for validation purposes.



(a)



(b)

Figure 2.3. Landsats: (a) L5, (b) L7



(a)



(b)

Figure 2.4. Landsat 8: (a) Launch, (b) On the air



Figure 2.5. OLI and TIRS sensors mounting

### 2.1.2 Terra and Aqua Satellites

Another two satellites used in this study are NASA's Earth Observing System Terra and Aqua. Both travel north to south. Terra loops over the equator in the morning, while Aqua moves in the opposite direction, passing south to north over the equator in the afternoon. Combining the images acquired from the visible part of the spectrum, a "true" or "natural" representation of the Earth's land, ocean, or atmosphere can be generated daily. Generally speaking, Terra explores the connections between Earth's atmosphere, land, snow and ice, ocean, and energy balance (<http://terra.nasa.gov/>). It carries mainly five state-of-the-art instruments which are shown on Table 2.5.

Table 2.5. Aqua and Terra instruments.

Aqua Instruments	Terra Instruments
Atmospheric Infrared Sounder (AIRS)	Advanced Spaceborne Thermal Emission and Reflection Radiometer (ASTER)
Advanced Microwave Sounding Unit (AMSU-A)	Clouds and the Earth's Radiant Energy System (CERES).
Humidity Sounder for Brazil (HSB),	Multi-angle Imaging SpectroRadiometer (MISR)
Advanced Microwave Scanning Radiometer for EOS (AMSR-E)	Moderate Resolution Imaging Spectroradiometer (MODIS)
Moderate Resolution Imaging Spectroradiometer (MODIS)	Measurements of Pollution in the Troposphere (MOPITT)
Clouds and the Earth's Radiant Energy System (CERES).	

Aqua similarly with Terra carries six state-of-the-art instruments in a near-polar low-Earth orbit. Each instrument has unique characteristics and capabilities, and all six serve together to form a powerful package for Earth observations. The instruments are also shown on Table 2.5. The combination of Terra and Aqua, especially using MODIS which is common to both of them, provides a complete view of the Earth every day.

### 2.1.3 Moderate Resolution Imaging Spectroradiometer (MODIS)

MODIS is a key instrument aboard the [Terra \(EOS AM\)](#) and [Aqua \(EOS PM\)](#) satellites (Figure 2.6). According to the above, Terra MODIS and Aqua MODIS are viewing the entire Earth's surface every 1 to 2 days, acquiring data in 36 spectral bands, or groups of wavelengths (Table 2.6). These data improve the understanding of global dynamics and processes occurring on the land, the oceans, and the lower atmosphere (<http://modis.gsfc.nasa.gov/about/>).

Table 2.6. MODIS bands.

Band	Bandwidth <sup>1</sup>	Spectral Radiance <sup>2</sup>	Required SNR <sup>3</sup>
1	620 - 670	21.8	128
2	841 - 876	24.7	201
3	459 - 479	35.3	243
4	545 - 565	29.0	228
5	1230 - 1250	5.4	74
6	1628 - 1652	7.3	275
7	2105 - 2155	1.0	110
8	405 - 420	44.9	880
9	438 - 448	41.9	838
10	483 - 493	32.1	802
11	526 - 536	27.9	754
12	546 - 556	21.0	750
13	662 - 672	9.5	910
14	673 - 683	8.7	1087
15	743 - 753	10.2	586
16	862 - 877	6.2	516
17	890 - 920	10.0	167
18	931 - 941	3.6	57
19	915 - 965	15.0	250
20	3.660 - 3.840	0.45 (300K)	0.05



21	3.929 - 3.989	2.38 (335K)	2.00
22	3.929 - 3.989	0.67 (300K)	0.07
23	4.020 - 4.080	0.79 (300K)	0.07
24	4.433 - 4.498	0.17 (250K)	0.25
25	4.482 - 4.549	0.59 (275K)	0.25
26	1.360 - 1.390	6.00	150 (SNR)
27	6.535 - 6.895	1.16 (240K)	0.25
28	7.175 - 7.475	2.18 (250K)	0.25
29	8.400 - 8.700	9.58 (300K)	0.05
30	9.580 - 9.880	3.69 (250K)	0.25
31	10.780 - 11.280	9.55 (300K)	0.05
32	11.770 - 12.270	8.94 (300K)	0.05
33	13.185 - 13.485	4.52 (260K)	0.25
34	13.485 - 13.785	3.76 (250K)	0.25
35	13.785 - 14.085	3.11 (240K)	0.25
36	14.085 - 14.385	2.08 (220K)	0.35

<sup>1</sup> Bands 1 to 19 are in nm; Bands 20 to 36 are in  $\mu\text{m}$

<sup>2</sup> Spectral Radiance values are ( $\text{W}/\text{m}^2 \cdot \mu\text{m}\cdot\text{sr}$ )

<sup>3</sup> SNR = Signal-to-noise ratio

According to the producer, MODIS' specifications are shown on Table 2.7 (taken from <http://modis.gsfc.nasa.gov/about/specifications.php>):

Table 2.7. MODIS specifications.

MODIS SPECIFICATIONS	
Orbit:	705 km, 10:30 a.m. descending node (Terra) or 1:30 p.m.

---

	ascending node (Aqua), sun-synchronous, near-polar, circular
Scan Rate:	20.3 rpm, crosstrack
Swath	2330 km (cross track) by 10 km (along track at nadir)
Dimensions:	
Telescope:	17.78 cm diam. off-axis, afocal (collimated), with intermediate field stop
Size:	1.0 x 1.6 x 1.0 m
Weight:	228.7 kg
Power:	162.5 W (single orbit average)
Data Rate:	10.6 Mbps (peak daytime); 6.1 Mbps (orbital average)
Quantization:	12 bits
Spatial	250 m (bands 1-2)
Resolution:	500 m (bands 3-7) 1000 m (bands 8-36)
Design Life:	6 years

---

#### 2.1.4 MODIS data products

There are many standard MODIS data products ready to be used by scientists, according to their topic. Table 2.8 illustrates MODIS products in use today.

Table 2.8. MODIS products.

---

Category	Name	Characterization
Calibration	MOD 01	Level-1A Radiance Counts
	MOD 02	Level-1B Calibrated Geolocated Radiances
	MOD 03	Geolocation Data Set
Atmosphere	MOD 04	Aerosol Product
	MOD 05	Total Precipitable Water (Water Vapor)
	MOD 06	Cloud Product
	MOD 07	Atmospheric Profiles

---

Land	MOD 08	Gridded Atmospheric Product
	MOD 35	Cloud Mask
	MOD 09	Surface Reflectance
	MOD 11	Land Surface Temperature & Emissivity
	MOD 12	Land Cover/Land Cover Change
	MOD 13	Gridded Vegetation Indices (Max NDVI & Integrated MVI)
	MOD 14	Thermal Anomalies, Fires & Biomass Burning
	MOD 15	Leaf Area Index & FPAR
	MOD 16	Evapotranspiration
	MOD 17	Net Photosynthesis and Primary Productivity
Cryosphere	MOD 43	Surface Reflectance
	MOD 44	Vegetation Cover Conversion
	MOD 10	Snow Cover
Ocean	MOD 29	Sea Ice Cover
	-	Angstrom Exponent
	-	Aerosol Optical Thickness
	-	Chlorophyll a
	-	Downwelling diffuse attenuation coefficient at 490 nm
	-	Level 2 Flags
	-	Photosynthetically Available Radiation
	-	Particulate Inorganic Carbon
	-	Particulate Organic Carbon
	-	Sea Surface Temperature Quality
	-	Sea Surface Temperature Quality - 4um
	-	Remote Sensing Reflectance
	-	Sea Surface Temperature
	-	Sea Surface Temperature 4um

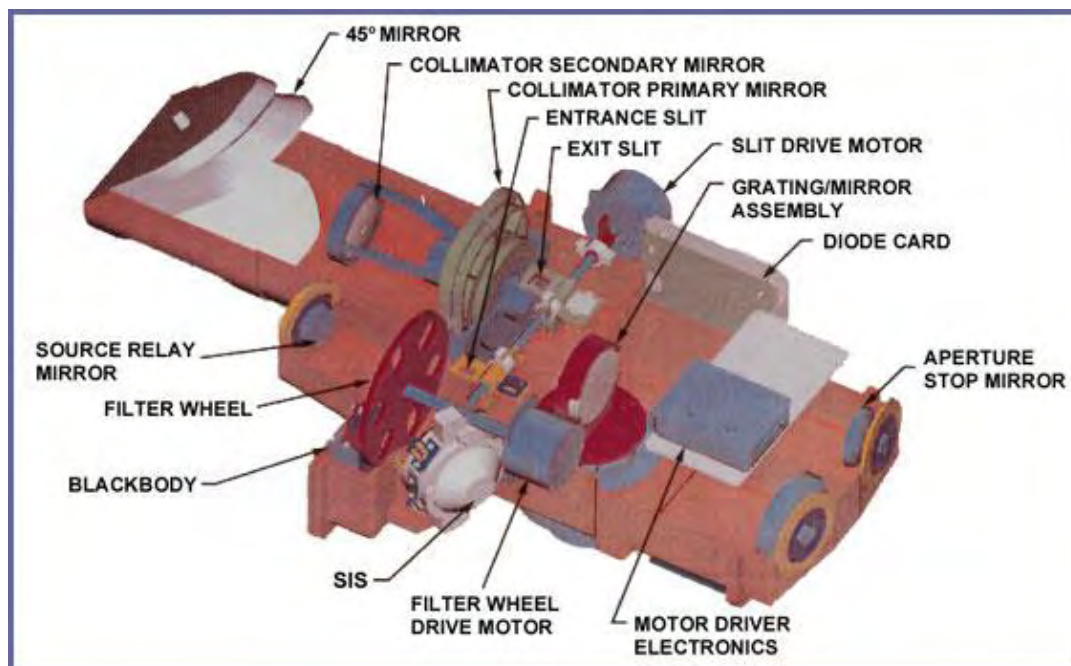


Figure 2.6. MODIS instrument (taken from [modis.gsfc.nasa.gov](http://modis.gsfc.nasa.gov))

## 2.2 The estimation of ET (Review of Methods)

Traditionally, evapotranspiration (ET) can be measured over a homogeneous surface using conventional techniques such as Bowen Ratio (BR), eddy covariance (EC), and lysimeter systems. However these techniques cannot be applied to the majority of cases worldwide for different reasons. The most convenient methodology for many years was the theoretically computation of ET.

## 2.3 Non Remote Sensing based methodologies

Evapotranspiration (ET) is a very important factor for energy, hydrologic, carbon and nutrient cycles and a key component of water balance. ET belongs to the category of secondary meteorological parameters. Actual or reference ET is a complex phenomenon, combining energy and water balance together, employing the scientific community for many decades. For the conventional calculation of Evapotranspiration, techniques are grouped into the following categories (Table 2.9):

Table 2.9. Calculation of evapotranspiration: Categories.

Type of methodology	Description
Hydrological	Water balance
Micrometeorological	Mass and energy transfer
Climatological	Empirical Relationships Based On Air Temperature
	Computational Relations Based On Solar Radiation
	Combined Computational Relations

Category 1: ET is calculated as a residual between parameters of water balance which of course can be measured or estimated (Thornthwaite, 1948; Blaney-Griddle, 1950; Hargreaves, 1974; Linacre, 1977). These methods are difficult to apply because many water balance parameters cannot be computed with satisfactory accuracy.

Category 2: ET is calculated through natural processes of mass and energy transfer in the boundary layer above the ground (Makkink, 1957; Stanhill, 1961; Turk, 1961; Jensen & Haise, 1963; Tanner 1967; Caprio, 1974; Idso *et. al.*, 1977). This method is more experimental and also not easy applicable due to the lack of sufficient measurements (insufficient number of meteorological stations and frequency data acquisition).

Category 3: It is the most prevailing category (Penman, 1948; Slatyer and Mac Ilroy, 1961; Penman-Monteith, 1965; Van Banel, 1966; Priestley-Taylor, 1972; Monteith, 1981). The reliability of these methods increases from the third to the first subcategory (Liakatas and Anadranistakis, 1992).

Since the calculation of ET is needed to a very wide range of applications, it is the type of the final application which is the criterion of the selection of the ET computation sub-method. Below this is a summary of the most prevailing equations using for the estimation of ET today:

## 2.4 The computation of potential evapotranspiration

### 2.4.1 Penman method

One of the most famous equations for the computation of potential evapotranspiration is Penman method (Penman, 1948; Michalopoulou and Papaioannou, 1991; Kerkides *et al.*, 1996). This is a combination of mass and energy transfer equation (2.1):

$$ET_{pen} = \frac{0.408R_n \Delta + \gamma f(u)(e_s - e_a)}{\Delta + \gamma} \quad (2.1)$$

where:

ET : reference evapotranspiration (mm day<sup>-1</sup>)

R<sub>n</sub> : net radiation (MJ m<sup>-2</sup> day<sup>-1</sup>)

Δ : slope vapour pressure curve (KPa°C<sup>-1</sup>)

γ : psychrometric constant (KPa°C<sup>-1</sup>)

e<sub>s</sub> : saturation vapour pressure (KPa)

e<sub>a</sub> : actual vapour pressure (KPa)

f(u) : «the wind function»

f(u)=0.263(1+0.537u) (mm day<sup>-1</sup> KPa<sup>-1</sup>)

where u is wind speed at 2 m above ground (m s<sup>-1</sup>)

### 2.4.2 Penman-Monteith method (1965)

This is a variation of Penman method:

$$\lambda ET = \frac{\Delta(R_n - G) + \rho_a c_a \frac{e_s - e_a}{r_a}}{\Delta + \gamma(1 + \frac{r_s}{r_a})} \quad (2.2)$$

where:

λ : latent heat of vaporization

λ= 2.45 MJ Kg<sup>-1</sup>

ET : reference evapotranspiration (mm day<sup>-1</sup>)

R<sub>n</sub> : net radiation (MJ m<sup>-2</sup> day<sup>-1</sup>)

- $\Delta$  : slope vapour pressure curve (KPa<sup>o</sup>C)  
 $\gamma$  : psychrometric constant (KPa<sup>o</sup>C<sup>-1</sup>)  
 $e_s$  : saturation vapour pressure (KPa)  
 $e_a$  : actual vapour pressure (KPa)  
 $G$  : soil heat flux (MJ m<sup>-2</sup> day<sup>-1</sup>)  
 $\rho_a$  : mean air density at constant pressure (Kg m<sup>-3</sup>)  
 $c_p$  : specific heat at constant pressure (MJ Kg<sup>-1o</sup>C<sup>-1</sup>)  
 $r_s$  : canopy resistance (s m<sup>-1</sup>)  
 $r_a$  : aerodynamic resistance (s m<sup>-1</sup>)

#### 2.4.3 FAO Penman Monteith method (Allen et al., 1998)

The panel of experts recommended the adoption of the Penman-Monteith combination method as a new standard for reference evapotranspiration and advised on procedures for calculation of the various parameters. By defining the reference crop as a hypothetical crop with an assumed height of 0.12 m having a surface resistance of 70 s m<sup>-1</sup> and an albedo of 0.23, closely resembling the evaporation of an extension surface of green grass of uniform height, actively growing and adequately watered, the FAO Penman-Monteith method was developed. The method overcomes shortcomings of the previous FAO Penman method and provides values more consistent with actual crop water use data worldwide (Allen *et al.*, 1998):

$$ET_o = \frac{0.408(R_n - G)\Delta + \gamma\left(\frac{900}{T_{mean} + 273}\right)u_2(e_s - e_a)}{\Delta + \gamma(1 + 0.34u_2)} \quad (2.3)$$

where:

- $T_{mean}$ : Mean temperature (°C)  
 $u_2$  : wind speed at 2 m height

#### 2.4.4 Priestley-Taylor method (1972)

Priestley-Taylor method is based on the hemi-empirical equation (2.4):

$$\lambda ET = \alpha \frac{\Delta}{\Delta + \gamma} (R_n - G) \quad (2.4)$$

where:

- E : reference evapotranspiration (mm day<sup>-1</sup>)
- $\lambda$  : latent heat of vaporization,  $\lambda=2.45$  MJ Kg<sup>-1</sup>
- R<sub>n</sub> : Net Radiation (MJ m<sup>-2</sup> day<sup>-1</sup>)
- $\Delta$  : slope vapour pressure curve (KPa°C)
- $\gamma$  : psychrometric constant (KPa°C<sup>-1</sup>)
- $\alpha$  : empirical constant (unitless)

#### 2.4.5 Partial equations for the computation of reference evapotranspiration

For every meteorological station, having altitude (z) and latitude ( $\phi$ ):

- Air pressure:

$$P = 101.3 \left[ \frac{293 - 0.0065z}{293} \right]^{5.26} \quad (2.5)$$

- Psychrometric constant:

$$\gamma = 0,665 \times 10^{-3} P \quad (2.6)$$

For each Julian day j (from 1 to 365 or 366 for lap years):

- Solar declination:

$$\delta = 0,409 \sin\left(\frac{2\pi}{365}j - 1.39\right) \text{ (rad)} \quad (2.7)$$

- The inverse relative distance Earth-Sun:

$$d_r = 1 + 0.033 \cos\left(\frac{2\pi}{365}j\right) \text{ (unitless)} \quad (2.8)$$

- The sunset hour angle:

$$\omega_s = \arccos(-\tan\phi \tan\delta) \text{ (rad)} \quad (2.9)$$



- The Extraterrestrial radiation for hourly or shorter periods:

$$R_a = \frac{24 \times 60}{\pi} G_{sc} d_r (\omega_s \sin \phi \sin \delta + \cos \phi \cos \delta \sin \omega_s) \quad (2.10)$$

where  $G_{sc}=0.082 \text{ MJ m}^{-2} \text{ min}^{-1}$

- The daylight hours:

$$N = \frac{24}{\pi} \omega_s \quad (2.11)$$

Short wave solar radiation,  $R_s$ , can be calculated with the Angstrom formula, which relates solar radiation to extraterrestrial radiation and relative sunshine duration:

$$R_s = R_a \left( a + b \frac{n}{N} \right) \quad (2.12)$$

where  $a=0.25$  and  $b=0.5$  are the suggested values.

- The actual vapour pressure:

$$e_a = \frac{RH}{100} \left[ \frac{e^0(T_{max}) + e^0(T_{min})}{2} \right] \quad (2.13)$$

where:

$$e^0(T) = 0.6108 \exp \left( \frac{17.27T}{T+237.3} \right) \quad (2.14)$$

is vapour pressure for temperature  $T$ .

- The saturation vapour pressure:

$$e_s = \frac{e_a}{RH} \quad (2.15)$$

- Net Radiation:

$$R_n = (1 - r) R_s - \sigma \left( \frac{T_{max}^4 + T_{min}^4}{2} \right) (0.34 - 0.14 \sqrt{e_a}) \left[ 1.35 \frac{R_s}{R_{s0}} - 0.35 \right] \quad (2.16)$$

Where:

$$R_{s0} = (0.25 + 0.5) R_a \quad (2.17)$$

is the solar radiation for totally clear sky,  $r$  is the albedo and  $\sigma$  is the Stefan Boltzmann constant  $\sigma=4.903 \cdot 10^{-9} \text{ MJ K}^{-4} \text{ m}^{-2} \text{ day}^{-1}$ .

- The slope vapour pressure curve:

$$\Delta = \frac{4098 \left[ 0.6108 \exp \left( \frac{17.27 T_{mean}}{T_{mean} + 237.3} \right) \right]}{(T_{mean} + 237.3)^2} \quad (2.18)$$

## 2.5 The computation of actual evapotranspiration

### 2.5.1 Using the complementary relationship

Bouchet (1963) suggested a relationship between actual and reference evapotranspiration under constant energy input:

$$dET_a + dET_p = 0 \quad (2.19)$$

Morton (1978) suggested that considering a wet environment  $ET_p=ET_a=ET_w$ , where  $ET_w$  is wet-environment ET, while considering a dry soil,  $ET_a=0$ , and  $ET_p=2ET_w$ . From these boundary conditions the «complementary relationship» is:

$$ET_a + ET_p = 2ET_w \quad (2.20)$$

Priestley and Taylor (1972), De Bruin and Keijman (1979), and Ozdogan *et al*, (2006) examined among others the complementary relationship and especially the constant  $a$  of the Priestley Taylor equation (2.4). Menzel *et al*. (2006) from the Center for Environmental Systems Research, University of Kassel, Germany suggest the value of 1.26 for humid regions ( $RH>60\%$ ) and the value of 1.74 for dry regions ( $RH<60\%$ ).

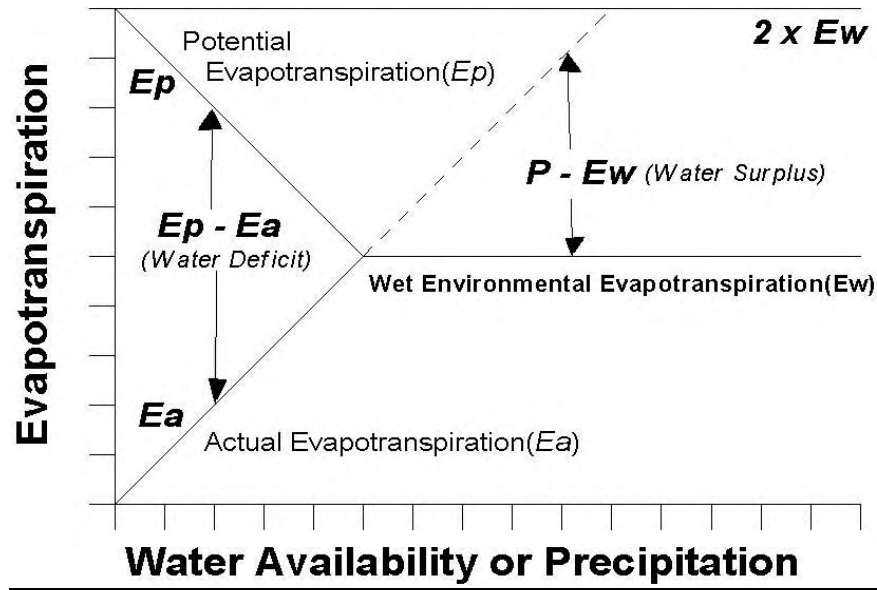


Figure 2.7. Complementary Relationship (retrieved from Kondoh, 1994).

Schematic representation of the Complementary Relationship, where  $ET_a$  is actual evapotranspiration,  $ET_p$  is potential evapotranspiration, and  $ET_w$  is wet-environment evapotranspiration. The x axis represents increasing wetness (from Ozdogan *et al.*, 2006).

From the complementary relationship actual evapotranspiration can be computed:

$$ET_a = 2ET_w - ET_0 \quad (2.21)$$

$ET_w$  can be computed from Priestley Taylor method defining the constant  $\alpha$  to each study and region.  $ET_0$  can be computed from FAO Penman-Monteith method (Allen *et al.*, 1998) or the classic Penman equation (1948).

## 2.6 Remote Sensing based Methodologies of ET Estimation

Since the 1980s, there has been an increasing effort to develop methods for estimating ET from remote sensing data. Gowda *et al.* (2007); Kalma *et al.* (2008); Li *et al.* (2009); and McMahon *et al.* (2013) offer a comprehensive survey of published methods known to date, pointing out the main issues and challenges to address in the future. There are also a lot of scientific works related with remote sensing for the estimation of ET in

Greece (Dalezios *et al.*, 2002; Loukas *et al.*, 2004; Loukas *et al.*, 2005; Tsouni *et al.*, 2005; Kanellou *et al.*, 2006; Loukas *et al.*, 2006; Tsouni *et al.*, 2008; Blanta *et al.*, 2011; Dalezios *et al.*, 2011, Spiliotopoulos *et al.*, 2013). Generally, the commonly applied ET models using remote sensing data can be categorized into two types: semi-empirical methods and analytical methods. Semi-empirical methods are often accomplished by employing empirical relationships and making use of data mainly derived from remote sensing observations with minimum ground-based measurements, while the analytical methods involve the establishment of the physical processes at the scale of interest with varying complexity and requires a variety of direct and indirect measurements from the remote sensing technology and ground-based instruments (Li *et al.* 2009; McMahon *et al.* 2013).

The most prevailing group of methodologies today is the Energy Balance (EB) algorithms and more specifically the residual methods. Remote sensing based EB algorithms convert satellite sensed radiances into land surface characteristics such as albedo, leaf area index, vegetation indices, surface roughness, surface emissivity, and surface temperature to estimate ET as a “residual” of the land surface energy balance equation (2.22) (Gowda *et al.*, 2007):

$$LE = \lambda ET = R_n - H - G \quad (2.22)$$

where LE is the latent heat flux ( $\text{W/m}^2$ ),  $R_n$  is net radiation ( $\text{W/m}^2$ ), G is soil heat flux ( $\text{W/m}^2$ ) and H is sensible heat flux ( $\text{W/m}^2$ ). ( $\text{W/m}^2$ ) in latent heat flux can easily later converted to mm.

Most recent EB models differ mainly in how H is estimated (Gowda *et al.*, 2007). These models include the Two Source Model (TSM; Kustas and Norman, 1996), where the energy balance of soil and vegetation are modeled separately and then combined to estimate total LE; the Surface Energy Balance Algorithm for Land (SEBAL; Bastiaanssen *et al.*, 1998a; b) and Mapping Evapotranspiration with Internalized Calibration (METRIC; Allen *et al.*, 2007a ;b) that uses hot and cold pixels within the satellite images

to develop an empirical temperature difference equation; and the Surface Energy Balance Index (SEBI; Menenti and Choudhury, 1993) based on the contrast between wet and dry areas. Other variations of SEBI include the Simplified Surface Energy Balance Index (S-SEBI; Roerink *et al.*, 2000), and the Surface Energy Balance System (SEBS; Su, 2002). Other EB models are: the excess resistance ( $k_B^{-1}$ ) (Kustas and Daughtry, 1990; Su, 2002), the aerodynamic temperature parameterization models proposed by Crago *et al.* (2004) and Chávez *et al.* (2005), the beta ( $\beta$ ) approach (Chehbouni *et al.*, 1996), and most recently the ET Mapping Algorithm (ETMA; Loheide and Gorelick, 2005; Gowda *et al.*, 2007). Finally, Triangle Method (Goward *et al.*, 1985; Jiang and Islam, 1999) derived from a simple Crop Water Stress Index (CWSI), and Trapezoid Method (Moran *et al.*, 1994) after introducing a Water Deficit Index (WDI) for ET estimation based on the Vegetation Index/Temperature trapezoid to extend the application of CWSI over fully to partially vegetated surface areas (Li *et al.* 2009), must be mentioned. Soil-Vegetation-Atmosphere-Transfer (SVAT) models (Olioso *et al.*, 1999) are very effective but the role of remote sensing can be only supportive on them and thus they are not presented in this report.

Table 2.10. Prevailed Energy Balance Methodologies.

Abbreviation	Definition
TSM	Two Source Model (Kustas and Norman, 1996)
SEBAL	Surface Energy Balance Algorithm for Land (Bastiaanssen <i>et al.</i> , 1998a; b)
METRIC	Mapping Evapotranspiration with Internalized Calibration (Allen <i>et al.</i> , 2007a;b)
SEBI	Simplified Surface Energy Balance Index (Roerink <i>et al.</i> , 2000)
SEBS	Surface Energy Balance System (Su, 2002)
$k_B^{-1}$	The excess resistance (Kustas and Daughtry, 1990; Su, 2002)
Beta ( $\beta$ ) approach	Chehbouni <i>et al.</i> , 1996
ETMA	ET Mapping Algorithm (Loheide and Gorelick, 2005;

	Gowda <i>et al.</i> , 2007)
CWSI	Crop Water Stress Index (Jackson <i>et al.</i> 1981).
Triangle Method	Based on CWSI (Goward <i>et al.</i> , 1985; Jiang and Islam, 1999)
Trapezoid Method	Based on the application of CWSI over fully to partially vegetated surface areas (Moran <i>et al.</i> , 1994; Li <i>et al.</i> , 2009)

---

### 2.6.1 Surface Energy Balance Algorithm for Land (SEBAL)

The basic concept in SEBAL is the equation of surface energy balance (2.22), where LE is the latent heat flux ( $\text{W/m}^2$ ),  $R_n$  is net radiation ( $\text{W/m}^2$ ),  $G$  is soil heat flux ( $\text{W/m}^2$ ) and  $H$  is sensible heat flux ( $\text{W/m}^2$ ). ( $\text{W/m}^2$ ) in latent heat flux can easily later converted to precipitation height (mm). Net radiation can be computed from the land surface radiation balance:

$$R_n = (1-\alpha)R_{S\downarrow} + R_{L\downarrow} - R_{L\uparrow} - (1-\epsilon_0)R_{L\downarrow} \quad (2.23)$$

where  $\alpha$  is surface albedo,  $R_{S\downarrow}$  ( $\text{W/m}^2$ ) is incoming solar radiation,  $R_{L\downarrow}$  ( $\text{W/m}^2$ ) is incoming long wave radiation,  $R_{L\uparrow}$  ( $\text{W/m}^2$ ) is the outgoing long wave radiation, and  $\epsilon_0$  is broad band surface emissivity. Soil Heat Flux  $G$  ( $\text{W/m}^2$ ) can be empirically estimated using a function by Bastiaanssen (2000) which is based on albedo, surface temperature and NDVI.

$$G = \frac{T_s}{a} (0.0038a^2)(1 - 0.98NDVI^4) \times R_n \quad (2.24)$$

Where  $T_s$  is surface temperature in K and NDVI is normalized difference vegetation index. The third parameter of equation (2.22) is sensible heat flux ( $\text{W/m}^2$ ):

$$H = p \times C_p \times \frac{(dT)}{r_{ah}} \quad (2.25)$$

where  $p$  is air density ( $\text{kg/m}^3$ ) related with atmospheric pressure,  $C_p$  is air specific heat capacity ( $1004 \text{ Jkg}^{-1}\text{K}^{-1}$ ),  $T_s$  is surface temperature in  $^{\circ}\text{K}$ , and  $r_{ah}$  is aerodynamic resistance to heat transport ( $\text{sm}^{-1}$ ). The definition of the function  $dT$  vs  $T_s$  is maybe the most significant philosophy of SEBAL, where  $dT$  is the difference between the air temperature very near the surface (at 0.1 m above the zero plane displacement height) and the air temperature at 2 m above the zero plane displacement height (Waters *et al.*, 2002). SEBAL methodology suggests linear change in  $dT$  with  $T_s$  (Bastiaanssen, 1998a). Equation (2.25) has two unknown parameters. This is where initial values from the selection of “cold” and “hot” pixels are used. These pixels serve as a solution for defining  $dT$  vs.  $T_s$ .

“Cold” pixel can be defined as a generally wet, well-irrigated crop surface with full ground cover by vegetation. It is assumed that all energy is used to evaporate water, thus there is no sensible heat flux in this pixel ( $H=0$  and  $ET=R_n-G$ ).  $ET$  at the “cold” pixel is closely predicted by the  $ET$  rate from a large expanse of alfalfa vegetation (Bastiaanssen, 1998a). For the selection of “cold” pixel a very moist terrain has to be found and a pixel with high NDVI, low temperature and low albedo seems to apply this specification. On the other hand, “hot” pixel is defined as a pixel which has low NDVI, high albedo and high temperature. “Hot” pixel can be defined as a dry, bare agricultural field. It is assumed that all the energy is used to heat the surface in such a way that there is no latent heat flux there ( $ET=0$ ). In other words, a very dry terrain is selected as a “hot” pixel. It seems that the selection of a “hot” pixel is more difficult than the selection of cold pixel because there is a broader range of temperatures for hot pixel candidates. After the selection of hot and cold pixels the boundary conditions are now ready for solving the  $H$ . This is the first estimation of  $H$  assuming neutral atmospheric conditions. SEBAL, then, uses an iterative process to correct for atmospheric instability caused by buoyancy effects of surface heating applying Monin-Obukhov theory (1954). More details about atmospheric stability correction equations can be found at the

original SEBAL papers (Bastiaanssen *et al.*, 1998a; 1998b). After the initial computation of H, new values of dT are computed for the “cold” and “hot” pixels and new values of a and b are computed. A corrected value for H is then computed and the stability correction is repeated until H stabilizes. The final step is the calculation of  $\lambda ET$  from the equation (2.22).

### 2.6.2 METRIC

A full description of METRIC<sup>TM</sup> can be found in Allen *et al.* (2007a). METRIC<sup>TM</sup> is based on SEBAL but with three main differences. The first is that METRIC does not assume  $H=0$  or  $LE=R_n-G$  at the hot pixel. Instead, it calculates the ET of the hot pixel by performing a soil water budget, using meteorological data from a nearby weather station, to verify that ET is indeed zero for that pixel (Gowda *et al.*, 2007). For the cold pixel,  $ET_{cold}$  is set equal to  $1.05 \cdot ET_r$ , where  $ET_r$  is the hourly crop reference (like alfalfa) ET calculated using the standardized ASCE Penman-Monteith equation applied to local meteorological observations. The second difference is that METRIC<sup>TM</sup> selects extreme pixels purely in an agricultural setting, where particularly the cold pixel needs to have biophysical characteristics (h or LAI) similar to the reference crop (e.g. alfalfa). The third difference is that METRIC uses the alfalfa reference evapotranspiration fraction ( $ET_rF$ ) mechanism to extrapolate instantaneous LE flux to daily ET rates instead of using the  $\Lambda$ .

The evaporative fraction ( $ET_rF$ ) can be defined as the fraction of the actual  $ET_a$  by the potential  $ET_r$  on an instantaneous basis that is computed from weather station data at overpass time.  $ET_rF$  is constant over the day and can be described as:

$$ET_rF = \frac{ET_{inst.}}{ET_r} \quad (2.26)$$

The  $ET_rF$  is the ratio of ET (remotely sensed instantaneous ET) to the reference  $ET_r$ . The benefits of using ET is the better calibration of temperature range (i.e., at the cold and hot pixels) as well as the ability to account for general advection impacts on ET.



Disadvantages are the requirement for relatively high-quality weather data on an hourly or shorter time step and reliance on the accuracy of the  $ET_r$  estimate (Gowda *et al.*, 2007). More details about differences between METRIC and SEBAL are described at chapter 4.

### 2.6.3 SEBI

SEBI first proposed by Menenti and Choudhury (1993), along with its derivatives like S-SEBI (Simplified-SEBI), SEBS, etc., are typically single-source energy balance models based on the contrast between dry and wet limits to derive pixel by pixel ET and EF from the relative evaporative fraction when combined with surface parameters derived from remote sensing data and a certain amount of ground-based variables measured at local and/or regional scale (Li *et al.*, 2009). The dry (wet) limit, no matter how it was specifically defined, often has the following characteristics: 1) generally maximum (minimum) surface temperature, 2) usually low or no (high or maximum) ET. In the SEBI method, the dry limit is assumed to have a zero surface ET (latent heat flux) for a given set of boundary layer characteristics (potential temperature, wind speed and humidity, etc.). So, the sensible heat flux is then equal to the surface available energy (Van den Hurk 2001). The minimum surface temperature can be derived from the wet limit where the surface is regarded to evaporate potentially and the ET can be calculated from Penman-Monteith equation. The relative evaporative fraction can be then calculated by interpolating the observed surface temperature with the min and max surface temperature giving finally the form:

$$1 - SEBI = \frac{LE}{LE_p} \quad (2.27)$$

SEBI is a function of T and friction velocity for all the dry and wet boundary conditions, respectively, and varies between 0 (for actual=potential ET) and 1 (for no ET) (Li *et al.*, 2009).

#### 2.6.4 SEBS

Su (2002) developed SEBS using the SEBI concept. In SEBS there is a distinction between the Atmospheric Boundary Layer and the Monin-Obukhov Atmospheric Surface Layer (ASL). SEBS requires theoretically defined wet and dry boundary conditions to estimate H. Input of SEBS include remote sensing derived land and ground parameters like LAI, fractional vegetation cover, albedo, wind speed, humidity and air temperature. The main limitation of SEBS is the requirement of aerodynamic roughness height. The main advantages of SEBS are 1) the uncertainty from the surface temperature or meteorological variables in SEBS can be limited with consideration of the energy balance in the limiting cases, 2) the new formulation of roughness height for heat transfer and 3) actual turbulent heat fluxes are not required (Gowda *et al.*, 2007; Li *et al.*, 2009; Byun *et al.*, 2014).

#### 2.6.5 S-SEBI

Roerink *et al.*, (2000), developed S-SEBI as a simplified method derived from SEBS to estimate surface fluxes from remote sensing data. The model is based also on  $\Lambda$  and the contrast between areas with extreme wet and extreme dry temperature (Gowda *et al.*, 2007). The evaporative fraction is bounded now by the dry and wet limits and formulated by interpolating the albedo dependent surface temperature between the albedo dependent maximum surface temperature and the albedo dependent minimum surface temperature (Li *et al.*, 2009). This can be expressed as:

$$EF = \frac{T_{s,max} - T_s}{T_{s,max} - T_{s,min}} \quad (2.28)$$

The disadvantage of this method is that extreme  $T_s$  values cannot always be found on every acquired image. On the other hand S-SEBI is a simpler method that does not need additional meteorological data, and it does not require roughness length as in the case of SEBS (Gowda *et al.*, 2007).

### 2.6.6 TSM

TSM methodology belongs to the category of “two-source approach” proposed by Shuttleworth and Guerney (1990). TSM first computes the EB of the soil and then the EB of vegetation separately. After these two independent calculations TSM combines the results to estimate the total ET. Although TSM does not require additional meteorological information, it requires some parameterizations related with vegetation components and turbulence exchange of energy and mass. The energy exchange is based on resistances to heat and momentum transport, while the sensible heat fluxes are estimated by the temperature gradient-resistance system (Gowda *et al.*, 2007). Other variables like radiometric temperatures, resistances, sensible and latent heat fluxes and soil components are derived by iterative procedures based on vegetation cover fraction and maximum potential canopy transpiration flux (Gowda *et al.*, 2007). One of the main disadvantages of this method is the incorporation of some semi-empirical submodels which are related to LAI and soil fraction cover, which can be easily lead to remarkable errors through the procedure.

### 2.6.7 TRIANGLE METHOD

Goward *et al.*, (1985) proposed the  $T_s$  versus VI triangle relationship which is characterized by two physical bounds: the upper decreasing dry and lower nearly horizontal wet edges (Tang *et al.*, 2010). The edges represent two limiting cases of soil moisture and evaporative fraction for each VI value. In other words at the dry edge there are low values of soil moisture, while at the wet edge potential ET is reaching.

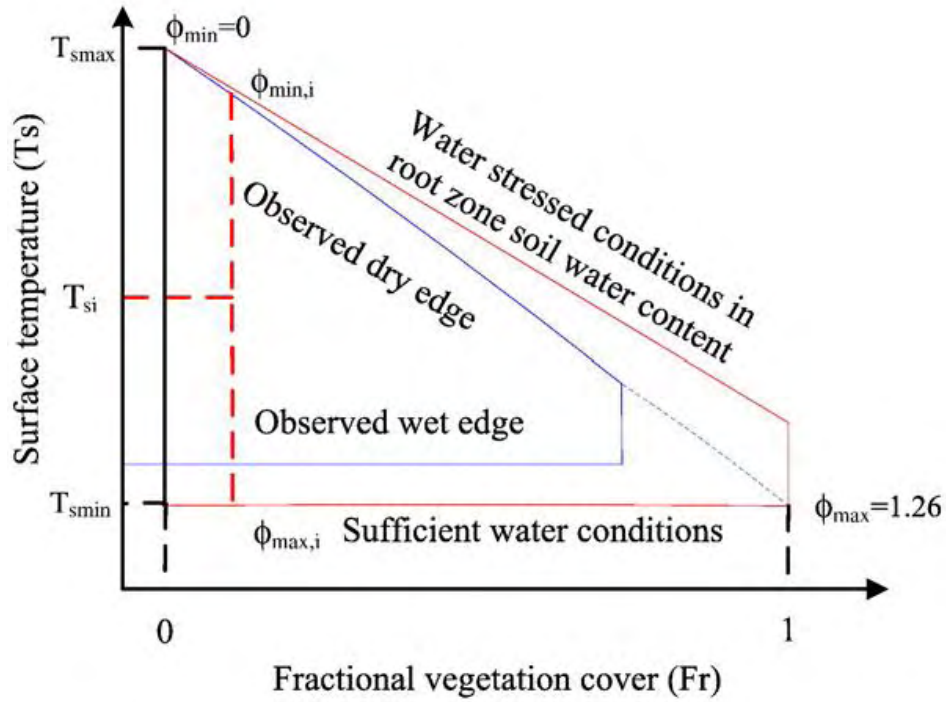


Figure 2.8. Schematic diagram of triangular  $T_s$  versus VI relationship (taken from Tang *et al.*, 2010).

Jiang and Islam (1999) proposed the Priestley-Taylor formulation adjusted to fully remotely sensed data. This extension has been employed to estimate regional EF and ET and can be expressed as:

$$LE = \phi[(R_n - G) \frac{\Delta}{\Delta + \gamma}] \quad (2.29)$$

Where  $\phi$  is a combined-effect parameter which accounts for aerodynamic resistance (dimensionless), while the  $R_n$ ,  $G$ ,  $\Delta$ , and  $\gamma$  are the Priestley-Taylor already known parameters.  $\phi$  ranges from 0 to 1.26 (Li *et al.*, 2009; Tang *et al.*, 2010) and can be derived using a two-step interpolation scheme from the wet and dry edges in the  $T_s$ -VI triangular space.  $\phi_{\min}=0$  and  $\phi_{\max}=1.26$  correspond to the driest bare soil pixel and the global wettest pixel respectively. This pixel assumed to have the largest NDVI and the lowest  $T_s$  values. After these initial conditions,  $\phi_{\min,i}$  for each NDVI interval (i) is linearly interpolated with NDVI between  $\phi_{\min}$  and  $\phi_{\max}$ , while  $\phi_{\max,i}$  for each NDVI interval (i) is calculated using the lowest surface temperature within that NDVI interval. It seems that  $\phi_i$  within NDVI interval is linearly increased with the decrease of  $T_s$  between  $\phi_{\min,i}$

and  $\phi_{\max,i}$  (Li *et al.*, 2009). Carlson *et al.*, (1995) showed that the scatter plots of  $T_s$ -VI seemed to depend more on the number of pixels rather than the spatial resolutions. Since then,  $T_s$ -VI triangle/trapezoid method can be found in many studies working with different sensors (Diak *et al.*, 1995; Batra *et al.*, 2006).

#### 2.6.8 TRAPEZOID METHOD

The basis of the trapezoid method is the Crop Water Stress Index (CWSI) developed by Jackson *et al.* (1981). CWSI is a measure of the relative transpiration rate occurring from a plant at the time of measurement using a measure of plant temperature and the vapor pressure deficit which is a measurement of the dryness of the air. CWSI is only appropriate for applying to full-cover vegetated areas and bare soils at local and regional scales. Based on the CWSI, Moran *et al.* (1994) introduced the Water Deficit index (WDI) as:

$$WDI = 1 - \frac{ET_a}{ET_p} \quad (2.30)$$

Where  $ET_a$  is actual Evapotranspiration and  $ET_p$  is potential Evapotranspiration. WDI is based on the VI-T trapezoid to extend the application of CWSI over fully to partially vegetated surface areas (Li *et al.*, 2009). One of the assumptions of the trapezoid approach is that values of  $T_s$ - $T_a$  vary linearly with vegetation cover along crop extreme conditions edges and the intermediate conditions relating  $T_s$ - $T_a$  to a vegetation index are included within the constructed trapezoid (Li *et al.*, 2009), where  $T_s$  is the soil surface temperature and  $T_a$  is the air temperature. In the following diagram one must include all the WDI values of pixels between the following four vortices:

1. Dry bare soil
2. Saturated bare soil
3. Well watered full-cover vegetation
4. Water-stress full-cover vegetation

Vegetation cover and soil moisture content for a specific time must be computed according to the four above vortices.

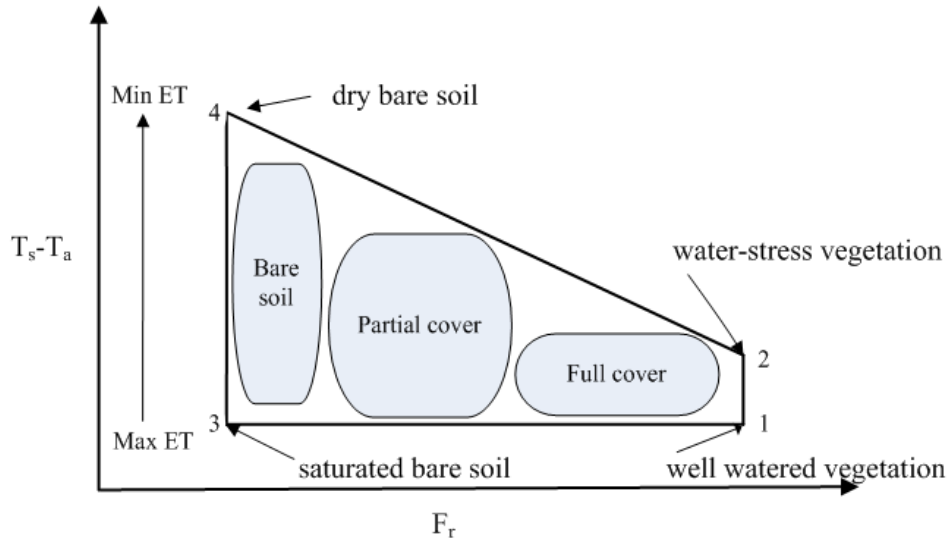


Figure 2.9. The hypothetical trapezoidal space between  $T_s - T_a$  and  $F_r$  (taken from Li *et al.*, 2009).

After these definitions WDI can be defined for a partially vegetated surface as:

$$WDI = 1 - \frac{LE}{LE_p} = \frac{(T_s - T_a)_{\min} - (T_s - T_a)_i}{(T_s - T_a)_{\min} - (T_s - T_a)_{\max}} \quad (2.31)$$

Moran *et al.* (1994) showed that WDI provided accurate estimates of field ET rates and relative field water deficit for both full cover and partially vegetated sites.

Comparing the trapezoidal with the triangular space it seems that VI- $T_s$  trapezoidal space does not require as large number of pixels to be existent as that in the triangular space (Li *et al.*, 2009). Variations in the VI- $T_s$  triangle space are not caused by differences in atmospheric conditions but by the variations in available soil water content. On the other hand a disadvantage of the latter method is the relatively more ground based parameters required for the processing of the methodology. WDI method does not also separate transpiration from soil evaporation.

In conclusion, VI-T<sub>s</sub> triangle method is more preferable because can estimate regional ET with the use only of remotely sensed data (without the use of meteorological or ground data) but has the limitation of the requirement of a large number of pixels over a flat area with a wide range of soil wetness and vegetation cover. This is important because the dry and wet limits must concentrate in the given VI-T<sub>s</sub> space.

## 2.7 Definition and Use of Crop Coefficients

Crop water use information is crucial for irrigation water supply scheduling and is directly related to evapotranspiration (ET). ET is a combination of the water evaporated from the soil surface and transpired through the plant (Allen *et al.*, 1998). ET can be measured using lysimeters, evaporation pans and atmometers or can be calculated using climate data. The ET information must be every time adjusted in order to correspond to each crop and climate. This is why, when studying ET, one very common concept is the reference ET. From now on, the following definitions will be adapted to this thesis:

ET<sub>o</sub> → ET calculated using grass as the reference crop

ET<sub>r</sub> → ET calculated using alfalfa as the reference crop

ET<sub>p</sub> → ET measured from lysimeter, pan or atmometer

From the time that reference ET has been determined, a crop coefficient ( $K_c$ ) value must be applied to adjust the reference ET value for the type of crop being irrigated according to the local climate and soil conditions. Different crops will have a different crop coefficient and resulting water use. The crop coefficient in other words adjusts the calculated reference ET<sub>o</sub> to obtain the crop evapotranspiration ET<sub>c</sub>. Crop coefficients primarily depend on the dynamics of canopies, light absorption by the canopy, and canopy roughness, which affects turbulence, crop physiology, leaf age and surface wetness (Townshend and Justice, 2002). For the computation of  $K_c$  the following formula is generally applied:

$$ET_c = ET_o \times K_c \Leftrightarrow K_c = ET_c / ET_o \quad (2.32)$$

where  $ET_c$  is the crop evapotranspiration or crop water use in mm,  $ET_o$  is the calculated reference ET for grass (mm) and  $K_c$  is the crop coefficient (unitless).

It is obvious that grass or alfalfa are used as reference crops because, usually, all the other crops use less water amount compared with them. The reference ET not only uses grass and alfalfa but recently, not crop-specific, when only a tall or short crop can also be used (Allen et al., 2005). Of course,  $K_c$  takes into account all the factors affecting the specific crop type and development to adjust the  $ET_o$  for that specific crop. Usually, growth stages and plant physiology as well as differences in rooting depth points to the use of different crop coefficients for a single crop throughout a growing season. It is worth to mention that  $K_c$  may also vary depending on how ET has been calculated or obtained.  $K_c$  values may be different according to which reference ET values are used. For example,  $K_c$  values developed using grass as the reference crop will be larger than those using alfalfa, because ET for alfalfa is usually greater than ET for grass.

#### 2.7.1 Pan evaporation

For the case that evaporation pans or similar devices also provide ET data, then  $ET_p$  must be converted to  $ET_c$  using a pan crop coefficient.

#### 2.7.2 Reference ET

Reference ET is calculated using climatic data obtained from a specific weather station, usually simulating a grass or alfalfa reference crop. It is very crucial to mention when comparing ET and  $K_c$  values for specific crops, which is the reference crop, because different values are expected otherwise. It is possible to convert alfalfa based  $K_c$  values to grass based  $K_c$  values applying factors given in the literature. A very common situation e.g. in British Columbia, Canada, is to multiply grass related  $K_c$  values with



0.83 to obtain alfalfa related  $K_c$  values (Gulik and Nyvall, 2001). For example, if the  $K_c$  value for one crop is 1 using a reference  $ET_o$  for grass, then the corresponding  $K_c$  value for alfalfa is  $1 \times 0.83 = 0.83$ .

### 2.7.3 Stages of growth – Phenological stages

Generally, crop growth periods can be divided into four distinct growth stages: the initial, the crop development, the mid-season and the late season, (Figure 2.10). The length of each of these stages is different for every crop and area, depending on the climate, latitude, elevation, planting date, crop type and different management practices (Gulik and Nyvall, 2001; Irmak, 2001). Local observations are the best way for determining the growth stage of the crop and decide which  $K_c$  values to use. Table 2.11 presents the phenological stages of the main crops examined in the study area of this thesis.

Table 2.11. Phenological stages of the main crops (assembled from Silleos et al., 1992; Migdakov and Gemtos, 1994 ; Toullos and Silleos, 1994).

Stage	Wheat	Cotton	Sugar beet	Stage	Maize	Alfalfa
Seeding	10-30 November	April 15-30th	About the 15th of March	Seeding	About the 15th of April	Semi-permanent Crop
Germination	+30 days	+15 days	+20 days	Germination	+15 days	4-years cycle
Stem Elongation	In the end of March			Vegetative Stage	About 40 days after seeding	
Heading	From the 15th of April	Bolls open 25 August (almost)		Reproductive Stage	A month later (depending on the	

					variety)
Flowering	In the end of April	Continuous ly from June 20th to the beginning of September	Seed Filling	130 days after seeding	
Milk Stage	May 15th	1-	Harvesti ng	Two months later	
Maturing	June 15th	5- In the end of September			
Harvesting	June 15th	5- October- December	August- October		

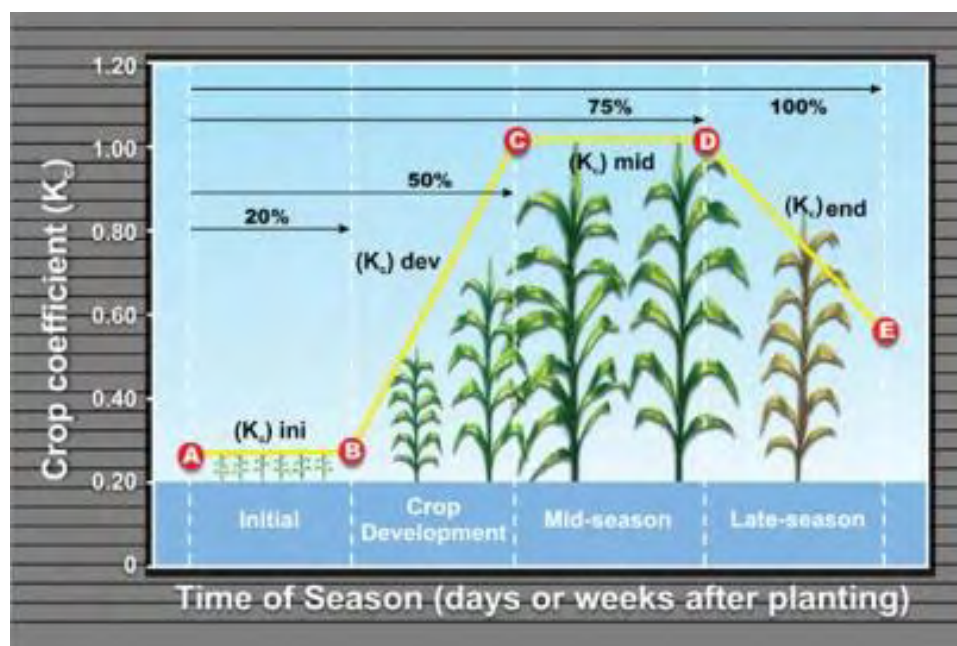


Figure 2.10. Crop coefficients during the growing season (taken from Irmak, 2001).

As a general rule for development, it can be said that, especially for annual crops, during the crop's germination and establishment, most of the ET can be encountered as evaporation from the soil surface. As the foliage develops, evaporation from the soil

surface is expected to decrease and transpiration is expected to increase. A similar pattern can be observed for perennial crops. The rate of ET can be generally determined from the percentage of canopy cover. Max ET occurs when the canopy cover is about 60-70% for tree crops and 70-80% for field and row crops (Gulik and Nyvall, 2001). The maximum canopy cover often coincides with the time of year that sun radiation and air temperature are at their greatest and this is usually the mid-season. In conclusion, in most cases, values for most agricultural crops increase from a minimum value at emergence, in relation to changes in canopy development, until a maximum  $K_c$  reached at about full canopy cover (Kamble *et al.*, 2013).  $K_c$  curves are often expressed as a smooth continuous function in time or some other time-related index. The  $K_c$  tends to decline at a point after a full cover is reached in the crop season (Kamble *et al.*, 2013). The total curve behavior primarily depends on the particular crop growth characteristics (Kamble and Irmak, 2008) and the irrigation management during the late season (Allen *et al.*, 2005). The most usual scenario is that a crop canopy in a developing stage has a decreased evaporation factor, until most of the evapotranspiration comes from transpiration, and soil evaporation is a minor component. Table 2.12 provides a description of the various plant growth stages which can be a very useful tool for the selection of an appropriate crop coefficient.

Table 2.12. Stages of Crop Development – British Columbia, Canada (taken from Gulik and Nyvall, 2001).

Stages of Crop Development		
Stage	Indicators	Crop Coefficient
Initial	Planting date (or the start of new leaves for perennials) to 10% ground cover.	$K_{c_{ini}}$
Crop development	10% ground cover to effective full cover, about 60-70% coverage for tree crops and 70-80% for field and row crops.	$K_{c_{ini}} - K_{c_{mid}}$
Mid-season	Effective full cover to maturity,	$K_{c_{mid}}$

---

	indicated by yellowing of leave, leaf drop, browning of fruit. This stage is long for perennials but relatively short for vegetables crops that are harvested for their fresh fruit.
Late-season	Maturity to harvest: the $K_c$ value $K_{C_{mid}} - K_{C_{end}}$ could be high if the crop is irrigated frequently until fresh harvest or low if the crop is allowed to dry out in the field before harvest.

---

From Table 2.12 it seems that the crop development has no specific  $K_c$  values. It is recommended to use a  $K_c$  value that is between  $K_{C_{ini}}$  and  $K_{C_{mid}}$ . The same approach should be taken for the time period between  $K_{C_{mid}}$  and  $K_{C_{end}}$ , but this time period may be much shorter and a leap directly from  $K_{C_{mid}}$  to  $K_{C_{end}}$  could be taken. An exception to the above is the case where the crops can be harvested several times during the growing season. These crops would have a series of curves during the entire season instead of one  $K_c$  curve. Such a case is the Greek alfalfa used in this study.

#### 2.7.4 Satellite based $K_c$ estimations

##### 2.7.4.1 $K_c$ analytical methods

$K_c$ -analytical approaches are usually limited to crops under standard non-stress conditions. These approaches are based on the theoretical ET equation to define the crop coefficient where  $ET_0$  and  $ET_c$  are produced by Monteith's schematization for the grass reference (D'Urso, 2001). This kind of approach requires a minimum set of climatic data, namely, the air temperature  $T_a$ , the relative humidity RH, the wind speed  $u_x$  and the incoming short wave radiation  $R_{s\downarrow}$ , as well as vegetation parameters

including surface albedo,  $a$ , the leaf area index (LAI), and the crop height,  $h_c$ , that are obtained from the processing of multispectral imagery (Rubio *et al.*, 2006).

#### 2.7.4.2 $K_c$ and Vegetation Indices

Correlation between ET and Vegetation Indices (VI) is very common in Remote Sensing for many years now (Bausch and Neale, 1989; Neale *et al.*, 1989; Choudhury *et al.*, 1994). The most common Remote Sensing approach for the assessment of  $K_c$  is the computation of NDVI which is called the  $K_c$  – NDVI approach. This falls to the category of assessing the relationships between spectral indices and crop coefficients which is highly recommended today (Hunsaker *et al.*, 2005; Glen *et al.*, 2011; Kamble *et al.*, 2013). Many researchers have used multispectral vegetation indices (VI) derived from remote sensing to estimate  $K_c$  values at the field scale for maize (Bausch and Neale, 1989; Jensen *et al.*, 1990; Bastiaanssen, 2000; Hunsaker *et al.*, 2005; Irmak, 2010), wheat, cotton (Hunsaker *et al.*, 2005) and beans (Jensen *et al.*, 1990; Irmak, 2010).

Vegetation Indices (VI) generally can be defined as a combination of surface reflectance values between two or more wavelengths. Each VI is related to a particular vegetation property, and for this reason every wavelength is selected according to each particular property. More than 150 VIs have been published in scientific literature, but only a small subset has been systematically tested. Selection of the most important vegetation categories and the best representative indices within each category was performed by Asner *et al.* (2010). The indices are grouped into categories that calculate similar properties. The main categories and indices are (Exelis VIS, 2010):

Table 2.13. Most widely used Vegetation Indices.

VI Category	Indices
Broadband	Normalized Difference Vegetation Index
Greenness	Simple Ratio Index
	Enhanced Vegetation Index
	Atmospherically Resistant Vegetation

---

	Index
	Sum Green Index
Narrowband	Red Edge Normalized Difference
Greenness	Vegetation Index
	Modified Red Edge Simple Ratio Index
	Modified Red Edge Normalized Difference
	Vegetation Index
	Vogelmann Red Edge Index 1
	Vogelmann Red Edge Index 2
	Vogelmann Red Edge Index 3
	Red Edge Position Index
Light Use	Photochemical Reflectance Index
Efficiency	Structure Insensitive Pigment Index
	Red Green Ratio Index
Canopy Nitrogen	Water Band Index
	Normalized Difference Water Index
	Moisture Stress Index
	Normalized Difference Infrared Index
Dry or Senescent	Normalized Difference Lignin Index
Carbon	Cellulose Absorption Index
	Plant Senescence Reflectance Index
Leaf Pigments	Carotenoid Reflectance Index 1
	Carotenoid Reflectance Index 2
	Anthocyanin Reflectance Index 1
	Anthocyanin Reflectance Index 2
Canopy Water	Water Band Index
Content	Normalized Difference Water Index
	Moisture Stress Index
	Normalized Difference Infrared Index

---

All VI require high-quality reflectance measurements from any particular sensor. Most VI formulas use a subscript as a reflectance identifier expressed in nanometers. This is not used for the broadband greenness indices where the formulas use the subscriptions RED, IR or BLUE indicating the specific spectral region for processing. Comparing the results of different VI, and correlating them to in-situ measurements, it is feasible to assess which indices are more appropriate for any particular application. Generally, for different soil properties and field conditions, some indices within a category provide results with higher or lower validity than others. Generally, the norm is that a high spectral resolution dataset can be used for the assessment of up to 25 indices, while a dataset utilizing only red and NIR bands can be used only for the assessment of the calculation of Normalized Difference Vegetation Index (NDVI) or similar. This is why, together with its powerful operation, NDVI is one of the most widely used VI today. NDVI has been extensively used for vegetation monitoring, crop yield assessment as well as drought detection (Sellers, 1985; Townshend and Justice, 2002; Domenikiotis *et al.*, 2004 a;b;c; 2005). Higher NDVI values generally indicate a greater level of photosynthetic activity (Tucker, 1979; Townshend and Justice, 2002; Kamble *et al.*, 2013). Several researchers (Sellers, 1985; Bausch and Neale, 1989; Benedetti and Rossinni, 1993; Choudhury *et al.*, 1994; Hubbard and Sivakumar, 2000; Jayanthi *et al.*, 2000; Allen *et al.*, 2005; Irmak and Kamble, 2009; Irmak *et al.*, 2011) also have shown that vegetation indices from remote sensing could be used to predict “basal” crop coefficients for agricultural crops. Similar Greek studies assessing this subject can be found in the literature (Tsakiris, 1995; Papazafiriou 1999; Kalavrouziotis, *et al.*, 2006; Tsirogiannis, *et al.*, 2012).

A useful and complete formulation for  $K_c$  (Allen *et al.*, 1998) is:

$$ET_r F = K_{cb} + K_e \quad (2.33)$$

where:

$K_{cb}$  is the basal crop coefficient of the vegetation and  $K_e$  is the soil evaporation coefficient.

$ET_rF$  is a term similar to  $K_c$  and is used mainly in METRIC methodology described later.  $K_{cb}$  is most directly related to NDVI, while  $K_e$  is dependent on the amount of moisture remaining in the surface layer of the soil and on the amount of vegetation covering the soil surface (Allen et al., 1998, 2005). In other words  $K_{cb}$  is expected to be proportional to VI because  $K_{cb}$  represents primarily the transpirative component of ET. The same it is not expected for  $K_e$  as the soil evaporation coefficient, but, when averaged over a large number of fields and regions where precipitation amounts and frequency are consistent from year to year, can be 'blended' into an  $ET_rF$  vs. VI with good results (Allen et al., 2010).

Higher  $K_c$  values caused by higher temperature lead to a decrease in soil water and a following decline of NDVI. On the other hand, dense vegetation induces more evapotranspiration and lowers the land surface temperature (Boegh *et al.*, 1998). Tasumi and It is well known that  $K_c$  and  $K_{cb}$  tend to be linear to NDVI (Allen *et al.*, 2005; Hunsaker, 2003; Duchemin *et al.*, 2006, Trezza and Allen, 2009). Allen (2007) showed that linear equations relating actual  $ET_rF$  to VI may be applicable for regional estimates when calibrated using energy balance-derived ET. The calibrated  $ET_rF$  values include also effects of evaporation from soil. VI approach, finally, showed that ET can be estimated without conducting a crop type classification, which can be costly and time consuming (Allen *et al.*, 2010).

Another approach for the estimation of  $K_c$  is estimation through the Leaf Area Index (LAI). This method has the advantage that it is suitable to apply to both stressed and unstressed crop conditions (Gamon *et al.*, 1995; Tasumi *et al.*, 2005). Of course special techniques must be applied in order to incorporate the LAI information into the irrigation use at the field or regional scale, as it is implicit the assumption that LAI must be specific to the crop located at each pixel. Such combination techniques are used at this study and described later.



## 2.8 The Use of CropWat Model

CropWat is a decision support system for irrigation planning and management, developed by the Land and Water Development Division of FAO (1992). The basic functions of CropWat include the calculation of reference evapotranspiration, crop water requirements, and crop and scheme irrigation. In such a way CropWat allows the development of recommendations for improved irrigation practices, the planning of irrigation schedules and the assessment of production under rainfed conditions or deficit irrigation (Marica and Cuculeanu, 1999). Typical applications of the water balance include also rainfed production as well as drought effects. Calculations and outputs are based on the CROPWAT version 8.0, available at the FAO Web site:

[http://www.fao.org/nr/water/infores\\_databases\\_CropWat.html](http://www.fao.org/nr/water/infores_databases_CropWat.html)). The procedure for the calculations of crop water requirements as well as irrigation requirements are based on methodologies presented in FAO irrigation and drainage papers No.24 “Crop water requirements” and No.33 “Yield response to water”. In other words CropWat in order to calculate reference crop evapotranspiration uses Penmann-Montieth methodologies (Smith, 1992).

### 2.8.1 Requirements

CropWat model generally requires:

- Climatic Data
- Rainfall data
- Crop data
- Soil data

Table 2.14 more specifically illustrates the data requirements of CROPWAT.

Table 2.14. CropWat requirements.

Climatic Data	Rainfall data	Crop data	Soil data
Min and max temperature (Monthly means)	Mean monthly rainfall	$K_c$ as a ratio between $ET_c$ and $ET_o$	Total available soil moisture = Field capacity-wilting

		point(mm/meter)	
Humidity (Monthly means)	Effective rainfall based on: <ul style="list-style-type: none"> <li>Fixed percentage</li> <li>Dependable rain</li> <li>Empirical formula</li> <li>USDA soil conservation service</li> </ul>	Stage days (initial, development,mid-season, late-season) or crop date, planting date e.t.c.	Maximum rain infiltration rate = Soil hydraulic conductivity under saturation (mm/day)
Sunshine duration (Monthly means)		Rooting depth (m) Critical depletion (m)	Maximum rooting depth (cm)

### 2.8.2 Soil parameters calculation

Soil parameters can be computed by the soil texture triangle (Figure 2.11), and especially the hydraulic properties calculator (K.E. Saxton et al., 1986).

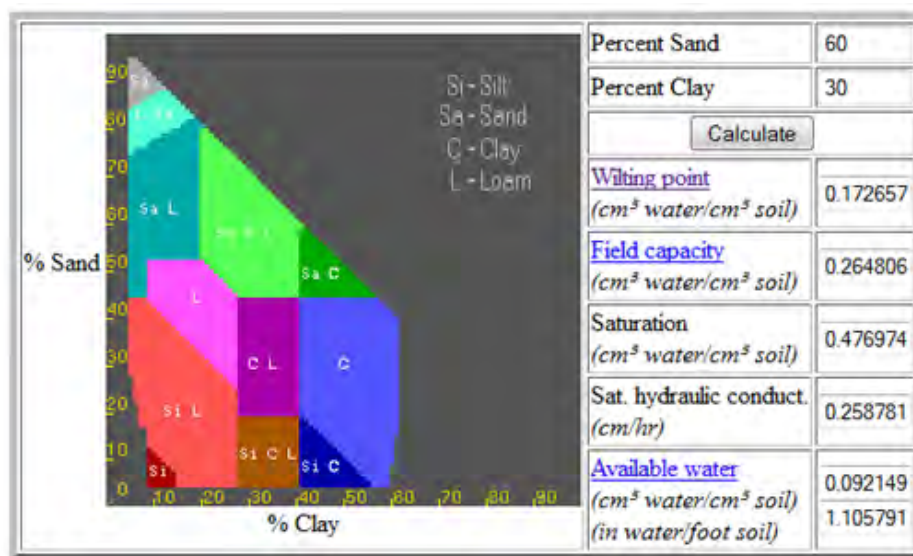


Figure 2.11. Soil Texture Triangle: Hydraulic Properties Calculator (taken from Saxton *et al.*, 1986).

### 2.8.3 ClimWat 2.0 software (used for accessing climatic data):

ClimWat is a climatic database to be used in combination with the computer program CropWat and allows the calculation of crop water requirements, irrigation supply and irrigation scheduling for various crops for a range of climatological stations worldwide. The data can be extracted for a single or multiple stations in the format suitable for their use in CropWat. Two files are created for each selected station. The first file contains long-term monthly rainfall data (mm/month). Additionally, effective rainfall is also included (calculated and included in the same file). The second file consists of long-term monthly averages for the needed climatic parameters. This file also contains the coordinates and altitude of the location (Figure 2.12).

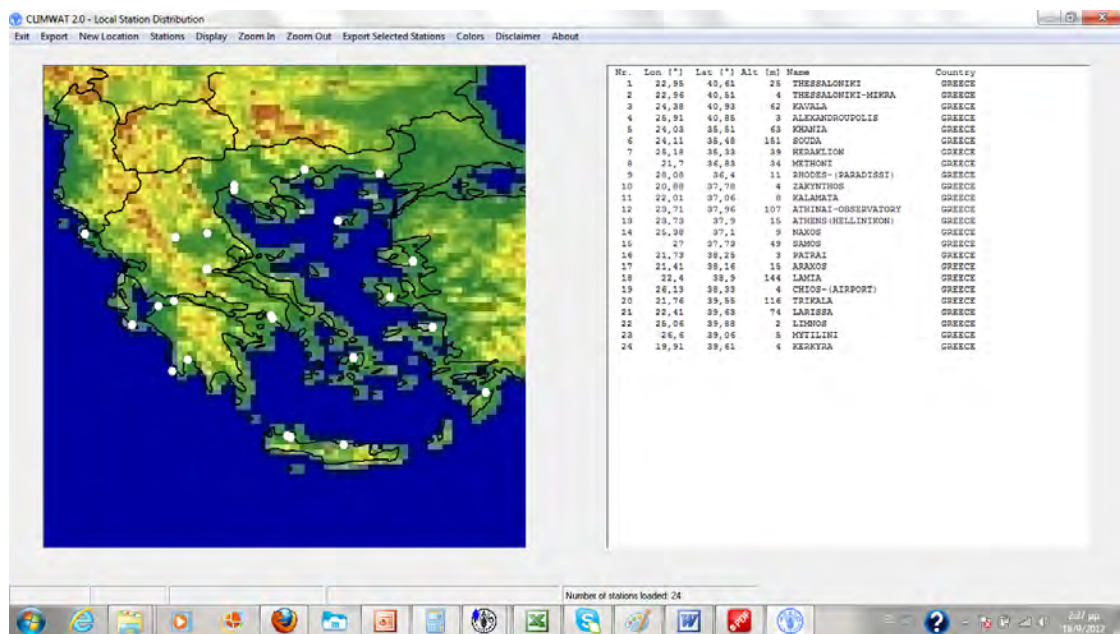


Figure 2.12. ClimWat: example.

### 2.8.4 Software Environment

CropWat 8.0 now operates in the Windows environment. After the insertion of climatic, rainfall, crop and soil data, CropWat gives the following results in a spreadsheet style (Figure 2.13):

Month	Decade	Stage	Kc	ETc	ETc	Eff rain	Irr. Req.
			coeff	mm/day	mm/dec	mm/dec	mm/dec
Apr	2	Init	0.63	2.24	18.0	0.0	18.0
Apr	3	Init	0.63	2.55	25.5	7.3	18.2
May	1	Init	0.63	3.05	30.5	0.6	29.9
May	2	Deve	0.65	3.47	34.7	13.7	20.9
May	3	Deve	0.72	3.86	42.4	22.9	19.5
Jun	1	Deve	0.78	4.15	41.5	17.1	24.4
Jun	2	Deve	0.84	5.00	50.0	4.1	45.9
Jun	3	Deve	0.91	6.17	61.7	0.0	61.7
Jul	1	Deve	0.97	5.62	56.2	0.0	56.2
Jul	2	Mid	1.00	5.74	57.4	0.0	57.4
Jul	3	Mid	1.00	5.59	61.5	0.0	61.5
Aug	1	Mid	1.00	4.83	48.3	17.3	31.1
Aug	2	Mid	1.00	4.84	48.4	0.0	48.4
Aug	3	Late	0.97	4.75	52.2	0.0	52.2
Sep	1	Late	0.78	2.88	28.8	13.6	15.2
Sep	2	Late	0.61	2.16	19.5	0.0	19.5
					<b>676.8</b>	<b>96.6</b>	<b>580.2</b>

Figure 2.13. CropWat : example.

The program needs input by its own file type which is:

- \*. pen for climatological data,
- \*. cli for rainfall data,
- \*. soi for soil data,
- \*. cro for crop data,

And returns

- \*. pem as output climatological data (together with estimated  $ET_0$ ) and
- \*. crm as output for rainfall data (together with estimated effective rainfall)
- \*. sch as output for schedule
- \*. pat as pattern

### 2.8.5 Improvements

ET-retrieval algorithms for ET and  $ET_F$  mapping are very crucial for the application of CropWat at this thesis. Having distributed crop coefficient values with a 30x30 m spatial resolution for every crop, and every stage (initial, development, mid-season and

late-season) is a very important development for CropWat's computations. Another improvement is the use of satellite derived land use maps (30 m x 30 m spatial resolution) produced especially for this work, which describe the land use of the Lake Karla watershed more accurately. The derivation of these maps will be described later. Finally, it should be mentioned that CropWat model in this dissertation has been applied utilizing the actual meteorological data of 2012 instead of using the default climatic data, from ClimWat's database.



## CHAPTER 3°

### STUDY AREA – LAND USE CLASSIFICATION

### 3 Study Area – Land Use Classification

#### 3.1 Lake Karla Basin

Lake Karla basin is located in the eastern part of Thessaly region, Greece (Figure 3.1). It is an intensively cultivated agricultural region lying between latitude 39°20'56' to 39°45'15' N and longitude 22°26'10" to 23°0'27" E. Most of the aquifer area is plain with an altitude ranging from 45 to 65 m (Loukas *et al.*, 2007). The climate is typical Mediterranean with an average temperature of 15–17° C and mean annual relative humidity of 67–72 %. Summers are usually hot and dry, and it is very usual that temperatures may reach up to 40°C. The average precipitation is 500–700 mm and occurs mainly in autumn, winter and spring (Figure 3.2, Figure 3.3).



Figure 3.1. Lake Karla Basin.



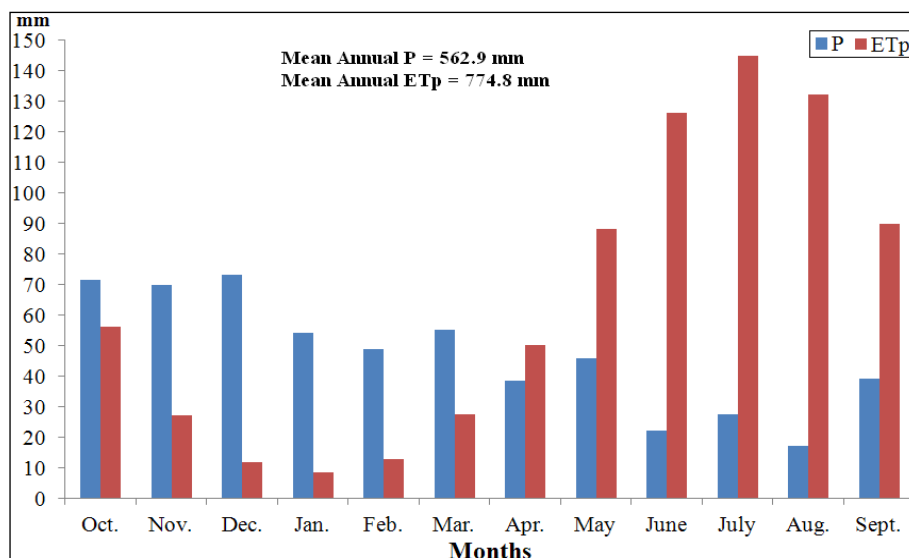


Figure 3.2. Mean monthly values of precipitation and potential evapotranspiration for Lake Karla basin (Vasiliades *et al.*, 2009).

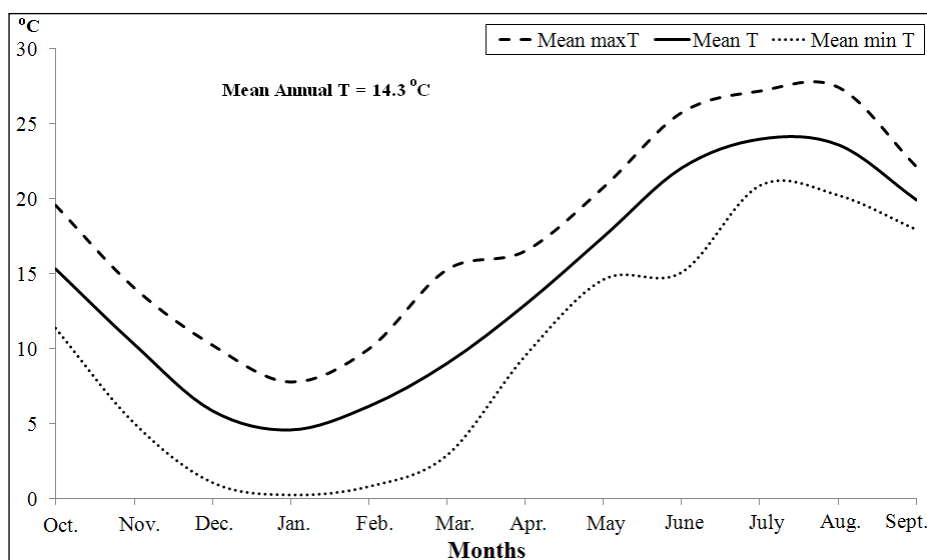


Figure 3.3. Mean monthly values of temperature for Lake Karla basin (Vasiliades *et al.*, 2009).

Various sizes of grains originating from Lake Karla deposits are generally prevailing in the area. The basement rocks consist of impermeable marbles and schist. Mavrovouni Mountain at the east side consists of impermeable bedrocks as schist and karstic limestones, while Halkodonion Mountain is located at the west side with similar composition (Constantinidis, 1978 ; Vasiliades *et al.*, 2009). The plain on the other side



consists of aquiferous, essentially sandy intercalations separated by layers of clay to silty-clay and is bound by schists and karstic limestones or marbles (Mylopoulos and Sidiropoulos, 2008; Sidiropoulos *et al.*, 2013). Impermeable geological structures cover a 30.6 % of the total area, karstic aquifers cover a 14.5 % and permeable structures, which appear mainly in the plain, cover a 54.9 % (Vasiliades *et al.*, 2009).

### 3.2 History: Drain of the Lake Karla

The old name of Lake Karla was Voiviis. The lake was formed in a tectonic depression at the beginning of the Quaternary period, when the first sediments were deposited. Eroded debris from Pinios River and other local sources of water were also contributed to the lake formation (Ananiadis, 1956; Mahairas, 1995; Rouskas, 2001; Laspidou *et al.*, 2011; Chamoglou, *et al.*, 2014). Lake Karla basin was one of the most important Greek wetlands and a natural reservoir, providing water storage and recharge to the groundwater system. Surface runoff from the watershed and floodwaters of Pinios supplied the lake with large quantities of fresh water (Zalidis *et al.*, 2005). The surface of the lake was not stable, fluctuating between 40 km<sup>2</sup> and 180 km<sup>2</sup> depending on the inflow-outflow balance (Moustaka *et al.*, 2002, Kokkinos *et al.*, 2009).

However, a political decision to drain the lake during the 60's was very significant for the future of the lake. One of the main reasons for this decision was health protection. Malaria, according to the locals, was a very serious disease associated with the lake. The need for flood protection of the surrounding plain area was also a very important parameter. A secondary reason was to offer agricultural fields to the local farmers. Finally, the lake was drained in 1962, but the smaller reservoir which has been initially suggested has never built. As a result, many environmental problems started to appear due to intensive agricultural activity. The most significant problem was an intensive decrease of the underground aquifer because of the drilling water for the farmlands. Other problems were impacts on fauna and flora, pollution on the surrounding environment, as well as damage on buildings (Rentzelou and Jong, 2012).

### 3.3 *The Lake Karla Restoration*

Year by year, the restoration of Lake Karla seemed to be necessary. In the last decades, after the worldwide recognition of the need to preserve wetland functions and values, the trend of wetland degradation in Greece, had already been decelerated or even been reversed in some cases, with the funding of pilot or medium scale projects aiming in the restoration of certain wetlands (Gnardelli, 2004). In 2000, the Greek government decided to restore Lake Karla, with the high costs being partially covered by the European Union. Finally, the works started, supported by the local communities which have recognized the importance of the lake for their quality of life. The project has been funded by the Operational Program 'Environment' which was approved by the European Commission for the period of 2000-2006. The restoration of ecological balance was planned to reverse these difficult environmental conditions caused by the lake drainage. A new environment would increase the underground aquifer, enhance the water supply of Volos city, and improve the soil quality of the region.

The restoration project suggested the creation of a large wetland area included the following (Ministry of Environment, Planning and Public Works, 2011):

- Construction of the reservoir and collectors
- Construction works for the water supply of the lake by the river Pinios
- Control works to halt the erosion of mountains around the lake basin to reduce sediment transport materials end up in the lake
- Works to transport water from the lake to the surroundings farmlands for irrigation purposes
- Works to strengthen the water supply of the city of Volos by using water from the underground aquifer
- Infrastructure works for enhancing the ecotourism of the area (museum and other buildings).

### 3.4 The technical works

The decision to restore part of the former lake has been taken in the early 1980's but the construction works started only a few years ago. The suggested plan proposed the creation of a 38 km<sup>2</sup> reservoir, through the construction of two embankments, one in the eastern part and one in the western part of the lake lying between latitude 39°26'49'' to 39°32'03' N and longitude 22°46'47'' to 23°51'50'' E. The reservoir was planned to be located at the lower part of the basin, and two main ditches will transfer the flood runoff of Pinios River to the reservoir. This will be very close to the prior conditions (the old Lake Karla). Four collector channels will concentrate the surface runoff from the higher elevation zones of the watershed and directly divert it into the reservoir. The surface runoff from the lower elevation areas will be pumped into the reservoir. While maximum allowable volume of the reservoir will reach up the 180 hm<sup>3</sup>, only 60 hm<sup>3</sup> will be available to cover the irrigation needs of the surrounding agricultures, due to environmental restraints. Today, all the necessary works that have to do with the construction of the reservoir have been completed. More work has to be done for the drilling of the new supply wells and the irrigation network (SIRRIMED, 2014). The partial restoration of the former Lake Karla is one of the most important environmental projects in Greece now.

The natural basin of Lake Karla has a total extent of 1,663 km<sup>2</sup>, but after the construction of complimentary works for the reservoir, the drainage area of the restored Lake Karla has almost 1200 km<sup>2</sup> (Loukas et al., 2007). More than 600 km<sup>2</sup> comprise a southern flat plain, while the east part is surrounded by mountain and hills. The water surface of the reservoir has a perimeter of 30.55 km, and it can be characterized by its shallow depth, with a maximum of 4,5 m and a mean depth of 2 m (Papadimitriou *et al.*, 2013). At the time of writing this thesis the mean depth of the reservoir is less than 1 m due to previous prevailed drought conditions.

### 3.5 *The present and future*

Two types of networks of water delivery systems exist in Lake Karla watershed consisted of open surface water networks and localized pressurized networks. The pressurized network designed to fulfil the water needs of a specific farm (individual network) and the water is pumped from Lake Karla's reservoir and is being distributed through a low pressured piped network. The open surface water network is that of Pinios LALR (Local Administration of Land Reclamation). This network consists of earth made open trapezoidal ditches where the water comes from surface water resources (i.e. small reservoirs). Twelve cooperative irrigation reservoirs located across the central part of the watershed are fed with 20 hm<sup>3</sup> of water directly from pumping stations found across the Pinios river. During the summer months these pumping stations provide water for the Pinios LALR irrigation network. Although Pinios LALR surface network covers a relatively large part of the watershed, however the total resources fail to meet the irrigation requirements and this deficit is covered with pumping wells situated at the area of the Lake Karla Aquifer. This is why the described combination of surface and groundwater resources is finally the total exploitation system of Lake Karla Basin (LKB). Figure 3.4 illustrates the zoning of the areas served from the aquifer (Greek Ministry of Environment, Regional Planning and Public Works, 1999; Γ.Γ.Δ.Ε./Γ.Δ.Υ.Ε., 2006; Sidiropoulos, 2007).

Figure 3.5 illustrates the areas irrigated by groundwater pumping (zones 1 to 6) after excluding the areas irrigated from Pinios LALR surface irrigation network (Γ.Γ.Δ.Ε./Γ.Δ.Υ.Ε., 2006; Sidiropoulos, 2007). Non coloured areas served by the two irrigation networks (Pinios LALR network-existing and Lake Karla network-future).

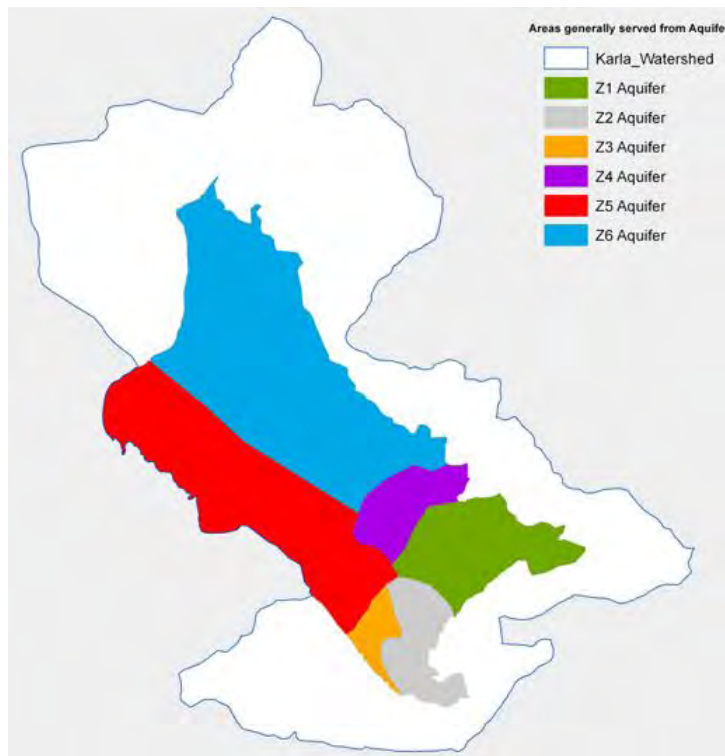


Figure 3.4. Zoning of areas served by the aquifer.

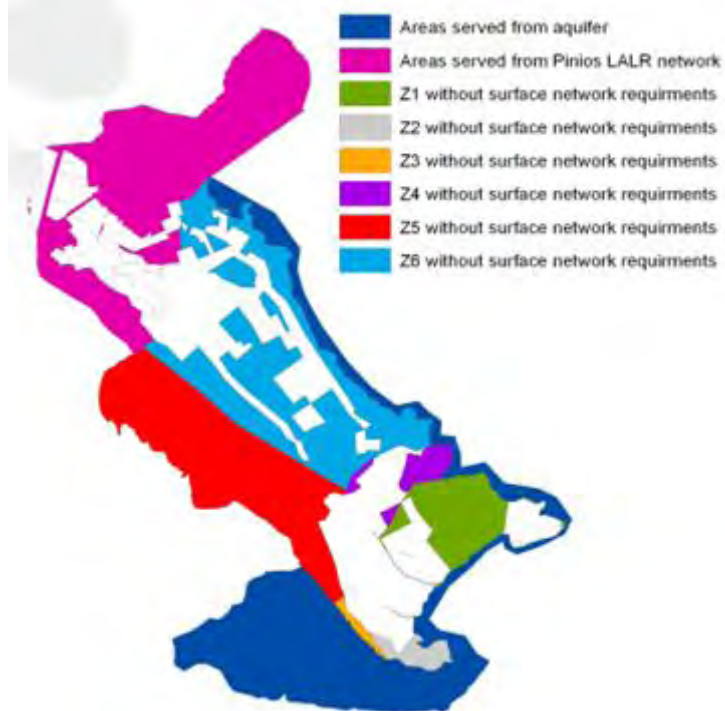


Figure 3.5. Zoning of areas irrigated by groundwater pumping.

Figure 3.6 finally, illustrates the zones that will be irrigated by the future network of Lake Karla reservoir (that is Lake Karla LALR network) (Sidiropoulos, 2007).

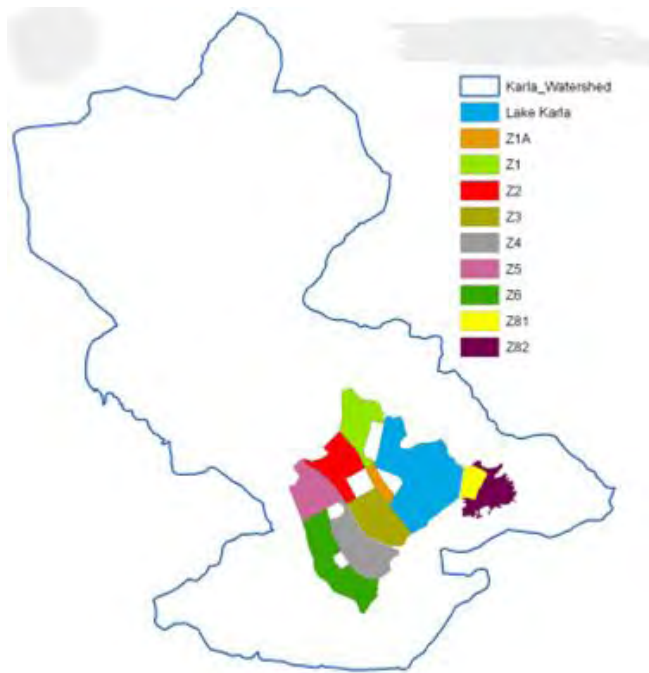


Figure 3.6. Zoning of future irrigation network.

The refilling of the lake started in 2009 and after almost five years of re-filling it is obvious that it is expected to improve the quantity and quality of the water table and other adverse environmental problems caused by the previous drainage as the reservoir will cover the irrigation needs of the nearby agricultures, which today are irrigated only by the groundwater resources.

### 3.6 Agriculture

Grasslands, cotton, wheat, sugar beet and maize are among the predominant crops cultivated in the area. There are also olive trees, tomatoes, vineyards, almond trees and many other individual cultivated crops. Grasslands, cotton and wheat occupy 77,1 % of the total available area (Hydromentor, 2014). These results were found according to a detailed classification made by processing data from all the municipalities of area. Figure 3.7 illustrates the surface area classification among the three prevailing categories (%).

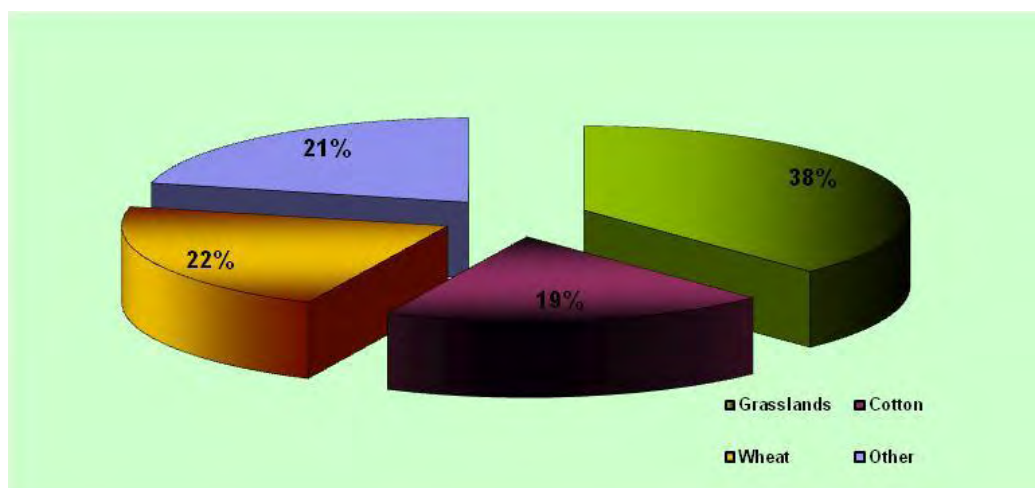


Figure 3.7. The prevailing crops in the study area (Hydromentor, 2014).

### 3.7 Land Use Mapping

Identification of land use/land cover for Lake Karla Watershed using remote sensing is a very important part of this thesis being an important input for the next procedures. Land use mapping is generally a very useful tool for the management of all man-kind activities. Land use also helps with making environmental related policies, being a basic priority for every scientist dealing with soil, precision agriculture, cartography, hydrology, geology, etc. Generally, any change in land use may be caused by anthropogenic factors, wildfires, or climate change, which in turn has an impact on biochemical cycles, erosion, or desertification, affecting significantly the local economy. Traditionally, the study of all these factors requires special statistics records per municipality or district of interest. This fact of course pre-supposes the existence of the relevant database which is often quite difficult to find and also very time consuming. This is why, modern technologies such as satellite remote sensing and geographic information systems are now the prevailing techniques at this area, providing reasonably data solutions on monitoring land use and changes detection (Defries and Belward, 2000).

### 3.7.1 Methodology

Land use mapping is performing in two separate periods. The first period is before the flooding of Lake Karla reservoir (summer of 2007) and the second is after the flooding (summer of 2012). For the purposes of the study, in-situ observations performed in the area using a handheld GPS device (Figure 3.8). Landsat 5 TM and Landsat 7 ETM+ images were downloaded from USGS Global Visualization Center EROS (<http://glovis.usgs.gov>). The images are then subject to a sequence of steps: For each original Landsat 7 ETM + and Landsat 5 TM image only the first four (4) channels, specifically blue, green, red and near infrared are implemented. For the purposes of our study, finally, Landsat 5 TM image of the 7<sup>th</sup> of July 2007 is chosen due to its high quality. A specific radiometric correction is done for each band, and a new image which now represents the radiance for each specific band is produced. The radiometric correction takes into account the Julian day of the image's acquisition and the sun elevation corresponding to specific values of gain and offset given by the USGS office in order to make the necessary corrections producing the values of radiance. The radiance is calculated by the rule:

$$L_{\lambda} = \text{"gain"} \times (L\text{-digital value at each pixel and } \lambda) + \text{"offset"} \quad (3.1)$$

The radiance is related to the at-ground reflectance characteristics of the Earth's surface materials and there is a need to convert this data into meaningful information. We can do this by statistically estimate the thematic land cover type using the multispectral values of a pixel. In such a way, all images per channel are merged into one image-file. The processing of images is done using ENVI 4.8, ERDAS IMAGINE 9.2 and ArcMap. But first of all a file map conversion projection is required. Specifically, GGRS87 coordinate system is chosen, which the official Greek coordinate system is.





Figure 3.8. Field observations with a GPS device.

### **3.7.2 Greek Geodetic Reference System 1987 (GGRS87)**

Greek Geodetic Reference System 1987 or GGRS87 is a geodetic system commonly used in Greece since 1990. This system specifies a local projection system and a specified geodetic datum.

### **3.7.3 GGRS87 projection**

GGRS87 projection is based on the Transverse Mercator (TM) cartographic projection. It covers 6 degrees of longitude east and west of 24 degrees east meridian (18-30 degrees east). Using this projection all the Greek surface is projected in one zone. The reference zone for the latitude is the equator.

### 3.7.4 GGRS87 datum

HGRS87 datum is tied to the coordinates of the key geodetic station at Dionysos Satellite Observatory (DSO) northeast of Athens (38.078400°N 23.932939°E). HGRS87 datum is implemented by a first order geodetic network, which consists of approximately 30 triangulation stations throughout Greece and is maintained by the Hellenic Military Geographical Service (Delikaroglou, 2008).

HGRS87 replaced an earlier *de facto* geodetic system based on the Bessel ellipsoid, with an accurate determination of the geodetic coordinates at the central premises of the National Observatory of Athens supplemented by an accurately measured azimuth from the observatory to Mount Parnes (Mitsakaki *et al.*, 2006).

Table 3.1.Hellenic Geodetic Reference System Characteristics (HGRS87).

HGRS87 - Transverse Mercator (UTM)	
Ellipsoid	GRS80
Geodetic Datum	none
Xshift	0.0000
Yshift	0.0000
Scale factor at central meridian	0.99960
Longitude of central meridian	24° 0' 0.000"
Latitude of origin	0° 0' 0.000"
False easting	500000.00000 (meters)
False northing	0.00000 (meters)
$\Delta x$	-199.87 m
$\Delta y$	74.79 m
$\Delta z$	246.62

Although Landsat TM images are georeferenced in the first stage, the process of geometric correction is repeated manually in order to increase the accuracy. Reflections of objects, building construction and water surfaces lead very often to errors in the brightness of images depending on the angle of incidence of the sun. "Cross Track Illumination" is applied for this reason which improves the results even with a simple visual observation (Giannopoulos, 2010). The derived image is then resized using a "shape" file corresponding to Lake Karla basin.

### 3.7.5 Supervised Classification

The potential range of applications for classified earth observation images is large (e.g. land use planning, vegetation, desertification e.t.c.) Land use classification is valuable for local, regional, continental and global monitoring of the biosphere. The most well known and widely used classification techniques are the unsupervised classification which does not need a prior knowledge of the area, and the supervised classification which needs prior knowledge of the area (Lillesand and Kiefer, 2000). In the supervised classification the image processing software is based on training classes created by the user, opposed to the unsupervised classification in which an operator recognises the present classes in the image. The process of gaining this knowledge is known as ground-truthing (Lillesand and Kiefer, 2000). Using these themes the software attempts to assign all pixels to one of the recognised themes resulting in a labelled map where each pixel is assigned to a theme. At the supervised classification selected pixels represent recognizable structures in the image. These structures are called training samples and are usually enclosed by polygons created by the user. The spectral characteristics of the identified structures used by the image processing software to identify pixels with similar characteristics are then assigned to each class (Cartalis and Feidas, 2006). In this dissertation CORINE LAND COVER 2000 methodology known as CLC2000 is used as a base. CLC2000 has been developed under the auspices of the European Environment Agency and aims to classify land use around the world with the aim of Landsat TM sensors. The accuracy of the method is a pixel with a resolution of 100 meters x 100 meters (Stathakis *and* Faraslis, 2014). The CLC2000 consists of land use categories of 1st, 2nd and 3rd level. CLC2000 categories are given in Annex 4. An

example of CLC2000 mapping for Thessaly, Greece is given in Figure 3.9 while Corine Land Cover classes are given in Figure 3.10.

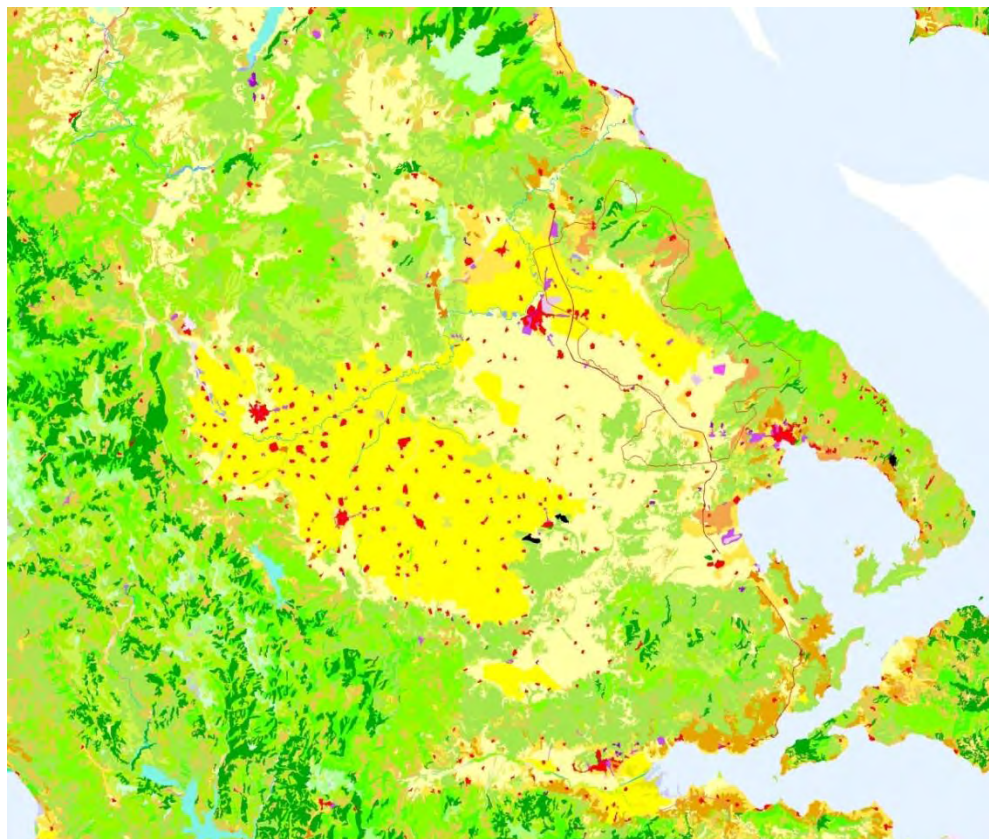


Figure 3.9. Corine Land Cover: Thessaly, Greece (Lake Karla watershed in marked with a thin red line).

#### 3.7.6 Maximum likelihood vs minimum and mahalanobis distance

Maximum likelihood, as used in remote sensing, is a statistical approach assuming multivariate normal distributions of pixels within classes. A pixel is then assigned to a class on the basis of its probability of belonging to a class whose mean and covariance are modelled as forming a normal distribution. In such a way, a discriminant function is built which calculates the probability of each pixel to be a member of a specific class. Finally, each pixel is assigned to the class having the highest probability of membership (Figure 3.11).



At minimum distance classification, all pixels in the image are classified according to the class mean to which they are closest. All regions of a n-dimensional space can be classified, but, having the significant assumption that spectral variability is the same in



Figure 3.10. Corine Land Cover Classes.

all directions, which is not the case. Mahalanobis distance is another classification procedure which is similar to minimum distance with the exception that the covariance

matrix is used instead. Mahalanobis in other words takes into account the variability of classes. This method tends to overclassify signatures with relatively large values in the covariance matrix and it is much slower than minimum distance methodology so it is not finally used in this classification. Comparing, finally, the three methodologies, maximum likelihood achieves good separation of classes if the mean and covariance of the classes are strongly defined (i.e. an adequate training samples exists).

An example applying minimum distance and maximum likelihood rules to a Landsat 5 TM multispectral image of 15-8-2011 is illustrated in Figure 3.12. The two training samples are the inland water of the Lake Karla, and the agricultural areas of the watershed respectively. The results of the classification are the generation of two classes. The green class is the water surface, while the red class is the land surface (Figure 3.12). It is obvious that minimum distance rule yields many errors to known to the user agricultural areas as well as to the sea waters of Pagasitikos Golf situated at the south-east of the image. For this reason, it is decided to use the maximum likelihood method. This method has been also used to other similar studies (Al-Ahmadi and Hames, 2009; Patil *et al.*, 2012).

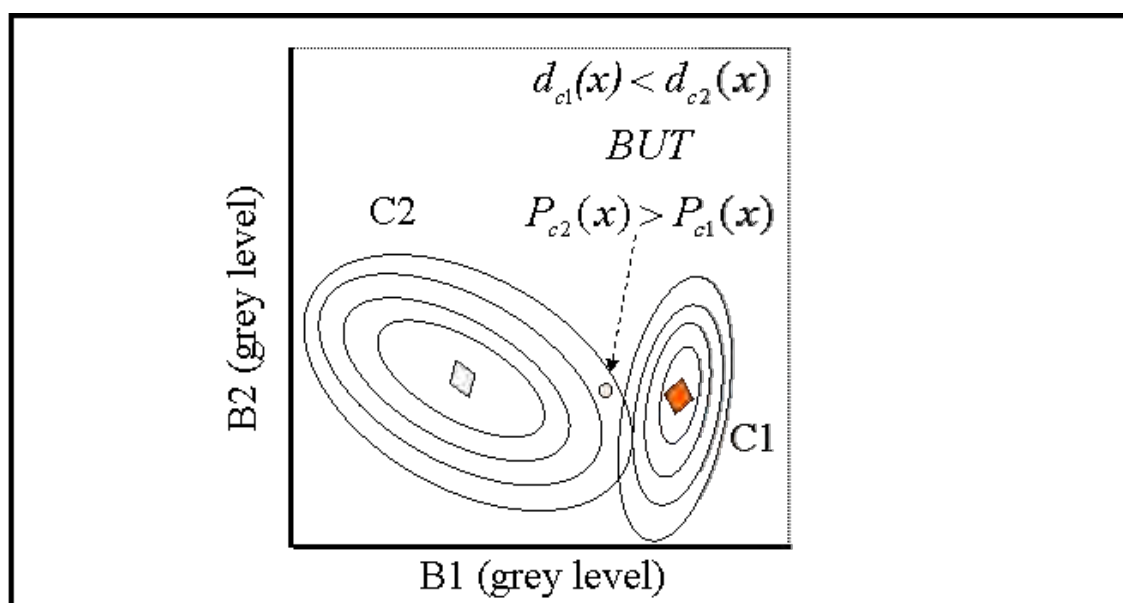


Figure 3.11. Maximum likelihood feature space illustration assuming two-dimensions (taken from Louise Mackay's lectures, University of Leeds, UK, 2005)

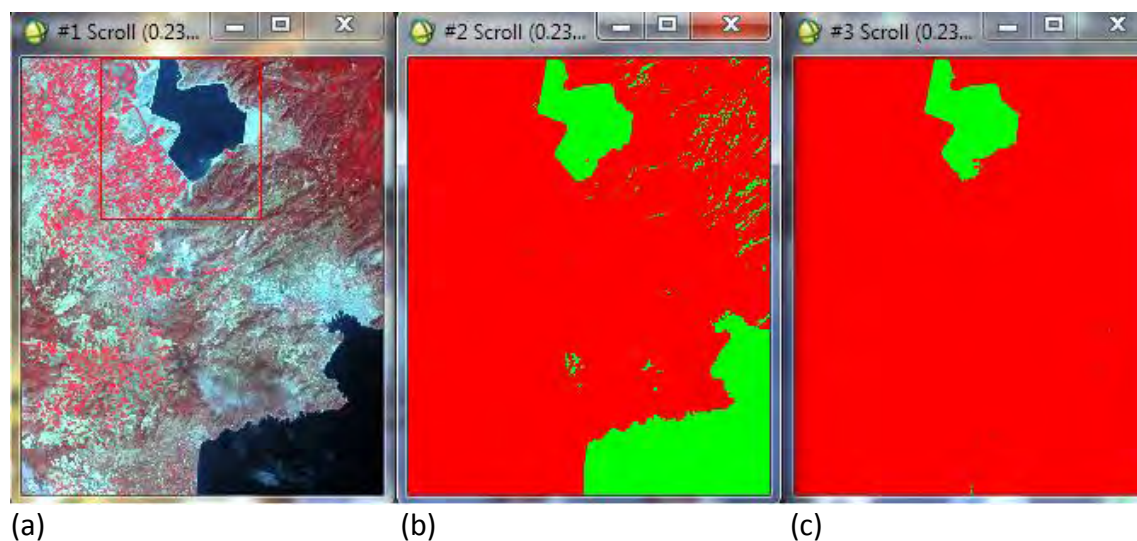


Figure 3.12. Supervised classification of the initial a) Landsat TM 15-8-2011. Green is water surface and red is land surface: b) Minimum distance classification, c) maximum likelihood classification.

### 3.7.7 Land use classes

Five (5) classes are selected for the first stage of the training process derived from the philosophy of the CLC2000 but with a higher accuracy (30x30 m). Additionally, the classes are not necessarily the same (Table 3.2). For example, the class "bare soil" is not included in the first level of CORINE land use.

Table 3.2. Land use classes.

Class name	Description
1	Water surfaces
2	Forests
3	Artificial surfaces
4	Bare Soil
5	Agricultural surfaces

The training of the classifier combines the study of pre-existing maps, previous experience and site visiting in the study area. The software then applies the algorithm

of maximum likelihood and the resulting map is depicted at Figure 3.13. The results seem to be very reasonable.

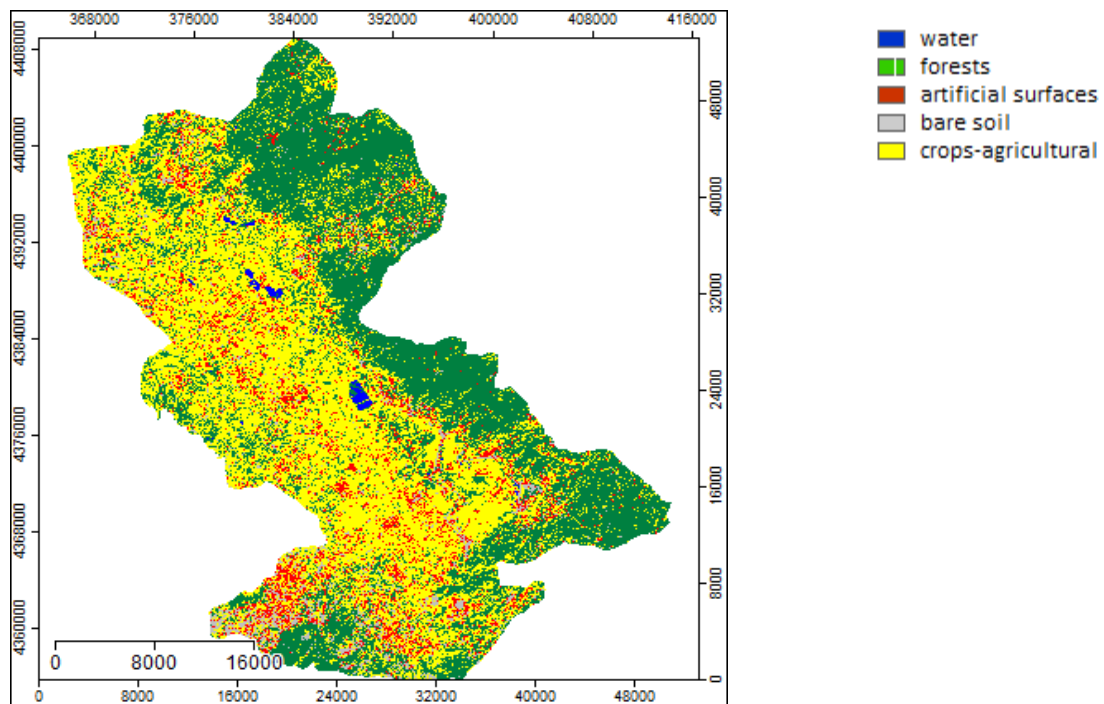


Figure 3.13. Supervised classification: Stage 1.

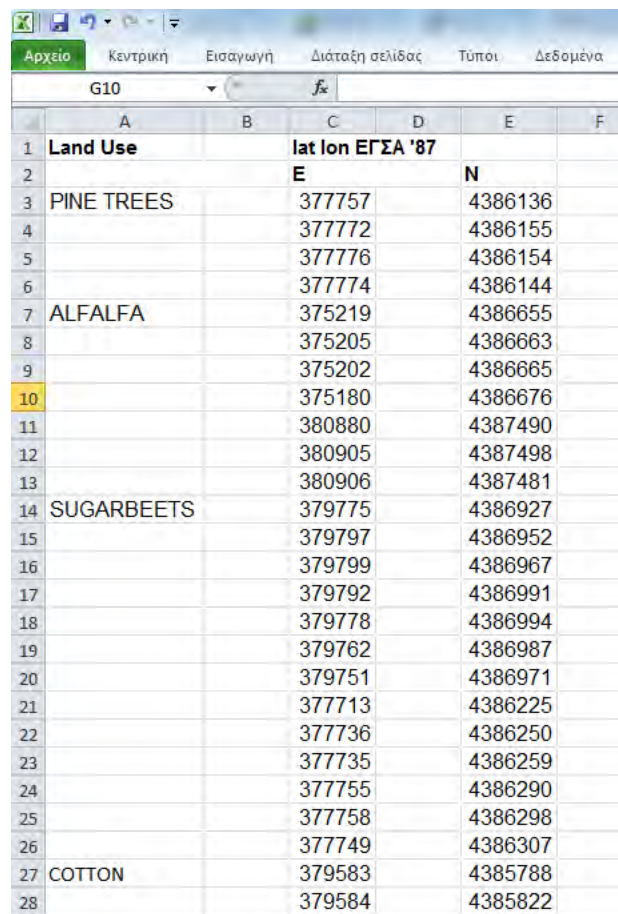
The next step of this study is the classification of individual crops. This is assigned as Stage 2 classification. At this stage supervised classification takes into account the classes coming directly from the needs of the user (Table 3.3).

Table 3.3. Class classification.

Class	Description
1	Grass-Clover
2	Sugar beet
3	Maize
4	Bare
5	Water
6	Pasture
7	Suburban
8	Cotton
9	Wheat
10	Forest Trees



Many field visits were carried out for the identification of the training pixels of the study area throughout the study period. A portable GPS device together with a camera was used for this reason. A spreadsheet was, then, used for each occasion (Figure 3.14). Special attention was given to areas with mixed land use. A typical example very close to the Lake Karla is given in Figure 3.15.



	A	B	C	D	E	F
1	Land Use		lat	lon	ΕΓΣΑ '87	
2			E		N	
3	PINE TREES		377757		4386136	
4			377772		4386155	
5			377776		4386154	
6			377774		4386144	
7	ALFALFA		375219		4386655	
8			375205		4386663	
9			375202		4386665	
10			375180		4386676	
11			380880		4387490	
12			380905		4387498	
13			380906		4387481	
14	SUGARBEETS		379775		4386927	
15			379797		4386952	
16			379799		4386967	
17			379792		4386991	
18			379778		4386994	
19			379762		4386987	
20			379751		4386971	
21			377713		4386225	
22			377736		4386250	
23			377735		4386259	
24			377755		4386290	
25			377758		4386298	
26			377749		4386307	
27	COTTON		379583		4385788	
28			379584		4385822	



Figure 3.14. Fields recording using GPS.

After recording hundred of different points, recognition of the thematic classes that are present in the multispectral image to be classified is carried out (Figure 3.16). A series of training areas or single pixels which characterise each thematic class are used. Statistics are applied in order to assign each multispectral pixel to one of the recognised themes (classes) present in the scene. Maximum distance rule is applied again using specialized software and the resulting map is finally illustrated in Figure 3.17.



Figure 3.15. Mixed land use.

Signature Editor (sig\_karlas\_5\_3\_2012.sig)

File Edit View Evaluate Feature Classify Help

Class #	>	Signature Name	Color	Red	Green	Blue	Value	Order
1	>	TRIFILLI		0.498	1.000	0.000	1	1
2		COTTON 1		1.000	1.000	1.000	2	2
3		SITARI 1			1.000	0.000	3	3
4		AMPELIA		0.000	0.392	0.000	4	4
5		VOSKOTOPOS		0.616	0.514	0.506	5	5
6		FISTIKIA		0.659	0.658	0.606	6	6
7		COTTON 2		1.000	1.000	0.878	7	7
8		SITARI PROIN VAMVAKI		1.000	1.000	0.000	8	8

Figure 3.16. Recognition of thematic classes.

Figure 3.17 illustrates separate classes which are very reasonably distributed across the study area. From the image analysis it seems that the whole Lake Karla Watershed has an area of 1208,78 km<sup>2</sup>.

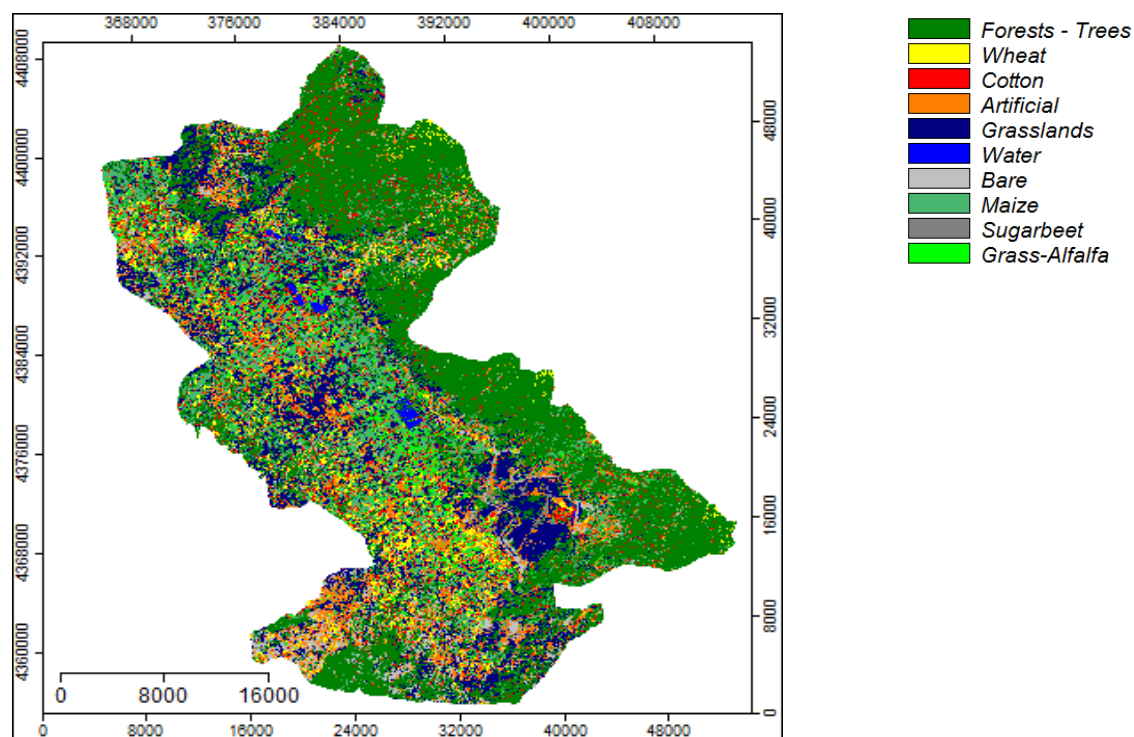


Figure 3.17. Supervised classification: Stage 2.

Table 3.4 gives class statistics converted to  $\text{m}^2$  (from the initial 30 m x 30 m pixels). Trees and forests have the majority of pixels at this analysis and this is totally justified, based on the large amount of mountainous regions at the area.

Table 3.4. Land use class statistics

Class	Total area ( $\text{km}^2$ )	Percentage (%)
Grass+ Clover	49,663,8	4,1
Sugar Beet	17,500,5	1,4
Maize	78,772,5	6,5
Bare	51,457,5	4,3
Water Surfaces	5,449,5	0,5
Pasture	194,835,6	16,1
Suburban	108,866,7	9,0
Cotton	175,653,9	14,6
Wheat	49,345,2	4,1
Forest Trees	477,237,6	39,4
Total	1208,783	100

### 3.7.8 Accuracy assessment

Classification should always be performed with accuracy assessment in order to quantify the quality of the product. Accuracy is generally assessed taking an independent random sample of known pixels from the original image and then generating a confusion (or contingency) matrix for the classified image. This would provide a careful examination of the distinctiveness of the classes. The assumed-true data are derived from ground-truth data. The relation between the set of reference pixels and the classified pixels is commonly illustrated in an error-matrix table also known as a confusion matrix or contingency table (Al-Ahmadi and Hames, 2009). Table 3.5 shows the accuracy estimation of the method by evaluating 69 random points applying Congalton and Green (2009) methodology. Independent known pixels from previous visits of the study area are utilized for this reason. In some cases well known areas are also utilized obtained from existing maps (e.g. dams, or mountains). Each class is described by two numbers: the first number on the diagonal is the “correct” number, that is the number of pixels which are correctly classified into the proper category, and the second number is the “wrong” number which is the number classified in a different class than the actual. These numbers represent how well training set pixels of the given crop type are classified. The total user’s accuracy is then computed by dividing the total number of correctly classified pixels (sum of major diagonal) by the total number of tested pixels in all categories (Lillesand and Kiefer, 2000; USACE, 2003; Al-Ahmadi and Hames, 2009). The value equal to 1 indicates the perfect classification (Otazu and Arbiol, 2000). All the results are illustrated in Table 3.5, together with the final total classification score which is 88.4%, indicating a very satisfactory classification accuracy and assuring that the individual classes are very well presented.

### 3.7.9 Classification after the filling of the reservoir

The same methodology has been applied, again, after the filling of the reservoir, utilizing Landsat TM imagery of 15-7-2012. The Land Use Classes have been enriched (Table 3.6) and the new classification is illustrated at Figure 3.18. Classification accuracy

is again very satisfactory (88,3%) evaluating 60 random points applying Congalton and Green methodology (Congalton and Green, 2009).

Table 3.5. Classification statistics-Error Matrix.

	Reference Data										Row Totals
	1	2	3	4	5	6	7	8	9	10	
Classification Data	1	<u>4</u>		1							5
	2		<u>5</u>								5
	3			<u>3</u>							3
	4			<u>4</u>							4
	5				<u>15</u>			1			16
	6					<u>4</u>					4
	7						<u>5</u>			1	6
	8			1		1		<u>7</u>			9
	9	1			1			1	<u>6</u>		9
	10									8	8
Column Totals	5	5	4	6	15	5	5	9	6	<u>9</u>	<u>69</u>
<u>Total classification accuracy (4+5+3+4+15+4+5+7+6+8)/69= 88,4%</u>											

Table 3.6. Land Use class classification.

Class	Description
1	Wheat
2	Fruit Trees
3	Vines
4	Shrubs - Bare
5	Pasture
6	Cotton
7	Artificial Surfaces

8	Water Surfaces
9	Maize
10	Alfalfa
11	Forest Trees
12	Sugar beet

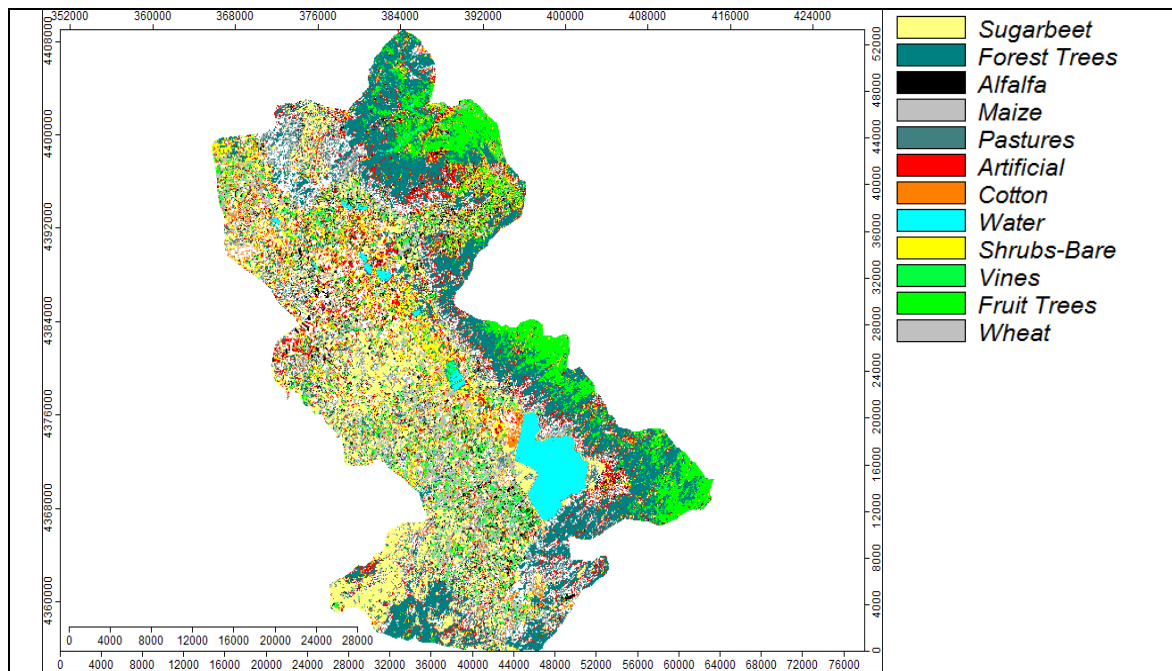


Figure 3.18. Supervised classification: Stage 2, 2012.

The latest 2012 classification is used in the proposed model described in the next Chapter of the dissertation.

## CHAPTER 4° METHODOLOGY

### 4 Methodology

The initial goal is to compute Landsat TM derived  $ET_a$  values for Lake Karla watershed using METRIC methodology, and, then, to combine local meteorological data including air temperature, humidity, wind speed, and solar radiation with  $ET_a$  values for estimating  $ET_rF$  values. The application of this “classical” methodology is used as background. The time period for developing and applying this methodology is the growing season of 2007. The crop coefficient values ( $ET_rF$ ) are then inserted to CropWat model described later to finally estimate irrigation requirements (in mm) for the main crops for every area (zone) of the watershed, using the previous land use/cover classification of the area. The procedure is repeated for every zone of the study watershed. This “background application” is illustrated at the simple version flow chart of Figure 4.1.

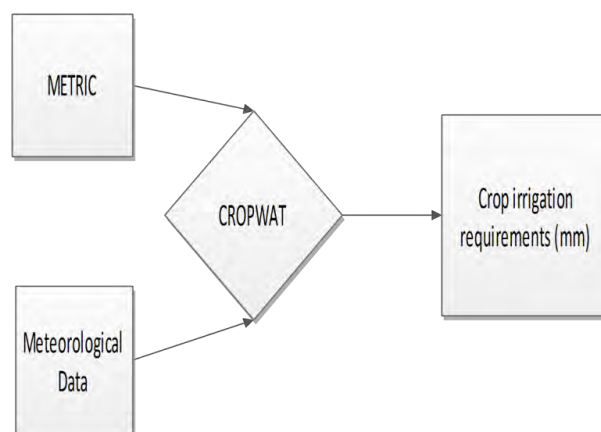


Figure 4.1. Flow chart of the “classical” methodology for the estimation of irrigation requirements

In the second stage, an integrated proposed methodology is applied in the study watershed. The proposed methodology combines the knowledge and the experience acquired from the application of the “classical” methodology of METRIC with the field spectroradiometric measurements, the downscaling of MODIS images to Landsat



spatial resolution and the CropWat model and provides daily estimates of crop water irrigation requirements with a spatial analysis of 30 m x 30 m.

More specifically, at this stage, Landsat ETM+ images are combined to produce  $ET_rF$  values with a 30 m x 30 m spatial resolution for the growing season of 2012.  $ET_rF$  vs NDVI relationships are produced using data derived from surface reflectance values measured in the field using specialized portable spectroradiometer. These values are filtered in order to be equivalent to Landsat ETM+ bands 1, 2, 3 and 4. Data collection was carried out during 2012 growing season, while a Global Positioning System (GPS) was used to spatially locate the fields.

MODIS Level 1B and Level 3 data are also utilized and downscaling techniques between them and Landsat ETM+ imagery are analyzed. MODIS based NDVI values are finally derived and then downscaled combining Landsat ETM+ based NDVI values using internal downscaling explained later. These NDVI values are finally inserted to the previous  $ET_rF$  vs NDVI relationship in order to produce a final daily  $ET_rF$  map with a 30 m x 30 m spatial resolution for the growing season of 2012. Figure 4.2 illustrates the simple version flow chart of the proposed integrated methodology.

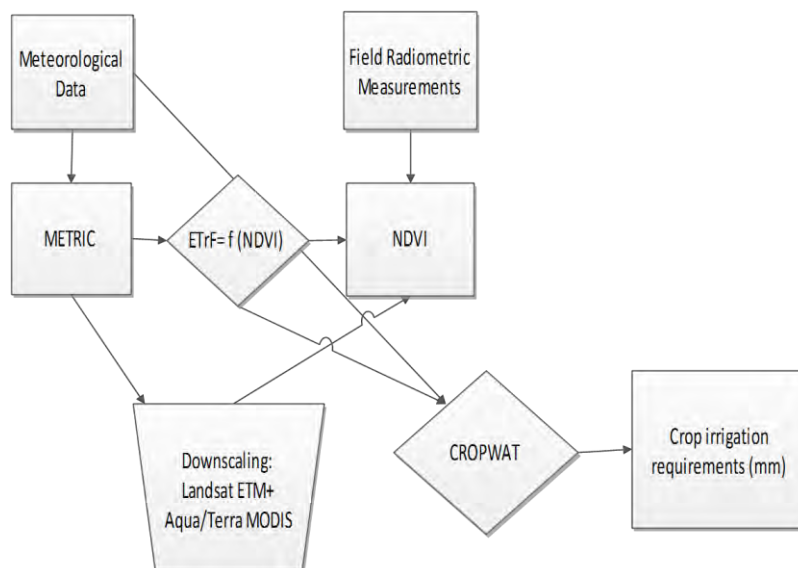


Figure 4.2. Flow chart of the proposed integrated methodology for the estimation of irrigation requirements.



#### 4.1 Preprocessing of data

One of the satellites series mainly used in this study is the Landsat series, which has provided the longest period of coverage, spanning from the present time back to 1972 when Landsat-1 (originally known as ERTS-1) was launched. Four different types of sensors have been included in various combinations on the Landsat missions, including the Thematic Mapper (TM) on Landsat 4 and 5, and the Enhanced Thematic Mapper Plus (ETM+) present on Landsat 6 and 7 which were described earlier. TM and ETM+ sensors present similar characteristics, and can be comparable (e.g. spectral, spatial and temporal resolution). An extremely useful free of charge dataset for the long-term monitoring of environment arises as a result (Woodcock *et al.*, 2008; Ju and Roy, 2008). During the preparation of this study, Landsat 8 has been established, extending the remarkable 40 year Landsat record. Landsat 8 has enhanced capabilities including new spectral bands in the blue and cirrus cloud-detection portion of the spectrum, two thermal bands, improved sensor signal-to-noise performance and associated improvements in radiometric resolution, as well as an improved duty cycle allowing collection of a significantly greater number of images per day (Roy *et al.*, 2014). NASA's Terra and Aqua satellites and the MODerate Resolution Imaging Spectroradiometer (MODIS), operational Bidirectional Reflectance Distribution Function (BRDF) and albedo products have also been used in this study.

Before the processing and analysis of the image, various pre-processing routines, appropriate to the desired output, must be applied to the imagery. These routines improve the quality of the image data by reducing or eliminating various radiometric and geometric errors caused by internal or external conditions. Geometric correction procedures address errors in the relative position of pixels due to factors such as variation in altitude, earth curvature, panoramic distortion, relief displacement and non-linearities in the sweep of a sensor (Lillesand and Kiefer, 2000). Radiometric correction procedures account for errors that affect the brightness value of pixels due to both a sensor system detector error and an environmental attenuation error (e.g. changes in scene illumination, atmospheric conditions and viewing geometry [Lillesand and Kiefer, 2000]). The elimination of these errors is of great importance, especially

when multitemporal or multispatial datasets are used. This is because radiometric corrections act as a normalization of conditions across time and space. Radiometric and geometric correction are always the essential steps, but in the aim of further analysis, other pre-processing steps and procedures used to emphasize the images' important information may be applied. One of these procedures can be for example the image enhancement. However it is important to keep in mind that the pre-processing methods can change the original information of the imagery.

#### 4.1.1 Radiometric correction

Radiometric correction is the procedure used to approximate the initial pixel values to their original reflectance values. These differences may arise from sensor failures or miscalibration, as well as from the effects of the atmosphere in electromagnetic radiation (atmospheric distortion). Distortions of the sensors may be reduced by radiometric correction. Missing lines of data (especially at Landsat 7 ETM+) can also be removed. Different sensitivity of the sensors can cause intensity difference between the bands which is also a very serious problem (miscalibration). Atmospheric correction can be reduced mainly by modifying the pixel values by specified repair values. Figure 4.3 illustrates missed lines correction (gapfill) for Landsat 7 ETM+ on 2012-10-03.

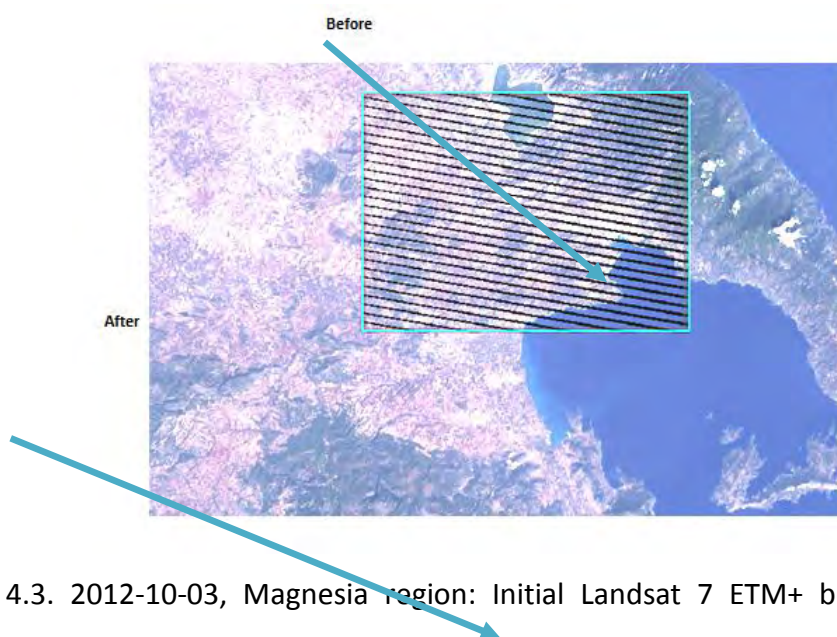


Figure 4.3. 2012-10-03, Magnesia region: Initial Landsat 7 ETM+ before and after gapfill.

Taking Landsat as an example in this chapter, it is essential to mention that the pixel values represent the sensitivity of the sensor and the number of discrete data bits used to record this data. The pixel values are, then, scaled to byte values prior to output (Landsat 7 Science Data Users Handbook). The following general Equation (4.1) is used to convert Digital Numbers (DNs) back to radiance (L):

$$L_{\lambda} = \text{"gain"} \times QCAL + \text{"bias"} \quad (4.1)$$

Which is also can be expressed as:

$$L_{\lambda} = \left( \frac{LMAX_{\lambda} - LMIN_{\lambda}}{(QCALMAX - QCALMIN) + LMIN_{\lambda}} \right) \times (QCAL - QCALMIN) \quad (4.2)$$

where:

$LMIN_{\lambda}$  and  $LMAX_{\lambda}$  are the minimum and maximum spectral radiance values scaled to  $QCALMAX$  and  $QCALMIN$ , which can be found in header data, and

$QCALMAX$  and  $QCALMIN$  are the maximum and minimum digital pixel values (DN) scaled to  $LMIN_{\lambda}$  and  $LMAX_{\lambda}$ .

For Landsat 7, where 8-bit data =  $2^8 = 256$  levels,  $QCALMAX = 255$  and  $QCALMIN = 0$ , equation (4.2) becomes:

$$L_{\lambda} = \left( \frac{LMAX - LMIN}{255} \right) \times DN + LMIN \quad (4.3)$$

Equation 4.3 finally converts the initial digital numbers (DNs) to at-satellite radiances (Figure 4.4).

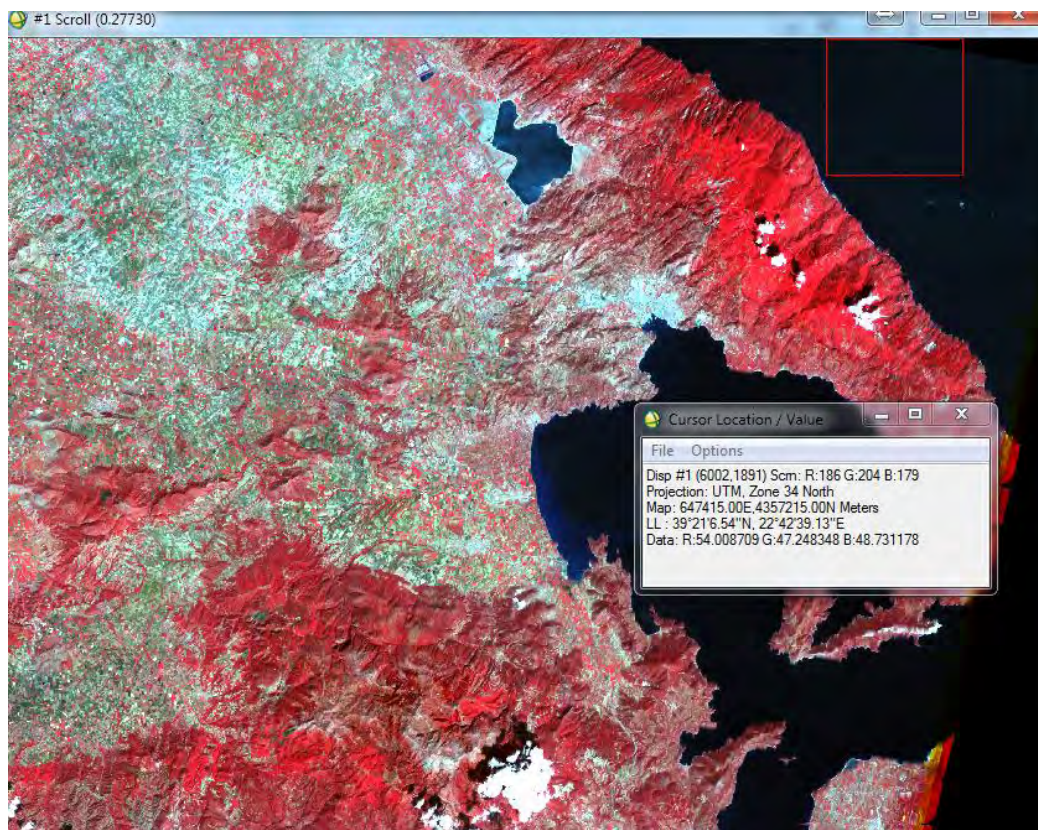


Figure 4.4. Magnesia region: Landsat 7 ETM+ at-satellite radiance on 03/10/2012

#### 4.1.2 Geometric correction

The geometric correction decreases and/or remove the geometric distortions appearing on the original satellite images. Distortion of terrain can be decreased by applying digital terrain models, while panoramic distortions caused by the earth can be corrected by orthorectification. Practically, the goal is to fit the image into a valid map projection. Spatial accuracy is always important, and a detailed geometric correction would be very useful for the combination of other raster or vector based products. These products could be other satellite images, land use maps, GIS layers etc. Working with the same coordinate system is the key, converting different coordinate systems into one common. Greek National Coordinate System (EGSA'87), the official geodetical system in Greece, is applied to all the images used in this study.

In the case that the satellite image has another projection system, then the process is the transformation between the two reference systems, which is called rectification. When the satellite systems do not have any projection system or it is unknown then the transformation can be done using ground control points. This is called georeferencing or geocoding. This process has been applied to all the satellite images used in this study.

Georeferencing uses Ground Control Points (GCP's) which are known points easily identified on the satellite images. These points can be known structures as airports or characteristic buildings, house corners, lakes, rivers, crossroads etc. These points can have known coordinates based on previous GPS measurements. Finally, applying this methodology each GCP has two pairs of coordinates. The one pair is from the original image which is called source, and the other is from the already known defined measurement which is called reference pair. Every single point of the new satellite image can be transformed into the new system applying a polynomial equation. It is desirable to follow simple rules about selecting GCP's:

- GCP's must be selected only if they have distinct features.
- It is not good to leave unsampled areas
- Sampling must be done intensively in areas where a considerable distortion is detected
- A large number of GCP's must be close to the image boundaries in order to avoid distortion

The number of the available control points defines the degree of the polynomial transformation applied. In this thesis more than twelve (12) control points are utilized in any case for all images. Figure 4.5 illustrates an example of applying an image to image registration for the image for the 27<sup>th</sup> of August, 2007 if a well known registered image is used as a reference image (26<sup>th</sup> of July 2007). The same procedure has been applied to all satellite images in this study.



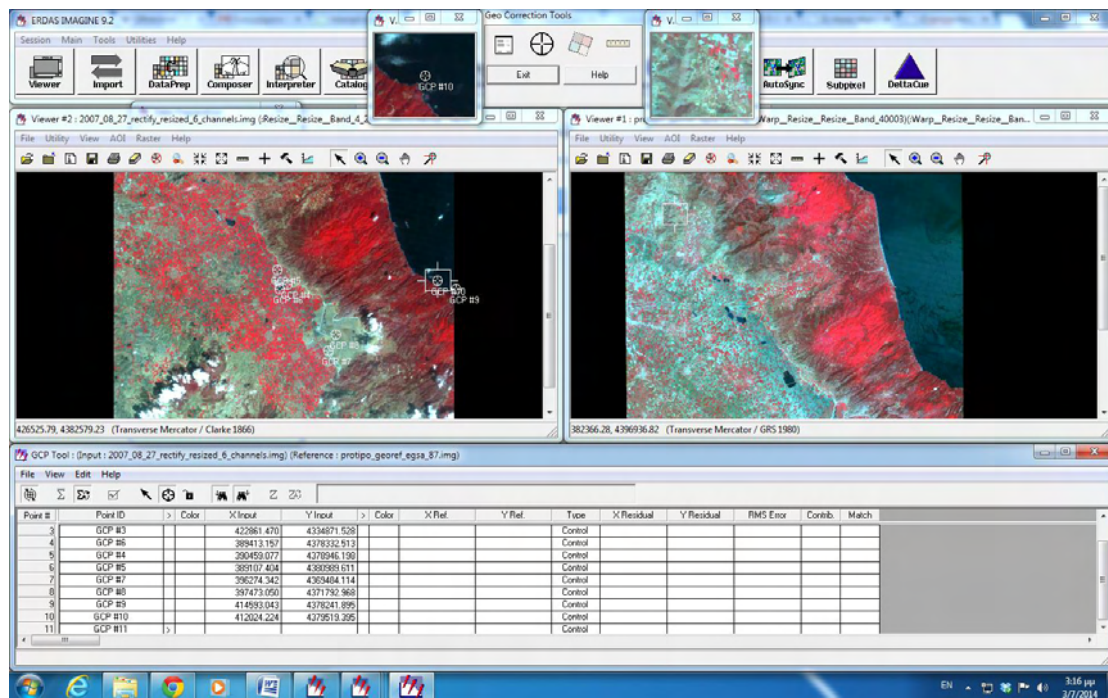


Figure 4.5. Landsat TM image to image registration for 27/7/2007.

The last application which can be used for the interpretation of the images is the image enhancement which has to do with the visual recognition of the objects on the image. It is very important to mention that this modification improves the visual quality of the image but is not keeping the original pixel values. In other words, a modification of the original information is taken place. The most important image enhancement techniques are the changing of contrast and the changing of brightness. One very common methodology is the linear histogram stretching where the pixel values change covering a wider range of values. In the case that the new image has again a poor contrast due to the fact that the value ranges are again very close to each other, then histogram equalization is the best technique to apply. This is based on a frequency distribution of the values. Histogram equalization (Figure 4.6) merges some classes in such a way that will have about the same number of pixels. The original information is changing, rearranging the classes of the pixels trying to create a uniform histogram, which is the final goal of the methodology.

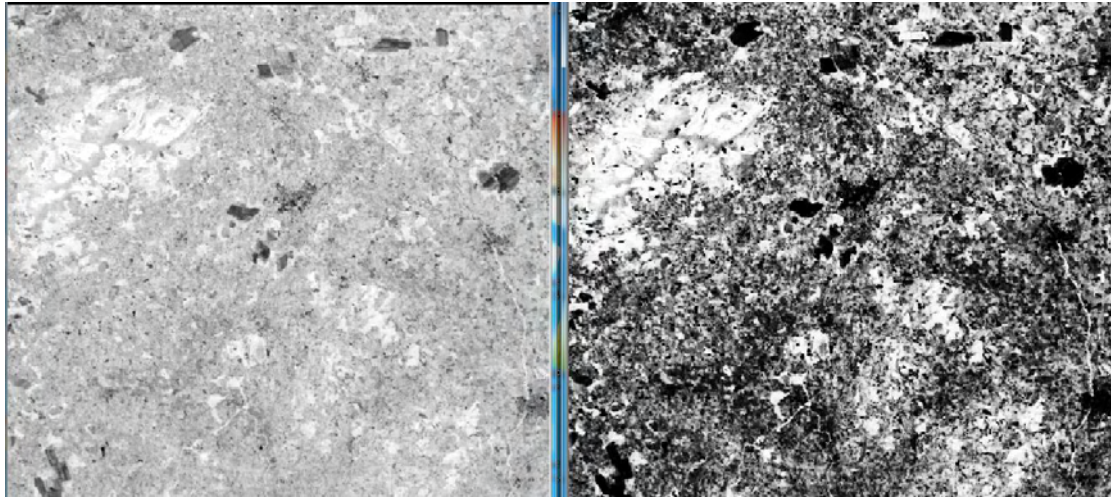


Figure 4.6 Image Histogram Equalization (Left: Before, Right: After).

Other image enhancement methodologies are the image filtering methodologies where each pixel value changes depending on the value of the surrounding pixels. Some of the most usually used filters are the high and pass filter kernel and the edge detection filter kernel. These filters are based on a matrix which is usually a moving window or kernel, running the whole image. The window is moving, changing accordingly the value of the middle pixel.

#### 4.1.3 Assessing Geometric Accuracy

The coordinates resulting from a transformation are only an estimate and there is a need for checking their degree of accuracy. Accuracy can be expressed as an overall Root Mean Square Error (RMSE). Figure 4.7 shows how control points have been evaluated for the degree of error they exhibit in both the X and Y direction. This error, then, produces an individual point error which then contributes to the overall RMSE. High RMSE values ( $> 1$  pixel) can indicate to the user how inaccurate the transformation is and whether the chosen GCPs were adequate; the process can then be repeated with additional/different GCPs in order to decrease the point and total error. It should be noted that a high RMSE for a particular point indicates to the user a GCP that should be removed or replaced.

Control Point Error: (X) 1.4723 (Y) 1.0820 (Total) 1.8271														
Point #	Point ID	>	Color	X Input	Y Input	>	X Ref.	Y Ref.	Type	X Residual	Y Residual	RMS Error	Contrib.	Match
1	GCP #1			419260.006	4321089.906		679056.109	4323001.253	Control	1.084	-1.435	1.799	0.984	
2	GCP #2			409061.844	4303058.544		669454.391	4304638.845	Control	-2.509	1.761	3.065	1.678	
3	GCP #3			422711.450	4334584.307		682061.025	4336606.606	Control	2.507	-1.441	2.892	1.583	
4	GCP #4			390308.831	4378659.224		648205.336	4379590.935	Control	0.128	-0.594	0.607	0.332	
5	GCP #5			388957.148	4380702.649		646786.104	4381588.373	Control	-0.135	-0.986	0.995	0.545	
6	GCP #6			389262.905	4378045.535		647180.335	4378942.644	Control	0.429	-0.575	0.718	0.393	
7	GCP #7			396124.139	4369197.086		654333.439	4370326.505	Control	1.211	0.757	1.428	0.781	
8	GCP #8			397322.853	4371505.956		655454.808	4372674.370	Control	0.674	0.553	0.872	0.477	
9	GCP #9			414442.947	4377954.934		672354.180	4379691.683	Control	-1.559	1.066	1.889	1.034	
10	GCP #10			411874.112	4379232.440		669743.494	4380983.137	Control	-1.831	0.894	2.037	1.115	
11	GCP #11	>					652912.912	4342556.482	Control					
12	GCP #12						656264.932	4343114.033	Control					
13	GCP #13						662858.133	4339563.848	Control					
14	GCP #14						664188.193	4338220.353	Control					
15	GCP #15						682150.720	4336635.029	Control					
16	GCP #17						679483.883	4328567.342	Control					
17	GCP #16						678624.046	4322763.444	Control					
18	GCP #18	>							Control					

Figure 4.7 RMSE errors for the first 10 control points tested for a geometric correction procedure.

#### 4.2 Surface Energy Balance Algorithms for Land (SEBAL) – Detailed Methodology

ET in the SEBAL model is computed from satellite images and meteorological data using the surface energy balance. This balance is based on the fact that evaporation consumes energy (Figure 4.8). Since satellite images provide information for the overpass time only, SEBAL computes an instantaneous ET flux for the image time. These ET values can be then extrapolated using a ratio of ET to reference crop ET to obtain daily or seasonal levels of ET.

ET flux is calculated for each pixel of the image as a “residual” of the surface energy budget equation, where soil heat flux (G) and sensible heat flux (H) are subtracted from the net radiation flux at the surface ( $R_n$ ) to compute the “residual” energy available for evapotranspiration ( $\lambda ET$ ) :

$$\lambda ET = R_n - G - H \quad (4.4)$$

where:  $\lambda ET$  is the latent heat flux ( $W/m^2$ ),

$R_n$  is the net radiation flux at the surface ( $W/m^2$ ),

G is the soil heat flux ( $W/m^2$ ), and

H is the sensible heat flux to the air ( $W/m^2$ ).





Figure 4.8. Surface Energy Balance.

Net radiation flux at the surface ( $R_n$ ) represents the actual radiant energy available at the surface. For the computation of  $R_n$  outgoing and ingoing radiant fluxes are taken into account, given the surface radiation balance Equation (4.5) by simply subtracting losses from the gain:

$$R_n = R_{s\downarrow} - \alpha R_{s\downarrow} + R_{L\downarrow} - R_{L\uparrow} - (1-\epsilon_0)R_{L\downarrow} \quad (4.5)$$

where:

$R_{s\downarrow}$  is the incoming shortwave radiation ( $\text{W/m}^2$ ),

$\alpha$  is the surface albedo (dimensionless),

$R_{L\downarrow}$  is the incoming longwave radiation ( $\text{W/m}^2$ ),

$R_{L\uparrow}$  is the outgoing longwave radiation ( $\text{W/m}^2$ ), and

$\epsilon_0$  is the surface thermal emissivity (dimensionless).

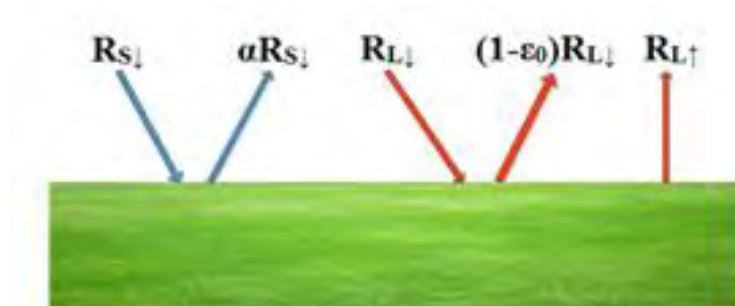


Figure 4.9. Net radiation = gain – losses.

Figure 4.9 illustrates the net radiation balance. From the initial value  $R_{s\downarrow}$  of incoming shortwave radiation (gain) a portion of a  $R_{s\downarrow}$  is a loss. Surface albedo  $\alpha$  is a reflection coefficient which is defined as the ratio of the reflected radiant flux to the incident radiant flux over the solar spectrum. Albedo is calculated separately using satellite image information on spectral radiance for each satellite band. Similarly, from the initial value  $R_{L\downarrow}$  of incoming longwave radiation a portion of  $(1 - \epsilon_o) * R_{L\downarrow}$  is a loss. Surface emissivity is defined as the ratio of the actual radiation emitted by a surface to that emitted by a black body at the same surface temperature. This is the fraction of incoming longwave radiation that is lost from the surface due to reflection. Finally,  $R_{L\uparrow}$  is the outgoing longwave radiation emitted from the vegetation surface under consideration.

The incoming shortwave radiation ( $R_{s\downarrow}$ ) can be computed using the solar constant, the solar incidence angle, a relative earth-sun distance, and a computed atmospheric transmissivity. The incoming longwave radiation ( $R_{L\downarrow}$ ) can be computed using the modified Stefan-Boltzmann equation with atmospheric transmissivity and a selected surface reference temperature. Outgoing longwave radiation ( $R_{L\uparrow}$ ) is computed using the Stefan-Boltzmann equation with a calculated surface emissivity and surface temperature. Surface temperature values are computed using satellite image information on thermal radiance (thermal bands). Finally, in SEBAL, emissivity is computed as a function of a vegetation index (e.g. NDVI).

Soil heat flux ( $G$ ) can be empirically calculated using vegetation indices, surface temperature, and surface albedo ( $\alpha$ ). Sensible heat flux is computed using wind speed data, estimated surface roughness, and surface to air temperature differences ( $dT$ ). SEBAL uses an iterative process to correct for atmospheric instability due to the buoyancy effects of surface heating (Bastiaanssen, 1998a).

From the moment that the latent heat flux ( $\lambda ET$ ) can be computed for each pixel, an equivalent amount of instantaneous ET (mm/hr) can be calculated by dividing by the latent heat of vaporization ( $\lambda$ ). Reference crop ET, which can be found as  $ET_r$ , is the ET

rate expected from a well-defined surface of full-cover alfalfa or clipped grass.  $ET_r$  in SEBAL can be computed using meteorological data. A detailed definition of reference ET is given in a separate chapter.

SEBAL can compute ET for flat, agricultural areas with the most accuracy and confidence. An application for mountain areas is slightly different because elevation, slope, and aspect need to be considered, but there was not such a need to apply for this study.

#### **4.2.1 Model Requirements**

SEBAL requires at least one satellite image and meteorological data. The construction of a land-use map for the area of interest is also desirable. The most important requirement for the total methodology is that the satellite images used must be cloudless (totally clear sky is preferable) since ET cannot be computed for cloud covered surfaces. Large errors in the calculation of sensible heat fluxes can be produced from the existence of clouds, mainly due to the influence of water vapour to the thermal bands in use. Special techniques can be applied for removing pixels with cloud covering, but generally it is preferable to work with totally cloud-free images.

#### **4.2.2 Satellite Image Information**

Satellite images always come with meta-data files which include all the necessary information about the image acquisition. These meta-data files usually can be found as “header” files. Table 4.1 shows which type of information must be obtained from the header files, while Figure 4.10 illustrates an example of a header file acquired for a Landsat 7 ETM+ image of 1-9-2012. The satellite overpass time usually can be found as Greenwich Mean Time (GMT) but it must be converted to local time. Latitude, longitude and elevation angles are expressed in degrees ( $^{\circ}$ ), while gains and biases are used to convert digital numbers (DN's) in the original files into energy units. For example, when applying to Landsat images, separate gain and bias values for each

band must be available. For the thermal band (band 6) both high and low gain images are supplied, but, the use of low gain image is recommended which generally yields slightly lower resolution, but is less likely to suffer from saturation (Waters et al., 2002).

Table 4.1. Required data for the application of SEBAL model.

Satellite meta-data information	Satellite overpass date and time Latitude and longitude of the center of the image Sun elevation angle ( $\beta$ ) at the overpass time Gain and Bias levels for each channel
Meteorological data	Wind speed Precipitation Humidity Solar radiation Air Temperature

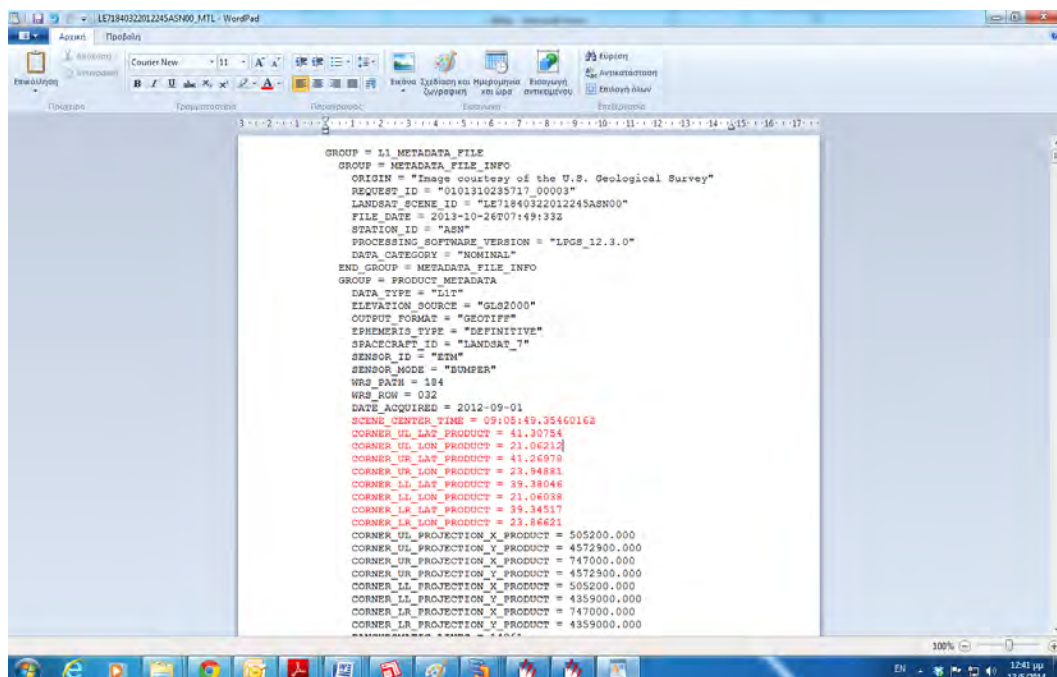


Figure 4.10. Header file for the 1-9-2012 Landsat 7 ETM+ image

#### 4.2.3 Meteorological Data

First of all, precipitation data is used to evaluate the general wetness condition of areas under consideration. A check must be done in order to determine if the areas have received rain within four or five days before the image date, otherwise a special rainfall balance must be applied. No rainfall recordings have recorded until five days before the image date, for all images used in this study.

Wind speed ( $u$ ) at the satellite overpass time is required for the computation of sensible heat flux ( $H$ ), while solar radiation data are useful especially for adjusting the atmospheric transmissivity ( $\tau_{sw}$ ).

Table 4.1 also shows all the necessary meteorological data for processing SEBAL. All these data are desirable on an hourly basis except precipitation data which are recommended on a several week period prior to the image. Reference ET in SEBAL is computed using alfalfa as a reference crop. It must be emphasized that if reference ET is available, there is no need for obtaining variables such humidity, air temperature and solar radiation which are needed for the computation of reference ET.  $ET_r$  is used in SEBAL to compute  $H$  at the “cold” anchor pixel and to compute the  $ET_r$  fraction ( $ET_r/F$ ) that is used to predict 24-hour and seasonal ET. The meaning of “cold” and “hot” pixels will be described later.

One very important fact to mention is that weather conditions generally are not uniform within a satellite image. It is very common that an average area has a variety of land-uses, vegetation and soils, mountains, lakes or deserts which can affect the weather conditions dramatically. One solution is to use data from two or more meteorological stations, but in most cases a station located in an agricultural area is assumed suitable. This reduction comes from the realistic fact that usually the primary interest is to compute ET over agricultural fields. The most important is to keep the station location at a distance no more than 50 km near the location of cold and hot pixels.

#### 4.2.4 Land Use Map

A land-use map is needed in SEBAL for the estimation of surface roughness parameter ( $z_{om}$ ) if there are no other data as explained later. This kind of map classifies the area of interest into various general classes of land-use such as water surfaces, agriculture crops, constructions, forests, etc. Two kind of land-use maps are generated for this reason and described in a separate chapter.

#### 4.2.5 Computation of $ET_r$

The initial satellite image is pre-processed, as described in a separate chapter, and it is saved in a separate file. Meteorological data are then collected and organized in a table. Reference  $ET$  is the first variable to be computed from the available data and this can be achieved with the specified REF-ET software package or manually using Penman-Monteith equations (Figure 4.11 and Figure 4.12).

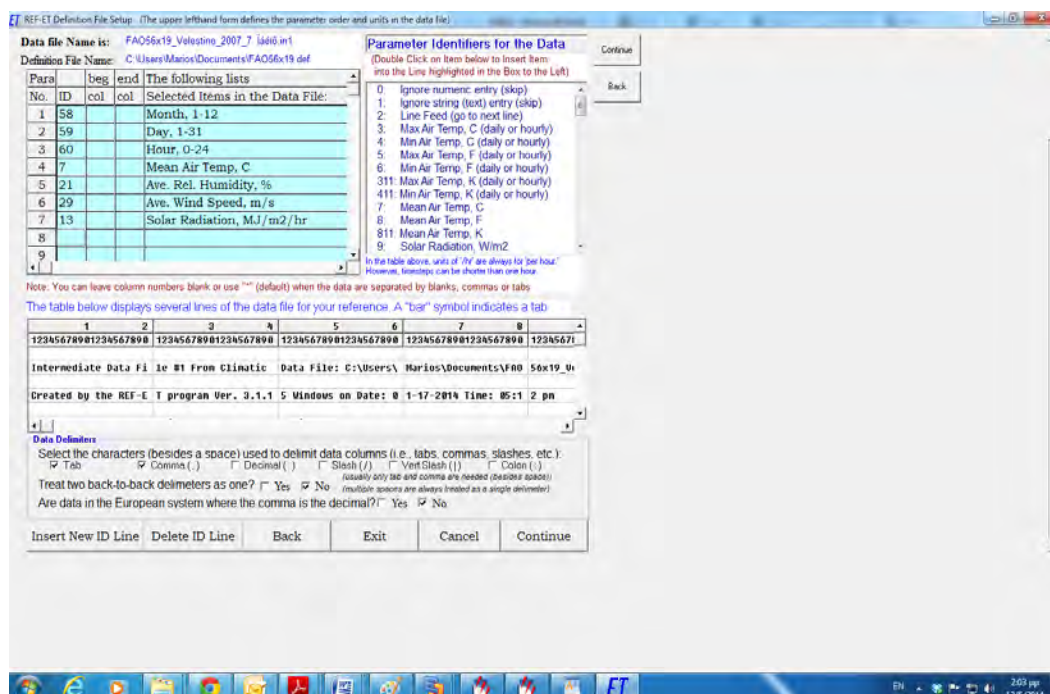
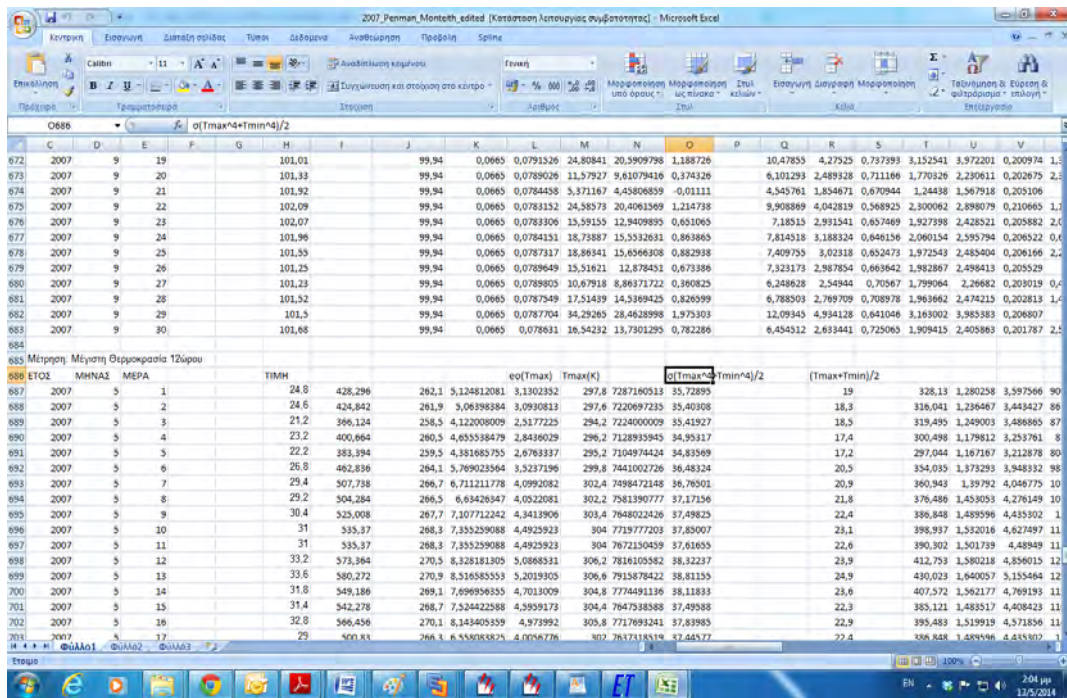


Figure 4.11. Computation of  $ET_r$  using “ref ET” package.

Figure 4.12. Computation of  $ET_c$  manually using Penman – Monteith methodology.

#### 4.2.6 Steps and sub-models.

The general concept of SEBAL, as well as METRIC explained later, is Equation (4.4) and the primary goal of the described methodology is to compute the three basic parameters of Equation (4.4), namely: Net Surface Radiation ( $R_n$ ), Soil Heat Flux ( $G$ ) and Sensible Heat Flux ( $H$ ). Many steps and sub-models are needed for the operation of SEBAL and/or METRIC methodology. Table 4.2 gives a summary of these steps and models which now will be described.

Table 4.2. Steps needed for the application of SEBAL.

Steps	Computation of:	Model
Step 1	Spectral radiance	Model 01
Step 2	Reflectivity	Model 02
Step 3	Albedo at the top of the atmosphere	Model 03

Step 4	Surface Albedo	Model 04
Step 5	NDVI, SAVI, LAI	Model 05
Step 6	Incoming shortwave radiation ( $R_{s\downarrow}$ )	spreadsheet
Step 7	Surface emissivity	Model 06
Step 8	Surface Temperature	Model 07-08
Step 9	Incoming longwave radiation ( $R_{L\downarrow}$ )	spreadsheet
Step 10	Outgoing longwave radiation ( $R_{L\uparrow}$ )	Model 9
Step 11	Net surface radiation flux	Model 10
Step 12	Soil Heat Flux (G)	Model 11
Step 13	friction velocity ( $u^*$ )	spreadsheet
Step 14	momentum roughness length ( $z_{om}$ )	Model 12
Step 15	$u_{200}$	spreadsheet
Step 16	$r_{ah}$	Model 13
Step 17	Sensible Heat for Neutral Conditions (H)	Models 14-15
Step 18	Monin-Obukhov length (L)	Definition of equations - spreadsheet
Step 19	First Correction of $u^*$ and $r_{ah}$	Models 16-17
Step 20	Second Correction of $u^*$ and $r_{ah}$	Model 18-19
Step 21	Third Correction of $u^*$ and $r_{ah}$	Model 20-21
Step 22	Fourth Correction of $u^*$ and $r_{ah}$	Model 22-23
Step 23	Fifth Correction of $u^*$ and	Model 24-25



	$r_{ah}$	
Step 24	Sixth Correction of $u^*$ and	Model 26-27
	$r_{ah}$	
.....	.....	As needed
Step xx	Latent Heat Flux ( $\lambda ET$ )	Model xy (e.g. 25)
Step x(x+1)	Instantaneous ET and $ET_r F$	Model x(y+1) (e.g. 26)

#### 4.2.7 **PART 1 : Net Surface Radiation ( $R_n$ )**

The first basic parameter to be computed is  $R_n$ , and equation (4.5) is used for this reason as explained previously, but before applying (4.5) a number of other parameters must be specified. From now on all the methodology will be described applying Landsat imagery which is the mainly used source of satellite data used in this study. Special MODIS procedures are described at the end of sub-chapter 4.2. The parameters needed for  $R_n$  calculation are presented in the next paragraphs.

##### 4.2.7.1 *The computation of spectral radiance*

The spectral radiance for each band ( $L_\lambda$ ) is initially computed (model 01 - Figure 4.13). This is the outgoing radiation energy of the band observed at the top of the atmosphere by the satellite. It is calculated using the following equation (4.6) given for Landsat 5 and 7:

$$L_\lambda = \frac{L_{max} - L_{min}}{QCAL_{max} - QCAL_{min}} \times (DN - QCAL_{min}) + L_{min} \quad (4.6)$$

where: DN is the digital number of each pixel for the initial image,  $L_{MAX}$  and  $L_{MIN}$  are calibration constants, while  $QCAL_{MAX}$  and  $QCAL_{MIN}$  are the highest and lowest range of values for rescaled radiance (in DN). The units for  $L_\lambda$  are  $W/m^2/sr/\mu m$ .

For Landsat 5 images where  $QCAL_{MAX}=255$  and  $QCAL_{MIN}=0$ , Equation (4.6) becomes:

$$L_{\lambda} = \frac{L_{max} - L_{min}}{255} \times (DN) + L_{min} \quad (4.7)$$

For recent Landsat 7 images with header files containing gains and biases:

$$L_{\lambda} = Gain \times (DN) + Bias \quad (4.8)$$

#### 4.2.7.2 The computation of reflectivity

The reflectivity of a surface ( $\rho_{\lambda}$ ) can be defined as the ratio of the reflected radiation flux to the incident radiation flux (model 02 - Figure 4.13). It is computed separately for each band using the following equation (4.9):

$$\rho_{\lambda} = \frac{\pi \times L_{\lambda}}{ESUN_{\lambda} \times \cos\theta \times d_r} \quad (4.9)$$

where:

$L_{\lambda}$  is the spectral radiance for each band computed previously,

$ESUN_{\lambda}$  is the mean solar exo-atmospheric irradiance for each band ( $W/m^2/\mu m$ ),

$\cos\theta$  is the cosine of the solar incidence angle (from nadir) and

$d_r$  is the inverse squared relative earth-sun distance.

Values for  $ESUN_{\lambda}$  are given in Table 4.3 while  $\theta = (90^\circ - \beta)$ , where angle ( $\beta$ ) is taken using the header file data on sun elevation. The term  $d_r$  can be defined as  $1/d_{e-s}^2$  where  $d_{e-s}$  is the relative distance between the earth and the sun in astronomical units.

$d_r$  can be computed using the following equation (4.10) by Duffie and Beckman (1980), also given in FAO 56 paper: Crop Evapotranspiration (Allen et al., 1998):

$$d_r = 1 + 0.033 \cos\left(DOY \frac{2\pi}{365}\right) \quad (4.10)$$

where: DOY is the Julian day of the year (given in Annex 1), and the angle ( $DOY \times 2\pi/365$ ) is given in radians. Values for  $d_r$ , which are dimensionless, range from 0.97 to 1.03.

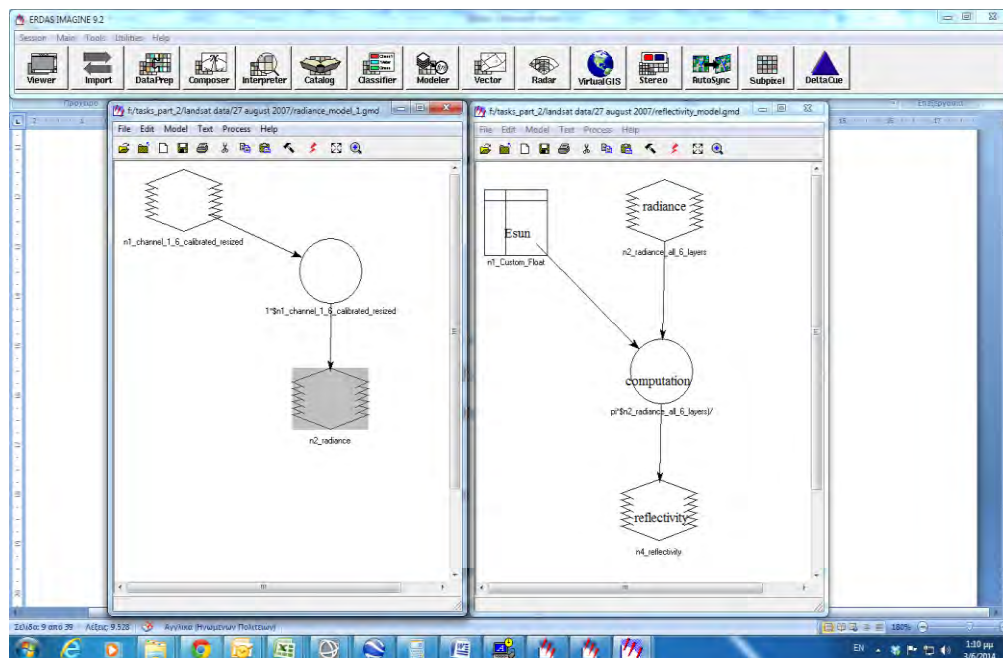


Figure 4.13. Computation of (a) radiance on the left side - Model 1 and (b) reflectivity on the right side – Model 2.

Table 4.3.  $ESUN_{\lambda}$  values for Landsat 5 and Landsat 7.

$ESUN_{\lambda}$ values	Band 1	Band 2	Band 3	Band 4	Band 5	Band 6	Band 7
Landsat 5	1957	1829	1557	1047	219.3	-	74.52
Landsat 7	1969	1840	1551	1044	225.7	-	82.07

Band number six has no values in Table 4.3 because it is actually a thermal band (is not a shortwave band), and it is not utilized for this computation. Finally, output file for reflectivity ( $\rho_{\lambda}$ ) as well as the model are saved, and kept for using at the next steps.

#### 4.2.7.3 The computation of albedo at the top of atmosphere

The albedo at the top of the atmosphere ( $\alpha_{toa}$ ) is the next step. This is the albedo unadjusted for atmospheric transmissivity and is computed as follows (Figure 4.14):

$$a_{toa} = \sum (\omega_{\lambda} \times \rho_{\lambda}) \quad (4.11)$$

Where:  $\rho_{\lambda}$  is the reflectivity computed previously and  $\omega_{\lambda}$  is a weighting coefficient for each band computed as follows:

$$\omega_{\lambda} = \frac{ESUN_{\lambda}}{\sum ESUN_{\lambda}} \quad (4.12)$$

Table 4.4 gives  $\omega_{\lambda}$  values for Landsat 5 and Landsat 7 satellites.

Table 4.4. Weighting coefficients  $\omega_{\lambda}$  values for Landsat 5 and Landsat 7.

$\omega_{\lambda}$ values	Band 1	Band 2	Band 3	Band 4	Band 5	Band 6	Band 7
<b>Landsat 5</b>	0.293	0.274	0.233	0.157	0.033	-	0.011
<b>Landsat 7</b>	0.293	0.274	0.231	0.156	0.034	-	0.012

#### 4.2.7.4 The computation of surface albedo

The computation of surface albedo is a correction of albedo at the top of the atmosphere with the factor  $a_{path\_radiance}$  which is a factor related with the atmospheric transmissivity. The relevant model 04 can be seen at Figure 4.15.

$$\alpha = \frac{\alpha_{toa} - \alpha_{path\_radiance}}{r_{sw}^2} \quad (4.13)$$

where:  $\alpha_{path\_radiance}$  is the average portion of the incoming solar radiation across all bands that is back-scattered to the satellite before it reaches the earth's surface, and  $\tau_{sw}$  is the atmospheric transmissivity.

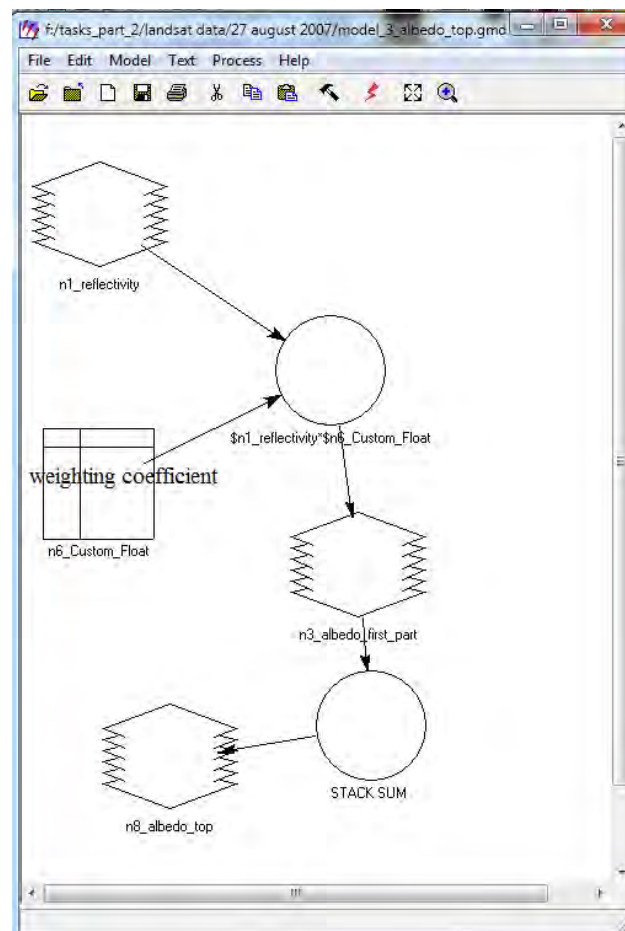


Figure 4.14. Computation of albedo at the top of atmosphere (model 03).

Atmospheric transmissivity can be defined as the fraction of incident radiation that is transmitted by the atmosphere representing the effects of absorption and reflection occurring within the atmosphere. This effect occurs both to incoming and to outgoing radiation and this is the reason why it is squared in Equation (4.13). It has to be mentioned that  $\tau_{sw}$  includes transmissivity of both direct solar beam radiation and scattered radiation to the surface (diffusion effect).  $\tau_{sw}$  can be calculated assuming clear sky and relatively dry conditions using an elevation-based relationship from FAO-56:

$$\tau_{sw} = 0.75 + 2 \times 10^{-5} \times z \quad (4.14)$$

where:  $z$  is the elevation above sea level (m). This value is usually the elevation of the relevant meteorological station.

Values for  $\alpha_{\text{path\_radiance}}$  range between 0.025 and 0.04 and for SEBAL it is recommended to use the value of 0.03 (Bastiaanssen, 2000).

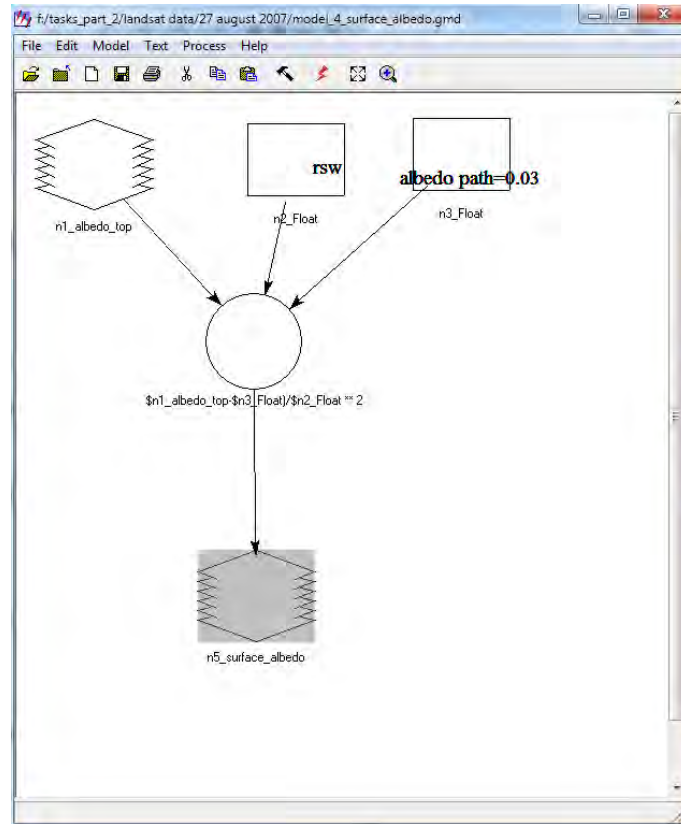


Figure 4.15. Computation of surface albedo at the top of atmosphere (model 04).

#### 4.2.7.5 The computation of incoming shortwave radiation ( $R_{S\downarrow}$ )

Incoming shortwave radiation can be defined as the direct and diffuse solar radiation flux reaching the earth's surface ( $\text{W/m}^2$ ).  $R_{S\downarrow}$  is assumed to be constant during the image time and it is calculated applying the formula:

$$R_{S\downarrow} = G_{sc} \times \cos \theta \times d_r \times r_{sw} \quad (4.15)$$

where:  $G_{sc}$  is the solar constant ( $1367 \text{ W/m}^2$ ),  $\cos \theta$  is the cosine of the solar incidence angle explained earlier,  $d_r$  is the inverse squared relative earth-sun distance, and  $\tau_{sw}$  is the atmospheric transmissivity. This calculation can be done assuming clear sky

conditions without a specialized image processing package, e.g. a spreadsheet or calculator. Values for  $R_{s\downarrow}$  can range from 200 – 1000 W/m<sup>2</sup> depending on the time and location of the image.

#### 4.2.7.6 The computation of outgoing longwave radiation ( $R_{L\uparrow}$ )

Outgoing longwave radiation can be defined as the thermal radiation flux emitted from the earth's surface to the atmosphere (W/m<sup>2</sup>). This is computed using the Stefan-Boltzmann equation (4.16):

$$R_{L\uparrow} = \epsilon_o \times \sigma \times T_s^4 \quad (4.16)$$

where:

$\epsilon_o$  is the “broad-band” surface emissivity (dimensionless),

$\sigma$  is the Stefan-Boltzmann constant ( $5.67 \times 10^{-8}$  W/m<sup>2</sup>/K<sup>4</sup>), and

$T_s$  is the surface temperature (K).

Values for  $R_{L\uparrow}$  can range from 200 – 700 W/m<sup>2</sup> depending on the location and the time of the image.

For the computation of  $R_{L\uparrow}$  the following steps are needed:

- The computation of vegetation indices
- The computation of Surface Emissivity ( $\epsilon$ )
- The computation of Surface Temperature  $T_s$

The above parameters are described at the next paragraphs.

#### 4.2.7.7 The computation of vegetation indices

First of all, the computation of three well-known vegetation indices must be done. Reflectivity values computed previously will be used for the computation of

Normalized Vegetation Index (NDVI), Soil Adjusted Vegetation Index (SAVI) and Leaf Area Index (LAI).

For Landsat if channel 4 is the near infrared band and channel 3 is the red band:

$$NDVI = \frac{\rho_4 - \rho_3}{\rho_4 + \rho_3} \quad (4.17)$$

where  $\rho$  denotes the reflectivity for each band. Values of NDVI range between -1 and +1. NDVI is a measure of greenness of vegetation and values above these surfaces range between 0 and 1, while on water surfaces or clouds are usually negative.

SAVI on the other hand is a variation of NDVI, where the background soil wetness is attempted to remove. It is computed as:

$$SAVI = \frac{(1+L)(\rho_4 - \rho_3)}{(L + \rho_4 + \rho_3)} \quad (4.18)$$

where  $L$  is a constant. This value can be derived analyzing multiple images or multiple soil types. Such an analysis is given later in a separate chapter. It has to be mentioned that if  $L=0$ , then SAVI is the same as NDVI.

LAI is an index which represents the ratio of the total area of all the leaves on a plant to the ground area representing by the plant. Originally, in SEBAL, LAI can be computed using the empirical formula:

$$LAI = - \frac{\ln\left(\frac{0.69 - SAVI}{0.59}\right)}{0.91} \quad (4.19)$$

The maximum value for LAI is 6.0, corresponding to a maximum SAVI value of 0.687. It was found that beyond SAVI = 0.687, the value for SAVI “saturates” with increasing LAI and does not change significantly (Waters *et al*, 2002). It has to be emphasized that



the relationship between SAVI and LAI can vary with location and crop type. A further exploration of LAI behavior is given later. Model 5 illustrates the computation of NDVI, SAVI and LAI (Figure 4.16).

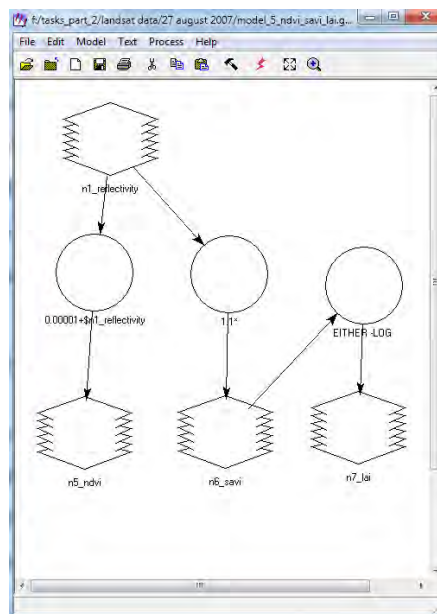


Figure 4.16. Computation of NDVI, SAVI and LAI (model 05).

#### 4.2.7.8 The computation of Surface Emissivity ( $\epsilon$ )

Surface emissivity ( $\epsilon$ ) is defined as the ratio of the thermal energy radiated by the surface to the thermal energy radiated by a blackbody at the same temperature. Two types of surface emissivity are used in SEBAL each one for a different reason. The first one is the emissivity representing surface behavior for thermal emission in the relatively **narrow band** 6 of Landsat (10.4 to 12.5  $\mu\text{m}$ ), expressed as  $\epsilon_{\text{NB}}$ . The second is an emissivity representing surface behavior for thermal emission in the **broad thermal spectrum** (6 to 14  $\mu\text{m}$ ), expressed as  $\epsilon_0$ .  $\epsilon_{\text{NB}}$  is used in calculation of surface temperature ( $T_s$ ) while  $\epsilon_0$  is used later for the calculation of total long wave radiation emission from the surface.

**Narrow band emissivity** is computed using the following empirical equations (4.20) and (4.21), where  $\text{NDVI} > 0$ :

$$\varepsilon_{NB} = 0,97 + 0,0033 * LAI \text{ for } LAI < 3 \quad (4.20)$$

$$\varepsilon_{NB} = 0,98 \quad \text{for } LAI \geq 3 \quad (4.21)$$

A filter has been set for water and snow surfaces (Table 4.5):

Table 4.5. Filters for the computation of narrow band emissivity.

	NDVI	$\alpha$	$\varepsilon_{NB}$
water	< 0	< 0.47	0.99
snow	< 0	$\geq 0.47$	0.99

**Broad band emissivity** is computed using the following empirical equations (4.22) and (4.23), where NDVI > 0:

$$\varepsilon_0 = 0,95 + 0,01 * LAI \quad \text{for } LAI < 3 \quad (4.22)$$

$$\varepsilon_0 = 0,98 \quad \text{for } LAI \geq 3 \quad (4.23)$$

A filter has also been set for water and snow surfaces (Table 4.6):

Table 4.6. Filters for the computation of broad band emissivity.

	NDVI	$\alpha$	$\varepsilon_0$
water	< 0	< 0.47	0.985
snow	< 0	$\geq 0.47$	0.985

Figure 4.17 illustrates the computation of surface emissivity (model 06).

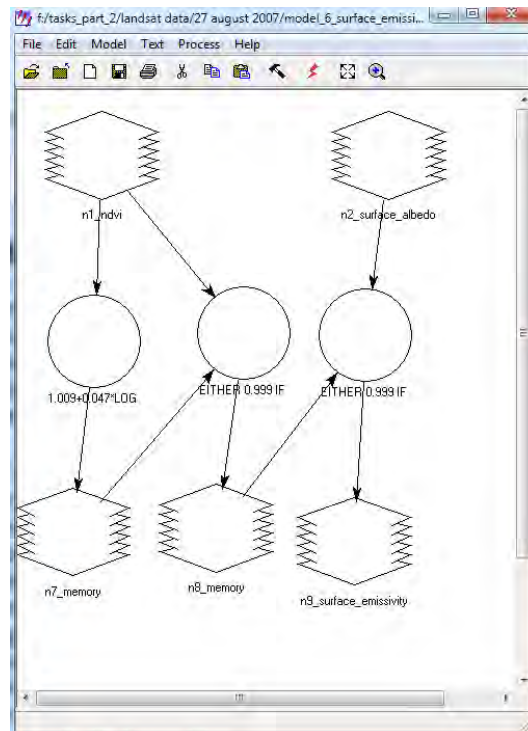


Figure 4.17. Computation of surface emissivity (model 06).

#### 4.2.7.9 The computation of Surface Temperature $T_s$

Surface temperature can be computed using the following modified Plank equation (4.24):

$$T_s = \frac{K_2}{\ln\left(\frac{(\varepsilon_{NB})K_1}{R_c} + 1\right)} \quad (4.24)$$

where:

$R_c$  is the corrected thermal radiance from the surface explained later,

$K_1$  and  $K_2$  are constants for Landsat images (Table 4.7). Units for  $R_c$  are the same as those for  $K_1$ .

The corrected thermal radiance ( $R_c$ ) is the actual radiance emitted from the surface. The space in between surface and satellite sensor is very important because has a strong influence on the actual radiance. A portion of the emitted radiation there is intercepted by the atmosphere. Additionally, some thermal radiation is emitted by the atmosphere in the direction of the satellite. This is

defined as path radiance and is always “confused” from the satellite sensor (before the correction).  $R_c$  can be computed by the formula:

$$R_c = \frac{L_6 - R_p}{\tau_{NB}} - (1 - \varepsilon_{NB})R_{sky} \quad (4.25)$$

where:

$L_6$  is the spectral radiance of band 6 ( $\text{W/m}^2/\text{sr}/\mu\text{m}$ ),

$R_p$  is the path radiance in the 10.4 – 12.5  $\mu\text{m}$  band ( $\text{W/m}^2/\text{sr}/\mu\text{m}$ ),

$R_{sky}$  is the narrow band downward thermal radiation for a clear sky ( $\text{W/m}^2/\text{sr}/\mu\text{m}$ ),  
and

$\varepsilon_{NB}$  is the narrow band transmissivity of air (10.4 – 12.5  $\mu\text{m}$ ).

Units for  $R_c$  are  $\text{W/m}^2/\text{sr}/\mu\text{m}$ .

The  $R_{sky}$  can be calculated applying a formula based on an Idso-Jackson style as revised by Wukelic *et al.* (1989):

$$R_{sky} = (1.807 \times 10^{-10})T_a^4 [1 - 0.26 \exp(-7.77 \times 10^{-4} [273.15 - T_a]^2)] \quad (4.26)$$

A significant problem arises relating with the computation of  $R_p$  and  $\tau_{NB}$  which is not very simple. One way is to use an atmospheric radiation transfer simulation model such as Modtran together with radiosonde profiles taken at the image date. Another solution is to ignore these values by simply setting  $R_p = 0$  and  $\tau_{NB} = 1$  while  $R_{sky}$  term can also be ignored by setting  $R_{sky} = 0$  (Waters *et al.*, 2002). This assumption has negligible effects because  $R_{sky}$  term is small enough to be ignored all of the time (Waters *et al.*, 2002). Finally, after all,  $R_c$  turns again into an uncorrected radiance ( $L_6$ ). The result of no correction to the reflectivity of band 6 will be a general underestimation of surface temperature ( $T_s$ ) by up to about 5 °C

especially for warmer portions of an image. But, fortunately, all these effects of the three described parameters on  $R_c$  are largely self-canceling. SEBAL invent the use of the “dT” function, strictly connected with the “cold” and “hot” pixels described later, which acts as a self-calibration procedure, resulting in no significant errors to the final ET values. This is the most significant innovation of SEBAL procedure. Figure 4.18 illustrates merged model 7-8, computing surface temperature using Erdas Imagine Modeler.

Table 4.7. Constants for the computation of surface temperature.

Temperature related coefficients	K1 (watts/(meter squared*ster* $\mu$ m))	K2 (Kelvin)
Landsat 5 TM Band 6	607.76	1260.56
Landsat 7 ETM+ Band 6	666.09	1282.71

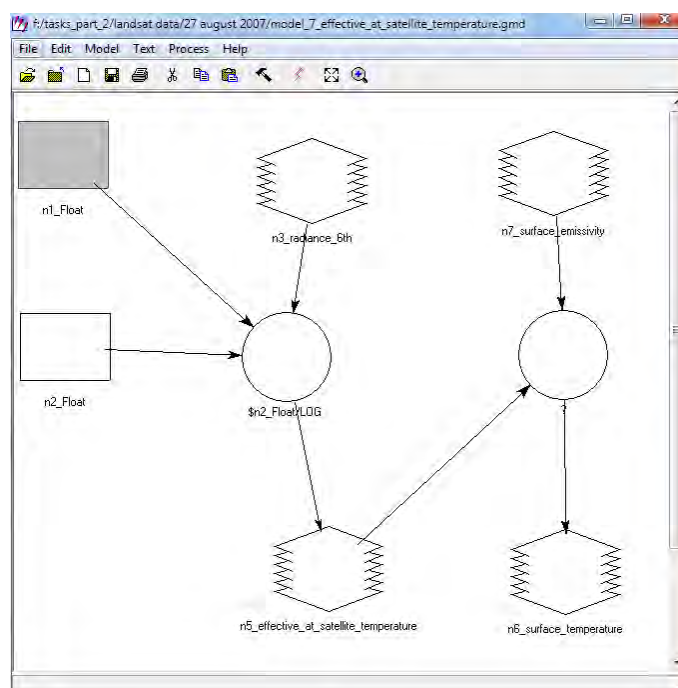


Figure 4.18. Computation of surface temperature (merged model 07-08).

Finally, **computation of outgoing longwave radiation  $R_{L\uparrow}$  using equation (4.16)** is achieved, making model 09 (Figure 4.19).

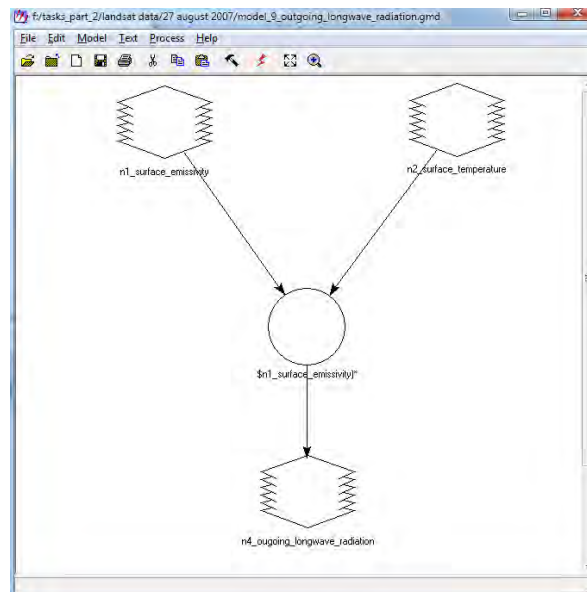


Figure 4.19. Computation of outgoing longwave radiation (model 09).

#### 4.2.8 Choosing the “Hot” and “Cold” Pixels

SEBAL methodology proposes two “anchor” pixels to define boundary conditions for the energy balance (Bastiaanssen, 1998a;b). These are the “hot” and “cold” pixels and must be located in the area of interest. The “cold” pixel is generally selected as a wet, well-irrigated crop surface. Cold pixel is desirable to have full ground cover by vegetation. At the cold pixel, surface temperature and near-surface air temperature are assumed to be equal. On the other hand, “hot” pixel is selected as a dry, bare agricultural field. ET is assumed to be zero at the hot pixel.

The quality of the ET outputs in SEBAL is totally dependent on a careful selection of these cold and hot pixels. And of course, it is obvious that the selection of cold and hot pixels requires scientific knowledge and experience. Annex 2 contains a guide for choosing the “hot” and “cold” pixels. Once selected, the surface temperature and x and y coordinates for these two pixels are recorded for future computations. Cold pixel must be defined before the computation of incoming longwave radiation ( $R_{L\downarrow}$ ).

#### 4.2.9 Incoming Longwave Radiation ( $R_{L\downarrow}$ )

The incoming longwave radiation can be defined as the downward thermal radiation flux from the atmosphere ( $\text{W/m}^2$ ). It is computed using the Stefan-Boltzmann equation (4.27):

$$R_{L\downarrow} = \varepsilon_a \times \sigma \times T_a^4 \quad (4.27)$$

where:

$\varepsilon_a$  is the atmospheric emissivity (dimensionless),

$\sigma$  is the Stefan-Boltzmann constant ( $5.67 \times 10^{-8} \text{ W/m}^2/\text{K}^4$ ),

$T_a$  is the near surface air temperature (K).

The following empirical equation for  $\varepsilon_a$  by Bastiaanssen (1995) is applied (based on alfalfa fields):

$$\varepsilon_a = 0.85 \times (-\ln \tau_{sw})^{0.09} \quad (4.28)$$

where:

$\tau_{sw}$  is the atmospheric transmissivity calculated already from Equation (4.14).

From equation (4.27) incoming longwave radiation can be computed, using  $T_{\text{cold}}$  from the “cold” pixel as SEBAL assumes. This computation can be done using a calculator or spreadsheet. Values for  $R_{L\downarrow}$  can range from 200 – 500  $\text{W/m}^2$ , depending again on the location and time of image.

#### 4.2.10 Running the Surface Radiation Balance Equation model for $R_n$

After the computation of all the above parameters, it is time to compute net surface radiation flux ( $R_n$ ) using Equation (4.5). Model 10 is produced for the computation of

( $R_n$ ) as illustrated on Figure 4.20. The model needs surface albedo ( $\alpha$ ), outgoing longwave radiation ( $R_{L\uparrow}$ ), and surface emissivity ( $\epsilon_o$ ) as input images, as well as incoming shortwave radiation ( $R_{s\downarrow}$ ) and incoming longwave radiation ( $R_{L\downarrow}$ ) as input values (from spreadsheet). Values for  $R_n$  range from  $100 - 700 \text{ W/m}^2$ , depending on the surface. This is the final step of PART1.

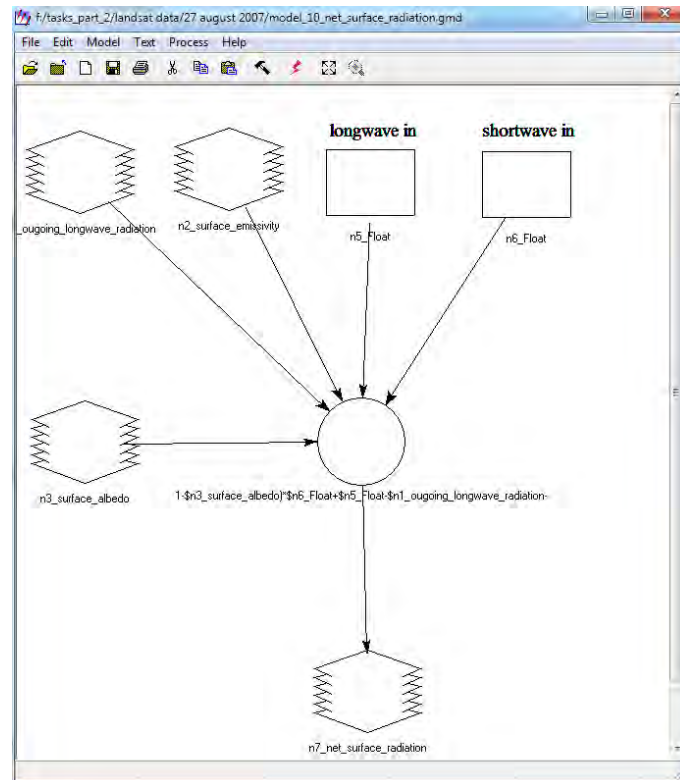


Figure 4.20. Computation of net surface radiation flux (model 10).

#### 4.2.11 PART 2 : Soil Heat Flux (G)

The second part of the SEBAL procedure is the computation of Soil Heat Flux (G). Soil heat flux can be defined as the rate of heat storage into the soil and vegetation due to conduction. At SEBAL methodology it is suggested to first compute the ratio  $G/R_n$ . This can be done using the following empirical equation (4.29) (Bastiaanssen, 2000):

$$\frac{G}{R_n} = \frac{T_s}{\alpha} (0,0038\alpha + 0,0074\alpha^2)(1 - 0,98 \times NDVI^4) \quad (4.29)$$



where:

$T_s$  is the surface temperature ( $^{\circ}\text{C}$ ),

$\alpha$  is the surface albedo, and

NDVI is the Normalized Difference Vegetation Index.

Equation (4.29) is more suitable to use about mid-day. Based on the fact that  $R_n$  is a known image already computed in Part 1, it is easy to calculate  $G$  by simply multiplying  $G$  by the value for  $R_n$ :

$$G = \frac{G}{R_n} R_n \quad (4.30)$$

Some typical values of  $G/R_n$  are shown on Table 4.8.

Table 4.8.  $G/R_n$  values for some selected surfaces.

Surface	$G/R_n$
Clear Water	0.5
Snow	0.5
Desert	0.2 - 0.4
Agriculture	0.05 - 0.15
Bare Soil	0.2 - 0.4
Full cover Alfalfa	0.04
Clipped Grass	0.1
Rock	0.2 - 0.6

Soil type could affect the values of  $G$  as shown on Table 4.8, leading to the thought that a land classification or land use map would be very usable for the identification of various surface types. Especially for surfaces such as water, snow, and wetlands other methods for defining  $G/R_n$  are needed. If negative values of NDVI denote water surfaces, then some filters can be applied (Table 4.9):

Table 4.9. Filters for the computation of  $G/R_n$ .

Type	Condition	Result
water	$NDVI < 0$	$G/R_n = 0.5$
snow	$T_s < 4^{\circ} \text{C}$ and $\alpha > 0.45$	$G/R_n = 0.5$
Turbid/shallow water	absorption of short-wave radiation near the water surface	$G/R_n < 0.5$
Wetlands		$G = -51 + 0.41 R_n$ (Burba et al, 1999).

Examining the study area before the application of SEBAL, it was found that there were no significant water bodies, before the restoration of Lake Karla. So, since, most of the work is done before the restoration and the agricultural crops are far enough from the water bodies, equation (4.30) was adequate. Finally, Model 11 is produced for the computation of (G) as illustrated on Figure 4.21.

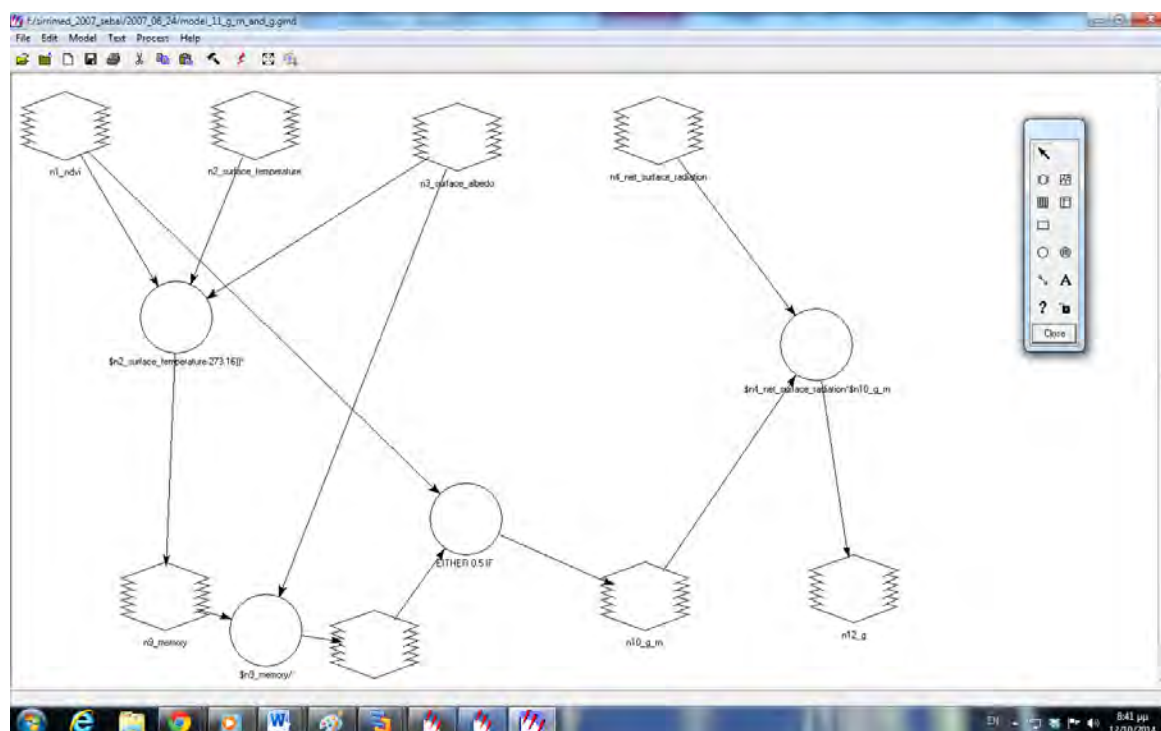


Figure 4.21. Computation of Soil Heat Flux (G) (model 11).

#### 4.2.12 PART 3 : Sensible Heat Flux (H)

The third part of SEBAL application is the computation of Sensible Heat. Sensible heat flux can be defined as the rate of heat loss to the air by convection and conduction, due to a temperature difference. The temperature difference is a very crucial parameter which is exploited later applying the methodology. Sensible heat flux (H) is a function of the temperature gradient, surface roughness, and wind speed, and can be computed using the following equation (4.31):

$$H = \frac{(\rho \times c_p \times dT)}{r_{ah}} \quad (4.31)$$

Where:

$\rho$  is air density ( $\text{kg/m}^3$ ),

$c_p$  is air specific heat (1004 J/kg/K),

$dT$  (K) is the temperature difference ( $T_1 - T_2$ ) between two reference heights ( $z_1$  and  $z_2$ ),

and

$r_{ah}$  is the aerodynamic resistance to heat transport (s/m).

In Equation (4.31) there are two unknowns,  $r_{ah}$  and  $dT$ , and this is why Part 3 (Sensible Heat Flux) is difficult to solve. To overcome this difficulty, SEBAL utilizes the two “anchor” pixels described earlier (cold and hot pixels). These pixels serve as boundary conditions for the estimation of Sensible Heat Flux regarding the temperature differences between two reference heights. The other unknown parameter is the aerodynamic resistance to heat transport ( $r_{ah}$ ) which can be computed for neutral stability as:

$$r_{ah} = \frac{(\ln \frac{z_2}{z_1})}{u^* k} \quad (4.32)$$

where:

$z_1$  and  $z_2$  are heights in meters above the zero plane displacement,

$u^*$  is the friction velocity (m/s), and

$k$  is von Karman's constant (0.41).

**It is important to note that equation (4.32) applies only for neutral atmospheric conditions.**

The friction velocity ( $u^*$ ) quantifies the turbulent velocity fluctuations in the air and can be computed using the logarithmic wind law (4.33) for neutral atmospheric conditions:

$$u^* = \frac{(ku_x)}{\left(\ln \frac{z_x}{z_{om}}\right)} \quad (4.33)$$

where:

$k$  is von Karman's constant,

$u_x$  is the wind speed (m/s) at height  $z_x$ , and

$z_{om}$  is the momentum roughness length (m).

$z_{om}$  is a measure of interaction between the surface and the adjacent layer of air above. Momentum transfer is mainly caused by turbulent drag on roughness elements (Yang and Friedl, 2003).

#### 4.2.12.1 Wind speed ( $u_x$ ).

The wind speed ( $u_x$ ) is proposed to be calculated at a specific height above the weather station. This is the height where it is assumed that no effect from the atmosphere is taken place. This height is 200 meters and is referred in SEBAL as the "blending height". It is denoted as  $u_{200}$  and it can be calculated using the equation (4.34):

$$u_{200} = u^* \frac{\left(\ln \frac{200}{z_{om}}\right)}{k} \quad (4.34)$$

Where  $u^*$  is the friction velocity at the weather station. This calculation is also done on a calculator or spreadsheet.

#### 4.2.12.2 Friction velocity

The friction velocity ( $u^*$ ) **at the weather station** is calculated for neutral atmospheric conditions as explained earlier using Equation (4.33).  $u^*$  requires two variables: The first is wind speed measurement ( $u_x$ ) at a known height ( $z_x$ ) at the time of the satellite image, and the second is the momentum roughness length ( $z_{om}$ ). Wind speed can be taken from the weather data already acquired from the meteorological station of the study, while the momentum roughness length ( $z_{om}$ ) **at the station** is empirically estimated from the average vegetation height around the weather station using the following equation (4.35) (Brutsaert, 1982):

$$z_{om} = 0.12 h \quad (4.35)$$

where:  $h$  is the vegetation height (m). This calculation is done again on a calculator or spreadsheet.

After this “trick”, friction velocity ( $u_*$ ) **for each pixel** can now be computed.  $u_{200}$  is assumed to be constant for all pixels of the image since it is unaffected by surface features. Equation (4.33) now becomes:

$$u^* = \frac{(ku_{200})}{\left(\ln \frac{200}{z_{om}}\right)} \quad (4.36)$$

where  $z_{om}$  is the particular momentum roughness length for each pixel.

#### 4.2.12.3 Momentum Roughness length ( $z_{om}$ )

The momentum roughness length ( $z_{om}$ ) **for each pixel** can be computed by two methods (Paul *et al.*, 2014):

## A) Using a land-use map and LAI:

For agricultural areas,  $z_{om}$  can be calculated as a function of crop height ( $h$ ) which in turn is defined as a function of Leaf Area Index (LAI):

$$z_{om} = 0.018 \times LAI \quad (4.37)$$

Equation (4.37) is a general equation, but there are also, other empirical relationships between  $h$  and LAI for specific crops. For non-agricultural areas, values of  $z_{om}$  surface features can be assigned using the following (

Table 4.10):

Table 4.10  $z_{om}$  values for some selected surfaces.

Surface	$z_{om}$
Water	0.005
Cities	0.2
Forests	0.5
Grasslands	0.02
Desert with Vegetation	0.1
Snow	0.005
Clipped Grass	0.1
Rock	0.2 - 0.6

A prerequisite is the use of a land-use map already created for SEBAL application.

## B) Using NDVI and surface albedo data:

An alternative way when a land-use map is not available, is to use NDVI and surface albedo data. This method was first introduced by Bastiaanssen (2000) and modified by Allen (2001). Equation (4.38) then can be used:

$$z_{om} = \exp\left[\left(a \times \frac{NDVI}{a}\right) + b\right] \quad (4.38)$$

where  $a$  and  $b$  are correlation constants derived from an empirical plot of  $\ln(z_{om})$  vs  $NDVI/\alpha$ . Plots of  $\ln(z_{om})$  against  $NDVI/\alpha$  are created in a spreadsheet examining two or more sample pixels representing specific vegetation types and the correlation coefficients,  $a$  and  $b$ , are derived by regression or visual fitting (Waters *et al.*, 2002). Constants  $a$  and  $b$  must be adjusted to the local vegetation types and conditions each time. The use of albedo ( $\alpha$ ) together with NDVI is that it helps to distinguish between some tall and short vegetation types having similar NDVI.

Finally, model 12 is created for the computation of surface roughness length (Figure 4.22):

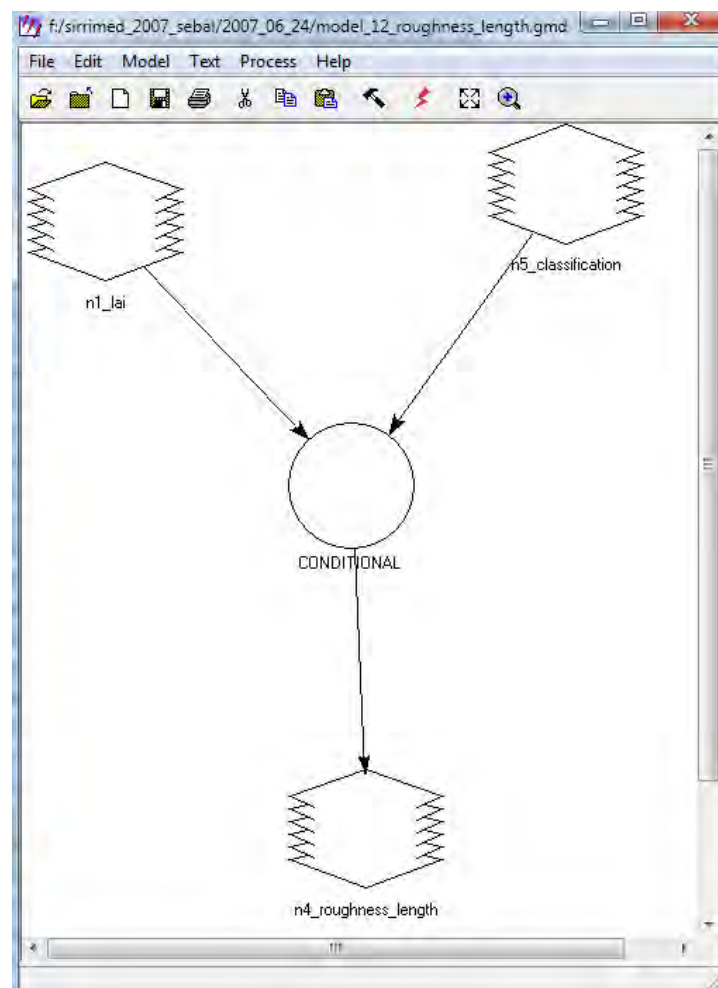


Figure 4.22. Computation of roughness length ( $z_{om}$ ) (model 12).

#### 4.2.12.4 The definition of zero plane displacement height ( $d$ )

The term zero plane displacement ( $d$ ) is the height in meters above the ground at which zero wind speed is achieved as a result of flow obstacles such as trees or buildings (Figure 4.23). It is generally approximated as  $2/3$  of the average height of the obstacles (Raupach and Thom, 1981). For example, if estimating winds over a forest canopy of height  $h = 30$  m, the zero-plane displacement would be  $d = 20$  m.

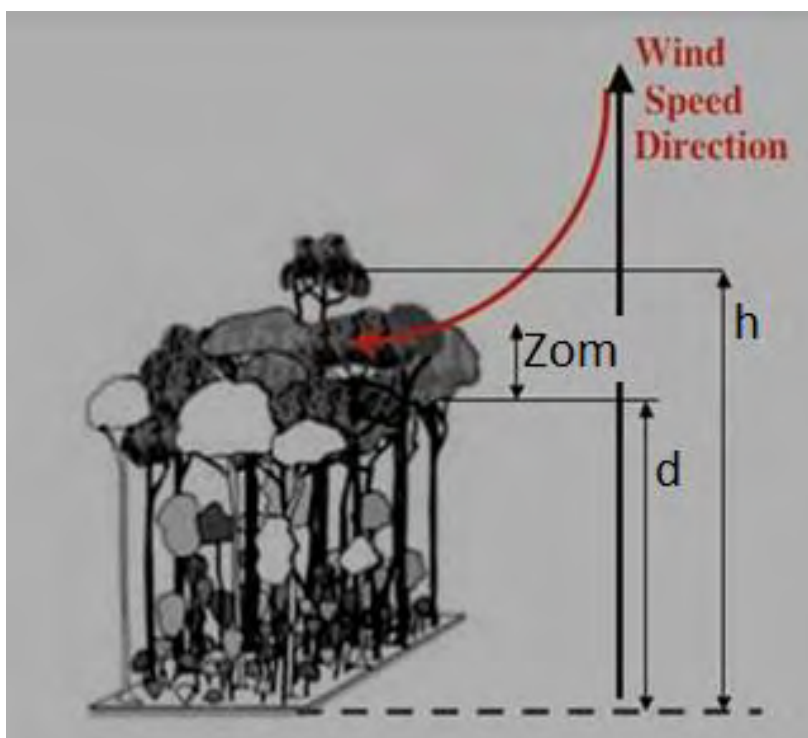


Figure 4.23. Wind speed direction over vegetation canopy, aerodynamic roughness length ( $z_{om}$ ) and zero plane displacement height ( $d$ ) (Saatchi, n.d.).

#### 4.2.12.5 Computation of aerodynamic resistance to heat transport ( $r_{ah}$ )

The aerodynamic resistance to heat transport ( $r_{ah}$ ) can be finally computed by equation (4.32) assuming the two reference heights like this:

$z_1$  is the height just above the zero plane displacement for the surface or crop canopy, and



$z_2$  is some distance above the zero plane displacement, but below the height of the surface boundary layer.

Simplifying the situation, and based on experimental analysis,  $z_1=0.1$  m and  $z_2=2.0$  m can be assigned for SEBAL. Finally, aerodynamic resistance to heat transport ( $r_{ah}$ ) can be computed creating Model 13 (Figure 4.24).

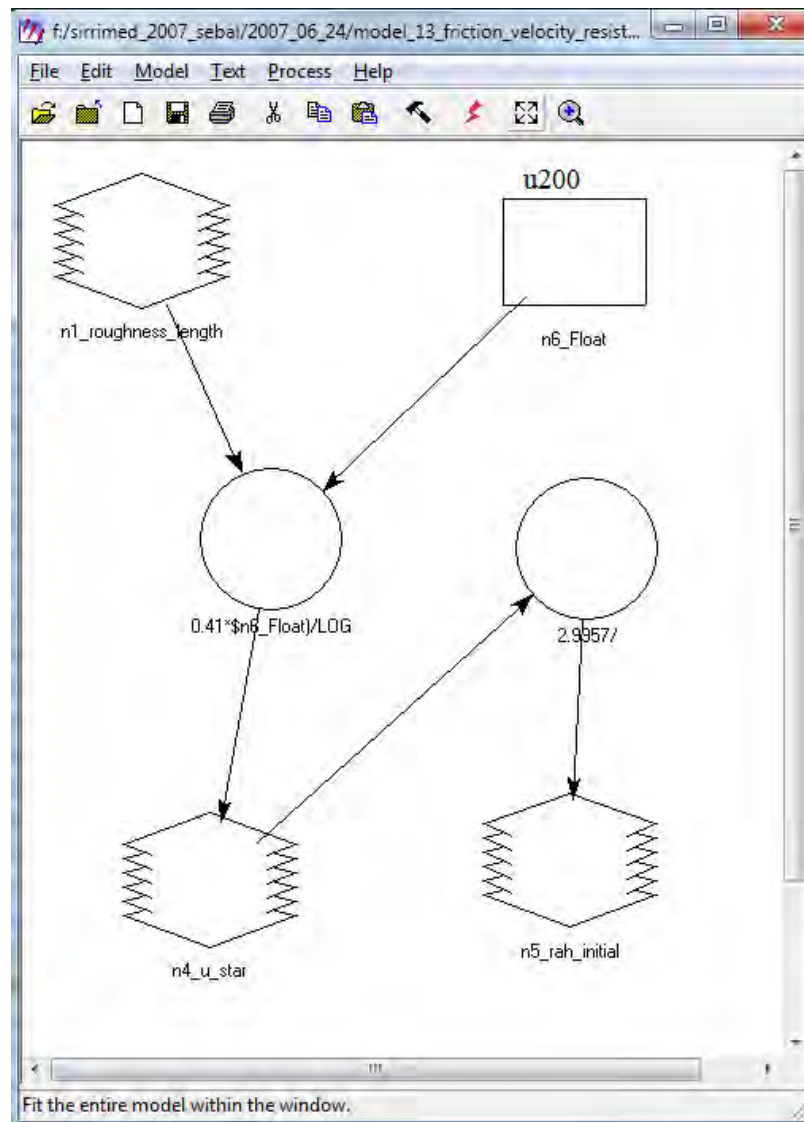


Figure 4.24. Computation of aerodynamic resistance to heat transport ( $r_{ah}$ ) (Model 13).

#### 4.2.12.6 Computation of Sensible Heat Flux for neutral conditions (H)

Sensible heat flux (H) can now be computed from Equation (4.31), if the near surface temperature difference (dT) for each pixel which is the last remaining parameter could

be defined. This temperature difference can be given as  $dT = T_{z1} - T_{z2}$ . At this point it is crucial to mention that not the absolute values but only the difference of the values is needed. This is where SEBAL computes  $dT$  for each pixel by assuming a linear relationship between  $dT$  and  $T_s$ :

$$dT = aT_s + b \quad (4.39)$$

where:

$a$  and  $b$  are correlation coefficients. For the definition of these coefficients SEBAL uses “hot” and “cold” pixels already defined as the “anchor” pixels.  $H$  values can be reliably estimated for these pixels which serve as boundary conditions for the total methodology. Values for  $H$  and  $dT$  for hot and cold pixels are computed in a spreadsheet. SEBAL assumes linearity of the  $dT$  vs  $T_s$  function, and indeed is validated even when applied to a large range of conditions (Bastiaanssen et al., 2000; 2005).

At the “hot” pixel,  $H_{hot} = R_n - G - \lambda ET_{hot}$  but it is assumed that  $ET_{hot}$  is zero (Table 4.11). A “hot” (dry) agricultural field has by definition a dry soil surface and no green vegetation. At the “cold” pixel,  $H_{cold} = R_n - G - \lambda ET_{cold}$  but sensible heat flux is assumed to be zero (Table 8).

$dT_{hot}$  and  $dT_{cold}$  can be computed in the spreadsheet using the equations (4.40) and (4.41) derived from equation (4.31):

$$dT_{Hot} = \frac{H_{Hot} \times r_{a_{h-Hot}}}{\rho_{Hot} \times c_p} \quad (4.40)$$

$$dT_{Cold} = \frac{H_{Cold} \times r_{a_{h-Cold}}}{\rho_{Cold} \times c_p} \quad (4.41)$$

$H_{hot}$  and  $H_{cold}$  can be computed in the spreadsheet using information taken from the previously generated images. Using all those values together with  $T_s$  values taken from the  $T_s$  image for hot and cold pixels, a  $dT$  vs  $T_s$  diagram can now be plotted (Figure 4.25)

and the correlation coefficients,  $a$  and  $b$ , can be estimated graphically. using the linear relationship:  $dT = aT_s + b$ .

Table 4.11. Boundary conditions for hot and cold pixels.

<b><u>"Anchor pixel"</u></b>	<b>H</b>	<b>LE</b>
<b>Hot pixel</b>	$R_n - G$	0
<b>Cold Pixel</b>	0	$R_n - G$
	(SEBAL)	
	$R_n - G - 1.05\lambda ET_r$	
	(METRIC)	

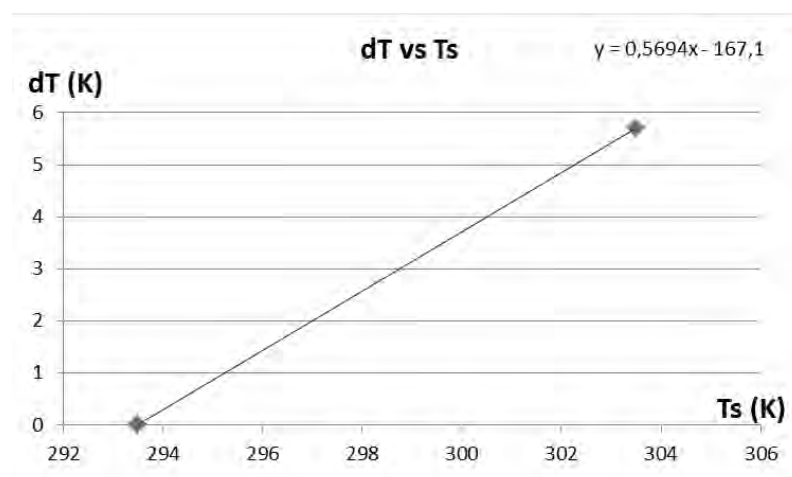


Figure 4.25. Deriving  $a$  and  $b$  constants from  $dT$  vs.  $T_s$  relationship (METRIC).

One of the main differences between SEBAL and METRIC already described at this thesis is that in SEBAL  $H_{cold} = 0$  and therefore,  $\lambda ET_{cold} = R_n - G$  and  $dT_{cold} = 0$ . Thus, it is very common to choose the cold pixel at a water body which is of course a very safe methodology. On the other hand, in METRIC it is very useful to consider the impact of regional advection and wind speed on  $ET$ . And this where  $ET_r$  helps the methodology.

Finally, sensible heat flux ( $H$ ) for each pixel can be computed using Equation (4.31). But it has again to be mentioned that this is only the first estimation of  $H$  assuming neutral

atmospheric conditions (Figure 4.26). (An explanation of neutral conditions and details of different stability conditions that can occur in the atmosphere is given in Annex 3).

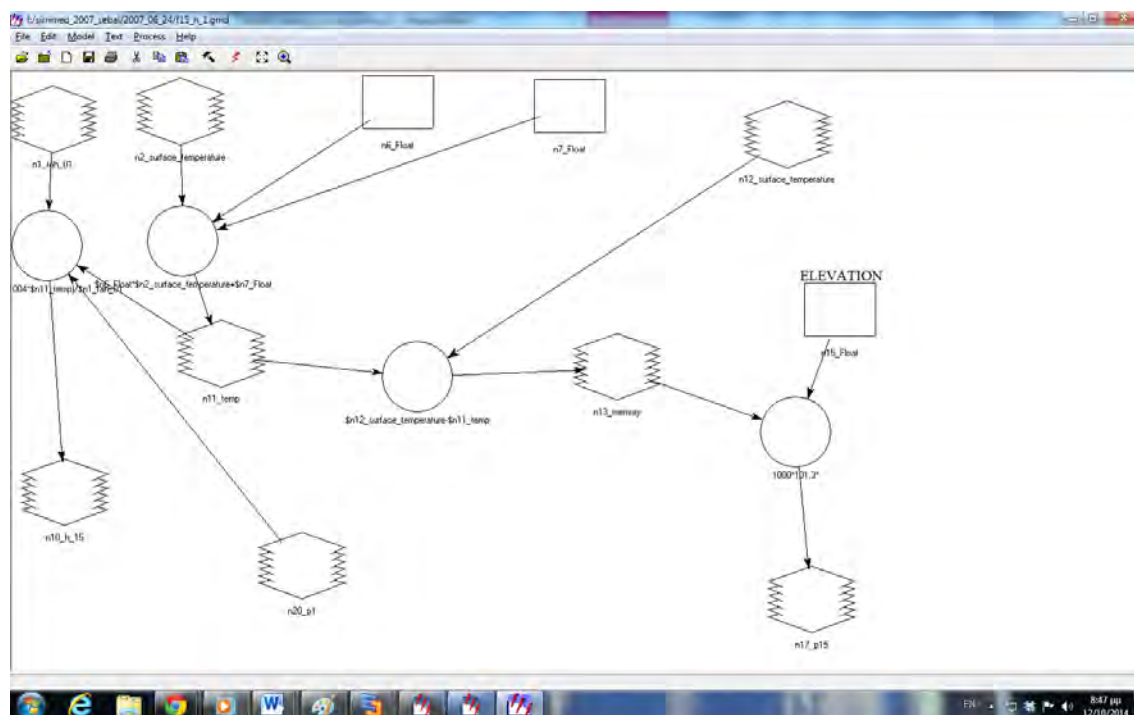


Figure 4.26. Computation of sensible heat flux (H) for Neutral Conditions (Model 14-15).

#### 4.2.13 Iterative process - Monin-Obukhov length

Atmospheric stability conditions have a large influence on the aerodynamic resistance ( $r_{ah}$ ) and must be seriously taken into account for the computation of sensible heat flux (H), especially for dry conditions occurring in Greece. In order to apply the necessary “corrections”, SEBAL repeats the computation of H through a number of iterations. Each iteration corrects for buoyancy effects, until the value for  $r_{ah}$  finally stabilizes. These iterations are based on Monin-Obukhov theory (1954).

The Monin-Obukhov length is a key component of the Monin-Obukhov similarity hypothesis stating that surface layer quantities become universal functions of  $z/L$ , where  $z$  is the height above ground (in meters) and  $L$  is the Monin-Obukhov length. The Monin-Obukhov length scale,  $L$ , is a fundamental scaling quantity in surface layer

theory. In other words it is a measure of the relative importance of mechanical and thermal forcing on atmospheric turbulence, and it is a term typically used to determine the wind speed profile in the stable surface layer. Monin-Obukhov lengths are calculated by many air quality models, given several variables. In SEBAL, the Monin-Obukhov length ( $L$ ) is used to define the stability conditions of the atmosphere in the iterative process. It has to be noted that the term “ $L$ ” has nothing to do with the same “ $L$ ” used in the SAVI computation. Monin-Obukhov length ( $L$ ) is a function of the heat and momentum fluxes and can be computed as follows:

$$L = -\rho C_p \frac{u^{*3} T_s}{kgH} \quad (4.42)$$

where:

$\rho$  is the density of air ( $\text{kg/m}^3$ ),

$c_p$  is the air specific heat ( $1004 \text{ J/kg/K}$ ),

$u^*$  is the friction velocity ( $\text{m/s}$ ),

$T_s$  is the surface temperature ( $\text{K}$ ),

$g$  is the gravitational constant ( $9.81 \text{ m/s}^2$ ), and

$H$  is the sensible heat flux ( $\text{W/m}^2$ ).

The Monin-Obukhov length is an objective measure of stability in the atmosphere. A positive value indicates stable conditions, while a negative value indicates unstable (convective) conditions. The larger the magnitude of the number, the weaker the relevant stability (ie. -5 is very unstable while -100 would only be slightly unstable).

The equations for the computation of  $L$  are different, depending on the atmospheric conditions. The values of the stability corrections for momentum and heat transport ( $\psi_m$  and  $\psi_h$ ) are computed using the formulations by Paulson (1970) and Webb (1970):

For unstable conditions,  $L < 0$  :

$$\begin{aligned} \psi_{m(200m)} &= 2 \ln \left( \frac{1 + x_{(200m)}}{2} \right) \\ &+ \ln \left( \frac{1 + x_{(200m)}^2}{2} \right) - 2 \text{ARCTAN}(x_{(200m)}) + 0.5\pi \end{aligned} \quad (4.43)$$

$$\psi_{h(2m)} = 2 \ln \left( \frac{1 + x_{(2m)}^2}{2} \right) \quad (4.44)$$

$$\psi_{h(0.1m)} = 2 \ln \left( \frac{1 + x_{(0.1m)}^2}{2} \right) \quad (4.45)$$

where:

$$x_{(200m)} = \left( 1 - 16 \frac{200}{L} \right)^{0.25} \quad (4.46)$$

$$x_{(2m)} = \left( 1 - 16 \frac{2}{L} \right)^{0.25} \quad (4.47)$$

$$x_{(0.1m)} = \left( 1 - 16 \frac{0.1}{L} \right)^{0.25} \quad (4.48)$$

For stable conditions,  $L > 0$  :

$$\psi_{m(200m)} = -5 \frac{2}{L} \quad (4.49)$$

$$\psi_{h(2m)} = -5 \frac{2}{L} \quad (4.50)$$

$$\psi_{h(0.1m)} = -5 \frac{0.1}{L} \quad (4.51)$$

For neutral conditions:

$\Psi_m$  and  $\Psi_h$  are zero.

After the definitions of the above parameters a corrected value of friction velocity ( $u^*$ ) can be computed for each iteration:

$$u^* = \frac{ku_{200}}{\ln\left(\frac{z_{200}}{z_{0m}}\right) - \psi_{m(200m)}} \quad (4.52)$$

where:

$u_{200}$  is the wind speed at 200 meters (m/s),

$k$  is von Karman's constant (0.41),

$z_{0m}$  is the roughness length for each pixel (m), and

$\psi_{m(200m)}$  is the stability correction for momentum transport at 200 meters.

After  $u^*$ , aerodynamic resistance to heat transport ( $r_{ah}$ ) can be also computed:

$$r_{ah} = \frac{\ln\left(\frac{z_2}{z_1}\right) - \psi_{h(z_2)} + \psi_{h(z_1)}}{u_* \times k} \quad (4.53)$$

where:

$z_2 = 2.0$  meters,

$z_1 = 0.1$  meters, and

$\psi_{h(z_2)}$  and  $\psi_{h(z_1)}$  are the stability corrections for heat transport at 2 meters and 1 meters respectively.

Equations (4.52) and (4.53) can now give the new values of  $u^*$  and  $r_{ah}$  after the first iteration (Figure 4.27, Figure 4.28). The total procedure has to be repeated again for the next iteration. From the spreadsheet, new  $dT$  values for the “cold” and “hot” pixel are utilized and new values of correlation coefficients  $a$  and  $b$  are computed, so,  $dT$  then is computed again using the new  $a$  and  $b$ . A new corrected  $H$  then is computed again, and then a new stability correction is repeated.

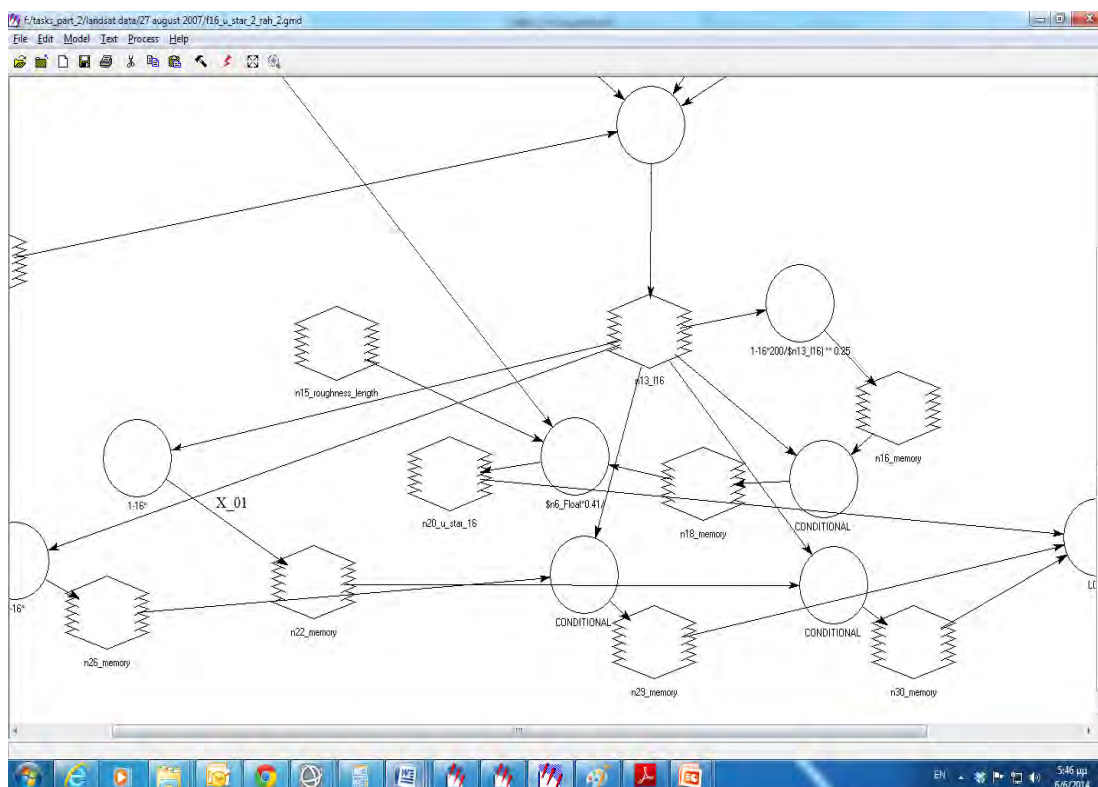


Figure 4.27. Computation of corrected  $u^*$  and  $r_{ah}$  for the first iteration (Model 16).



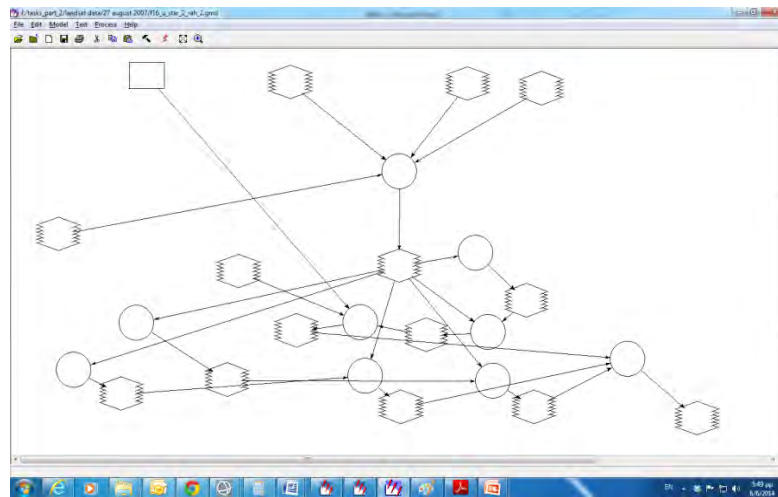


Figure 4.28. Overview of model 16.

The end of this process reaches when the successive values for  $dT_{hot}$  and  $r_{ah}$  at the “hot” pixel are finally stabilized. For example, if another six iterations are needed, the procedure is repeated again and again, and models 17,18,19,20,21,22,23,24,25,26,27, and 28 are created using the same philosophy as models 15 and 16. Finally, the computation of the final corrected value for the sensible heat flux ( $H$ ) at each pixel, will be used in the computation of the instantaneous ET at each pixel at the last stage of SEBAL methodology.

The total iterative process is illustrated on Figure 4.29.

#### 4.2.14 Computation of Latent Heat Flux ( $\lambda ET$ ), Instantaneous ET ( $ET_{inst}$ ), and Reference ET Fraction ( $ET_r$ )

Latent heat flux can be defined as the rate of latent heat loss from the surface due to evapotranspiration. It can be computed for each pixel using Equation (4.54):

$$\lambda ET = R_n - G - H \quad (4.54)$$

where:

$\lambda ET$  is an instantaneous value for the time of the satellite overpass ( $W/m^2$ ).

When mm of precipitation has to be the equivalent unit, then  $ET_{inst}$  can be computed as follows:

$$ET_{inst} = 3600 \frac{\lambda ET}{\lambda} \quad (4.55)$$

Where:

$ET_{inst}$  is the instantaneous ET (mm/hr),

3600 is the time conversion from seconds to hours, and

$\lambda$  is the latent heat of vaporization or the heat absorbed when a kilogram of water evaporates (J/kg).

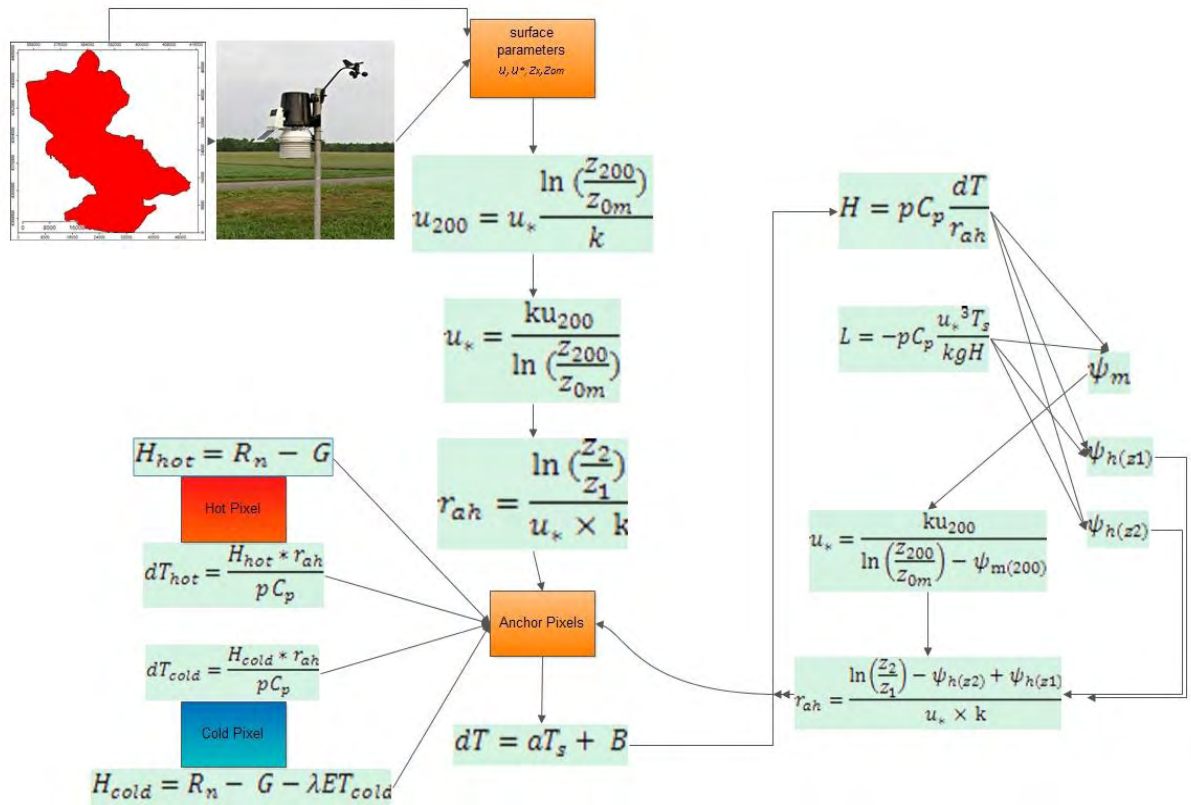


Figure 4.29. Monin-Obukhov based iteration flow chart.

Furthermore, the Reference ET Fraction ( $ET_rF$ ) can be defined as the ratio of the computed instantaneous ET ( $ET_{inst}$ ) for each pixel to the reference ET ( $ET_r$ ) computed from weather data:

$$ET_rF = \frac{ET_{inst}}{ET_r} \quad (4.56)$$

where:

$ET_{inst}$  can be derived from Equation (4.55) (mm/hr), and

$ET_r$  is the reference ET at the time of the image.

$ET_rF$  is similar to the well-known crop coefficient,  $K_c$  as it is explained in a separate chapter.  $ET_rF$  then is used to extrapolate ET from the image time to 24-hour or longer periods (Waters *et al.*, 2002).

$ET_r$  generally represents an upper limit value for ET. So, since at a totally dry pixel,  $ET = 0$  and  $ET_rF = 0$ , it could be expected that  $ET_rF$  values could range from 0 to 1. But it is very usual that a pixel in a well-established field of alfalfa or maize can occasionally have an ET slightly greater than  $ET_r$ . Therefore sometimes  $ET_rF > 1$ , perhaps up to 1.1 or 1.2. On the other hand, negative values for  $ET_rF$  may occur in SEBAL due to systematic errors caused by various assumptions made earlier in the energy balance process. Keeping in mind these assumptions,  $ET_{inst}$  and  $ET_rF$  can be computed finally in model 25 (Figure 4.30). The number 25 is indicative and it is applicable for four iterations. If the number of iterations are 5, 6, or 7, then the final remote sensing based model could have named as the 27<sup>th</sup>, 29<sup>th</sup> or 31<sup>th</sup>.

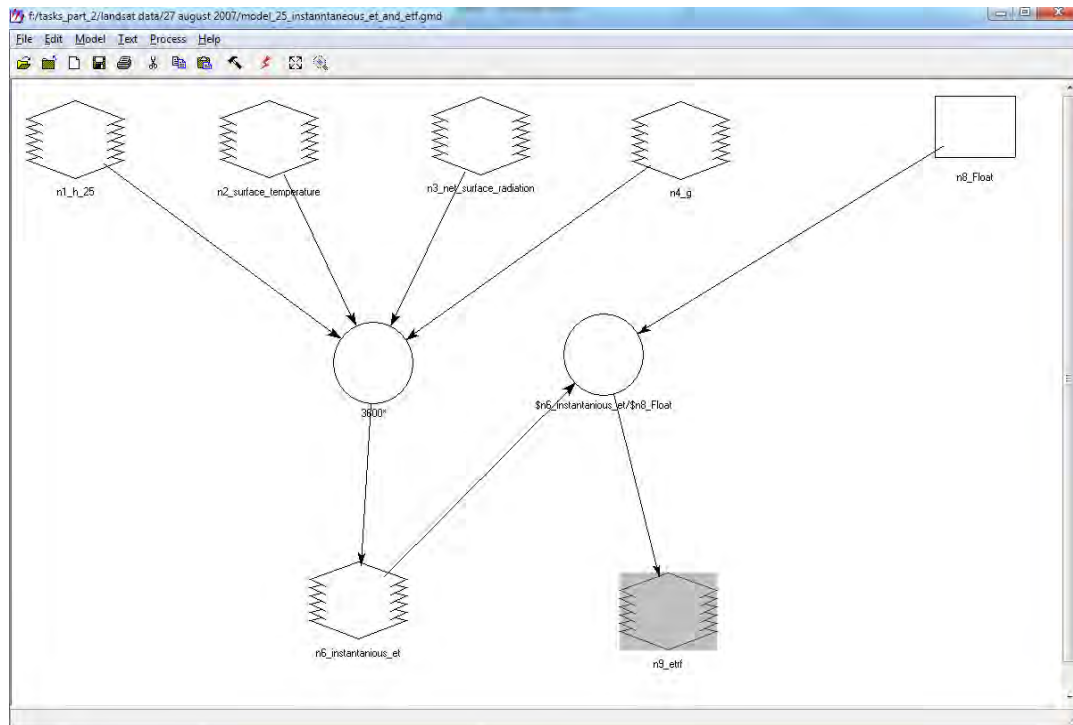


Figure 4.30. Computation of Instantaneous ET ( $ET_{inst}$ ), and Reference ET Fraction ( $ET_rF$ ) (Model 25).

#### 4.2.15 ET computations for longer periods

All the previous computations till now are based to the idea of instantaneous estimations of ET. But it is obvious that daily or longer period estimations could be more useful. SEBAL methodology can estimate  $ET_{24}$  making the assumption that the instantaneous  $ET_rF$  computed in model 25 is the same as the 24-hour average  $ET_rF$  value. Keeping this assumption, then:

$$ET_{24} = \frac{ET_rF}{ET_{r-24}} \quad (4.57)$$

where:

$ET_{r-24}$  is the cumulative 24-hour  $ET_r$  for the day of the image.

$ET_{r-24}$  can be calculated simply by adding the hourly  $ET_r$  values for all-day period. It is implied that the computations can be taken place over the same day where the satellite image is available. Similarly, a seasonal evapotranspiration map covering an entire growing season is often desirable. This can be derived extrapolating the  $ET_{24}$  values with a similar manner.

It is assumed that the ET values for the entire study area change accordingly to the change in the  $ET_r$ . This is an important assumption even if  $ET_r$  is computed for a specific location (e.g. the place where the meteorological station is situated) and therefore does not represent the actual condition for every pixel. The second assumption is that computed  $ET_r F$  is constant for the entire period represented by the image. Each satellite image of course may be representative of a limited time period which must be specified. For example, if the length of the season for which ET has to be computed is from May 1 to September 30 and the first two images of the above period are for example on May 14 and May 30, then the period represented by the first image is May 1 to May 22. This is the beginning of the period until the period between the first two images.

Another task is the computation of the total cumulative value of  $ET_r$  for the represented period which is the sum of the daily  $ET_r$  values of this period. Finally:

$$ET_{period} = ET_r F_{period} \sum_{1}^n ET_{r-24} \quad (51) \quad (4.58)$$

where:

$n$  is the number of days in the period,

$ET_{r-24}$  is the daily  $ET_r$ , and

$ET_r F_{period}$  is the representative  $ET_r F$  for the period.

Units for ET are in mm.

The final step is the computation of the seasonal ET simply by summing all the  $ET_{period}$  values for the length of the season.

#### 4.2.16 Limitations.

There is an opportunity that in some fields, an irrigation schedule could apply and in that case a sudden increase in ET for this field could be recorded. It is obvious that this situation will not be representative for the computation of seasonal ET. This problem could be overtaken if more satellite images used for the computation of seasonal ET. In that case each image could represent a shorter time period. Similarly, no representative ET or  $ET_r F$  values could be a result in the case of a series of cloud cover days. This could be overtaken by applying interpolation between the ET or  $ET_r F$  values. Another difficult case could be that of a weather station which is not representative of the entire area. This could be happen if there are a lot of different surfaces with different characteristics (e.g. coastal or mountain areas with different climatic behavior). A solution then could be the splitting into new sub-images, where SEBAL could be run separately, giving to each image its own ET or  $ET_r F$  values.

#### 4.2.17 Differences between SEBAL and METRIC.

METRIC uses principles and techniques used by the pioneering model SEBAL, and it is not peculiar to consider the METRIC/SEBAL methodology as one methodology. In both SEBAL and METRIC, ET is estimated as the residual of an energy balance. Net radiation, soil heat flux and sensible heat flux are generally computed by the same way.

The definition of “hot” and “cold” pixels is also the same at both methodologies. But there are some differences. In METRIC a fully-vegetated field resembling alfalfa is assigned as alfalfa reference evapotranspiration ( $ET_r$ ) which can be computed from locally observed hourly weather data (Tasumi *et al.*, 2005). In METRIC  $ET_{cold}$  is set by default equal to  $1.05 \cdot ET_r$ , where  $ET_r$  is the hourly crop reference (e.g. for alfalfa) ET calculated using the standardized ASCE Penman-Monteith equation applied to local meteorological observations. Additionally, the cold pixel needs to have biophysical characteristics (h or LAI) similar to the reference crop. In SEBAL on the other hand the cold pixel is usually selected on water surfaces assuming that  $H = 0$  or  $LE = R_n - G$ .

At the hot pixel sensible heat can be modified by any residual evaporation occurring from recent precipitation events (Tasumi *et al.*, 2005). This amount of sensible heat can be estimated solving the simple daily surface layer water balance model by FAO-56 (Allen *et al.*, 1998). This model may provide a daily water balance calculation providing a general estimation of any residual evaporation from bare soil. This water balance is essential on the day of a satellite image as well as the much previous days. If there was some precipitation 1-4 days before the image date, then  $ET_{hot}$  should be estimated using a water balance model using ground-based weather measurements and tracking the soil moisture of the “hot” pixel. Generally, the ET from a bare soil can be roughly estimated to be equal to  $0.8 ET_r$ ,  $0.5 ET_r$ ,  $0.3 ET_r$ ,  $0.2 ET_r$ , and  $0.1 ET_r$ , 1, 2, 3, 4, and 5 days following a substantial rain event with a total amount of rain 15 mm or more (Waters *et al.*, 2002). This kind of water balance can be especially useful when in some cases after a rainfall event  $H > 0$  for all pixel candidates (Tasumi *et al.*, 2005). In the study area during this research, there was no rainfall before the passage of the satellite. In some cases, there were some events, but the images followed were not used due to heavy cloud cover. This kind of calibration in the METRIC model improves the quality of the product especially where a good network of meteorological stations exists. In the SEBAL model, there is no similar calibration.

In SEBAL, after the estimation of latent heat flux (equation (4.54)) the evaporative fraction (EF) can be calculated as:

$$EF = (\lambda E) / (R_n - G) \quad (4.59)$$

In METRIC, on the other hand,  $ET_r$  fraction ( $ET_r F$ ) is used instead, which represents the ratio of ET to the alfalfa reference ET ( $ET_r$ ).  $ET_r$  fraction is essentially the same as the crop coefficient  $K_c$  (ASCE-EWRI, 2005):

$$ET_r F = \frac{ET}{ET_r} = K_c \quad (4.60)$$

It has to be mentioned again that  $ET_r$  is calculated from weather data, and it is recommended to use ASCE standardized Penman-Monteith alfalfa reference method (ASCE-EWRI, 2005; Tasumi *et al.*, 2005) for this estimation.

EF at SEBAL it is assumed to remain constant throughout the day, and it is very usual to use extrapolation for passing from short periods to daily periods (Shuttleworth *et al.*, 1989; Brutsaert and Sugita, 1992; Crago, 1996). Solving equation (4.55) for a daily period a number “86400” must be multiplied for the estimation of  $ET_{24}$ :

$$ET_{r24} = \frac{86400 \times EF \times (R_{n24} - G_{24})}{\lambda} \quad (4.61)$$

Where  $R_{n24}$  is the average net radiation for the day,  $\lambda$  is the latent heat of vaporization,  $G_{24}$  is the soil heat flux of the day, and 86400 is the product of the total seconds of the day ( $60 \times 60 \times 24$ ). For vegetation and soil surfaces  $G_{24}$  is assumed to be zero during the whole day. In METRIC, the ratio of the actual ET to  $ET_r$  at short time step is expressed with  $ET_rF$  and the  $ET_{24}$  is estimated by multiplying  $ET_rF$  by  $ET_r$  for a 24h period, which is now obtained by summing up hourly values of  $ET_r$  (Mkhwanazi and Cavez, 2013). This is a very significant difference from SEBAL. Additionally, Romero (2004) showed that the instantaneous to 24h similarity is closer for  $ET_rF$  than for EF under agricultural conditions affected by advection (Tasumi *et al.*, 2005). This is one of the main reasons why METRIC is preferred for this dissertation.

A linear interpolation can also be applied for monthly and seasonal cases as well, assuming linearity in the period between two consecutive images (Tasumi *et al.*, 2005):

$$\sum_{i=a}^b ET = \sum_{i=a}^b (ET_r F_{(i)} ET_{r(i)}) \quad (4.62)$$

At equation (4.62) which is very similar to (4.58), a and b are the start and end dates of integration respectively,  $ET_rF_{(i)}$  is  $ET_rF$  for day  $i$  which is predicted by linear interpolation, and  $ET_{r(i)}$  is alfalfa-reference ET for day  $i$ , calculated from meteorological data. Possible errors generated by the interpolation tend to be random over time and errors are initially minimized for long-term seasonal ET (Tasumi *et al.*, 2005).

In conclusion, METRIC uses the SEBAL calculation methodology, especially, for estimating the near-surface temperature gradient,  $dT$ , as an indexed function of radiometric surface temperature, thereby eliminating the need for absolutely accurate



aerodynamic surface temperature and the need for air temperature measurements for estimating sensible heat flux at the surface (Allen *et al.*, 2011). METRIC utilizes internal calibration of the satellite-based energy balance at two extreme conditions, using alfalfa-based reference ET. The use of reference ET for calibration and extrapolating from instantaneous to 24-h ET helps to account for regional advection effects on ET and improves congruency with the traditional reference ET- $K_c$  approach (Allen *et al.*, 2011). After all, METRIC methodology is chosen as the processing methodology for the present dissertation.

#### 4.2.18 METRIC flow chart

Finally, a flow chart showing the basic steps needed for the application of METRIC methodology is illustrated at Figure 4.31.

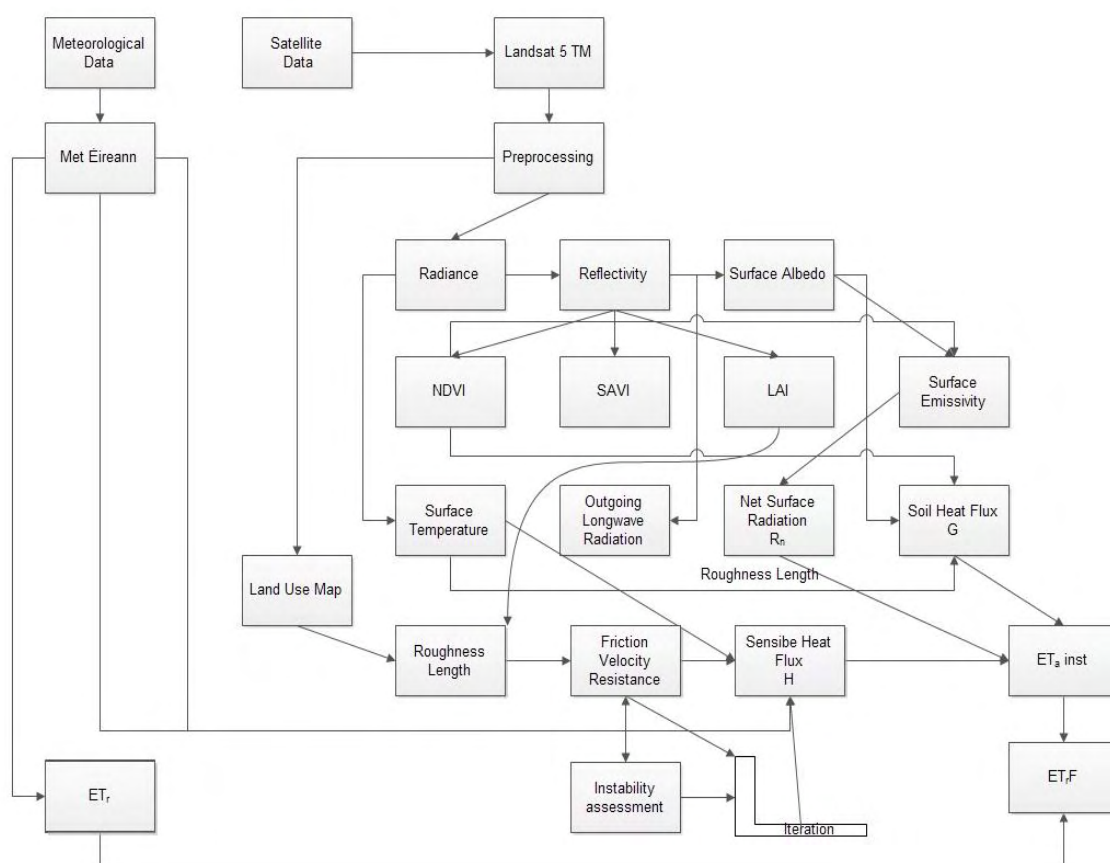


Figure 4.31. Flow chart of the METRIC model

#### 4.2.19 METRIC using MODIS imagery.

MODIS imagery is also a very significant tool when estimating surface albedo, energy fluxes and evapotranspiration (Bisht *et al.*, 2005; Ahmad *et al.*, 2006; Cleugh *et al.*, 2007; Venturini *et al.*, 2008). When applying MODIS imagery the procedures are slightly different from the case when Landsat images are used. Although, the main METRIC methodology remains unchanged, there are some differences due to the fact that MODIS bands have different spectral and spatial resolution comparing to Landsat. One main difference is that MODIS thermal data usually has a coarser spatial resolution than sensors with non-thermal response for example in the visible, near infrared or shortwave infrared regions (Spiliotopoulos *et al.*, 2013).

MODIS is operating onboard Terra and Aqua satellites, where a  $\pm 55^\circ$  scanning pattern at 705 km altitude achieves a 2,330 km swath providing global coverage every one to two days. MODIS product MOD09 gives estimates of spectral reflectance from the surface in seven short-wave spectral bands. MOD11A1 corresponds to land surface temperature ( $T_s$ ) on cloud-free days. Pixels are selected using a cloud mask (MOD35L2) which excludes pixels affected by aerosols and clouds. The accuracy of the  $T_s$  data is better than 1K, and is 0.5K in most cases (Wan, 2010; Ruhoff *et al.*, 2012). However, in pixels contaminated by cloud cover and heavy aerosols, the accuracy may vary from 4 to 11 °C, since the cloud-cover mask does not discard all affected pixels, particularly those near cloud edges (Wan and Li, 2008; Ruhoff *et al.*, 2012). MOD13A1 provide information on vegetation spatial and temporal variations, NDVI, as well as conditions of photosynthetic activity and biophysical and phenological changes (Huete *et al.*, 2002; Huete *et al.*, 2011).

For the application of METRIC, Aqua and Terra MODIS remote sensing datasets are used. For the present application Hierarchical Data Format (\*.hdf) files are downloaded from GLOVIS tool. From the available data sets h19v05 sets (19<sup>th</sup> horizontal and 5<sup>th</sup> vertical row) are selected. For the estimation of surface-energy balance: (a) daily surface reflectance MOD09GA and MYD09GA (Vermote *et al.*, 2010), (b) daily land surface temperature MOD11 A1 and MYD11 A1 (Wan *et al.*, 2004; Wan, 2010) and (c)

16-day vegetation indices MOD13 and MYD13 (Solano *et al.*, 2010) are utilized. An example of initial MODIS image used is illustrated at Figure 4.32.

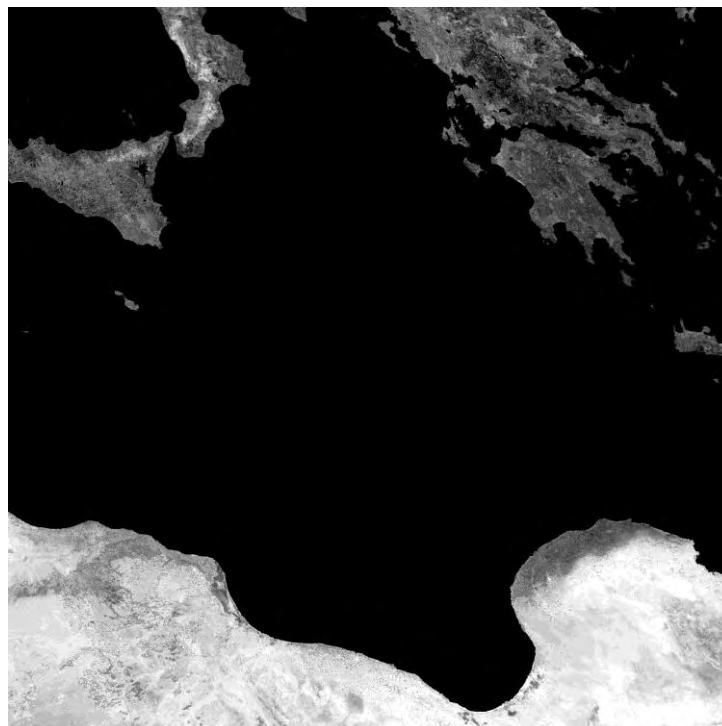


Figure 4.32. MYD13 NIR Reflectance 26-7-2007.

MODIS \*.hdf files should be opened using MODIS reprojection tool (MRT). MRT is a Java application requiring a detailed study of MRT manual available at Land Processes Distributed Active Archive Center (LP DAAC) of NASA US Geological Survey (MRT, 2011). MODIS imagery is then geolocated to the Greek georeference system EGSA 87 and finally can be used for the application of METRIC. The basic steps are the same as the Landsat procedure, but there are some changes:

- (a) Computation of net radiation. Net radiation can be computed from Equation (4.5).

Albedo ( $\alpha$ ) can be simply calculated by integrating band reflectance within the short-wave spectrum using a weighting function (Starks *et al.* 1991):

$$\alpha = \sum_{i=1}^n \rho_i w_i \quad (4.63)$$

where  $n$  is the number of satellite bands ( $n=7$ ),  $\rho_i$  is the reflectance of the seven MODIS bands of MOD09GA product, and  $w_i$  is a weighting coefficient with values shown at Table 4.12.

Table 4.12 MODIS Weighting Coefficients for each band for the computation of albedo (from Tasumi *et al.*, 2008).

Band	Weighting Coefficient
1	0.215
2	0.215
3	0.242
4	0.129
5	0.101
6	0.062
7	0.036

Incoming and outgoing long wave radiation is a function of surface radiation which now is computed directly from MOD11A1 product. Land surface emissivity ( $\epsilon_0$ ) at the same equation can be computed by taking the average of the emissivity values of Bands 31 and 32 containing within the MOD11A1 product (Zhang *et al.*, 2011; Ruhoff *et al.*, 2012; Du *et al.*, 2013).

(b) Computation of Soil Heat Flux (G). Soil Heat flux can be computed from Equation (4.30) where NDVI is retrieved from the MOD13 product.

(c) Computation of Sensible Heat Flux (H). Sensible Heat flux can be computed from Equation (4.31) where temperature is derived from the MOD11A1 product. All the other parameters have no difference in their computation when compared with Landsat procedures.

### 4.3 Field spectroscopy

One of the tasks of this thesis is the acquisition of spectral reflectance of the main crops in the study region. This is done through field measurements using specialized equipment (i.e. spectroradiometer). The acquisition of information about the spectral signatures of different features is what is called field spectroscopy. The reason for the in-situ acquisition of spectral reflectance is that there is a need for a better accuracy of crops behavior. In other words, there is a need for assessing the spectral discrimination of the plants in their various phenological stages. This is the reason why field spectroradiometry has been widely used in similar studies (Psomas *et al.*, 2005; Artigas and Yang, 2006; Manevski *et al.*, 2011). After acquiring accurate spectral reflectances values for the main crops of the study, it is possible, then, to find relationships between them and crop coefficient values. This procedure will be described later.

A lot of discussion has been made about field spectroscopy generally as a scientific technology (Milton, 1987; Milton *et al.*, 1995; D'Urso and Calera, 2006). Field spectroscopy generally has the role to measure the spectral characteristics of ground surfaces in the natural environment and used to characterize the spectral behavior of ground targets monitoring their suitability as targets over time. It also helps with the inter-calibration of data from different platforms or the calibration of data from the same sensor at different times (Agapiou *et al.*, 2009). Quantitatively speaking, field spectroscopy measures radiance, irradiance and reflectance in the field. For this reason, portable, battery powered spectro-radiometers are typically used to make these measurements. For this study GER1500 instrument is used (Spectra Vista Corporation).

GER1500 field spectro-radiometer (Figure 4.33) is a light-weight, high performance instrument covering the ultraviolet, visible and near-infrared wavelengths from 350 nm to 1050 nm. GER 1500 uses a diffraction grating with a silicon diode array which has 512 discrete detectors and provides the capability to read 512 spectral bands. The instrument makes a very rapid scanning, acquiring spectra in milliseconds. GER1500 uses the idea of «lambertian» surface as a panel. Spectralon reflectance material

(Figure 4.34) gives the highest diffuse reflectance of any known material or coating over the UV-VIS-NIR region of the spectrum and exhibits a highly Lambertian behavior (Figure 4.35). The reflectance is generally  $>99\%$  over a range from 400 to 1500 nm and  $>95\%$  from 250 to 2500 nm (Labsphere). The reflectance of the target is obtained then by applying the ratio of reflected radiance from the target to the reflectance radiance from the panel. Special account must be taken to the control panel correction. GER1500 (Figure 4.33) and spectralon (Figure 4.34) for this study were kindly provided by the Technological University of Cyprus.



Figure 4.33. GER1500 field spectro-radiometer.



Figure 4.34. Spectralon.

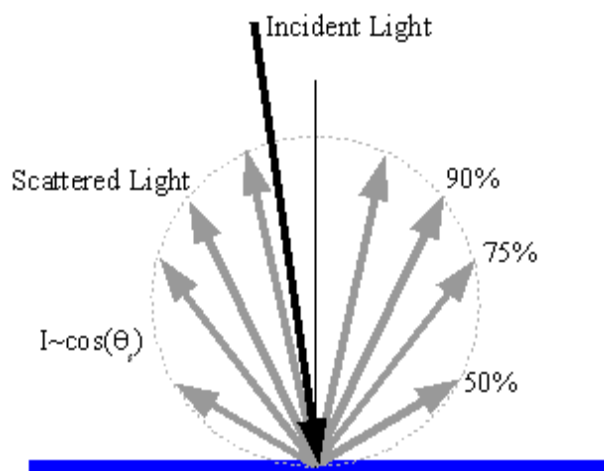


Figure 4.35. A Lambertian surface where scatter of light is governed by a cosine intensity relationship.

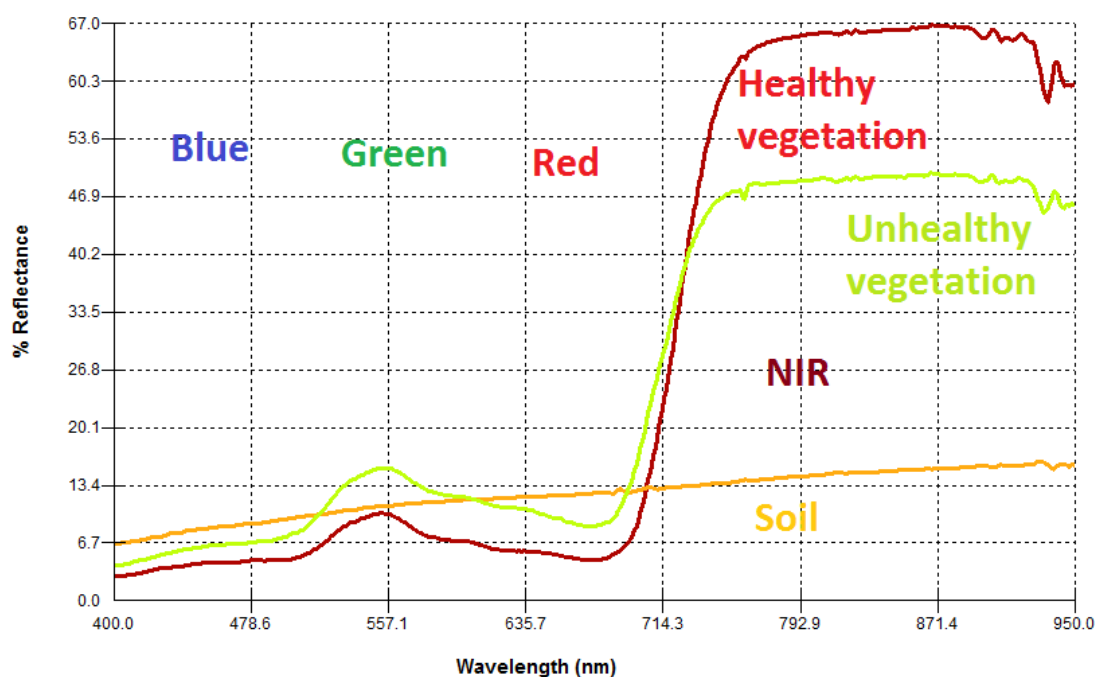


Figure 4.36. Reflectance of crops as a status of vegetation health.

The domain of optical observations extends from 400 nm in the visible region of the electromagnetic spectrum to 2500 nm in the shortwave infrared region. The strong absorption of light by photosynthetic pigments dominates green leaf properties in the visible spectrum (400-700nm), leaf chlorosis causes an increase in visible reflectance and transmission while the near-infrared region (NIR, 700-1100 nm) is a region where biochemical absorptions are limited to the compounds typically found in dry leaves,

primarily cellulose, lignin and other structural carbohydrates (Wang *et al.*, 2005). Figure 4.36 displays differences of crop reflectance according to vegetation health. This diagram depicts in other words the “spectral signature” of each crop. The x-axis illustrates the wavelength ( $\mu\text{m}$ ) and the y-axis illustrates the reflectance (%). A similar diagram is illustrated at Figure 4.37 where values for some selected crops are plotted together with specified Landsat TM 5 bands’ wavelengths (for comparison purposes).

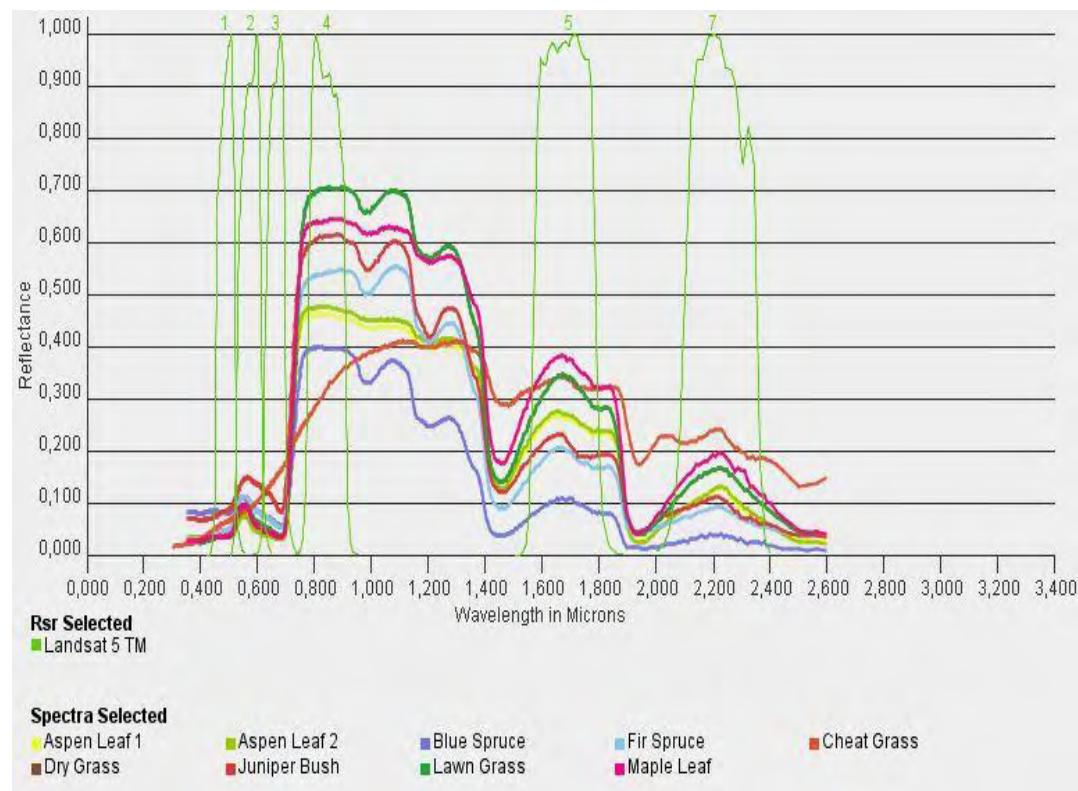


Figure 4.37. Relative spectral response for LANDSAT TM

(Source: <http://gis.stackexchange.com/>).

#### 4.3.1 Phenological stages of the crops

Phenology can be defined as the study of the timing of biological events and the interrelation among phases of the same or different species (Shaykewich, 1994; Papadavid, 2012). As McCloy (2010) mentions, the phenological cycle can be defined as the trace or record of the changes in a variable or attribute over the phenological period (usually one agricultural year) and a phenophase is defined as an observable stage or phase in the seasonal cycle of a plant that can be defined by start and end



points. Obvious changes in each crop cycle can be identified in Figure 4.38 that show how a crop grows during its life-cycle. Cotton is selected as an example.

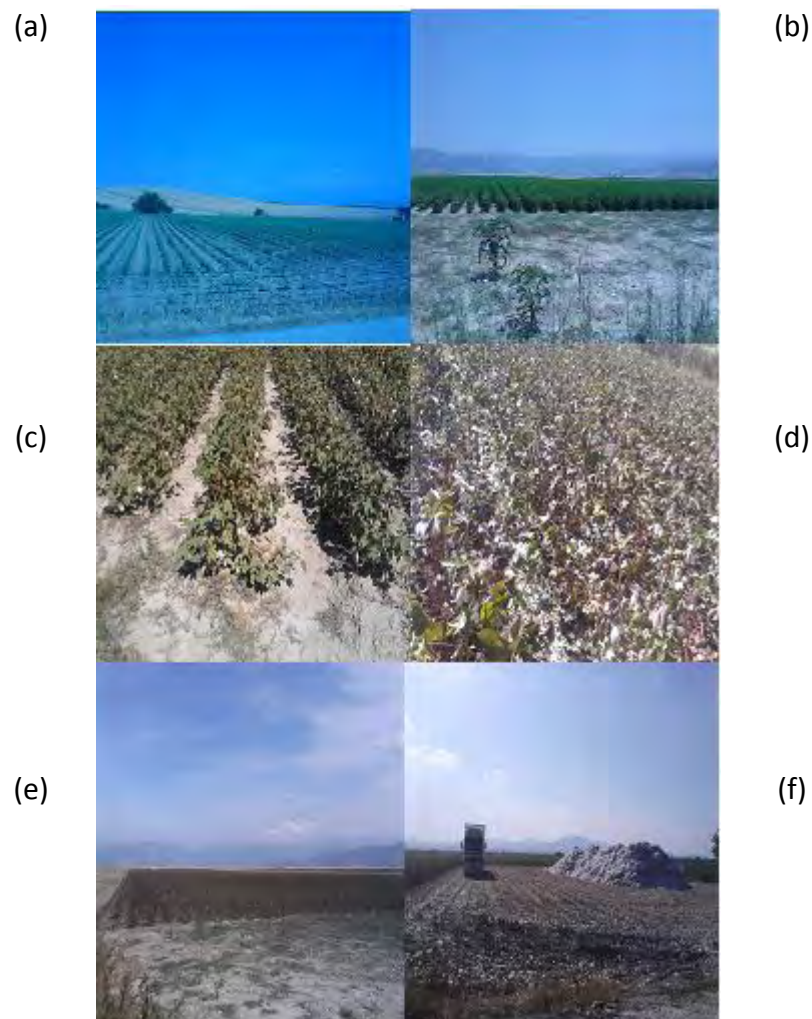


Figure 4.38. Cotton phenological stages (a) heading 15/6, (b) flowering 31/7, (c) flowering 1/9, (d) maturing 21/9, (e) before harvesting 12/10, (f) harvesting (19/10)

#### 4.3.2 Procedure

GER1500 spectroradiometer in-situ measurements are taken at Lake Karla watershed for this study. The measurements are repetitive over the same fields for consistency (Figure 4.39).



Figure 4.39. Multiple GER1500 measurements across the fields.

Generally, the spectral resolution on broadband spectral measurements such as Landsat TM/ETM+ is indicated by the relative spectral response (RSR) of the spectral bands. RSR describes the quantum efficiency of a sensor at specific wavelengths over the range of a spectral band (Fleming, D.J., 2006). In order to match another spectral measurement with a TM/ETM+ band, it is necessary to use the TM/ETM+ relative spectral response functions (SRF) (Fleming, D.J., 2006) and take the average within the limits of every TM/ETM+ bands to obtain the equivalent in-band reflectance values (Agapiou *et al.*, 2012). Figure 4.40 and Figure 4.41 illustrate RSR for Landsat 7 bands 3 and 4.

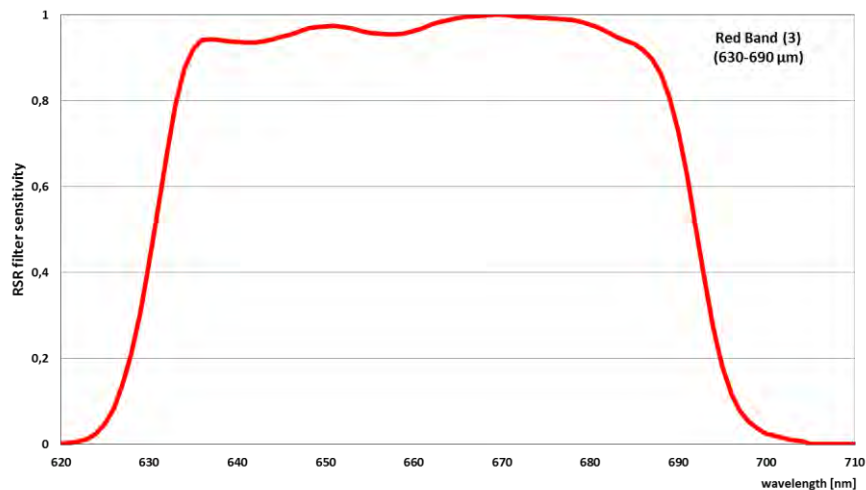


Figure 4.40. Landsat in - Band Average RSR: band 3 (retrieved from USGS Spectral Viewer).

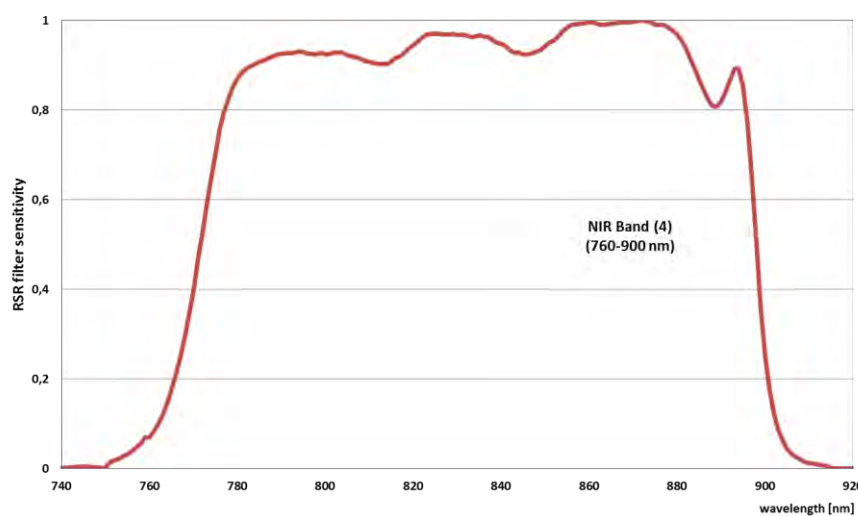


Figure 4.41. Landsat in - Band Average RSR: band 4 (retrieved from USGS Spectral Viewer).

The goal of this conversion is the calculation of surface reflectance values which are equivalent to Landsat ETM+ bands 1, 2, 3 and 4. The filtering of the data through the RSR values of Landsat ETM+, is made through the interpolation of the initial GER1500 reflectance values (Figure 4.42).



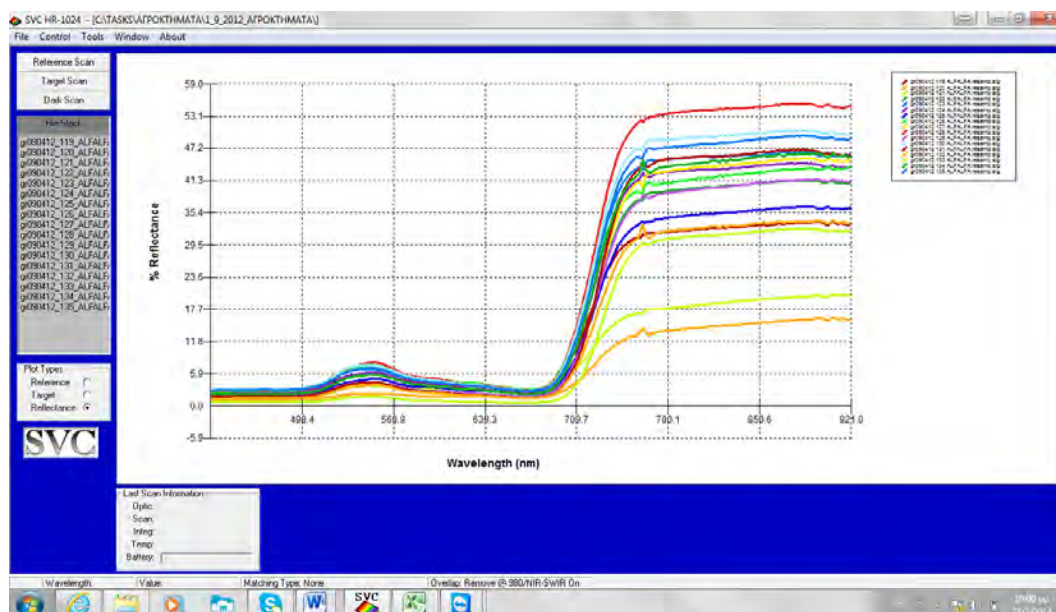


Figure 4.42. Initial GER1500 reflectance values for selected alfalfa fields.

The result is the generation of reflectance values at the incremental wavelength of the RSR (at 450, 451, 452 nm etc.). This procedure (Figure 4.43) is done since the GER1500 reflectance values are given at a different incremental wavelength scale (e.g. 449.81, 451.48, 453.15 nm) and this conversion seems to be necessary (Papadavid *et al.*, 2012).

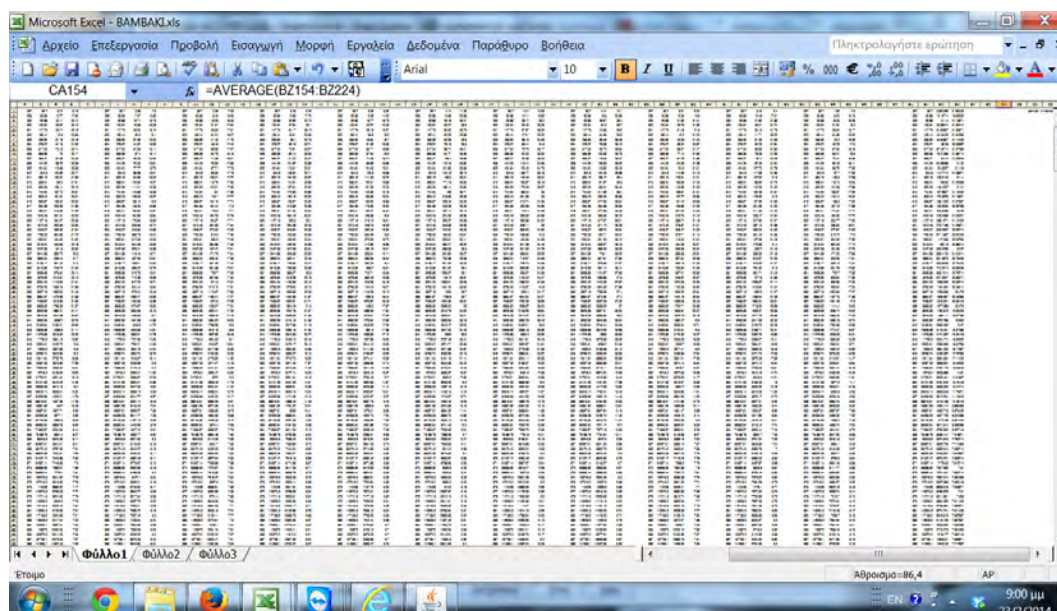


Figure 4.43. Interpolation of the average initial reflectance values.

Figure 4.44, Figure 4.45, Figure 4.46, and Figure 4.47 illustrate some examples of spectral measurements for alfalfa, cotton, maize and sugar beet, respectively, for specific experimental days of field measurements. The experimental days are eleven and are detailed described at the next chapter. For each experimental date, up to 30 measurements for each crop are taken, and finally, the average values are processed. Figure 4.48 illustrates an example of temporal evolution of spectral signatures for cotton.

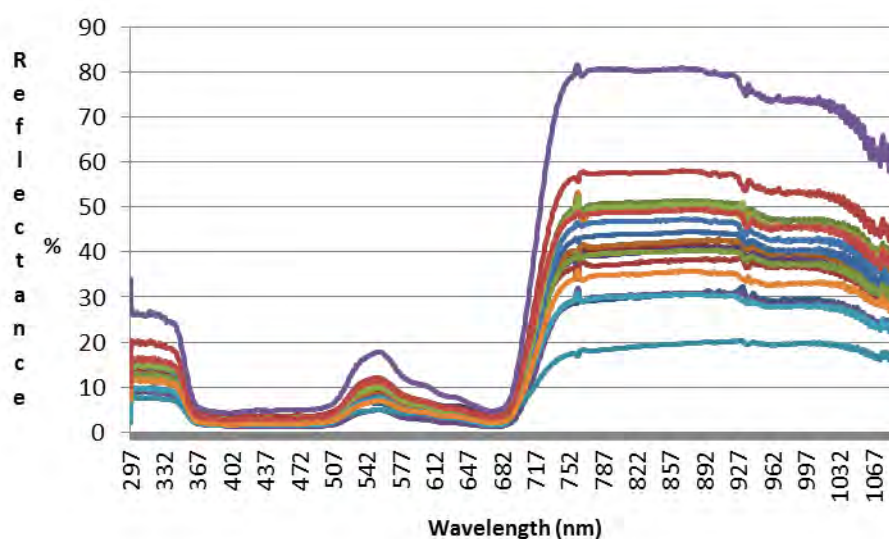


Figure 4.44. Alfalfa spectral measurements for 21/9/2012.

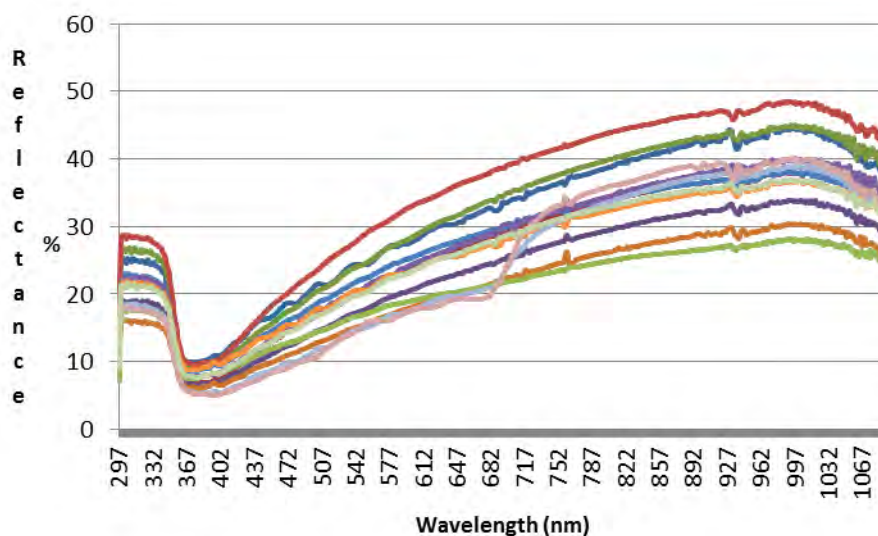


Figure 4.45. Cotton spectral measurements for 13/7/2012.

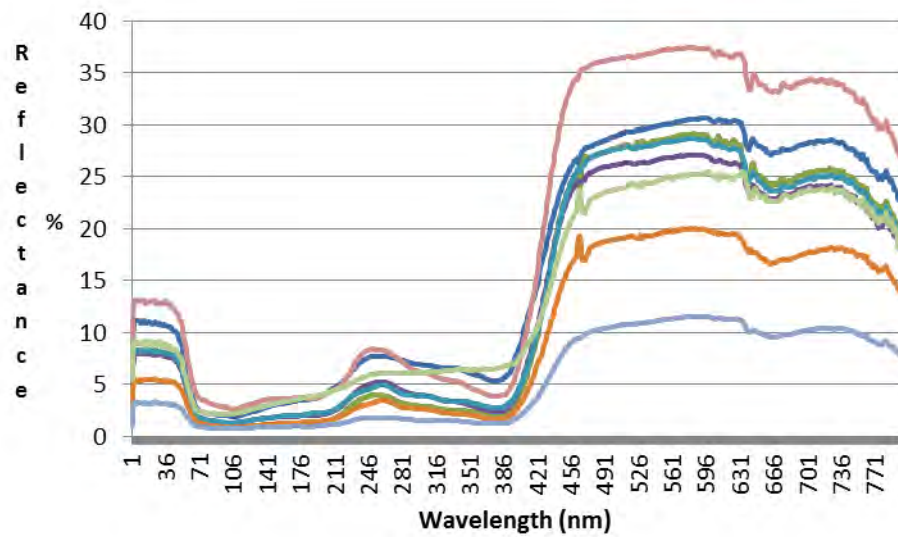


Figure 4.46. Maize spectral measurements for 29/6/2012.

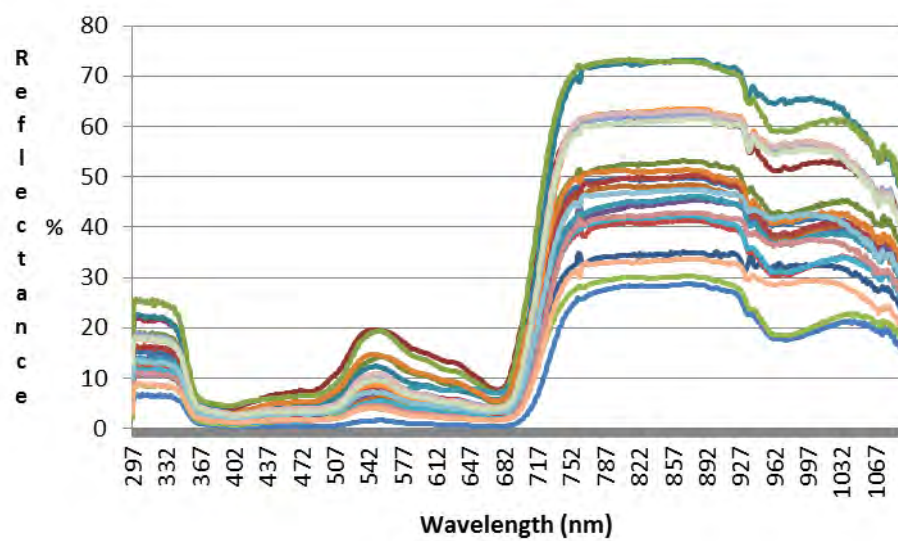


Figure 4.47. Sugar beet spectral measurements for 13/7/2012.

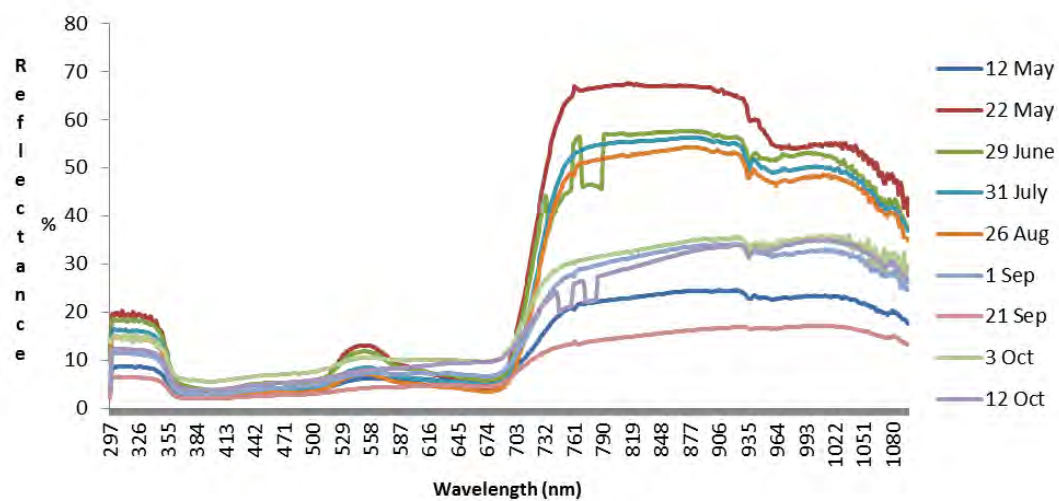


Figure 4.48. Temporal evolution of spectral signatures for cotton.

After that, GER 1500 experimental data are filtered through the RSR functions and averaged within the limits of the first four TM/ETM+ bands, to yield the in-band reflectance values. These reflectance values are used for the computation of vegetation indices and finally NDVI which is the product used for the downscaling as it is explained later.

#### 4.4 Downscaling

It is obvious that satellite – borne sensors providing thermal data usually have a coarser spatial resolution than sensors with non-thermal response for example in the visible, near infrared or shortwave infrared regions. Data from a coarse spatial resolution image often cause inaccurate ET estimation due to the potential high level of spatial heterogeneity in the land use. For example, ET maps produced with the use of MODerate resolution Imaging Spectroradiometer (MODIS) or the Advanced Very High Resolution Radiometer (AVHRR) are too coarse to be useful in hydrological detailed studies as the pixel size is larger than the individual agricultural fields. That is, pixels have multiple use and vegetation types with significant differences in cover, roughness and/or moisture content (Kustas *et al.*, 2004). On the other hand, high spatial resolution satellite images, for example from Landsat 5 or 7 are available every 16 days



or longer with a relatively small coverage area (swath width 185 km) and a 30 m x 30 m spatial resolution, while images of lower spatial resolution from MODIS are available daily with a swath width of 2,330 km and a 250 m x 250 m spatial resolution. Image downscaling methods are used to overcome spatial (and temporal) scaling issues in remote sensing applications. High temporal resolution images contribute to accurate land cover change detection while high spatial resolution allows the accurate identification of land surfaces as well exact shapes and boundaries of surfaces of interest. Downscaling is typically defined as an increase in spatial resolution following disaggregation of an original data set (Bierkens *et al.*, 2000; Liang, 2004). Reliable downscaling methods have been proposed, while some of them have to do with the downscaling of land surface temperatures (LST) on ET maps.

These downscaling methods can be broadly classified in two groups: (1) scale based traditional downscaling and (2) image fusion (pan sharpening or data fusion) methods. Both these methods are used for the enhancement of the spatial resolution of the satellite images. By applying these methods, there is a conversion of the lower (coarser) spatial resolution to the higher (finer) spatial resolution on the basis of statistical based models, process-based models or hybrid models. This process does not alter the image radiometric properties (Luo *et al.*, 2008).

In this thesis, downscaling of METRIC derived evapotranspiration map from the MODIS (500 m x 500 m) to the Landsat (30 m x 30 m) scale has been tested, performed and finally applied separately to NDVI at the last stage of the proposed methodology as is described below.

Clear sky Landsat 5 and TERRA/MODIS images from 26 July and 27 August 2007 are selected for applying and testing the downscaling methods. Although the time interval between the two dates could be 16 days according to Landsat's temporal resolution, only monthly coverage (2x16=32 days) is a reasonable expectation for the availability of clear high-resolution satellite images due to atmospheric conditions (Moran *et al.*, 1996). Both Landsat and MODIS (MOD09GA and MOD11A1) data are geolocated to the Greek georeference system EGSA 87. It must be highlighted that the METRIC algorithm



eliminates the need for refined atmospheric correction of surface temperature and albedo due to its internal calibration (Bastiaanssen *et al.*, 2005). This is done, because ET estimates depend only on radiometric temperature differences in the scene and not on the absolute temperature values. Meteorological data for the study period are available from Centre for Research and Technology, Thessaly (Velesino station). Wind, air temperature, relative humidity data as well as radiation values used as input parameters in METRIC methodology and for the initial calculation of  $ET_a$ . The images used in this study cover the whole area of Thessaly, Greece, which is one of the more important agricultural areas in Greece, but finally a relatively smaller rectangle area of 32.5 km x 22.5 km at Lake Karla watershed is processed mainly for atmospheric reasons (clouds). This center of this region is situated at latitude/longitude 39° 38' 16" North and 22° 34' 33" East.

METRIC methodology is applied at the two Landsat-5 TM and TERRA/MODIS satellite images which are acquired and utilized for the estimation of  $ET_a$  on a pixel-by-pixel basis. Disaggregation consists of the use of information derived from large scales (MODIS) to small scales (Landsat). Two downscaling methods have been applied in this study: a) the regression method and b) the subtraction method.

Linear regression between the two MODIS images is applied first and, then, the developed regression equation is applied to the second Landsat image assuming the first Landsat image as the input. The whole procedure is illustrated at Figure 4.49. The coefficients  $a$  and  $b$ , in this study, are found to be 0.6865 and 1.523, respectively. The regression method is based on two assumptions: a) the linear relationship between coarse resolution images (i.e. MODIS images) is valid between fine-scale resolution imagery (i.e. Landsat images) and b) the variability changes linearly during the time interval between two satellite estimated maps (Hong *et al.*, 2012).

For comparison purposes, the subtraction method (Hong *et al.*, 2012) is also applied (Figure 4.50). In this method, the pixel by pixel difference between two MODIS images or products is added to the first Landsat product in order to disaggregate the final Landsat product.

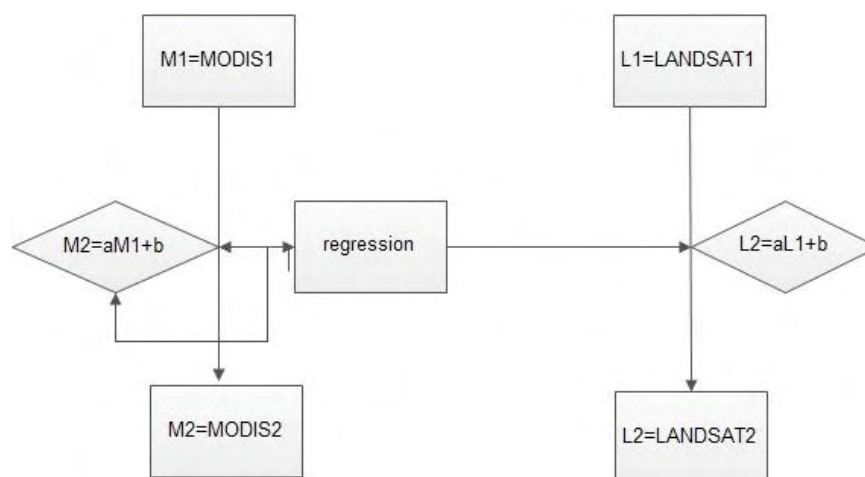


Figure 4.49. Regression based downscaling.

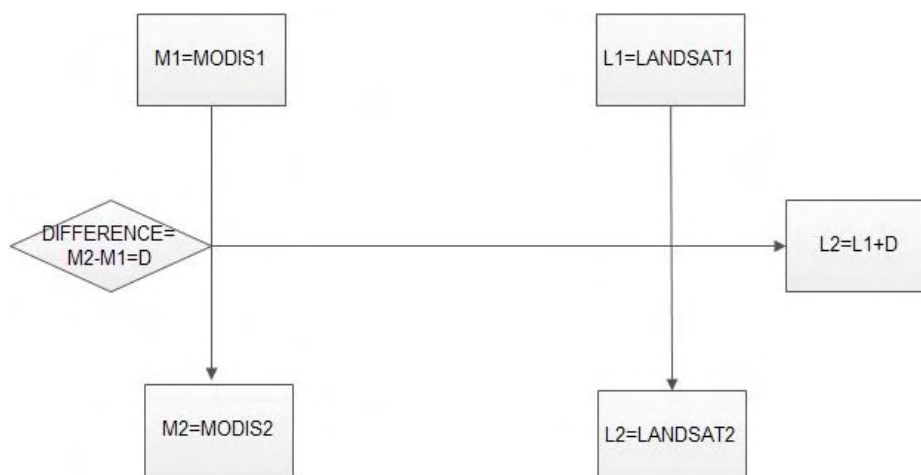


Figure 4.50. Subtraction based downscaling.

Figure 4.51 presents the four initial METRIC based  $ET_a$  maps for the two different types of sensors and different dates.

Figure 4.52 presents the predicted Landsat based METRIC  $ET_a$  map as well the difference between Landsat predicted and initial  $ET_a$  map. Figure 4.53 presents 2D scatterplots between predicted and original  $ET_a$  maps for the regression and subtraction methodologies. The mean value of original  $ET_a$  map for August is greater than Landsat original map for July. The same is predicted for the downscaled map as well, in both cases (i.e. regression and subtraction methodologies). It is remarkable that subtraction method presents much higher values of standard deviation. This may be caused from the uncertainty that prevails inside the larger (coarse resolution) pixel in comparison with the fine scale-resolution pixel. The reason for this is that a larger pixel

incorporates many dynamic sources of different radiance and thermal variability affecting the final radiometric value of the pixel. Generally, mean values are very satisfactory for the predicted  $ET_a$  maps but the regression methodology prevailing again as it can be seen from

Figure 4.52. These results are in total accordance with Hong *et al.* (2012), who applied the regression methodology at Middle Rio Grande Valley in New Mexico with a high accuracy.

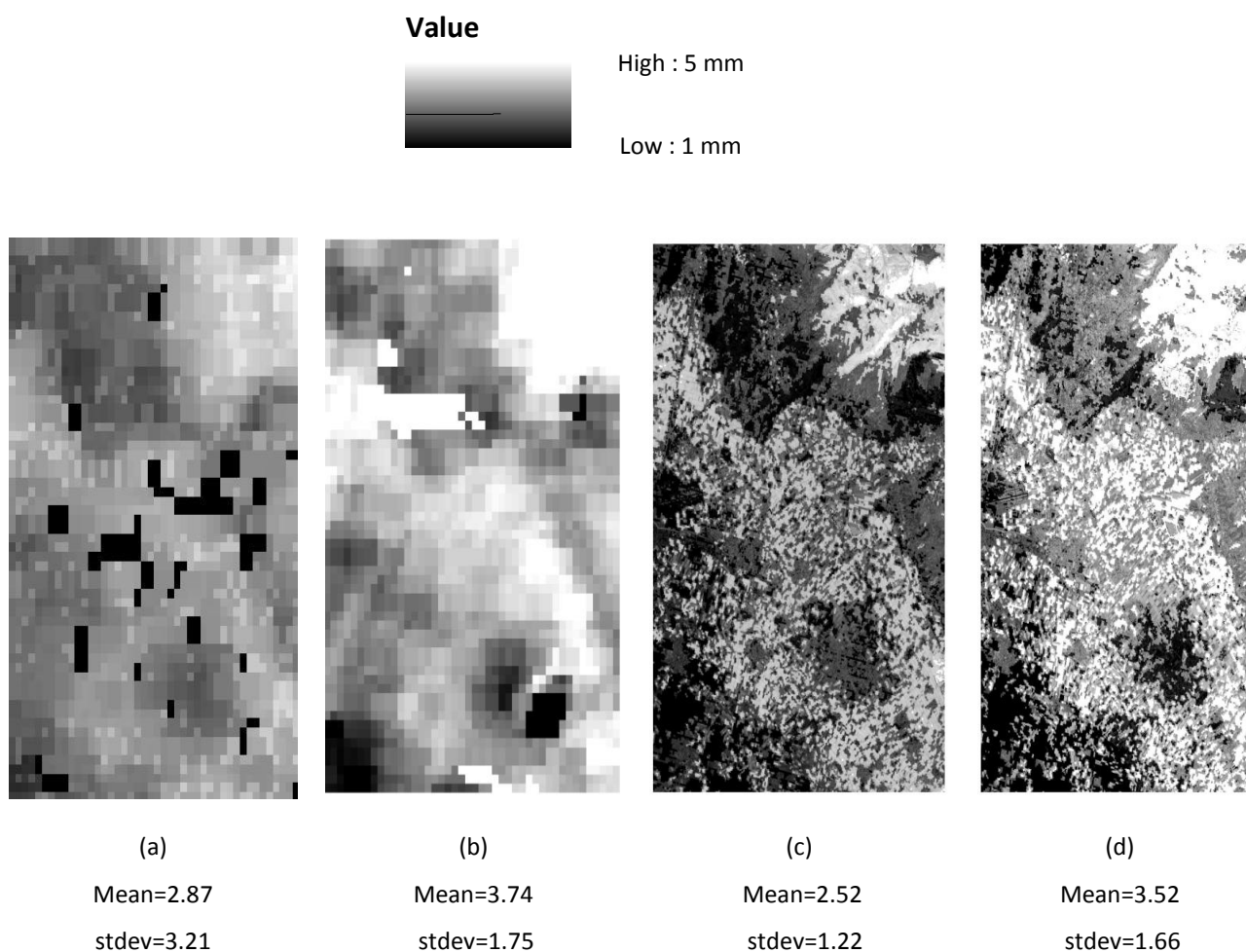


Figure 4.51. METRIC  $ET_a$  maps: (a) 26/7/2007 MODIS, (b) 27/8/2007 MODIS, (c) 26/7/2007 Landsat TM, (d) 27/8/2007 Landsat TM

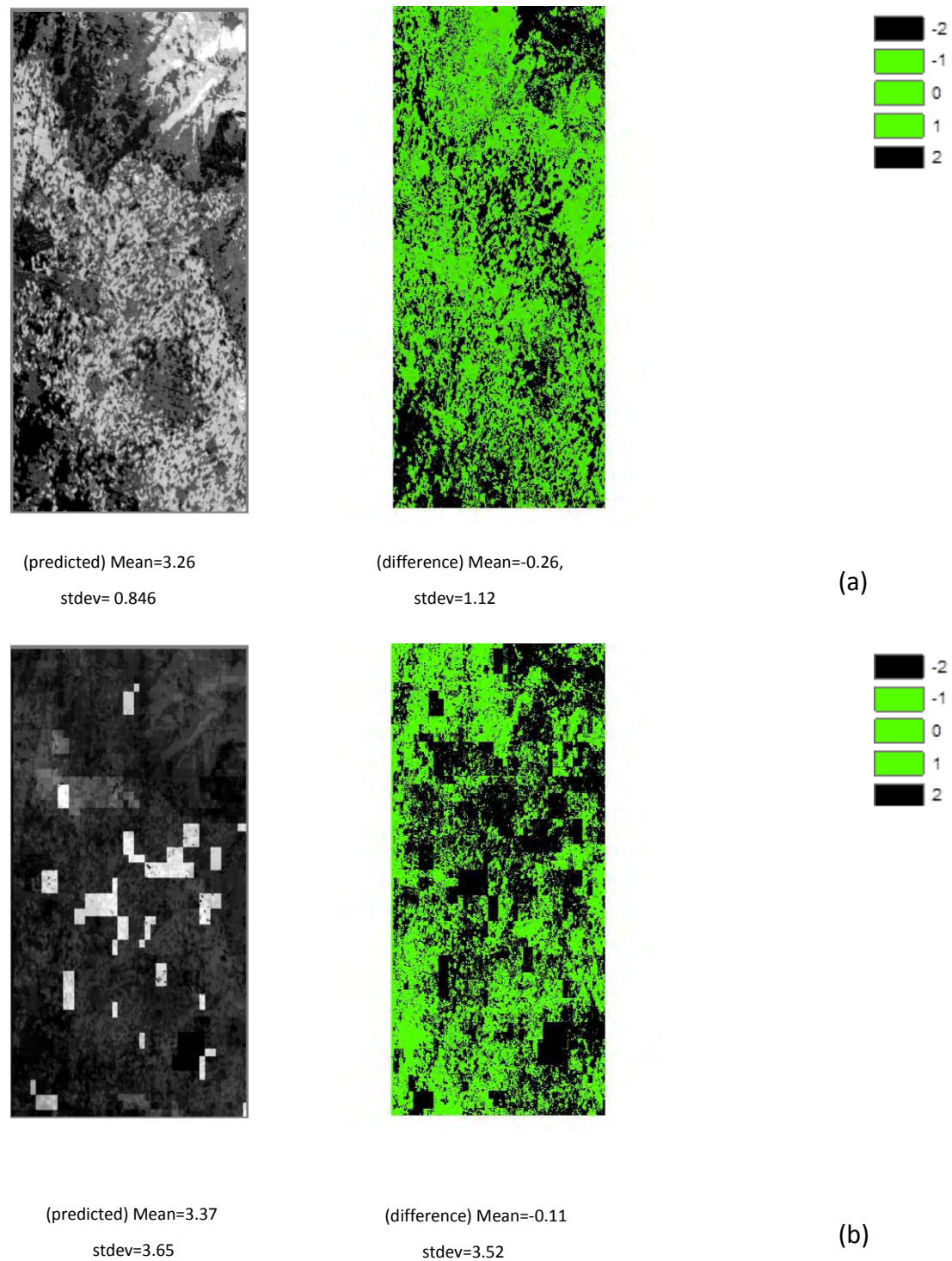


Figure 4.52. Predicted  $ET_a$  maps and difference between predicted and original maps: (a) regression, (b) subtraction.

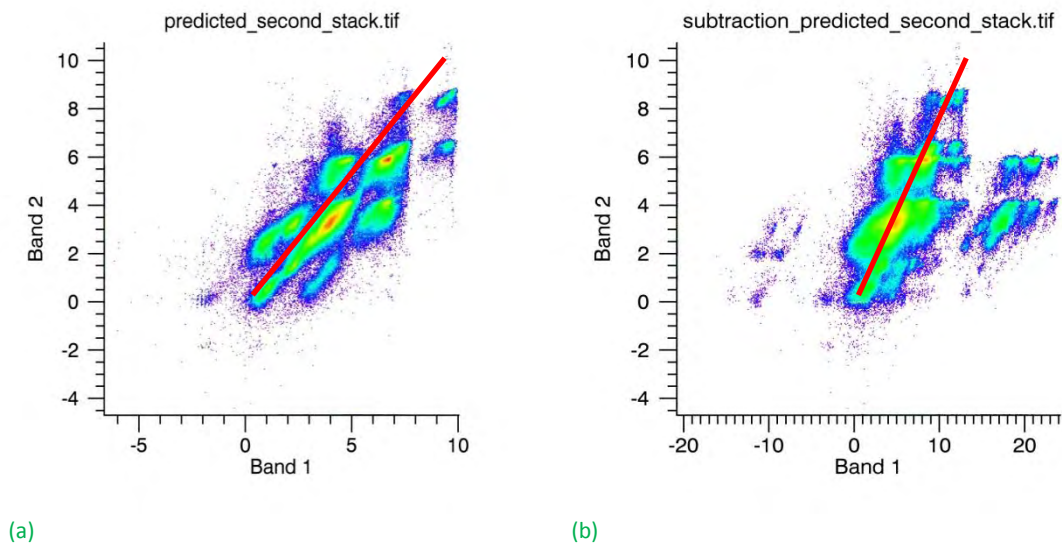


Figure 4.53. 2D Scatterplots for predicted-original 27/7/2007 Landsat ET<sub>a</sub> for (a) regression downscaling method and (b) subtraction downscaling method. The red line is the 1:1 line of perfect agreement.

This study shows that it is feasible to predict a 30 m x 30 m Landsat based ET<sub>a</sub> map for Thessaly, Greece with satisfactory results applying a simple linear regression derived from 500 m x 500 m MODIS images. One very significant hypothesis for the application of the downscaling procedure is that the fine-scale variability inside a MODIS pixel (500 m x 500 m) is assumed fixed between the times of the first and the second Landsat image acquisition. It is obvious that regression methodology provides better results than the subtraction method. Prevailing noise, especially in MODIS images, when they are used in the METRIC methodology, is a critical problem which produces larger values than the expected ones. This is expected as the spatial resolution is much coarser than Landsat. Finally, a critical issue is the time interval length between the two images used in the proposed downscaling methodology. Results are expected to improve for smaller time intervals in the future according to the satellite data acquiring policies (Spiliotopoulos *et al.*, 2013).

Following the above analysis, regression downscaling is chosen to be used at the purposed methodology. Landsat based NDVI images, previously computed as METRIC sub-products and MODIS based NDVI images are now downscaled. The same

methodology is described in previous studies as “input” ET downscaling (Hong *et al.*, 2012; Spiliotopoulos *et al.*, 2013). This is exactly the same methodology as the previous one, with the only difference that the product is now NDVI instead of ET. In this method, pixel by pixel difference between two MODIS products is added to the first Landsat product in order to disaggregate the final Landsat product (which is now the NDVI). Results are described at the next chapter.

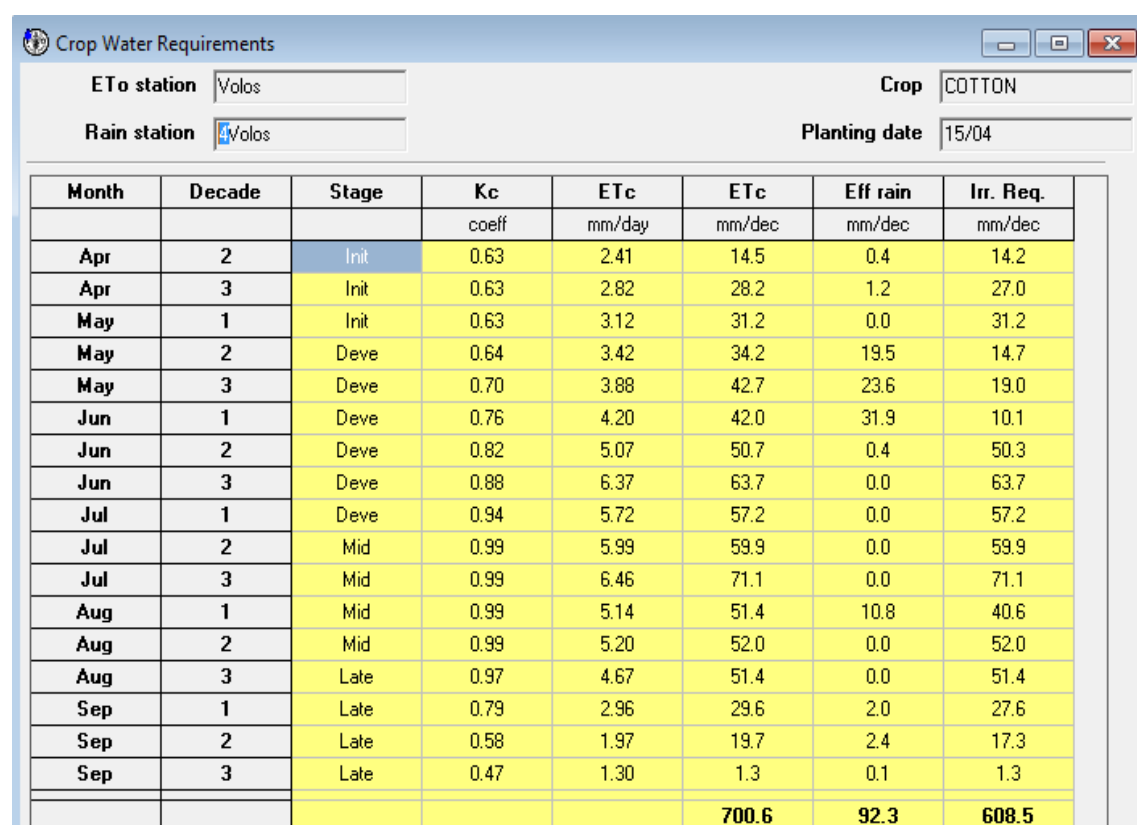
#### 4.5 Application of CropWat model

CropWat developed by the Land and Water Development Division of FAO (FAO, 1992) is already described at the chapter 2.8. The basic functions of CropWat include the calculation of reference evapotranspiration, and the crop water requirements. CropWat model generally requires climatic data, separate rainfall data, crop data and finally soil data. Rainfall data as well as the other climatic parameters needed for CropWat application can be computed using ClimWat.

ClimWat used in combination with CropWat works as a climatic database for the main meteorological stations worldwide. The data can be extracted in a format suitable for CropWat. Two files are created for each selected station. The first file contains long-term monthly rainfall data (mm/month). Additionally, effective rainfall is also included (calculated and included in the same file). The second file consists of long-term monthly averages for the needed climatic parameters. This file also contains the coordinates and altitude of the location (Figure 2.12). In this dissertation, an alternative way is followed. Meteorological data series are used at the study area instead of climatic. Velestino station inside the watershed is utilized for this reason. During the year of 2012 Stefanovikeio station started, also, its operation. So, ClimWat is used only for cross-checking the results.

After the insertion of climatic and rainfall data, crop and soil data must be inserted. Soil conditions from FAO databases are used, while previous studies relating with soil maps in the regions are also taken into account especially for crosschecking (Karioti, 2013).

After all, the most important parameter at the present application is the crop data, where  $K_c$  coefficients derived from METRIC are now inserted manually in the program. This adds a special uniqueness to the application, keeping in mind that each study area keeps its own crop peculiarities which are finally taken into account for the internal computations. Finally, after modifying and inserting the \*. pen files for climatological data, \*. cli files for rainfall data, \*. soi files for soil data, and \*. cro files for crop data, CropWat returns the output in a spreadsheet style (Figure 4.54):



The screenshot shows the 'Crop Water Requirements' application window. At the top, there are input fields for 'ETo station' (Volos), 'Rain station' (Volos), 'Crop' (COTTON), and 'Planting date' (15/04). Below these is a table with 8 columns: Month, Decade, Stage, Kc, ETc (mm/day), ETc (mm/dec), Eff rain (mm/dec), and Irr. Req. (mm/dec). The table lists data for each month from April to September, divided into three decades each. The stages are Init, Deve, and Late. The final row shows totals: 700.6 for ETc (mm/dec), 92.3 for Eff rain (mm/dec), and 608.5 for Irr. Req. (mm/dec).

Month	Decade	Stage	Kc	ETc	ETc	Eff rain	Irr. Req.
			coeff	mm/day	mm/dec	mm/dec	mm/dec
Apr	2	Init	0.63	2.41	14.5	0.4	14.2
Apr	3	Init	0.63	2.82	28.2	1.2	27.0
May	1	Init	0.63	3.12	31.2	0.0	31.2
May	2	Deve	0.64	3.42	34.2	19.5	14.7
May	3	Deve	0.70	3.88	42.7	23.6	19.0
Jun	1	Deve	0.76	4.20	42.0	31.9	10.1
Jun	2	Deve	0.82	5.07	50.7	0.4	50.3
Jun	3	Deve	0.88	6.37	63.7	0.0	63.7
Jul	1	Deve	0.94	5.72	57.2	0.0	57.2
Jul	2	Mid	0.99	5.99	59.9	0.0	59.9
Jul	3	Mid	0.99	6.46	71.1	0.0	71.1
Aug	1	Mid	0.99	5.14	51.4	10.8	40.6
Aug	2	Mid	0.99	5.20	52.0	0.0	52.0
Aug	3	Late	0.97	4.67	51.4	0.0	51.4
Sep	1	Late	0.79	2.96	29.6	2.0	27.6
Sep	2	Late	0.58	1.97	19.7	2.4	17.3
Sep	3	Late	0.47	1.30	1.3	0.1	1.3
					700.6	92.3	608.5

Figure 4.54. CropWat irrigation requirements output.

Having distributed crop coefficient values with a 30 m x 30 m spatial resolution for every crop, and every stage (initial, development, mid-season and late-season) is a very important development for CropWat's computations as it will be described later on.

## 4.6 Methodological Framework

### 4.6.1 Background application of the “classical” METRIC method

The first goal of the dissertation is the computation of irrigation requirements (in mm) for the main crops of Lake Karla Watershed using FAO’s CropWat model incorporating two main improvements. The first is that crop coefficient values are now computed for each crop using remote sensing techniques instead of using values acquired from the literature. The second improvement is that meteorological time series for the growing season of 2007 are used instead of climatic data. For the achievement of this goal Landsat TM derived  $ET_a$  values for Lake Karla watershed are estimated using METRIC methodology for the growing season of 2007. Landsat 5 TM images are downloaded and radiometrically calibrated using the relevant calibration constants using the provided header files. Calibrated bands are then used to obtain albedo, net radiation, soil and heat fluxes, as well as brightness temperature at the top of the atmosphere that is converted to surface temperatures used for further applications and analysis. Finally, METRIC methodology is applied to produce instantaneous actual evapotranspiration maps. Local meteorological data including air temperature, humidity, wind speed, and solar radiation are also combined with  $ET_a$  values in order to compute  $ET_{rF}$  values. The crop coefficient values ( $ET_{rF}$ ) are then used as input to CropWat model in order to finally produce irrigation requirements (in mm) for the main crops in the region. The previous land use/cover classification of the area is used for the estimation of irrigation requirements for the main crops in the area. The procedure is repeated for each zone of interest. Figure 4.55 illustrates the “background” methodology as a flow chart.



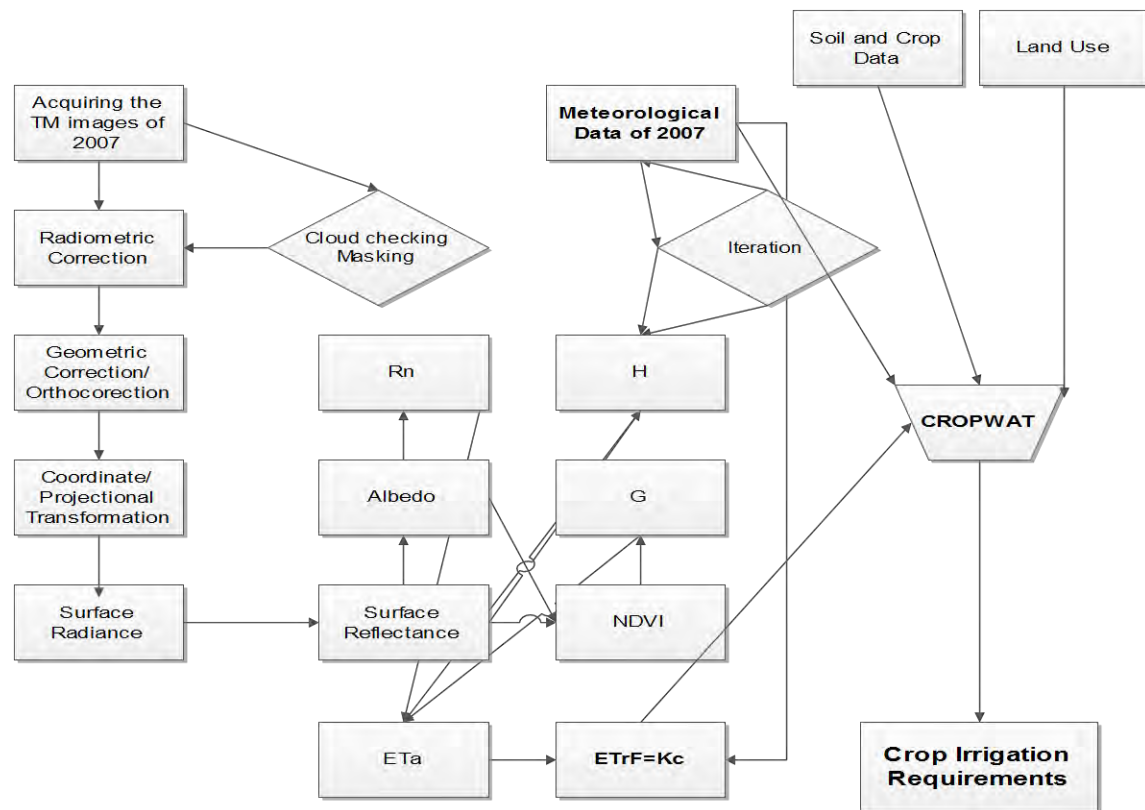


Figure 4.55. “Background” methodology detailed flow chart.

#### 4.6.2 Proposed Integrated methodology

The proposed integrated methodology uses the knowledge and experience acquired from the application of the “classical” METRIC method. The proposed methodology uses the field spectroradiometric data for selected agricultural fields of Karla Lake watershed, the downscaling method for coupling the temporal and spatial resolution of MODIS and Landsat images and the CropWat model to produce daily crop water irrigation requirements for the main crops of the study area and a spatial analysis of 30 m x 30 m. Assuming the growing season of 2012 as the study period, local meteorological data including air temperature, humidity, wind speed, and solar radiation are first collected as input for METRIC methodology. Spatial GIS data (shapefiles etc.) are collected and/or generated from the local authorities to be used as input too. Moreover, a new land use/cover classification of the study area is completed.

In the second stage, digital image processing of the satellite imagery is carried out. Raw MODIS Level 1B and Level 3 as well as Landsat 7 ETM+ images are downloaded and radiometrically calibrated using the relevant calibration constants using the provided header files. Calibrated bands are then used to obtain albedo, net radiation, soil and heat fluxes, as well as brightness temperature at the top of the atmosphere. Finally, METRIC methodology is applied to produce instantaneous actual evapotranspiration maps.  $ET_rF$  values are the final products of this stage.

In the third stage, field work for the retrieving of surface reflectance values through portable scientific equipment is undertaken. The goal of this stage is the calculation of surface reflectance values which are equivalent to Landsat ETM+ bands 1, 2, 3 and 4. The filtering of the data through the RSR values of Landsat ETM+ is made through the interpolation of the initial reflectance values. Data collection is carried out during 2012 growing season, while a Global Positioning System (GPS) is used to locate the fields.

In the fourth stage, Vegetation Indices (VI) based on field work are computed and then correlated with  $ET_rF$  values. Specific relationships are derived through regression. NDVI has a better performance and a linear  $ET_rF$  vs NDVI relationship is derived and recorded. In the fifth stage, MODIS based NDVI values are derived and then, downscaled combining Landsat ETM+ based NDVI values. The previous  $ET_rF$  vs NDVI relationship is applied again to the new downscaled NDVI daily values, producing the final daily 30 m x 30 m  $ET_rF$  product. The new  $ET_rF$  values are then used as an input to CropWat model which can give the final daily crop water requirements. Figure 4.56 illustrates the proposed integrated methodology as a flow chart.

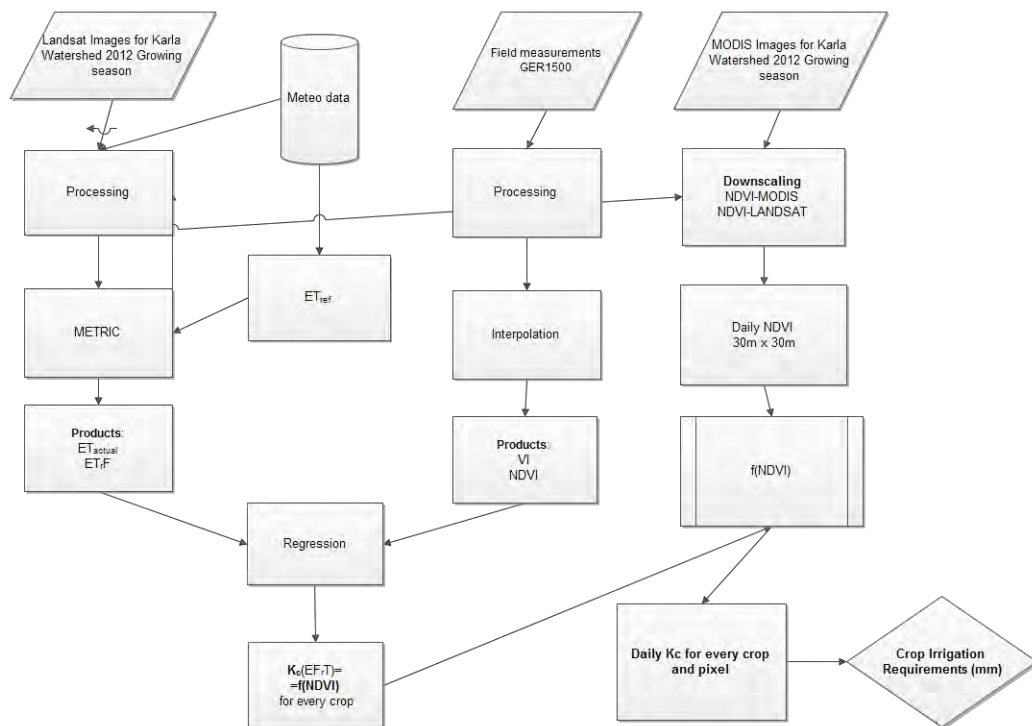


Figure 4.56. Proposed integrated methodology detailed flow chart.



## CHAPTER 5°

### RESULTS

## 5 Results

### 5.1 Background methodology

#### 5.1.1 Application of classical METRIC methodology

Twelve (12) high quality Landsat 5 TM images (Table 5.1) were downloaded from USGS (US Geological Survey) via <http://glovis.usgs.gov> platform and after the radiometric correction, they corrected for geolocation, applying Greek National Coordinate System EGSA 87. These twelve images are merged into six after creating mosaic images in order to include the entire Lake Karla Watershed which is lying across two different Landsat passes (Path/Row: 184/032 and Path/Row: 184/033).

Table 5.1. Landsat 5 TM images used for Lake Karla Watershed

Landsat 5 ETM+ used for spatial analysis			
Date of acquisition	Julian Day of acquisition	Path	Row
07/05/2007	127	184	032
24/06/2007	175	184	032
10/07/2007	191	184	032
26/07/2007	207	184	032
27/08/2007	239	184	032
28/09/2007	271	184	032
07/05/2007	127	184	033
24/06/2007	175	184	033
10/07/2007	191	184	033
26/07/2007	207	184	033
27/08/2007	239	184	033
28/09/2007	271	184	033

### 5.1.2 $ET_a$ mapping

Considering all the sub-models described in the methodology, and running consequently all of them, an image file indicating instantaneous  $ET_a$  is produced for each initial image. “Instantaneous  $ET_a$ ” means that the file is derived from remotely sensed imagery at a single time of day. Figure 5.1, Figure 5.2 and Figure 5.3 illustrate instantaneous  $ET_a$  values for the six described cases of 2007. Temporal variations in  $ET_a$  values are fully justified since different weather and crop characteristics are prevailed at each time.

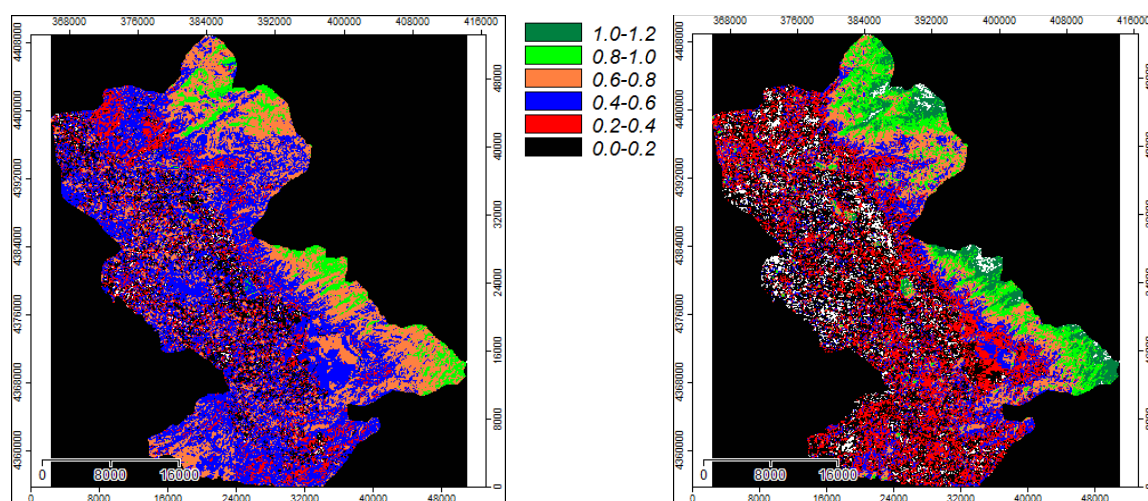


Figure 5.1.  $ET_a$  map for 7/5/2007 (left) and 24/6/2007 (right)

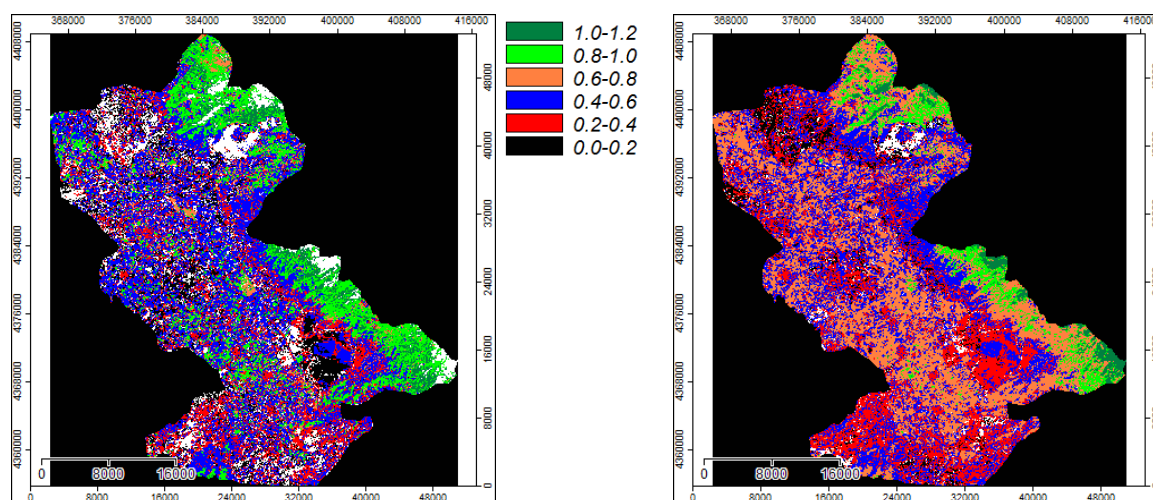


Figure 5.2.  $ET_a$  map for 10/7/2007 (left) and 26/7/2007 (right)

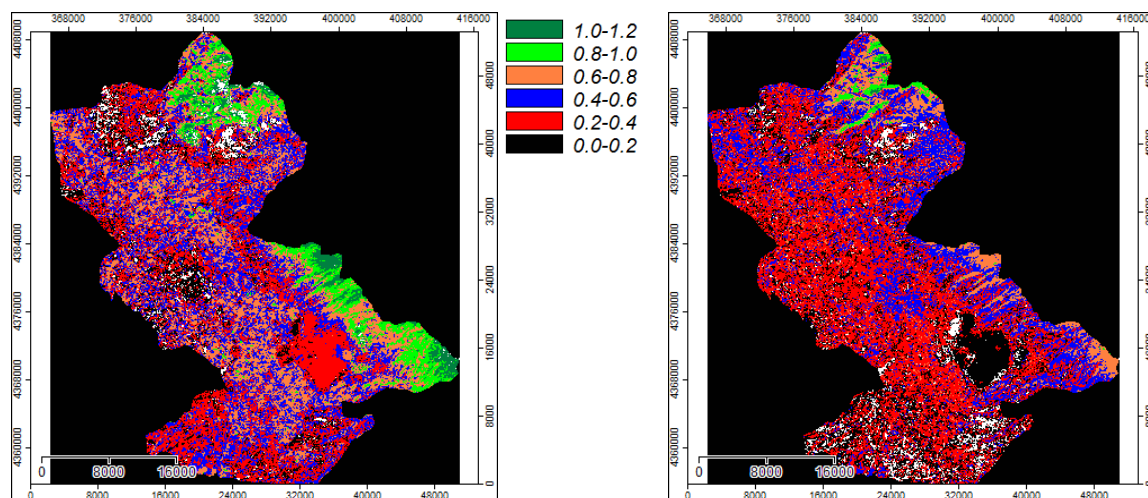


Figure 5.3.  $ET_a$  map for 27/8/2007 (left) and 28/9/2007 (right)

### 5.1.3 $ET_rF$ mapping

At the next step of the procedure,  $ET_r$  is used as a weighting factor for the transition of  $ET$  values to  $ET_rF$  values. This is accomplished by applying equation (2.32), where  $ET_rF$  coefficient is computed, considering that  $ET_r$  is constant for the duration of the day. Six (6) high quality  $ET_rF$  maps are generated for Lake Karla watershed from the initial images given on Table 5.1 according to the methodology described previously. Figure 5.4, Figure 5.5 and Figure 5.6 illustrate the  $ET_rF$  maps. White colour represent pixels with missing information (e.g. cloudiness) which are finally excluded. Fortunately, the majority of these pixels are not related to crops.

Spatial variation is occurring between the fields and this is totally expected since every pixel has its own special features. An example of spatial variation between  $ET_rF$  values is illustrated below. Figure 5.7 shows how  $ET_rF$  values are varying across a cotton field. This is the reason of using average values when a specific value is needed for each field.



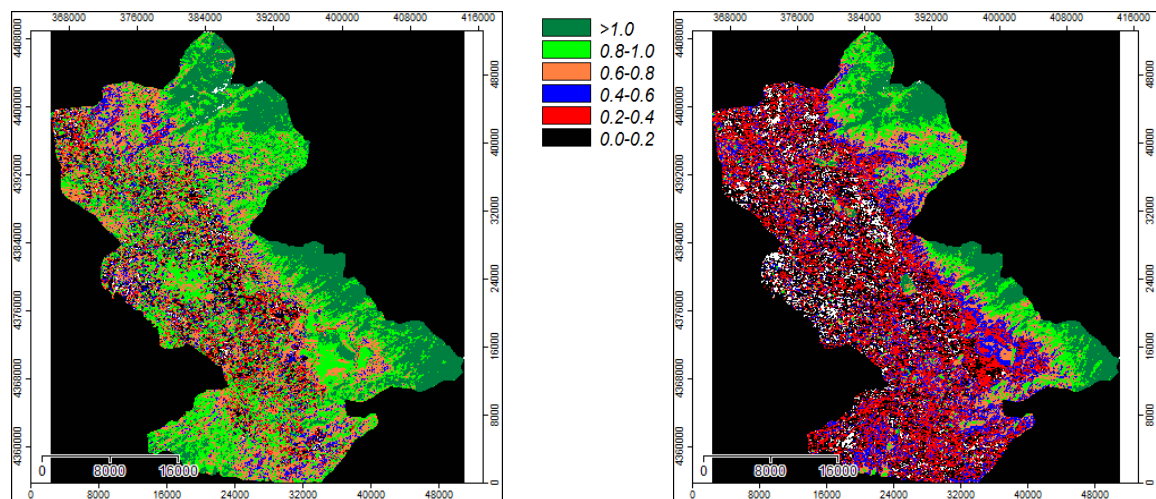


Figure 5.4.  $ET_rF$  map for 7/5/2007 (left) and 24/6/2007 (right)

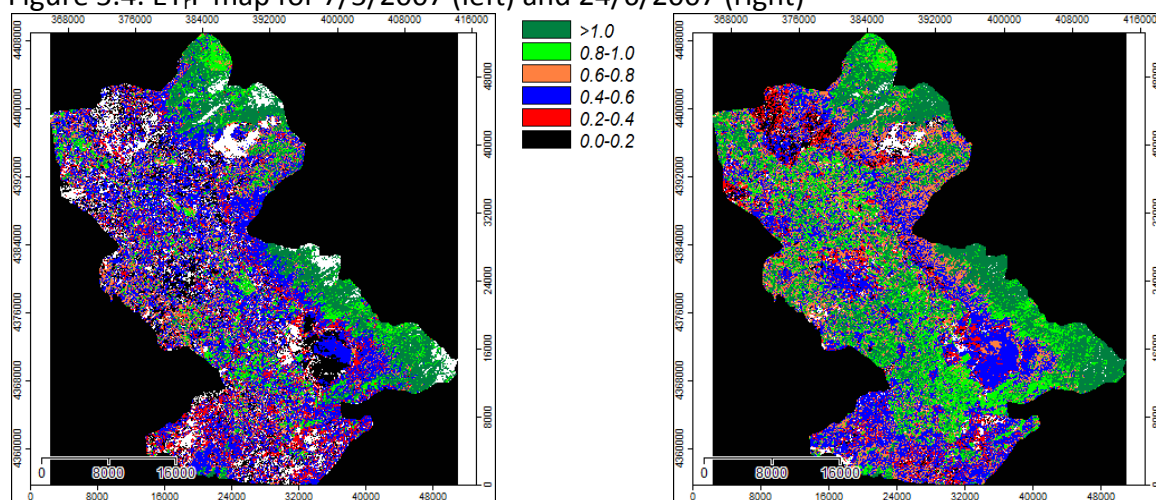


Figure 5.5.  $ET_rF$  map for 10/7/2007 (left) and 24/7/2007 (right).

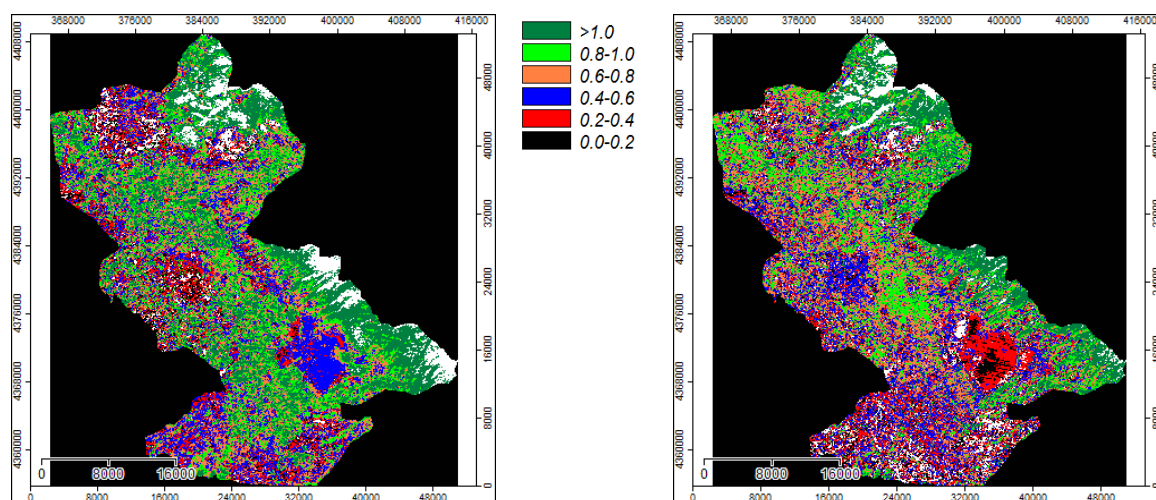


Figure 5.6.  $ET_rF$  map for 7/5/2007 (left) and 26/7/2007 (right)



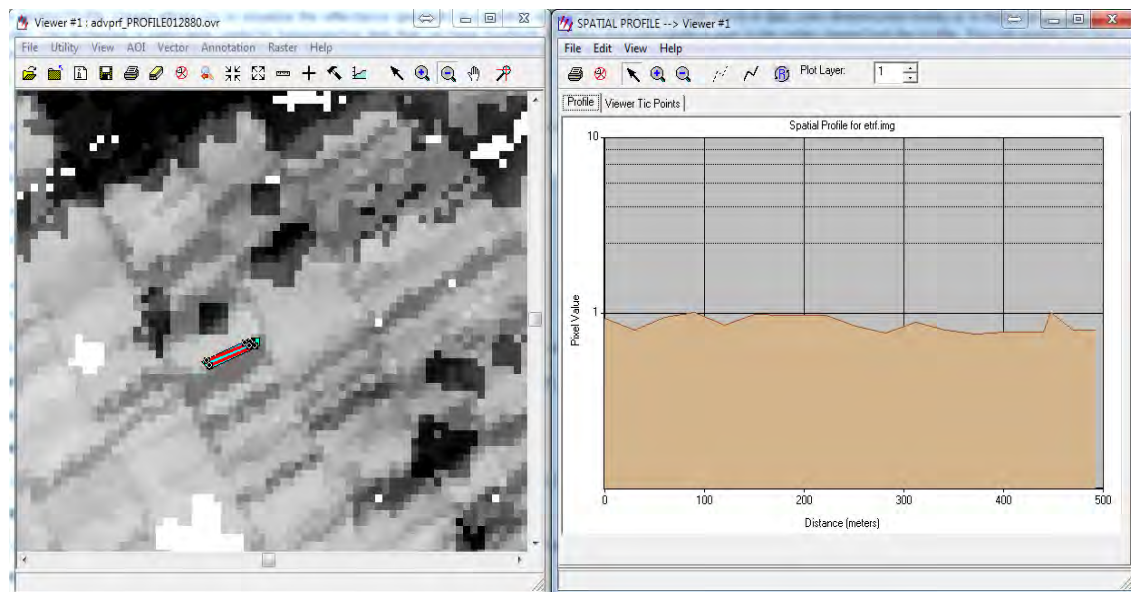


Figure 5.7. Spatial variation of ET values (right) across a specific cotton field (left)

By applying the above procedure, the crop coefficient values distributed over the study watershed with a 30 m x 30 m spatial resolution for every crop, and every phenological stage (initial, development, mid-season and late-season) are estimated. These crop coefficients are, then, used as an input to CropWat for the estimation of monthly crop irrigation requirements, as is shown later in this chapter.

#### 5.1.4 Zoning of the area.

GIS tools have been used for the determination of specific zones inside Lake Karla watershed which play an important role to water resource management practices. The new zones are defined based on their origin. First, surface network is determined which is subdivided into two zones (Figure 5.8). The first zone (red color) is defined as the new surface network according to the study of Greek Reclamation Project Management (2006). The second zone (yellow color) is defined as the surface irrigation network in charge of Pinios Local Administration of Land Reclamation (Pinios LALR).

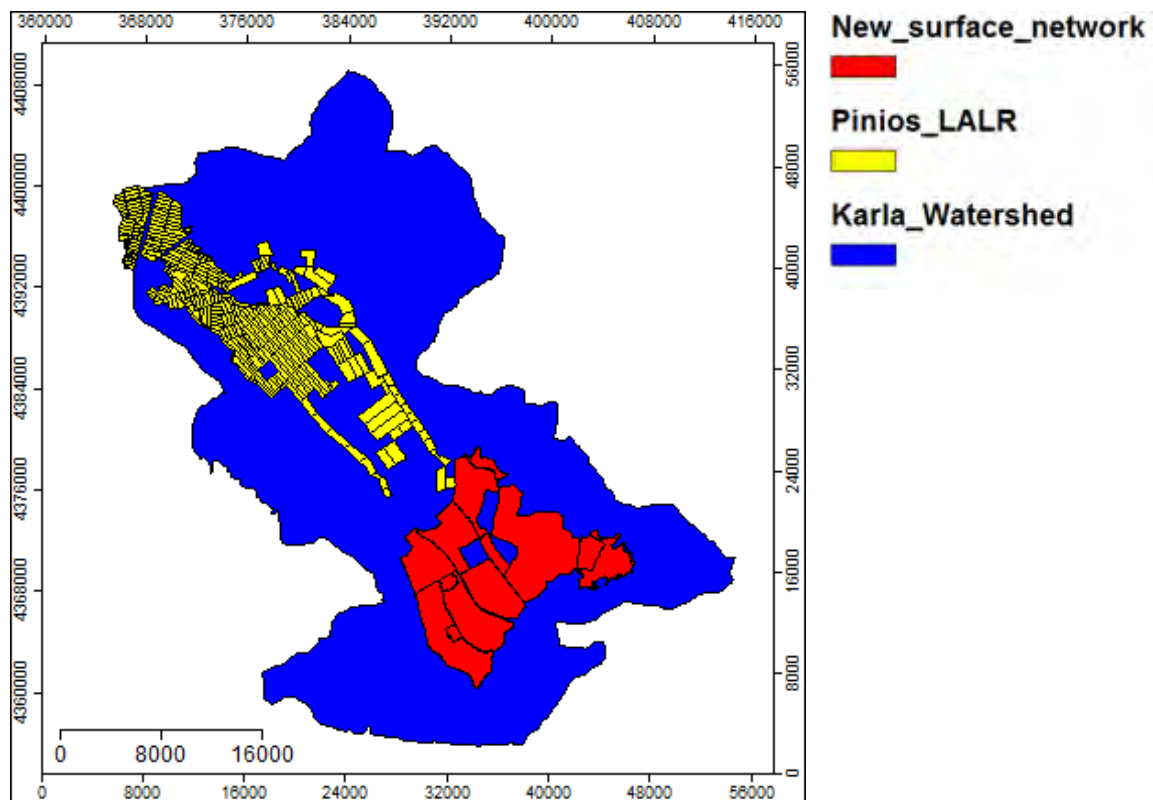


Figure 5.8. The surface network of Lake Karla Watershed.

Figure 5.9 illustrates the three zones of the watershed generated when taking into account groundwater as a criterion. The vectors of the north (yellow) and the south zone (red) are generated according to geographical criteria while the central zone (green) is defined as the initial groundwater region (taken from Greek Reclamation Project Management) after excluding the regions which are common with the new surface irrigation network.

#### 5.1.5 Crop zoning

According to the previous land use classification and the described zoning of the watershed, new vectors are defined and these vectors are applied to the previous  $ET_rF$  maps. The result is the generation of new  $ET_rF$  maps for each crop/zone. Initially, five crops were examined, namely cotton, maize, sugar beet, alfalfa and wheat. But, after realizing that wheat has a totally different phenological cycle than the other crops, it is finally excluded from the study. Figures 5.10 to 5.14 illustrate how cotton, maize, sugar beet, and alfalfa fields are classified on each zone when applying the land use

classification illustrated at Figure 3.13. Yellow colour denotes maize, red colour denotes cotton, green colour denotes alfalfa and light brown denotes sugar beet. Separate  $ET_rF$  maps are generated for each crop for every zone. The average value of  $ET_rF$  for each crop and zone is taken into account for each ETM+ image and finally three different values are assigned for each zone and crop type. These values correspond to initial, mid-season and late season  $ET_rF$  values. These are the values which are finally used as a new input to CropWat model together with meteorological data for 2007 from Volos and Larissa stations collected from the network of [www.meteo.gr](http://www.meteo.gr) stations.

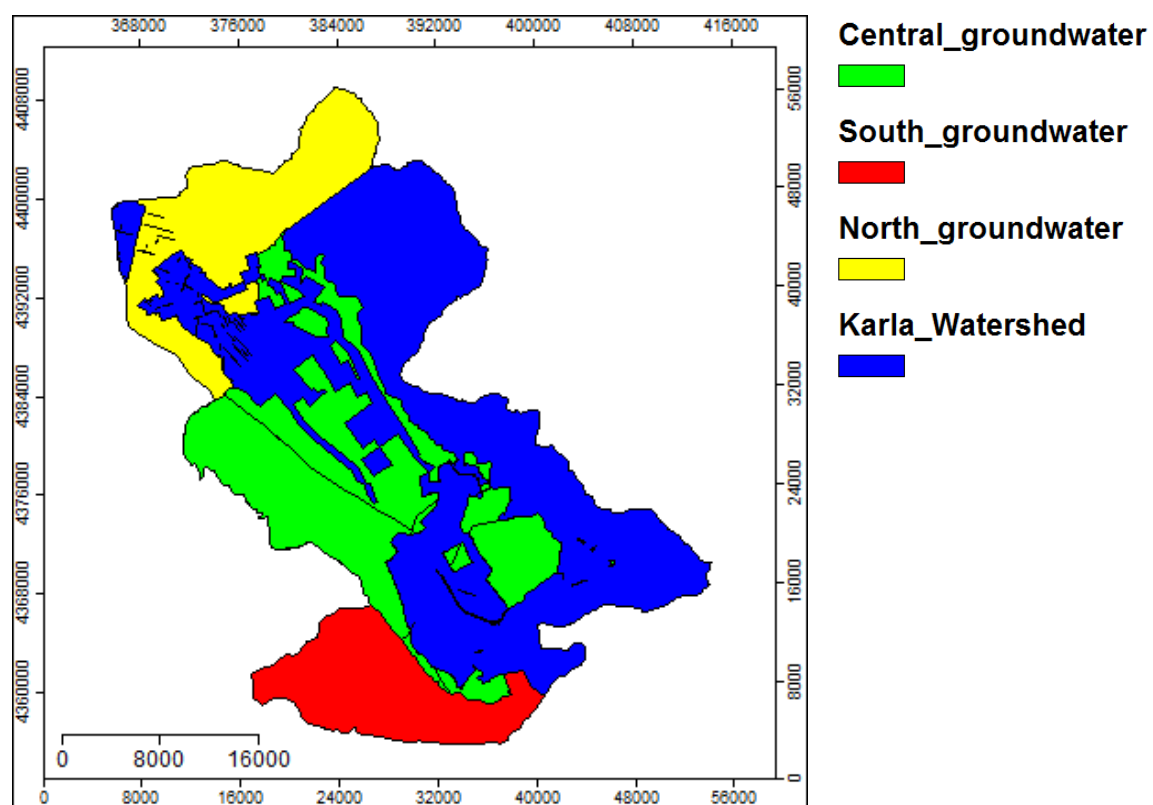


Figure 5.9. The groundwater network of Lake Karla Watershed.

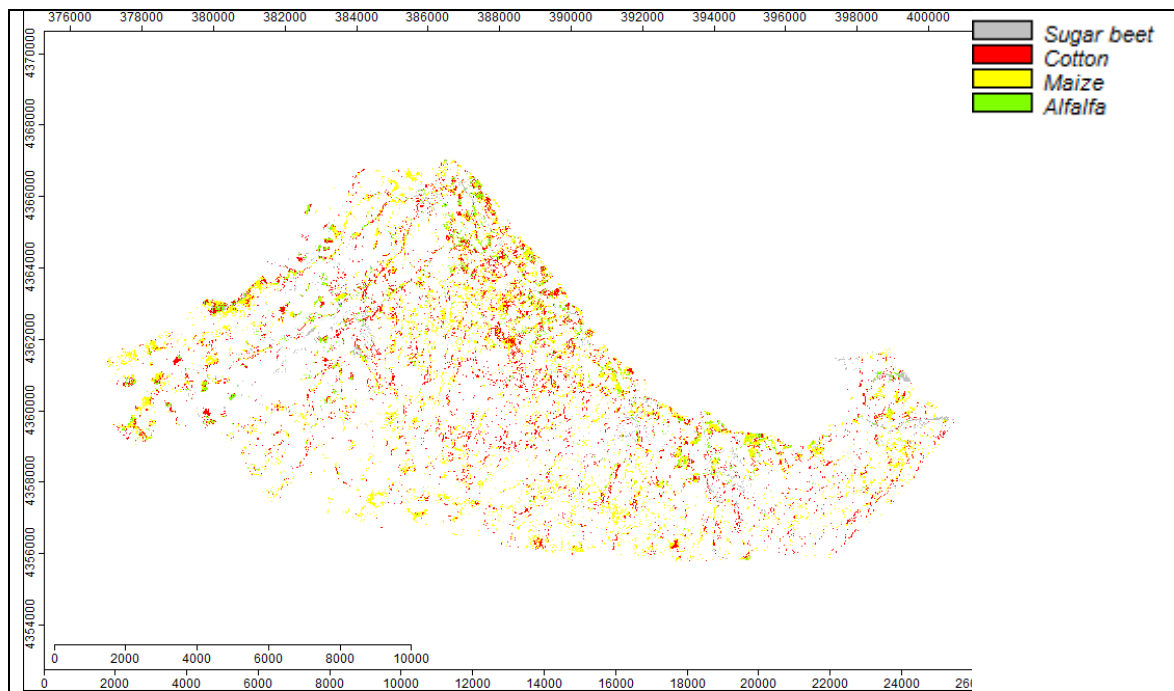


Figure 5.10. Classification of the south groundwater network of Lake Karla Watershed.

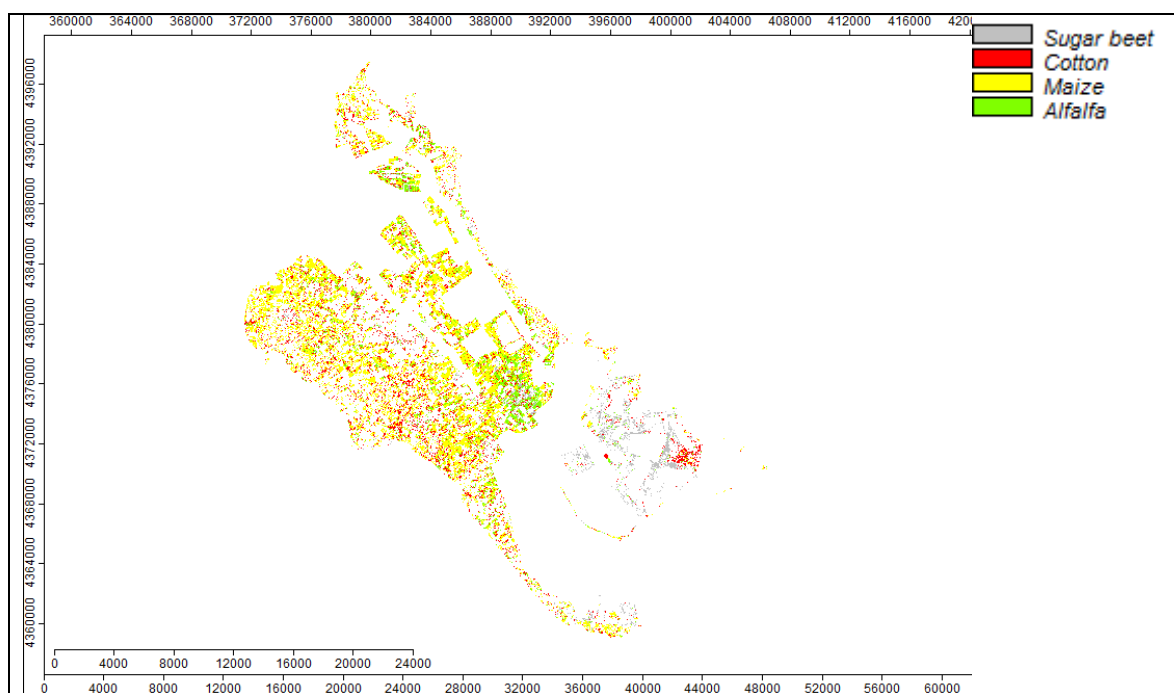


Figure 5.11. Classification of the central groundwater network of Lake Karla Watershed.

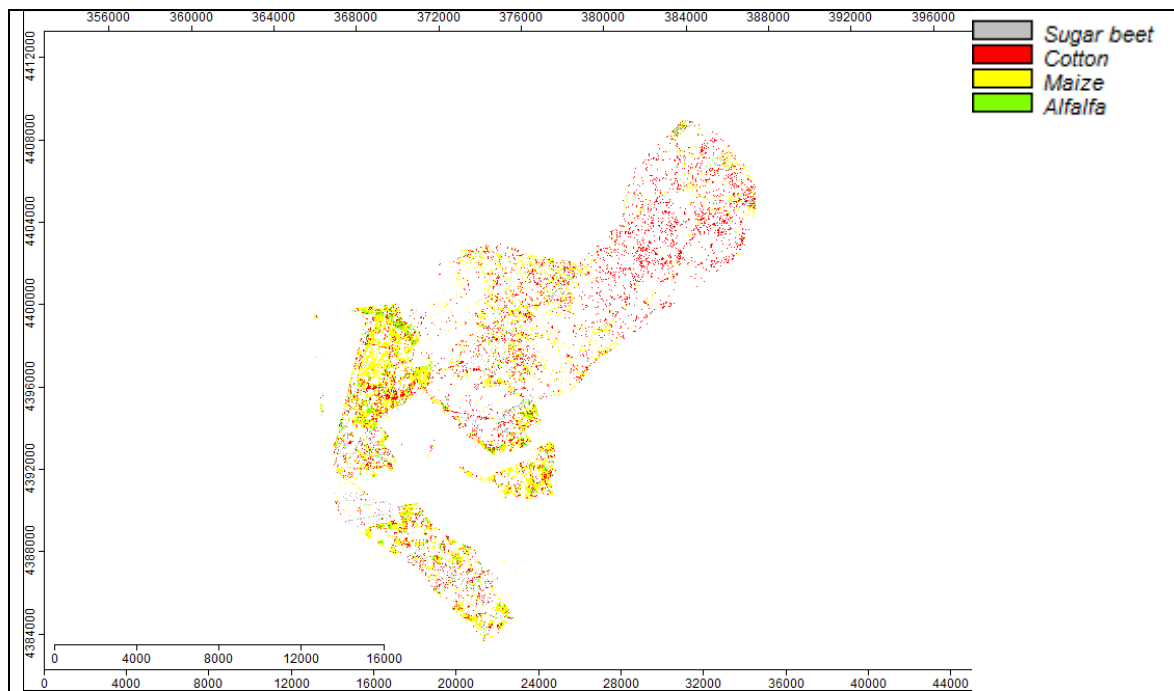


Figure 5.12. Classification of the north groundwater network of Lake Karla Watershed.

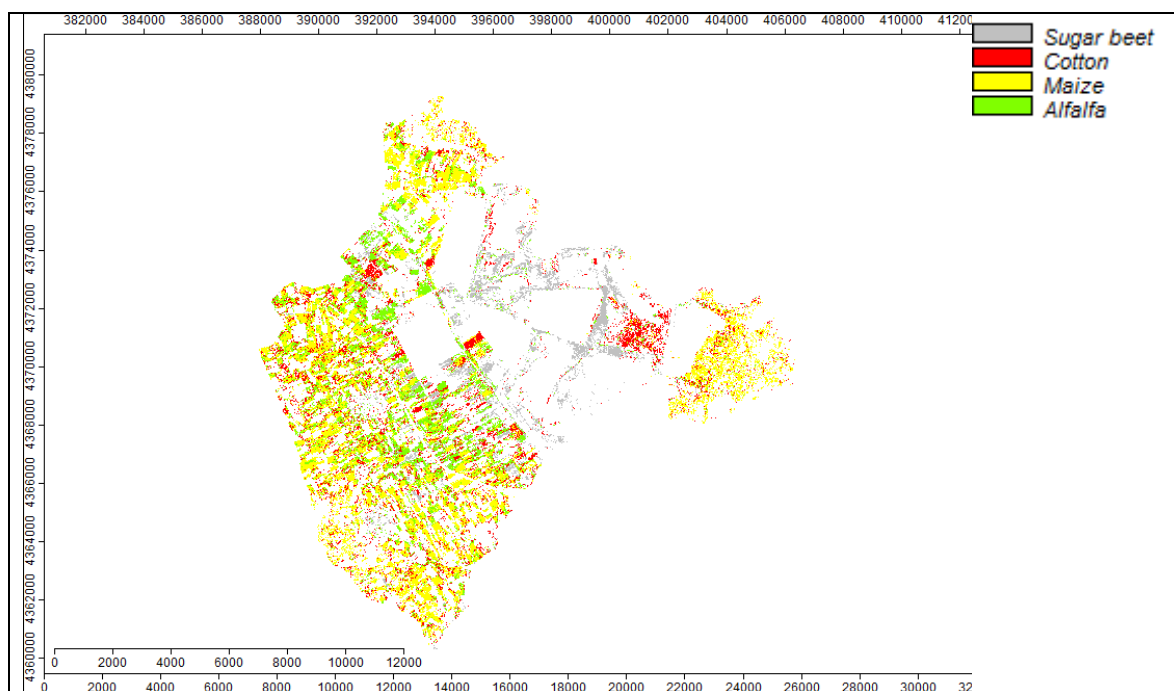


Figure 5.13. Classification of the new surface network of Lake Karla Watershed.

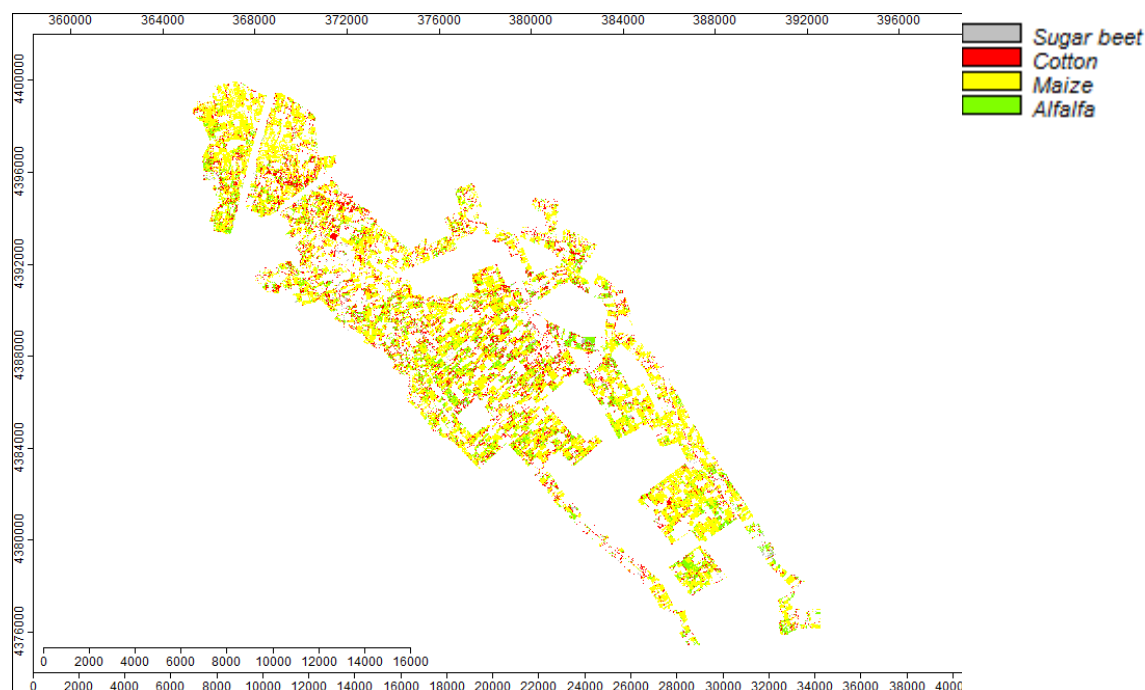


Figure 5.14. Classification of Pinios LALR surface network of Lake Karla Watershed.

#### 5.1.6 Irrigation requirements.

The CropWat model is now used for each zone and crop type for the growing season of 2007 giving total water needs for the growing season of 2007. CropWat model is operated as described at 2.8.1 and 4.5, where specific input files are generated. First of all, a file containing minimum and maximum temperature data, as well as humidity, wind and sun duration (or radiation) data for 2007 is generated after collecting all these data and put them in the appropriate format. Larissa file is shown at Figure 5.15.

Monthly ETo Penman-Monteith - C:\TASKS\SIRRIMED\CROPWAT\LARISSA.pem

Country  Station

Altitude  m. Latitude  °N Longitude  °E

Month	Min Temp °C	Max Temp °C	Humidity %	Wind km/day	Sun hours	Rad MJ/m <sup>2</sup> /day	ETo mm/day
January	0.5	9.6	79	104	2.1	5.6	0.75
February	1.5	11.8	74	138	3.1	8.2	1.21
March	3.4	14.9	74	138	3.9	11.5	1.75
April	6.3	20.0	70	138	6.3	17.1	2.81
May	10.8	25.7	64	138	7.5	20.4	3.99
June	15.0	30.9	53	173	8.7	22.7	5.49
July	17.6	33.0	50	181	9.9	24.0	6.15
August	17.1	32.4	50	173	9.7	22.2	5.69
September	14.1	28.7	59	147	7.5	16.6	3.96
October	9.8	22.1	71	121	4.7	10.5	2.15
November	5.5	16.0	80	78	3.4	7.0	1.07
December	1.8	10.9	83	78	1.9	4.9	0.68
Average	8.6	21.3	67	134	5.7	14.2	2.97

Figure 5.15. Meteorological data input for 2007.

Subsequently, a separate file containing rainfall data is produced and used as an input for CropWat (Figure 5.16).

	Rain	Eff rain
	mm	mm
January	29.7	28.3
February	34.9	33.0
March	36.3	34.2
April	28.9	27.6
May	37.1	34.9
June	23.5	22.6
July	20.3	19.6
August	15.5	15.1
September	29.4	28.0
October	47.1	43.6
November	58.2	52.8
December	52.3	47.9
Total	413.2	387.5

Figure 5.16. Rainfall data input for 2007 (Larissa).

The next file which is used as an input for CropWat is the “crop file”. A separate file for each crop and zone is needed. This file must contain the planting and harvest date which is inserted as an average value. It also contains phenological stage days (Papazafiriou, 1999), rooting depth (m), critical depletion (fraction), as well as yield response according to FAO methodology. Crop height (m) which has been already measured during the in-situ experimental days described later, can be added optionally. Of course, the most important input at this stage are the  $K_c$  values. These values are taken from the  $ET_rF$  values produced by METRIC as explained earlier. Distributed crop coefficient values with a 30 m x 30 m spatial resolution for every crop, and every stage is the input. It has to be mentioned that average  $K_c$  values for each crop and specific zones are finally utilized according to the previous classification. The stages (initial, development, mid-season and late-season) are well described at Table 2.12. These values are finally interpolated in time, in order to estimate the respective values for the appropriate days. CropWat model produce then an internal pattern similar with that illustrated at

Figure 2.10, in order to make the data processing possible (Figure 5.17). A soil data input is also needed according to FAO as shown at (Figure 5.18).

Finally, utilizing the already described (\*.pem) file, (\*.crc) file, (\*.cro) file, and (\*.soi) files (Figure 5.15, Figure 5.16, Figure 5.17, and Figure 5.18, respectively), CropWat provides, as an output, the crop water requirement file (Figure 5.19).

The above files are generated for every one of the five zones, and the total process is repeated again for the four crops under consideration resulting in twenty (20) different files. The results which are CropWat’s output are illustrated on Table 5.2.



Dry crop - C:\ProgramData\CROPWAT\data\crops\Cotton\_Volos\_1.CRO

Crop Name  Planting date  Harvest

	initial	development	mid-season	late season	total
<b>Kc Values</b>	0.63		1.04		0.55
<b>Stage (days)</b>	30	60	45	25	160
<b>Rooting depth (m)</b>	0.30			1.40	
<b>Critical depletion (fraction)</b>	0.65		0.65	0.90	
<b>Yield response f.</b>	0.20	0.50	0.50	0.25	0.85
<b>Cropheight (m)</b>			1.30 (optional)		

Figure 5.17. Crop file input for 2007.

Soil - C:\ProgramData\CROPWAT\data\soils\RED SANDY.SOI

Soil name

General soil data

Total available soil moisture (FC - WP)	<input type="text" value="100.0"/>	mm/meter
Maximum rain infiltration rate	<input type="text" value="30"/>	mm/day
Maximum rooting depth	<input type="text" value="900"/>	centimeters
Initial soil moisture depletion (as % TAM)	<input type="text" value="0"/>	%
Initial available soil moisture	<input type="text" value="100.0"/>	mm/meter

Figure 5.18. Soil file input for 2007.

ETo station		Larissa					
Rain station		Larisa					
Month	Decade	Stage	Kc	ETc	ETc	Eff rain	Irr. Req.
			coeff	mm/day	mm/dec	mm/dec	mm/dec
Apr	2	Init	0.63	2.24	18.0	0.0	18.0
Apr	3	Init	0.63	2.55	25.5	7.3	18.2
May	1	Init	0.63	3.05	30.5	0.6	29.9
May	2	Deve	0.65	3.47	34.7	13.7	20.9
May	3	Deve	0.72	3.86	42.4	22.9	19.5
Jun	1	Deve	0.78	4.15	41.5	17.1	24.4
Jun	2	Deve	0.84	5.00	50.0	4.1	45.9
Jun	3	Deve	0.91	6.17	61.7	0.0	61.7
Jul	1	Deve	0.97	5.62	56.2	0.0	56.2
Jul	2	Mid	1.00	5.74	57.4	0.0	57.4
Jul	3	Mid	1.00	5.59	61.5	0.0	61.5
Aug	1	Mid	1.00	4.83	48.3	17.3	31.1
Aug	2	Mid	1.00	4.84	48.4	0.0	48.4
Aug	3	Late	0.97	4.75	52.2	0.0	52.2
Sep	1	Late	0.78	2.88	28.8	13.7	15.1
Sep	2	Late	0.61	2.16	19.5	0.0	19.5

Figure 5.19. Crop water requirements output for 2007.

Table 5.2. New Surface Network irrigation requirements.

## a) Cotton

Month	Decade	Stage	Kc coeff	ETc mm/day	ETc mm/dec	Eff rain mm/dec	Irr. Req. mm/dec
Apr	2	Init	0.69	2.64	15.9	0.4	15.6
Apr	3	Init	0.69	3.09	30.9	1.2	29.7
May	1	Init	0.69	3.41	34.1	0	34.1
May	2	Deve	0.69	3.69	36.9	19.5	17.4
May	3	Deve	0.7	3.88	42.7	23.6	19
Jun	1	Deve	0.71	3.92	39.2	31.9	7.2
Jun	2	Deve	0.72	4.44	44.4	0.4	44
Jun	3	Deve	0.73	5.27	52.7	0	52.7
Jul	1	Deve	0.74	4.5	45	0	45
Jul	2	Mid	0.75	4.54	45.4	0	45.4
Jul	3	Mid	0.75	4.9	53.9	0	53.9
Aug	1	Mid	0.75	3.89	38.9	10.8	28.1
Aug	2	Mid	0.75	3.94	39.4	0	39.4
Aug	3	Late	0.74	3.54	38.9	0	38.9
Sep	1	Late	0.6	2.24	22.4	2	20.4
Sep	2	Late	0.44	1.48	14.8	2.4	12.4

Sep	3	Late	0.35	0.98	1	0.1	1
Total					596.3	92.3	504.1

## b) Sugar beet

Month	Decade	Stage	Kc coeff	ETc mm/day	ETc mm/dec	Eff rain mm/dec	Irr. Req. mm/dec
Apr	1	Init	0.3	0.99	9.9	3.7	6.2
Apr	2	Init	0.3	1.15	11.5	0.6	10.9
Apr	3	Init	0.3	1.34	13.4	1.2	12.2
May	1	Deve	0.35	1.71	17.1	0	17.1
May	2	Deve	0.43	2.29	22.9	19.5	3.4
May	3	Deve	0.52	2.87	31.6	23.6	7.9
Jun	1	Deve	0.61	3.34	33.4	31.9	1.5
Jun	2	Mid	0.67	4.14	41.4	0.4	41
Jun	3	Mid	0.68	4.89	48.9	0	48.9
Jul	1	Mid	0.68	4.12	41.2	0	41.2
Jul	2	Mid	0.68	4.12	41.2	0	41.2
Jul	3	Mid	0.68	4.44	48.8	0	48.8
Aug	1	Mid	0.68	3.53	35.3	10.8	24.5
Aug	2	Mid	0.68	3.57	35.7	0	35.7
Aug	3	Mid	0.68	3.27	35.9	0	35.9
Sep	1	Mid	0.68	2.54	25.4	2	23.4
Sep	2	Late	0.62	2.09	20.9	2.4	18.6
Sep	3	Late	0.48	1.34	9.4	1	8
Total					523.9	97.1	426.3

## c) Maize

Month	Decade	Stage	Kc coeff	ETc mm/day	ETc mm/dec	Eff rain mm/dec	Irr. Req. mm/dec
May	1	Init	0.6	2.97	29.7	0	29.7
May	2	Init	0.6	3.2	32	19.5	12.5
May	3	Deve	0.61	3.38	37.2	23.6	13.5
Jun	1	Deve	0.67	3.68	36.8	31.9	4.8
Jun	2	Deve	0.73	4.48	44.8	0.4	44.4
Jun	3	Deve	0.79	5.68	56.8	0	56.8
Jul	1	Mid	0.84	5.06	50.6	0	50.6
Jul	2	Mid	0.84	5.08	50.8	0	50.8
Jul	3	Mid	0.84	5.48	60.3	0	60.3
Aug	1	Mid	0.84	4.36	43.6	10.8	32.8
Aug	2	Mid	0.84	4.41	44.1	0	44.1

Aug	3	Mid	0.84	4.04	44.4	0	44.4
Sep	1	Late	0.79	2.96	29.6	2	27.6
Sep	2	Late	0.66	2.22	22.2	2.4	19.9
Sep	3	Late	0.54	1.52	10.6	1	9.2
Total					593.3	91.6	501.3

## d) Alfalfa

Month	Decade	Stage	Kc coeff	ETc mm/day	ETc mm/dec	Eff rain mm/dec	Irr. Req. mm/dec
Apr	1	Init	0.6	1.47	14.7	9.5	5.2
Apr	2	Init	0.6	1.68	16.8	8.5	8.3
Apr	3	Init	0.6	1.92	19.2	9.6	9.6
May	1	Init	0.6	2.16	21.6	11.4	10.2
May	2	Init	0.6	2.4	24	12.5	11.4
May	3	Init	0.6	2.7	29.7	10.9	18.8
Jun	1	Init	0.6	3	30	8.6	21.3
Jun	2	Init	0.6	3.3	33	7.1	25.8
Jun	3	Init	0.6	3.43	34.3	6.9	27.3
Jul	1	Init	0.6	3.6	36	6.9	29
Jul	2	Init	0.6	3.75	37.5	6.6	30.9
Jul	3	Init	0.6	3.64	40	6.1	33.9
Aug	1	Init	0.6	3.54	35.4	5	30.4
Aug	2	Init	0.6	3.47	34.7	4.2	30.5
Aug	3	Deve	0.6	3.13	34.5	5.9	28.5
Sep	1	Deve	0.68	3.06	30.6	7.8	22.8
Sep	2	Deve	0.76	3.02	30.2	9.2	21
Sep	3	Mid	0.85	2.84	28.4	11	17.4
Oct	1	Mid	0.87	2.38	23.8	13	10.9
Oct	2	Mid	0.87	1.86	18.6	14.8	3.8
Oct	3	Mid	0.87	1.55	17	15.7	1.3
Nov	1	Mid	0.87	1.24	12.4	17	0
Nov	2	Mid	0.87	0.92	9.2	18.2	0
Nov	3	Mid	0.87	0.81	8.1	17.5	0
Dec	1	Mid	0.87	0.7	7	16.9	0
Dec	2	Mid	0.87	0.59	5.9	16.6	0
Dec	3	Mid	0.87	0.61	6.7	14.2	0
Jan	1	Mid	0.87	0.63	6.3	10.9	0
Jan	2	Mid	0.87	0.65	6.5	8.3	0
Jan	3	Mid	0.87	0.78	8.6	9.2	0
Feb	1	Mid	0.87	0.91	9.1	10.5	0
Feb	2	Mid	0.87	1.05	10.5	11.1	0
Feb	3	Late	0.86	1.19	9.5	11.2	0

Mar	1	Late	0.79	1.24	12.4	11.5	0.9
Mar	2	Late	0.71	1.24	12.4	11.7	0.6
Mar	3	Late	0.63	1.31	14.5	10.9	3.6
Total					729.1	387.3	403.6

Table 5.3. Pinios LALR Network irrigation requirements

## a) Cotton

Month	Decade	Stage	Kc coeff	ETc mm/day	ETc mm/dec	Eff rain mm/dec	Irr. Req. mm/dec
Apr	2	Init	0.59	2.26	13.6	0.4	13.3
Apr	3	Init	0.59	2.64	26.4	1.2	25.2
May	1	Init	0.59	2.92	29.2	0	29.2
May	2	Deve	0.6	3.18	31.8	19.5	12.2
May	3	Deve	0.62	3.45	37.9	23.6	14.3
Jun	1	Deve	0.65	3.59	35.9	31.9	4
Jun	2	Deve	0.68	4.19	41.9	0.4	41.5
Jun	3	Deve	0.71	5.12	51.2	0	51.2
Jul	1	Deve	0.74	4.47	44.7	0	44.7
Jul	2	Mid	0.76	4.6	46	0	46
Jul	3	Mid	0.76	4.96	54.6	0	54.6
Aug	1	Mid	0.76	3.94	39.4	10.8	28.7
Aug	2	Mid	0.76	3.99	39.9	0	39.9
Aug	3	Late	0.75	3.59	39.4	0	39.4
Sep	1	Late	0.61	2.28	22.8	2	20.8
Sep	2	Late	0.45	1.53	15.3	2.4	12.9
Sep	3	Late	0.37	1.02	1	0.1	1
Total					571.1	92.3	478.9

## b) Sugar beet

Month	Decade	Stage	Kc coeff	ETc mm/day	ETc mm/dec	Eff rain mm/dec	Irr. Req. mm/dec
Apr	1	Init	0.3	0.99	9.9	3.7	6.2
Apr	2	Init	0.3	1.15	11.5	0.6	10.9
Apr	3	Init	0.3	1.34	13.4	1.2	12.2
May	1	Deve	0.35	1.73	17.3	0	17.3
May	2	Deve	0.44	2.35	23.5	19.5	4
May	3	Deve	0.54	2.96	32.6	23.6	9

Jun	1	Deve	0.63	3.47	34.7	31.9	2.8
Jun	2	Mid	0.7	4.33	43.3	0.4	42.9
Jun	3	Mid	0.71	5.11	51.1	0	51.1
Jul	1	Mid	0.71	4.3	43	0	43
Jul	2	Mid	0.71	4.3	43	0	43
Jul	3	Mid	0.71	4.63	50.9	0	50.9
Aug	1	Mid	0.71	3.68	36.8	10.8	26
Aug	2	Mid	0.71	3.72	37.2	0	37.2
Aug	3	Mid	0.71	3.41	37.5	0	37.5
Sep	1	Mid	0.71	2.65	26.5	2	24.5
Sep	2	Late	0.64	2.17	21.7	2.4	19.3
Sep	3	Late	0.49	1.35	9.5	1	8.1
Total					543.5	97.1	445.9

## c) Maize

Month	Decade	Stage	Kc coeff	ETc mm/day	ETc mm/dec	Eff rain mm/dec	Irr. Req. mm/dec
May	1	Init	0.56	2.77	27.7	0	27.7
May	2	Init	0.56	2.98	29.8	19.5	10.3
May	3	Deve	0.57	3.17	34.8	23.6	11.2
Jun	1	Deve	0.64	3.52	35.2	31.9	3.2
Jun	2	Deve	0.71	4.36	43.6	0.4	43.2
Jun	3	Deve	0.78	5.62	56.2	0	56.2
Jul	1	Mid	0.84	5.06	50.6	0	50.6
Jul	2	Mid	0.84	5.08	50.8	0	50.8
Jul	3	Mid	0.84	5.48	60.3	0	60.3
Aug	1	Mid	0.84	4.36	43.6	10.8	32.8
Aug	2	Mid	0.84	4.41	44.1	0	44.1
Aug	3	Mid	0.84	4.04	44.4	0	44.4
Sep	1	Late	0.81	3.01	30.1	2	28.1
Sep	2	Late	0.71	2.41	24.1	2.4	21.7
Sep	3	Late	0.63	1.76	12.3	1	10.9
Total					587.6	91.6	495.6

## d) Alfalfa

Month	Decade	Stage	Kc coeff	ETc mm/day	ETc mm/dec	Eff rain mm/dec	Irr. Req. mm/dec
Apr	1	Init	0.6	1.47	14.7	9.5	5.2
Apr	2	Init	0.6	1.68	16.8	8.5	8.3
Apr	3	Init	0.6	1.92	19.2	9.6	9.6

May	1	Init	0.6	2.16	21.6	11.4	10.2
May	2	Init	0.6	2.4	24	12.5	11.4
May	3	Init	0.6	2.7	29.7	10.9	18.8
Jun	1	Init	0.6	3	30	8.6	21.3
Jun	2	Init	0.6	3.3	33	7.1	25.8
Jun	3	Init	0.6	3.43	34.3	6.9	27.3
Jul	1	Init	0.6	3.6	36	6.9	29
Jul	2	Init	0.6	3.75	37.5	6.6	30.9
Jul	3	Init	0.6	3.64	40	6.1	33.9
Aug	1	Init	0.6	3.54	35.4	5	30.4
Aug	2	Init	0.6	3.47	34.7	4.2	30.5
Aug	3	Deve	0.6	3.13	34.5	5.9	28.5
Sep	1	Deve	0.68	3.06	30.6	7.8	22.8
Sep	2	Deve	0.76	3.02	30.2	9.2	21
Sep	3	Mid	0.85	2.84	28.4	11	17.4
Oct	1	Mid	0.87	2.38	23.8	13	10.9
Oct	2	Mid	0.87	1.86	18.6	14.8	3.8
Oct	3	Mid	0.87	1.55	17	15.7	1.3
Nov	1	Mid	0.87	1.24	12.4	17	0
Nov	2	Mid	0.87	0.92	9.2	18.2	0
Nov	3	Mid	0.87	0.81	8.1	17.5	0
Dec	1	Mid	0.87	0.7	7	16.9	0
Dec	2	Mid	0.87	0.59	5.9	16.6	0
Dec	3	Mid	0.87	0.61	6.7	14.2	0
Jan	1	Mid	0.87	0.63	6.3	10.9	0
Jan	2	Mid	0.87	0.65	6.5	8.3	0
Jan	3	Mid	0.87	0.78	8.6	9.2	0
Feb	1	Mid	0.87	0.91	9.1	10.5	0
Feb	2	Mid	0.87	1.05	10.5	11.1	0
Feb	3	Late	0.86	1.19	9.5	11.2	0
Mar	1	Late	0.82	1.28	12.8	11.5	1.3
Mar	2	Late	0.77	1.34	13.4	11.7	1.6
Mar	3	Late	0.71	1.49	16.4	10.9	5.5
Total					732.5	387.3	407

Table 5.4. South groundwater Network irrigation requirements

## a) Cotton

Month	Decade	Stage	Kc coeff	ETc mm/day	ETc mm/dec	Eff rain mm/dec	Irr. Req. mm/dec
Apr	2	Init	0.73	2.8	22.4	0.5	21.8
Apr	3	Init	0.73	3.27	32.7	1.2	31.5

May	1	Init	0.73	3.61	36.1	0	36.1
May	2	Deve	0.73	3.88	38.8	19.5	19.2
May	3	Deve	0.72	3.97	43.7	23.6	20.1
Jun	1	Deve	0.71	3.91	39.1	31.9	7.1
Jun	2	Deve	0.7	4.32	43.2	0.4	42.8
Jun	3	Deve	0.69	5	50	0	50
Jul	1	Deve	0.69	4.16	41.6	0	41.6
Jul	2	Mid	0.68	4.14	41.4	0	41.4
Jul	3	Mid	0.68	4.46	49	0	49
Aug	1	Mid	0.68	3.54	35.4	10.8	24.7
Aug	2	Mid	0.68	3.58	35.8	0	35.8
Aug	3	Late	0.66	3.17	34.8	0	34.8
Sep	1	Late	0.54	2.01	20.1	2	18.1
Sep	2	Late	0.42	1.41	12.7	2.1	10.3
Total					576.8	92.1	484.4

## b) Sugar beet

Month	Decade	Stage	Kc coeff	ETc mm/day	ETc mm/dec	Eff rain mm/dec	Irr. Req. mm/dec
Apr	1	Init	0.3	0.99	9.9	3.7	6.2
Apr	2	Init	0.3	1.15	11.5	0.6	10.9
Apr	3	Init	0.3	1.34	13.4	1.2	12.2
May	1	Deve	0.33	1.64	16.4	0	16.4
May	2	Deve	0.39	2.07	20.7	19.5	1.2
May	3	Deve	0.45	2.49	27.3	23.6	3.7
Jun	1	Deve	0.51	2.81	28.1	31.9	0
Jun	2	Mid	0.56	3.42	34.2	0.4	33.8
Jun	3	Mid	0.56	4.03	40.3	0	40.3
Jul	1	Mid	0.56	3.39	33.9	0	33.9
Jul	2	Mid	0.56	3.39	33.9	0	33.9
Jul	3	Mid	0.56	3.65	40.2	0	40.2
Aug	1	Mid	0.56	2.9	29	10.8	18.3
Aug	2	Mid	0.56	2.94	29.4	0	29.4
Aug	3	Mid	0.56	2.69	29.6	0	29.6
Sep	1	Mid	0.56	2.09	20.9	2	18.9
Sep	2	Late	0.53	1.79	17.9	2.4	15.5
Sep	3	Late	0.46	1.27	8.9	1	7.5
Total					445.4	97.1	351.7



## c) Maize

Month	Decade	Stage	Kc coeff	ETc mm/day	ETc mm/dec	Eff rain mm/dec	Irr. Req. mm/dec
May	1	Init	0.74	3.66	36.6	0	36.6
May	2	Init	0.74	3.94	39.4	19.5	19.9
May	3	Deve	0.73	4.05	44.5	23.6	20.9
Jun	1	Deve	0.7	3.83	38.3	31.9	6.3
Jun	2	Deve	0.66	4.05	40.5	0.4	40.1
Jun	3	Deve	0.62	4.47	44.7	0	44.7
Jul	1	Mid	0.59	3.58	35.8	0	35.8
Jul	2	Mid	0.59	3.57	35.7	0	35.7
Jul	3	Mid	0.59	3.85	42.3	0	42.3
Aug	1	Mid	0.59	3.06	30.6	10.8	19.8
Aug	2	Mid	0.59	3.09	30.9	0	30.9
Aug	3	Mid	0.59	2.83	31.2	0	31.2
Sep	1	Late	0.56	2.08	20.8	2	18.8
Sep	2	Late	0.47	1.58	15.8	2.4	13.4
Sep	3	Late	0.39	1.09	7.6	1	6.2
Total					494.9	91.6	402.9

## d) Alfalfa

Month	Decade	Stage	Kc coeff	ETc mm/day	ETc mm/dec	Eff rain mm/dec	Irr. Req. mm/dec
Apr	1	Init	0.7	1.72	17.2	9.5	7.7
Apr	2	Init	0.7	1.96	19.6	8.5	11.1
Apr	3	Init	0.7	2.24	22.4	9.6	12.8
May	1	Init	0.7	2.52	25.2	11.4	13.8
May	2	Init	0.7	2.8	28	12.5	15.4
May	3	Init	0.7	3.15	34.6	10.9	23.7
Jun	1	Init	0.7	3.5	35	8.6	26.3
Jun	2	Init	0.7	3.85	38.5	7.1	31.3
Jun	3	Init	0.7	4	40	6.9	33
Jul	1	Init	0.7	4.2	42	6.9	35
Jul	2	Init	0.7	4.37	43.7	6.6	37.1
Jul	3	Init	0.7	4.24	46.7	6.1	40.6
Aug	1	Init	0.7	4.14	41.4	5	36.3
Aug	2	Init	0.7	4.05	40.5	4.2	36.3
Aug	3	Deve	0.7	3.63	39.9	5.9	34
Sep	1	Deve	0.7	3.19	31.9	7.8	24.1

Sep	2	Deve	0.71	2.81	28.1	9.2	18.9
Sep	3	Mid	0.72	2.4	24	11	13
Oct	1	Mid	0.72	1.97	19.7	13	6.7
Oct	2	Mid	0.72	1.54	15.4	14.8	0.6
Oct	3	Mid	0.72	1.28	14.1	15.7	0
Nov	1	Mid	0.72	1.02	10.2	17	0
Nov	2	Mid	0.72	0.76	7.6	18.2	0
Nov	3	Mid	0.72	0.67	6.7	17.5	0
Dec	1	Mid	0.72	0.58	5.8	16.9	0
Dec	2	Mid	0.72	0.49	4.9	16.6	0
Dec	3	Mid	0.72	0.5	5.5	14.2	0
Jan	1	Mid	0.72	0.52	5.2	10.9	0
Jan	2	Mid	0.72	0.54	5.4	8.3	0
Jan	3	Mid	0.72	0.65	7.1	9.2	0
Feb	1	Mid	0.72	0.76	7.6	10.5	0
Feb	2	Mid	0.72	0.86	8.6	11.1	0
Feb	3	Late	0.71	0.98	7.8	11.2	0
Mar	1	Late	0.64	1	10	11.5	0
Mar	2	Late	0.56	0.98	9.8	11.7	0
Mar	3	Late	0.48	1	11	10.9	0.1
Total					761	387.3	457.9

Table 5.5. Central groundwater Network irrigation requirements

## a) Cotton

Month	Decade	Stage	Kc coeff	ETc mm/day	ETc mm/dec	Eff rain mm/dec	Irr. Req. mm/dec
Apr	2	Init	0.63	2.41	19.3	0.5	18.7
Apr	3	Init	0.63	2.82	28.2	1.2	27
May	1	Init	0.63	3.12	31.2	0	31.2
May	2	Deve	0.64	3.4	34	19.5	14.4
May	3	Deve	0.66	3.64	40	23.6	16.4
Jun	1	Deve	0.68	3.74	37.4	31.9	5.4
Jun	2	Deve	0.7	4.3	43	0.4	42.6
Jun	3	Deve	0.72	5.19	51.9	0	51.9
Jul	1	Deve	0.74	4.49	44.9	0	44.9
Jul	2	Mid	0.75	4.56	45.6	0	45.6
Jul	3	Mid	0.75	4.91	54.1	0	54.1
Aug	1	Mid	0.75	3.91	39.1	10.8	28.3
Aug	2	Mid	0.75	3.95	39.5	0	39.5
Aug	3	Late	0.74	3.54	38.9	0	38.9
Sep	1	Late	0.65	2.43	24.3	2	22.3

Sep	2	Late	0.56	1.9	17.1	2.1	14.8
Total					588.5	92.1	496

## b) Sugar beet

Month	Decade	Stage	Kc coeff	ETc mm/day	ETc mm/dec	Eff rain mm/dec	Irr. Req. mm/dec
Apr	1	Init	0.3	0.99	9.9	3.7	6.2
Apr	2	Init	0.3	1.15	11.5	0.6	10.9
Apr	3	Init	0.3	1.34	13.4	1.2	12.2
May	1	Deve	0.33	1.64	16.4	0	16.4
May	2	Deve	0.39	2.07	20.7	19.5	1.2
May	3	Deve	0.45	2.49	27.3	23.6	3.7
Jun	1	Deve	0.51	2.81	28.1	31.9	0
Jun	2	Mid	0.56	3.42	34.2	0.4	33.8
Jun	3	Mid	0.56	4.03	40.3	0	40.3
Jul	1	Mid	0.56	3.39	33.9	0	33.9
Jul	2	Mid	0.56	3.39	33.9	0	33.9
Jul	3	Mid	0.56	3.65	40.2	0	40.2
Aug	1	Mid	0.56	2.9	29	10.8	18.3
Aug	2	Mid	0.56	2.94	29.4	0	29.4
Aug	3	Mid	0.56	2.69	29.6	0	29.6
Sep	1	Mid	0.56	2.09	20.9	2	18.9
Sep	2	Late	0.52	1.77	17.7	2.4	15.3
Sep	3	Late	0.44	1.23	8.6	1	7.2
Total					444.9	97.1	351.3

## c) Maize

Month	Decade	Stage	Kc coeff	ETc mm/day	ETc mm/dec	Eff rain mm/dec	Irr. Req. mm/dec
May	1	Init	0.58	2.87	28.7	0	28.7
May	2	Init	0.58	3.09	30.9	19.5	11.4
May	3	Deve	0.59	3.26	35.9	23.6	12.2
Jun	1	Deve	0.64	3.53	35.3	31.9	3.4
Jun	2	Deve	0.7	4.29	42.9	0.4	42.5
Jun	3	Deve	0.75	5.42	54.2	0	54.2
Jul	1	Mid	0.8	4.82	48.2	0	48.2
Jul	2	Mid	0.8	4.84	48.4	0	48.4
Jul	3	Mid	0.8	5.22	57.4	0	57.4
Aug	1	Mid	0.8	4.15	41.5	10.8	30.7
Aug	2	Mid	0.8	4.2	42	0	42
Aug	3	Mid	0.8	3.84	42.3	0	42.3

Sep	1	Late	0.76	2.86	28.6	2	26.6
Sep	2	Late	0.67	2.25	22.5	2.4	20.2
Sep	3	Late	0.58	1.63	11.4	1	10
Total					570.2	91.6	478.1

## d) Alfalfa

Month	Decade	Stage	Kc coeff	ETc mm/day	ETc mm/dec	Eff rain mm/dec	Irr. Req. mm/dec
Apr	1	Init	0.6	1.47	14.7	9.5	5.2
Apr	2	Init	0.6	1.68	16.8	8.5	8.3
Apr	3	Init	0.6	1.92	19.2	9.6	9.6
May	1	Init	0.6	2.16	21.6	11.4	10.2
May	2	Init	0.6	2.4	24	12.5	11.4
May	3	Init	0.6	2.7	29.7	10.9	18.8
Jun	1	Init	0.6	3	30	8.6	21.3
Jun	2	Init	0.6	3.3	33	7.1	25.8
Jun	3	Init	0.6	3.43	34.3	6.9	27.3
Jul	1	Init	0.6	3.6	36	6.9	29
Jul	2	Init	0.6	3.75	37.5	6.6	30.9
Jul	3	Init	0.6	3.64	40	6.1	33.9
Aug	1	Init	0.6	3.54	35.4	5	30.4
Aug	2	Init	0.6	3.47	34.7	4.2	30.5
Aug	3	Deve	0.6	3.13	34.4	5.9	28.4
Sep	1	Deve	0.66	2.97	29.7	7.8	21.9
Sep	2	Deve	0.72	2.85	28.5	9.2	19.3
Sep	3	Mid	0.78	2.62	26.2	11	15.2
Oct	1	Mid	0.8	2.19	21.9	13	8.9
Oct	2	Mid	0.8	1.71	17.1	14.8	2.3
Oct	3	Mid	0.8	1.42	15.7	15.7	0
Nov	1	Mid	0.8	1.14	11.4	17	0
Nov	2	Mid	0.8	0.85	8.5	18.2	0
Nov	3	Mid	0.8	0.75	7.5	17.5	0
Dec	1	Mid	0.8	0.64	6.4	16.9	0
Dec	2	Mid	0.8	0.54	5.4	16.6	0
Dec	3	Mid	0.8	0.56	6.2	14.2	0
Jan	1	Mid	0.8	0.58	5.8	10.9	0
Jan	2	Mid	0.8	0.6	6	8.3	0
Jan	3	Mid	0.8	0.72	7.9	9.2	0
Feb	1	Mid	0.8	0.84	8.4	10.5	0
Feb	2	Mid	0.8	0.96	9.6	11.1	0
Feb	3	Late	0.79	1.1	8.8	11.2	0
Mar	1	Late	0.76	1.19	11.9	11.5	0.4

Mar	2	Late	0.72	1.25	12.5	11.7	0.8
Mar	3	Late	0.68	1.42	15.6	10.9	4.7
Total					712.2	387.3	394.8

Table 5.6. North groundwater Network irrigation requirements

## a) Cotton

Month	Decade	Stage	Kc coeff	ETc mm/day	ETc mm/dec	Eff rain mm/dec	Irr. Req. mm/dec
Apr	2	Init	0.63	2.24	18	0	18
Apr	3	Init	0.63	2.55	25.5	7.3	18.2
May	1	Init	0.63	3.05	30.5	0.6	29.9
May	2	Deve	0.65	3.47	34.7	13.7	20.9
May	3	Deve	0.72	3.86	42.4	22.9	19.5
Jun	1	Deve	0.78	4.15	41.5	17.1	24.4
Jun	2	Deve	0.84	5	50	4.1	45.9
Jun	3	Deve	0.91	6.17	61.7	0	61.7
Jul	1	Deve	0.97	5.62	56.2	0	56.2
Jul	2	Mid	1	5.74	57.4	0	57.4
Jul	3	Mid	1	5.59	61.5	0	61.5
Aug	1	Mid	1	4.83	48.3	17.3	31.1
Aug	2	Mid	1	4.84	48.4	0	48.4
Aug	3	Late	0.97	4.75	52.2	0	52.2
Sep	1	Late	0.78	2.88	28.8	13.6	15.2
Sep	2	Late	0.61	2.16	19.5	0	19.5
Total					676.8	96.6	580.2

## b) Sugar beet

Month	Decade	Stage	Kc coeff	ETc mm/day	ETc mm/dec	Eff rain mm/dec	Irr. Req. mm/dec
Apr	1	Init	0.3	0.99	9.9	9.2	0.7
Apr	2	Init	0.3	1.07	10.7	0	10.7
Apr	3	Init	0.3	1.22	12.2	7.3	4.8
May	1	Deve	0.38	1.84	18.4	0.6	17.8
May	2	Deve	0.52	2.78	27.8	13.7	14
May	3	Deve	0.67	3.62	39.9	22.9	16.9
Jun	1	Deve	0.82	4.37	43.7	17.1	26.6
Jun	2	Mid	0.94	5.56	55.6	4.1	51.5
Jun	3	Mid	0.95	6.44	64.4	0	64.4

Jul	1	Mid	0.95	5.5	55	0	55
Jul	2	Mid	0.95	5.42	54.2	0	54.2
Jul	3	Mid	0.95	5.28	58.1	0	58.1
Aug	1	Mid	0.95	4.56	45.6	17.3	28.4
Aug	2	Mid	0.95	4.57	45.7	0	45.7
Aug	3	Mid	0.95	4.65	51.1	0	51.1
Sep	1	Mid	0.95	3.47	34.7	13.6	21.2
Sep	2	Late	0.82	2.92	29.2	0	29.2
Sep	3	Late	0.52	1.55	10.9	2.3	7.5
Total					666.9	108.1	557.8

## c) Maize

Month	Decade	Stage	Kc coeff	ETc mm/day	ETc mm/dec	Eff rain mm/dec	Irr. Req. mm/dec
May	1	Init	0.73	3.54	35.4	0.6	34.8
May	2	Init	0.73	3.88	38.8	13.7	25.1
May	3	Deve	0.73	3.95	43.5	22.9	20.6
Jun	1	Deve	0.75	3.99	39.9	17.1	22.8
Jun	2	Deve	0.77	4.58	45.8	4.1	41.7
Jun	3	Deve	0.79	5.39	53.9	0	53.9
Jul	1	Mid	0.81	4.69	46.9	0	46.9
Jul	2	Mid	0.81	4.63	46.3	0	46.3
Jul	3	Mid	0.81	4.51	49.6	0	49.6
Aug	1	Mid	0.81	3.9	39	17.3	21.7
Aug	2	Mid	0.81	3.91	39.1	0	39.1
Aug	3	Mid	0.81	3.97	43.7	0	43.7
Sep	1	Late	0.79	2.9	29	13.6	15.4
Sep	2	Late	0.74	2.64	26.4	0	26.4
Sep	3	Late	0.7	2.1	14.7	2.3	11.4
Total					592.1	91.7	499.5

## d) Alfalfa

Month	Decade	Stage	Kc coeff	ETc mm/day	ETc mm/dec	Eff rain mm/dec	Irr. Req. mm/dec
Apr	1	Init	0.6	1.47	14.7	9.5	5.2
Apr	2	Init	0.6	1.68	16.8	8.5	8.3
Apr	3	Init	0.6	1.92	19.2	9.6	9.6
May	1	Init	0.6	2.16	21.6	11.4	10.2
May	2	Init	0.6	2.4	24	12.5	11.4
May	3	Init	0.6	2.7	29.7	10.9	18.8
Jun	1	Init	0.6	3	30	8.6	21.3

Jun	2	Init	0.6	3.3	33	7.1	25.8
Jun	3	Init	0.6	3.43	34.3	6.9	27.3
Jul	1	Init	0.6	3.6	36	6.9	29
Jul	2	Init	0.6	3.75	37.5	6.6	30.9
Jul	3	Init	0.6	3.64	40	6.1	33.9
Aug	1	Init	0.6	3.54	35.4	5	30.4
Aug	2	Init	0.6	3.47	34.7	4.2	30.5
Aug	3	Deve	0.6	3.12	34.4	5.9	28.4
Sep	1	Deve	0.65	2.96	29.6	7.8	21.8
Sep	2	Deve	0.71	2.83	28.3	9.2	19
Sep	3	Mid	0.77	2.59	25.9	11	14.9
Oct	1	Mid	0.79	2.16	21.6	13	8.7
Oct	2	Mid	0.79	1.69	16.9	14.8	2.1
Oct	3	Mid	0.79	1.41	15.5	15.7	0
Nov	1	Mid	0.79	1.12	11.2	17	0
Nov	2	Mid	0.79	0.84	8.4	18.2	0
Nov	3	Mid	0.79	0.74	7.4	17.5	0
Dec	1	Mid	0.79	0.64	6.4	16.9	0
Dec	2	Mid	0.79	0.53	5.3	16.6	0
Dec	3	Mid	0.79	0.55	6.1	14.2	0
Jan	1	Mid	0.79	0.57	5.7	10.9	0
Jan	2	Mid	0.79	0.59	5.9	8.3	0
Jan	3	Mid	0.79	0.71	7.8	9.2	0
Feb	1	Mid	0.79	0.83	8.3	10.5	0
Feb	2	Mid	0.79	0.95	9.5	11.1	0
Feb	3	Late	0.78	1.08	8.7	11.2	0
Mar	1	Late	0.75	1.18	11.8	11.5	0.3
Mar	2	Late	0.71	1.25	12.5	11.7	0.7
Mar	3	Late	0.67	1.42	15.6	10.9	4.7
Total					709.4	387.3	393.4

The above results seem to be very reasonable. Cotton seems to be the more consuming crop, but with not a very significant difference between the other crops. North surface irrigation zone is generally more consuming, and this can be justified from the fact that Larissa weather station has a bigger weight at this zone, being more continental. Unfortunately, there are not reliable irrigation data in order to validate all these results in the region. For this reason, an internal validation is applied, where CropWat model is applied again keeping constant all the other variables except crop coefficients. Crop coefficients values, in this application, are taken from the literature

(Papazafiriou, 1999), while meteorological data from 2007 is utilized again instead of climatic. Table 5.7 shows the results:

Table 5.7. Total irrigation requirements per zone

Irrigation requirements (mm)	New Surface Network	Pinios LALR Network	North Ground water network	Central Ground water network	South Ground water network	Average Values	Reference Values
Cotton	504,1	478,9	580,2	496	484,4	508,72	553,3
Sugar beet	426,3	445,9	557,8	351,3	351,7	426,6	638,0
Maize	501,3	495,6	499,5	478,1	402,9	475,48	552,6
Alfalfa	403,6	407	393,4	394,8	457,9	411,34	360,5

The same results of Table 5.7 are also illustrated in a different way at Figure 5.20 for convenience. The results show that there are not very significant differences between the zones. Of course slight differences are expected. The only exception is the south groundwater zone where is a big variance between the irrigation requirement values of the crops. Topography could be a reason for this variance.

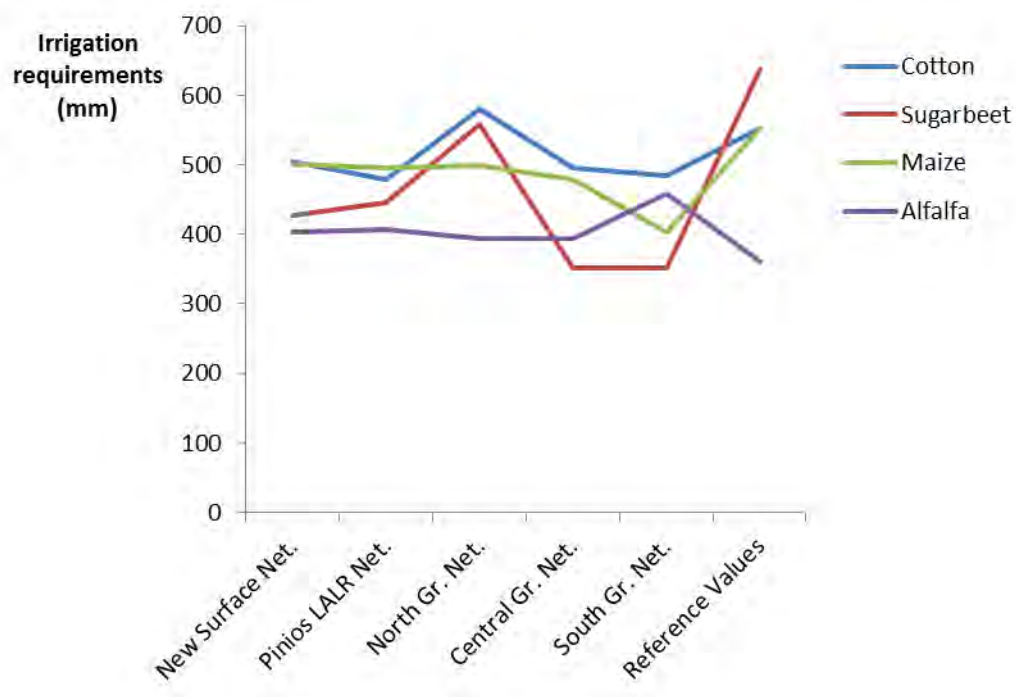


Figure 5.20. Crop water requirements per zone.



Cotton has an average of 508,72 mm irrigation requirements, while sugar beet have 426,6 mm, maize 475,48 mm and alfalfa 411,34 mm. Comparing these values with the last row of Table 5.7 where reference values are shown, some variations are detected. The variations are expected, because crops in the study area have their own peculiarity as well as slightly different phenological stages. It is obvious that most fields have different owners, and the farmers have different schedules between them, yielding to a difference to the phenological stages of the crops. The most significant variation can be seen at sugar beet where a reference value is much bigger than the average value of the previous CropWat computations. This could be justified thinking that METRIC based derivation of crop coefficient values has a spatial resolution of 30 m x 30 m, and it has to be considered that in most cases at Lake Karla watershed sugar beet fields are next to cotton fields. As a result many pixels acquire spectral information from both fields, resulting in a significant error. This could be corrected in the future utilizing data from new sensors having a better spatial resolution.

## 5.2 Validation of $ET_a$ using METRIC

### 5.2.1 P.M. $ET_{ref}$ vs METRIC $ET_a$ values

Generally, in research it is usual to validate the results of a proposed methodology. Unfortunately, in Lake Karla case, as well as many regions in the world, there are no available ground-truth measurements of evapotranspiration (e.g. pan lysimeters). Additionally, there are not reliable irrigation requirements measurements because the collaboration and efficiency of the local authorities is very complex. As a result, theoretical procedures are followed in order to validate the methodologies. In this work, at the first stage Penmann-Monteith procedure is followed in order to produce  $ET_{ref}$  values. For the computation of  $ET_{ref}$  values equation (2.2) is applied.  $ET_{ref}$  values from equation (2.2) are computed for two points where the two respective available meteorological stations of Lake Karla Watershed are situated (Figure 5.21).

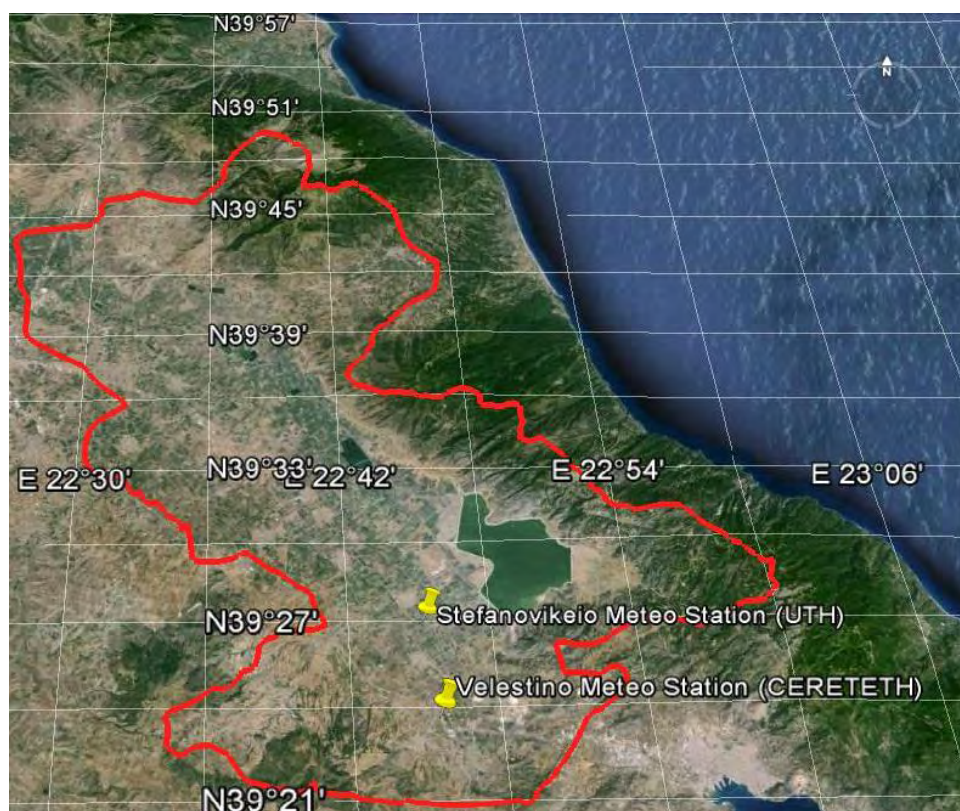


Figure 5.21. Location of the meteorological stations of the study area.

Then, Penman-Monteith (P.M.) derived  $ET_{ref}$  values are compared with instantaneous  $ET_a$  values derived from METRIC. The units are mm/hour. The total cases which are tested are eleven (11), taken from the independent period of 2012 growing season. Table 5.8 shows the described values. Gaps on the table are due to the existence of gaps at the acquisition procedure of Landsat 7 ETM+ sensor.

Table 5.8.  $ET_{ref}$  vs METRIC  $ET_a$  values: Independent period 2012

Date	Velestino		Stefanovikeio	
	$ET_{ref}$ (mm/hour)	$ET_a$ (mm/hour)	$ET_{ref}$ (mm/hour)	$ET_a$ (mm/hour)
26/04/2012	0,6	0,45	0,47	0,45
12/05/2012				
13/06/2012	0,68	0,36	0,76	0,62
29/06/2012			0,66	0,65
15/07/2012	0,65	0,5	0,69	0,65

31/07/2012	0,74	0,69	0,71	0,69
01/09/2012				
03/10/2012	0,53	0,41	0,54	0,47
19/10/2012				

After plotting the values shown at Table 5.8, Figure 5.22 is generated, illustrating the respective scatterplot together with a 1:1 line representing the case where  $K_c=1$ , plotted for comparing purposes. The results seem to be reasonable:  $ET_{ref}$  values are bigger than METRIC  $ET_a$  ones following the trend line, while  $R^2=0.59$ .

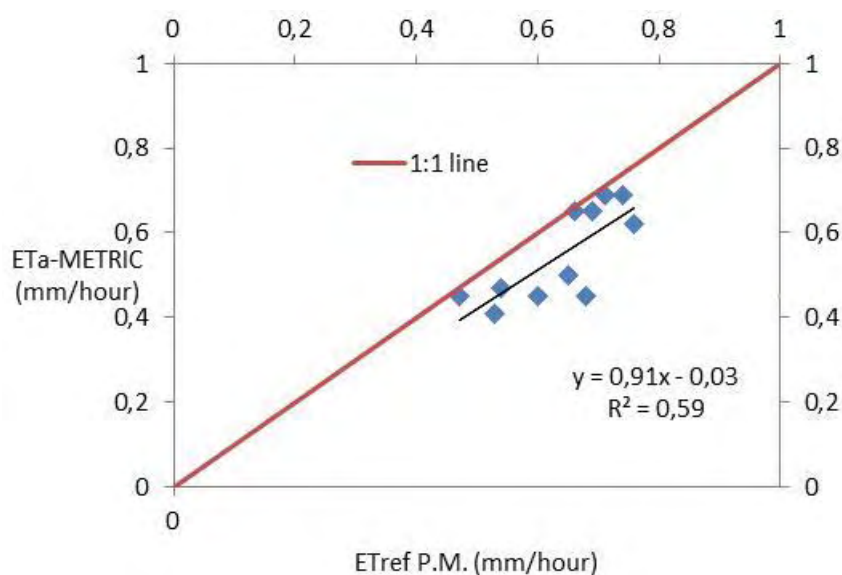


Figure 5.22.  $ET_a$  METRIC vs  $ET_{ref}$  P.M. values: 2012.

Next to this, the same methodology is followed for the growing season of 2007 which is the period applied for the development of the methodology.

Table 5.9 shows the respective values from 2007 period only for Velestino station (Stefanovikeio station was out of order), while Figure 5.23 illustrates the respective scatterplot.

Table 5.9.  $ET_{ref}$  vs METRIC  $ET_a$  values: Dependent period 2007.

Date	Velesino	
	ET <sub>ref</sub> (mm/hour)	ET <sub>a</sub> (mm/hour)
7/5/2007	0,64	0,63
24/6/2007	0,91	0,66
10/7/2007	0,91	0,84
26/7/2007	0,76	0,71
27/8/2007	0,67	0,63
28/9/2007	0,52	0,56
7/5/2007	0,64	0,63

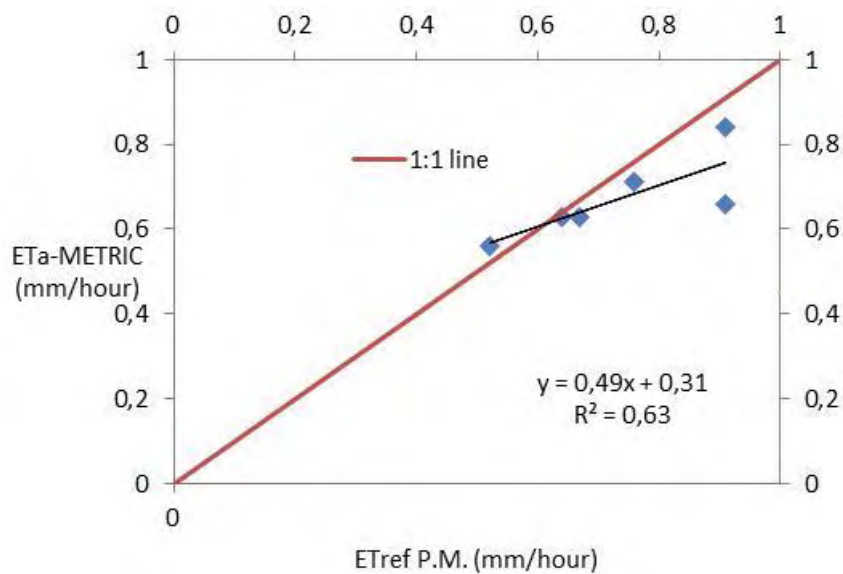


Figure 5.23. ET<sub>a</sub> METRIC vs ET<sub>ref</sub> P.M. values: 2007.

ET<sub>ref</sub> values are bigger again than METRIC ET<sub>a</sub> ones, following the trend line, while  $R^2=0.63$ . Finally, values from 2007 are plotted together with those of 2012 giving Figure 5.24.

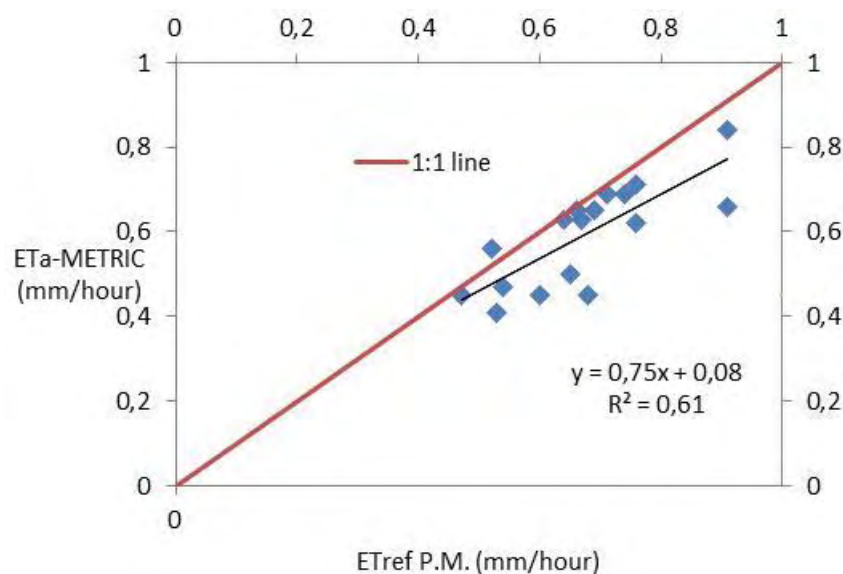


Figure 5.24.  $ET_a$  METRIC vs  $ET_{ref}$  P.M. values: 2012 + 2007.

Figure 5.24 illustrates a very good agreement of METRIC  $ET_a$  values in the diagram, while  $R^2=0.61$ . These results indicate that METRIC can produce reliable  $ET_a$  values with a satisfactory agreement with  $ET_{ref}$  values derived applying Penman – Monteith methodology.

### 5.2.2 METRIC $ET_a$ values vs P.M. $ET_a$ values

It is obvious that comparing  $ET_{ref}$  values with  $ET_a$  values it is not exactly the same thing. For this reason,  $ET_a$  values are computed using  $K_c$  values appropriate for central Greece according to each phenological stage retrieved from the literature (Papazafiriou, 1999), and multiplying them with P.M.  $ET_r$  values. Cotton, sugar beet and maize  $K_c$  values are shown on Table 5.10. These values are retrieved from Papazafiriou (1999) after modifying the periods for the year of 2012 according to personal research and visits.

Table 5.10.  $K_c$  values according to each phenological stage for crops at Lake Karla watershed.

Crop	Stage 1		Stage 2		Stage 3		Stage 4	
	Duration (days)	$K_c$	Duration (days)	$K_c$	Duration (days)	$K_c$	Duration (days)	$K_c$
Cotton					30/7/2011		18/9/2012	
			25/5/2012		2-		-	
	20/4/2012- 24/5/2012	0,45	-		17/9/2011	1,0	22/10/2011	1,05-
Sugar beet			29/7/2012	0,45-1,05	2	5	2	0,60
					14/5/2011			
			31/3/2012		2-		13/8/2012	
Maize	1/3/2012- 30/3/2012	0,45	-		12/8/2011	1,0	12/10/2011	1,00-
			14/5/2012	0,45-1,00	2	0	2	0,50
					19/6/2011			
Maize			5/4/2012-		2-		19/8/2012	
	15/4/2012-		18/6/2012	0,50-1,05	18/8/2011	1,0	-	1,05-
	4/5/2012	0,50			2	5	17/9/2012	0,60

For the derivation of  $K_c$  values for specific dates where Landsat imagery is available, linear interpolation is used. The interpolation is based on the plots shown on Figure 5.25.

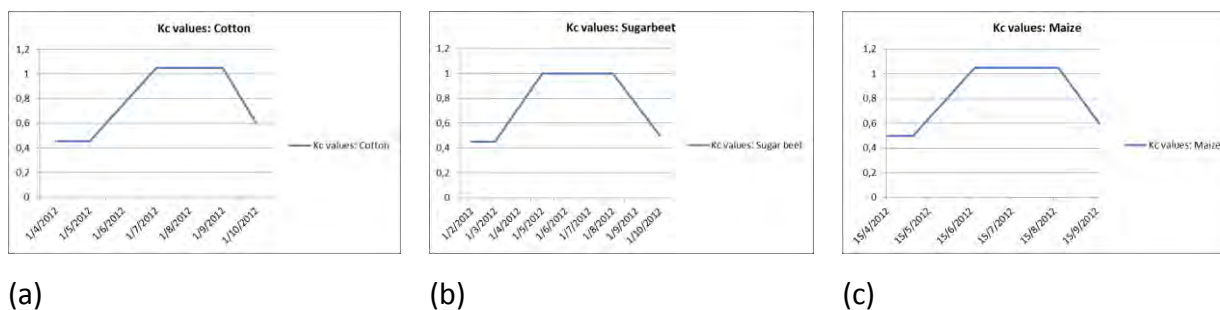


Figure 5.25.  $K_c$  values during the growing season: a) Cotton, b) Sugar beet, c) Maize

Multiplying the interpolated values of  $K_c$  with  $ET_{ref}$  values, P.M. derived  $ET_a$  values are finally produced. These values are compared with the METRIC based ones (Table 5.11).

Table 5.11. 2012 METRIC based  $ET_a$  vs P.M. based  $ET_a$  values for Velestino (a, b, c) and Stefanovikeio stations (d,e,f) for cotton, sugar beet and maize respectively.

<b>a) Cotton: Velestino</b>			
Date	Julian Day	$ET_a$ METRIC	$ET_a$ P.M.
26/04/2012	117	0,28	0,27
12/05/2012	133	-	0,09
13/06/2012	165	0,45	0,43
29/06/2012	181	0,38	0,49
15/07/2012	197	0,54	0,60
31/07/2012	213	0,66	0,78
01/09/2012	245	0,33	0,64
03/10/2012	277	0,38	0,45
19/10/2012	293	0,18	0,23
<b>b) Sugar beet: Velestino</b>			
Date	Julian Day	$ET_a$ METRIC	$ET_a$ P.M.
26/04/2012	117	0,45	0,47
12/05/2012	133	-	0,20
13/06/2012	165	0,66	0,68
29/06/2012	181	0,56	0,63
15/07/2012	197	0,58	0,65
31/07/2012	213	0,67	0,74
01/09/2012	245	0,35	0,51
03/10/2012	277	0,27	0,31
19/10/2012	293	0,18	0,18
<b>c) Maize: Velestino</b>			
Date	Julian Day	$ET_a$ METRIC	$ET_a$ P.M.
26/04/2012	117	0,29	0,30
12/05/2012	133	-	0,20

13/06/2012	165	0,44	0,67
29/06/2012	181	0,61	0,66
15/07/2012	197	0,60	0,68
31/07/2012	213	0,81	0,78
01/09/2012	245	0,54	0,51
03/10/2012	277	0,30	0,32
19/10/2012	293	0,22	0,22

**d) Cotton: Stefanovikeio**

Date	Julian Day	ET <sub>a</sub> METRIC	ET <sub>a</sub> P.M.
26/04/2012	117	0,22	0,21
12/05/2012	133	-	0,09
13/06/2012	165	0,47	0,48
29/06/2012	181	0,51	0,51
15/07/2012	197	0,59	0,64
31/07/2012	213	0,66	0,75
01/09/2012	245	0,33	0,67
03/10/2012	277	0,35	0,46
19/10/2012	293	-	-

**e) Sugar beet: Stefanovikeio**

Date	Julian Day	ET <sub>a</sub> METRIC	ET <sub>a</sub> P.M.
26/04/2012	117	0,35	0,37
12/05/2012	133	-	0,19
13/06/2012	165	0,48	0,76
29/06/2012	181	0,56	0,66
15/07/2012	197	0,64	0,69
31/07/2012	213	0,67	0,71
01/09/2012	245	0,37	0,54
03/10/2012	277	0,29	0,31
19/10/2012	293		0,18



f) Maize: Stefanovikeio			
Date	Julian Day	ET <sub>a</sub> METRIC	ET <sub>a</sub> P.M.
26/04/2012	117	0,23	0,23
12/05/2012	133	-	0,11
13/06/2012	165	0,49	0,75
29/06/2012	181	0,57	0,69
15/07/2012	197	0,65	0,72
31/07/2012	213	0,68	0,75
01/09/2012	245	0,36	0,54
03/10/2012	277	0,31	0,32
19/10/2012	293		

After putting together all the values which are corresponding to the independent period of 2012 (showing on Table 5.11), and making the important processing, Figure 5.26 is derived. The scatterplot shows a very good agreement between the ET<sub>a</sub> values derived from these two different sources ( $R^2=0.81$ ).

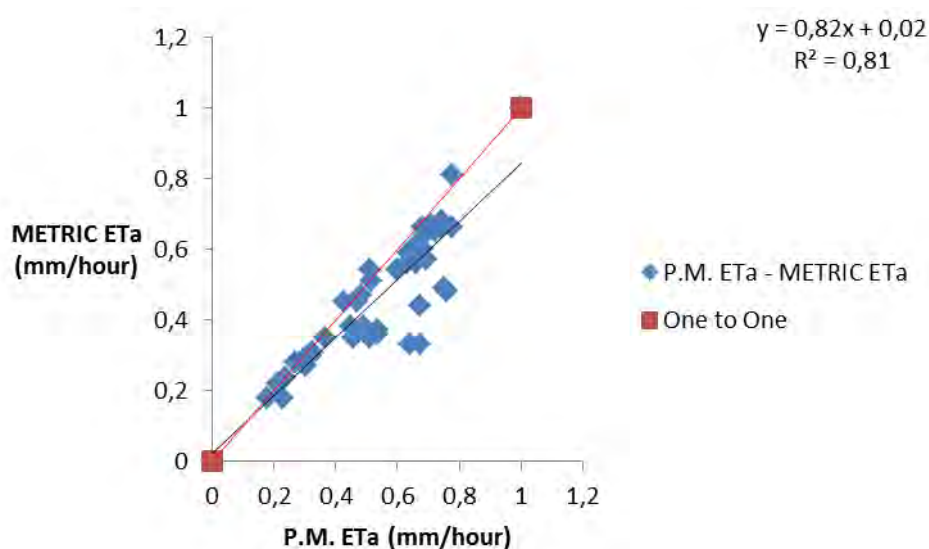


Figure 5.26. METRIC based ET<sub>a</sub> values vs P.M. based ET<sub>a</sub> values: 2012.

The next thought is to incorporate values derived from the growing season of 2007 to the previous ET<sub>a</sub> plot. Table 5.12 shows the 2007 respective values.

Table 5.12. 2007 METRIC based  $ET_a$  vs P.M. based  $ET_a$  values for Velestino (a, b, c) for cotton, sugar beet and maize respectively.

<b>a) Cotton: Velestino</b>			
Date	Julian Day	$ET_a$ METRIC	$ET_a$ P.M.
7/5/2007	127	0,27	0,29
24/6/2007	175	0,43	0,58
10/7/2007	191	0,84	0,81
26/7/2007	207	0,74	0,77
27/8/2007	239	0,59	0,70
28/9/2007	271	0,36	0,47
<b>b) Sugar beet: Velestino</b>			
Date	Julian Day	$ET_a$ METRIC	$ET_a$ P.M.
7/5/2007	127	0,51	0,59
24/6/2007	175	0,65	0,91
10/7/2007	191	0,88	0,91
26/7/2007	207	0,75	0,76
27/8/2007	239	0,67	0,58
28/9/2007	271	0,39	0,31
<b>c) Maize: Velestino</b>			
Date	Julian Day	$ET_a$ METRIC	$ET_a$ P.M.
7/5/2007	127	0,37	0,32
24/6/2007	175	0,66	0,95
10/7/2007	191	0,84	0,95
26/7/2007	207	0,78	0,80
27/8/2007	239	0,46	0,58
28/9/2007	271	0,36	0,31

The final comparison after adding all the previous values is produced taking into account sixty three (63) cases of cotton, sugar beet and maize fields through time. In a general view, METRIC  $ET_a$  values are smaller than P.M.  $ET_a$  values and this is totally justified, because Penman-Monteith procedure is based on an identical crop condition which is not the case in the study region. The graphic results (Figure 5.27) indicate that there is a very good agreement between METRIC  $ET_a$  values and P.M.  $ET_a$  values ( $R^2 = 0.79$ ), and it is finally assumed safe enough to validate the previous procedure (Sub-chapters 5.1.1 - 5.1.6) even with this “internal type validation”.

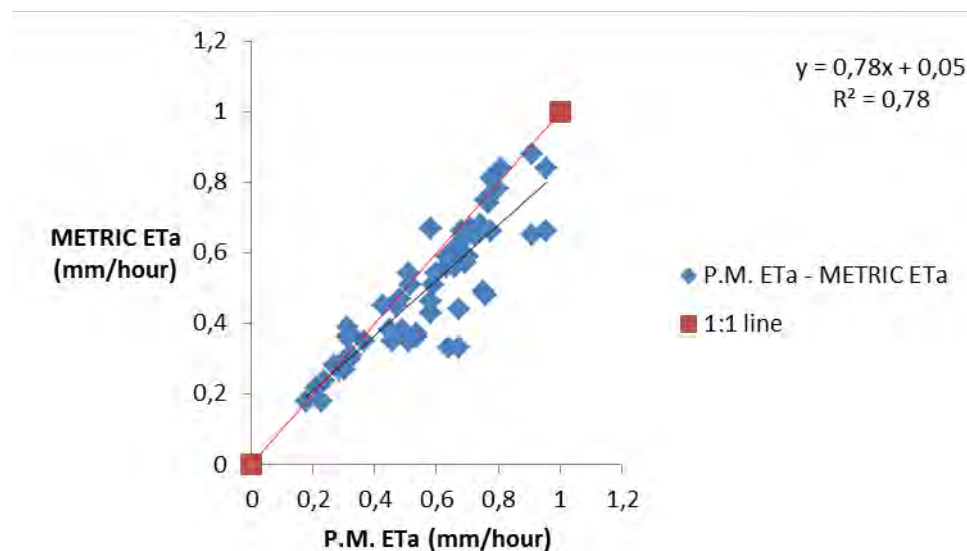


Figure 5.27. METRIC based  $ET_a$  values vs P.M. based  $ET_a$  values: 2012 + 2007.

### 5.3 Proposed integrated methodology

#### 5.3.1 Field measurements – Vegetation indices

A new research has been now conducted working with the growing season of 2012 for the same study area. GER1500 spectroradiometer in-situ observations are taken during April – October of 2012. Several representative cotton, winter wheat, sugar beet, maize and alfalfa fields are observed during this season. The total experiment days are eleven (Table 5.13). However, winter wheat is finally excluded from this study

due to its totally different phenological stages. Alfalfa fields are also excluded due to irregular cuttings according to individual farmers' schedules.

Table 5.13. GER1500 experimental days for **Lake** Karla Watershed

Date of measurement	Julian Day of measurement
03/04/2012	94
04/05/2012	125
12/05/2012	133
22/05/2012	143
29/06/2012	181
13/07/2012	195
31/07/2012	213
16/08/2012	229
01/09/2012	245
21/09/2012	265
03/10/2012	277

In-situ measurements can finally result to in-band reflectance values according to Landsat ETM+, as explained in methodology. This makes possible the calculation of Vegetation Indices similar to Landsat methodology. Four VI, namely Normalized Difference Vegetation Index (NDVI), Soil Adjusted Vegetation Index (SAVI), Enhanced Vegetation Index (EVI) and Enhanced Vegetation Index 2 (EVI2), are finally selected for processing. The basic criterion for the selection was the previous personal experience (Domenikiotis *et al.*, 2004a; 2004b). EVI uses three spectral bands, while NDVI and SAVI use only two bands. For this reason, EVI2 was decided to be used as an alternative, omitting the blue band (Jiang *et al.*, 2008; O'Connell *et al.*, 2013). The formulas used for the computations of the above indices similar to Landsat methodology are:

$$NDVI = \frac{Ch_4 - Ch_3}{Ch_3 + Ch_4} \quad (5.1)$$

$$SAVI = (1 + L) \frac{Ch_4 - Ch_3}{(Ch_3 + Ch_4 + L)} \quad (5.2)$$

$$EVI = 2.5 \frac{Ch_4 - Ch_3}{(6Ch_3 + Ch_4 - 7.5Ch_1 + 1)} \quad (5.3)$$

$$EVI2 = 2.5 \frac{Ch_4 - Ch_3}{(Ch_4 + 2.4Ch_3 + 1)} \quad (5.4)$$

Constant L in equation (5.2) requires a special procedure to derive. In original METRIC formulation it is suggested that the appropriate value of L for a particular area can be derived from an analysis of multiple images for the area (Waters *et al.*, 2002). Utilizing a series of images, and especially some pixels of vegetation that is not likely to change much, SAVI is computed using a range of values for L and then a diagram SAVI vs. L is plotted. The selected L is the value that provides for a consistent value of SAVI, which is where the minimum standard deviation exists (Waters *et al.*, 2002). This value for our thesis is: L=0.55 (Figure 5.28) which has been used from this point on.

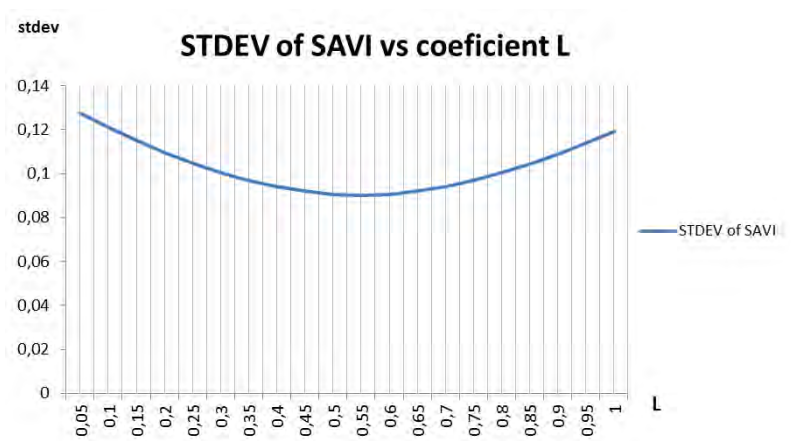


Figure 5.28. Standard deviation of SAVI vs coefficient L.

Landsat 7 ETM+ high quality images (Table 5.14) are downloaded using GloVis tool from USGS for the growing season of 2012, and after the necessary radiometric and geometric correction are adjusted to the local EGSA 87 coordinate system. ENVI 5.0 and ERDAS Imagine 9.2 software are used repeatedly for the interpretation and analysis of all remote sensing images. Wind, air temperature, relative humidity data as well as radiation values are used as input parameters in the METRIC methodology. Reference evapotranspiration was also computed for all these dates.

Table 5.14. Landsat 7 images used for Lake Karla Watershed

Date of acquisition	Julian Day of acquisition	Path	Row
26/04/2012	117	184	032
12/05/2012	133	184	032
13/06/2012	165	184	032
29/06/2012	181	184	032
15/07/2012	197	184	032
31/07/2012	213	184	032
01/09/2012	245	184	032
03/10/2012	277	184	032
19/10/2012	293	184	032
26/04/2012	117	184	033
12/05/2012	133	184	033
13/06/2012	165	184	033
29/06/2012	181	184	033
15/07/2012	197	184	033
31/07/2012	213	184	033
01/09/2012	245	184	033
03/10/2012	277	184	033
19/10/2012	293	184	033

METRIC based  $ET_rF$  values are first estimated for Lake Karla Watershed, Greece, and these values are then plotted against VI throughout the growing season of 2012 for all the examined crops. An average of twenty separate measurements for each experiment day is computed for every crop, and linear relationships between  $ET_rF$  and VI are generated. A general relationship is also established, incorporated all crops for NDVI, SAVI, EVI and EVI2. These relationships are very useful for the estimation of  $ET_rF$  from VI especially in cases where there is no knowledge of specific crop type/land use.

It is evident from Table 5.15 that NDVI performs better than the other three indices for all the three specific crops. Maize has the best fitting according to  $R^2$  (0.983). On the other hand EVI2 performs better than EVI in all cases. It seems that red and NIR channel override the omission of the blue channel, which in turn maybe causes some undesirable errors due to the nature of these especially low reflected values in this part of the electromagnetic spectrum. The general case performs better applying SAVI. This was partly expected because SAVI was computed using the constant  $L=0,55$  adjusted to the local conditions. Minimizing the standard deviation of SAVI with this local adjusted value of  $L$ , is maybe the reason why SAVI performs better than NDVI especially at the general case. However, NDVI is still very reliable (Figure 5.29). NDVI is simpler than SAVI, EVI and EVI2, and it seems to perform better than the others applied for individual crops. This is the reason why it is chosen for the next part of the methodology.

Table 5.15. Linear relationships between  $ET_rF$  and VI.

Crop	NDVI		SAVI		EVI		EVI2	
	Equation	$R^2$	Equation	$R^2$	Equation	$R^2$	Equation	$R^2$
Cotton	$y=0.509x+0.359$	0.825	$y=0.499x+0.285$	0.835	$y=0.586x+0.132$	0.623	$y=0.556x+0.120$	0.668
Sugar Beet	$y=0.879x-0.159$	0.909	$y=0.967x-0.104$	0.899	$y=0.839x-0.113$	0.851	$y=0.796x-0.101$	0.854
Maize	$y=1.127x-0.983$	0.983	$y=0.906x-0.003$	0.959	$y=0.623x+0.033$	0.837	$y=0.625x-0.855$	0.855
General	$y=0.6892x+0.2381$	0.856	$y=0.834x+0.020$	0.873	$y=0.725x-0.006$	0.796	$y=0.697x-0.012$	0.817

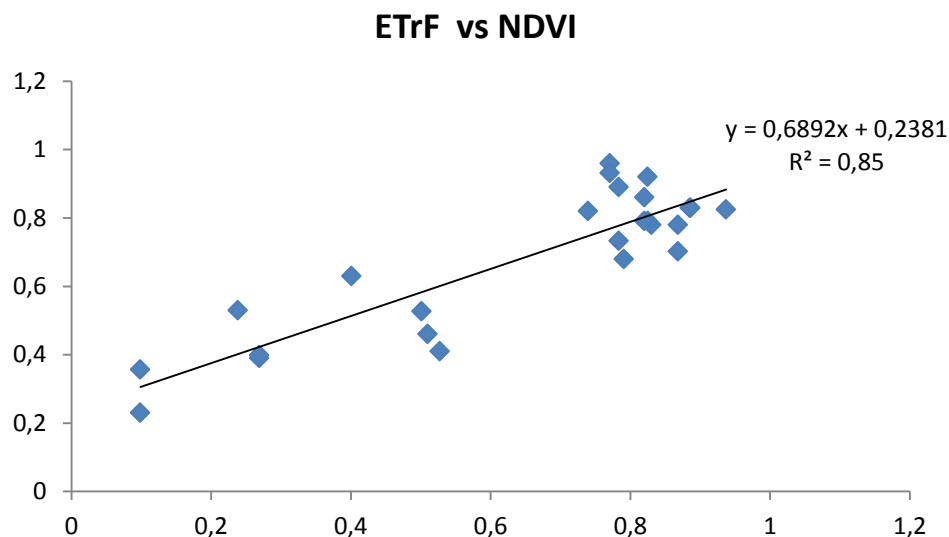


Figure 5.29. ET<sub>r</sub>F vs NDVI general equation

In-situ radiometric measurements seem to be a very important additional tool of this thesis. These measurements are helped to improve the accuracy of the land use mapping but the most important is that are served as a new source of reflectance data. Modelling of crop coefficient values with new vegetation indices is now possible without the use of atmospheric correction.

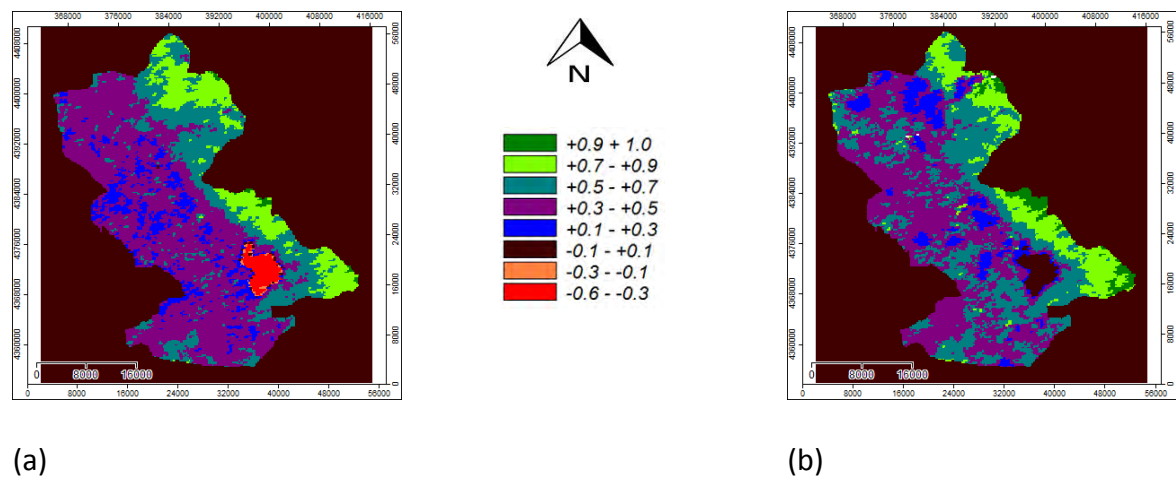
### 5.3.2 MODIS based NDVI – Downscaling

Surface Reflectance Daily L2G Global 250M AQUA V5 MODIS products are downloaded from GLOVIS with a 250 m x 250 m spatial resolution. Images are interpreted and projected to the EGSA 87 map conversion system as ETM+ images too. NDVI values can be simply computed without applying an atmospheric correction using equation (4.17) just replacing Landsat channel 4 and 3 with MODIS 2 and 1 respectively. MODIS based daily NDVI maps are finally generated for the summer period of 2012. Potentially, daily NDVI maps can be computed for all the growing season. Landsat based NDVI images, previously computed as METRIC sub-products and MODIS based NDVI images are then



downscaled. The methodology used is described as “input” ET downscaling in previous studies (Hong *et al.*, 2012; Spiliotopoulos *et al.*, 2013). The preferable downscaling scheme is the regression (Hong *et al.*, 2012) and is illustrated on Figure 4.49 as previously explained.

Figure 5.30 shows the four initial NDVI maps for the two different types of sensors and different dates, and the new downscaled one. Cases (a) and (b) illustrate the new MODIS based NDVI maps just computed for 13<sup>th</sup> of June and 29<sup>th</sup> of June respectively. Case (c) represents the base NDVI map based on the Landsat image from 13<sup>th</sup> of June, and case (d) the test NDVI image used for 29<sup>th</sup> of June. Assuming a linear relationship between MODIS based NDVI images for 13<sup>th</sup> of June and 29<sup>th</sup> of June (case a and b), and after regression, constants  $A=0.2444$  and  $B=0.5929$  are resulted.



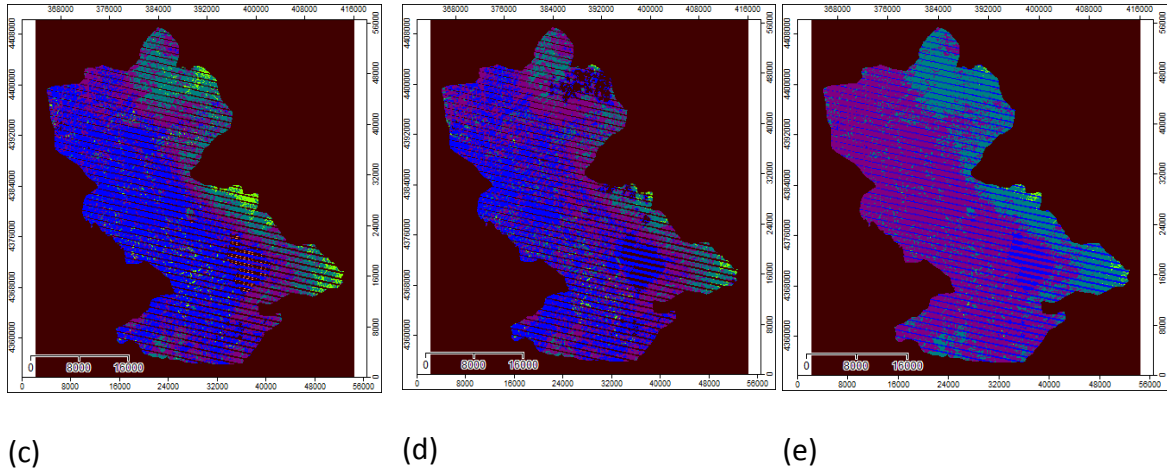


Figure 5.30. (a) MODIS based NDVI 13<sup>th</sup> of June 2012, (b) MODIS based NDVI 29<sup>th</sup> of June 2012, (c) LANDSAT based NDVI 13<sup>th</sup> of June 2012 (d) LANDSAT based NDVI 29<sup>th</sup> of June 2012, (e) Downscaled NDVI map (29<sup>th</sup> of June 2012).

Applying these constants  $a$  and  $b$  to the regression downscaling methodology explained on Figure 4.49, a new MODIS based, Landsat NDVI is now generated (Figure 5.30, case e). It has to be mentioned again that the first “base” image is related with the 13<sup>th</sup> of June while the second “product” image is related with the 29<sup>th</sup> of June. The new NDVI map has a 30 m x 30 m spatial resolution, and from this daily product, a new daily  $ET_rF$  map can now be computed applying the already established  $ET_rF=f(NDVI)$  relationship.

### 5.3.3 Estimation of crop coefficients using the $ET_rF=f(NDVI)$ relationship

Linear regression between  $ET_rF$  values and NDVI based on the GER 1500 in-situ measurements for selected crop fields is applied excluding alfalfa fields (Figure 5.29), giving the following general formula (equation (5.5)):

$$ET_rF = 0.689 \times (NDVI) + 0.238 \quad (5.5)$$

More than 40 different radiometric measurements in the fields per experiment day were conducted, but for the generation of equation (5.5) only average reflectance values for each crop type are taken into account.

Field spectroscopy plays a crucial role in equation (5.5), because applying the described procedure, it is possible to take into account the most important crops that are not easy to classify on a year-by-year basis using satellite sensors alone. In reality, it is common for farmers to change crops every year, or even to leave their fields uncultivated. Using equation (5.5) ensures that crops are entered accurately, thus avoiding significant sources of error.

The result of applying equation (5.5) to the downscaled NDVI map is the generation of a new computed  $ET_rF$  map with the same spatial resolution as Landsat ETM+ while its original source is MODIS (Figure 5.31). This is a daily product after applying the suggested methodology and it has to be tested using the “original” METRIC based  $ET_rF$  map. The difference between these two images must be minimum (Figure 5.32). Of course it is expected that this is not the case for every pixel of the study area, but the mean value of the difference map is -0.08 and the standard deviation is 0.30 which are very encouraging values. Physically, the next thought is to apply a mask (Figure 5.33) where all the non-crop pixels could be excluded from the methodology. For this reason a new 2012 land use map has already generated for this study (Figure 5.34). The result is now that the mean value of the difference map is -0.06 and the standard deviation is 0.21 which is a very remarkable improvement. This improvement is very reasonable because the initial  $ET_rF$  vs NDVI equation was relied only on crop values.

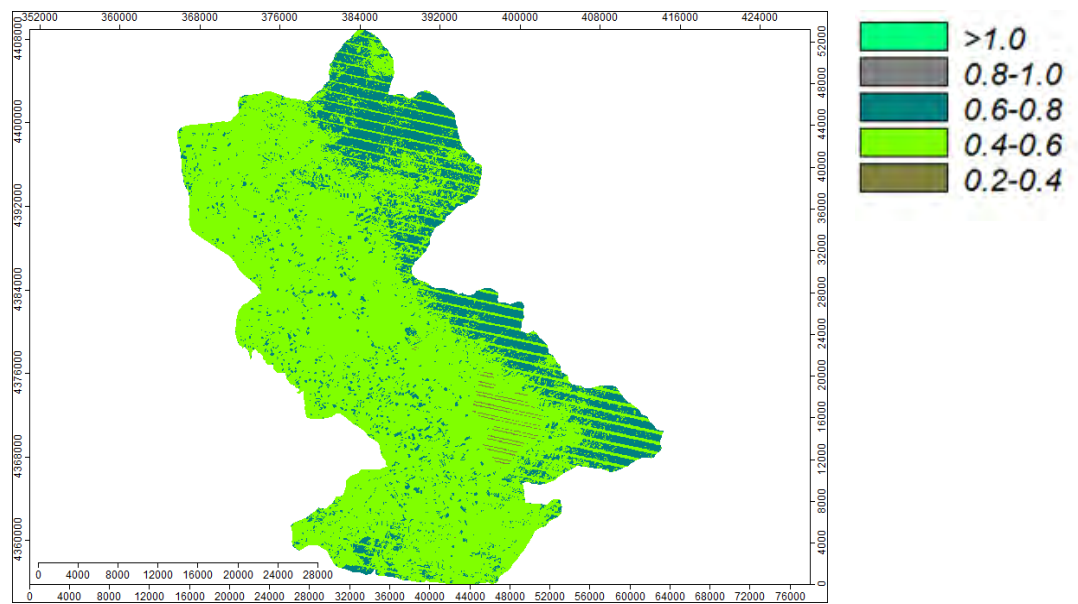


Figure 5.31.  $ET_rF$  computed, 29<sup>th</sup> of June 2012.

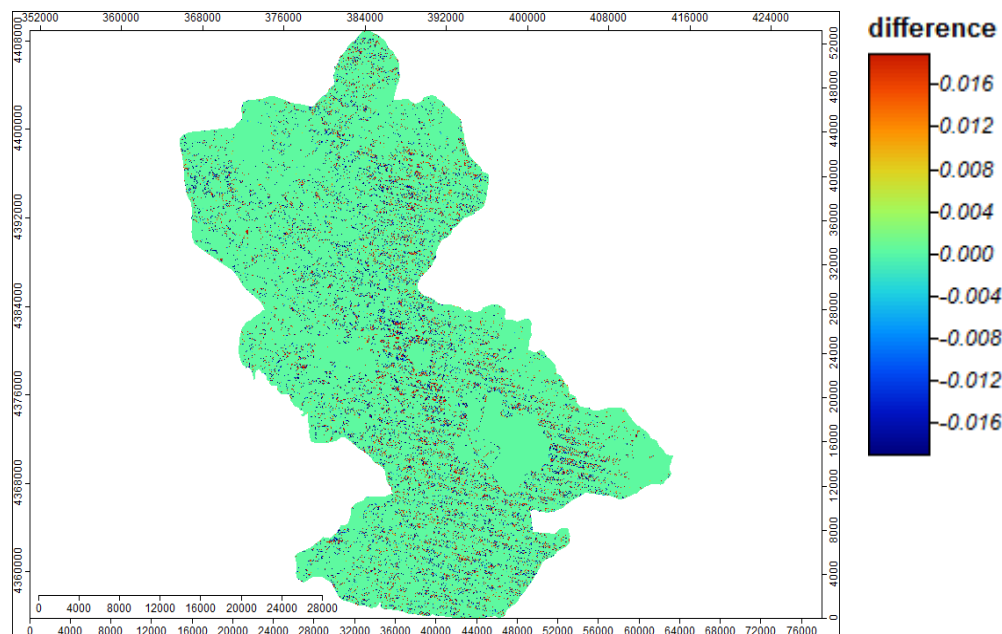


Figure 5.32.  $ET_rF$  difference, 29<sup>th</sup> of June 2012.

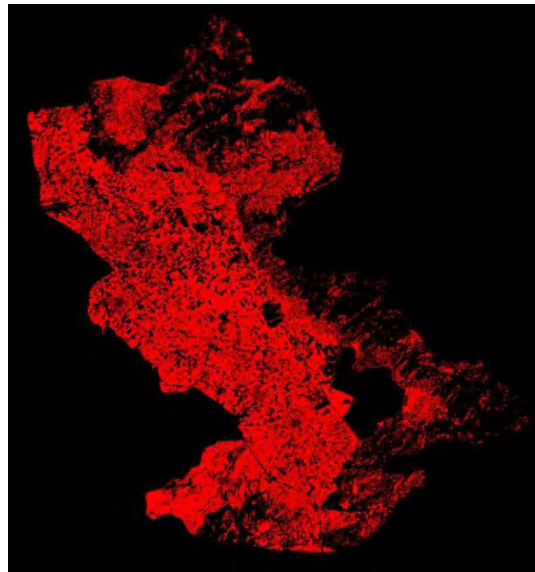


Figure 5.33. A “crop mask” applied in the study (in red).

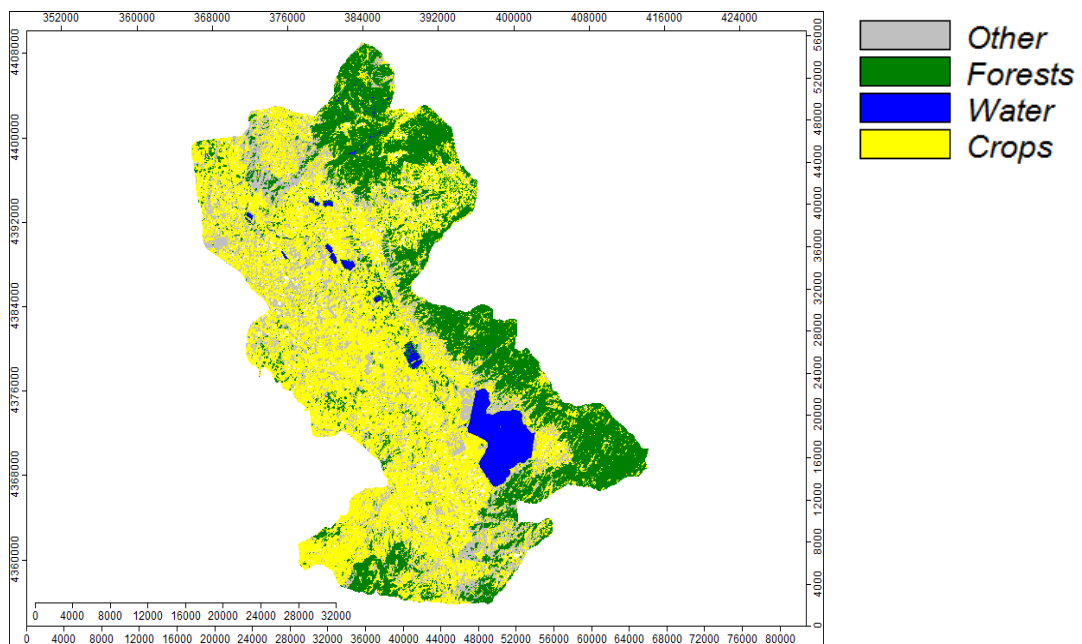


Figure 5.34. Lake Karla watershed classification map 2012.

## 5.4 *Validation of the proposed methodology*

### 5.4.1 **Landsat 8 imagery**

For validation purposes only, Landsat 8 imagery is utilized using the same base image. Special attention is given to the wavelengths of the bands of the new OLI sensor (Table 2.4). For this reason, the first band (0.43 - 0.45  $\mu\text{m}$ ) has been omitted from the computations of albedo. METRIC methodology is then applied again keeping the same principles and equations which have been already described. Meteorological data from Velestino station are used for the computation of reference ET for the 24<sup>th</sup> of June, 2013. For the same day, two Landsat 8 scenes are downloaded from NASA's GLOVIS tool, because Lake Karla watershed occupying more than one Landsat scene (which has a swath width of 185 km). These are the 184/032 and the 184/033 (path/row) scenes. These images are radiometrically and geometrically corrected and then put into a special mosaic (Figure 5.35). EGSA' 87 coordinate system is applied again. After, running the already described sub-models needed for the computation of METRIC,  $ET_rF$  map is finally produced for Lake Karla watershed (Figure 5.36(a)).



Figure 5.35. Landsat 8: 184/032 and 184/033 (path/row) scenes (24-6-2013)/

Daily L2G Global 250M AQUA V5 MODIS surface reflectance values are also downloaded from GLOVIS with a 250 m x 250 m spatial resolution, for the same day. Projection to EGSA 87 map conversion system is utilized. A new Landsat based MODIS NDVI image is produced then using the downscaling methodology and then equation (5.5) is applied giving a new computed ET<sub>r</sub>F image (Figure 5.36(b)). The mean value of the difference map between the new ET<sub>r</sub>F image and the METRIC based image (Figure 5.36 (c)) is now -0.11, while the standard deviation is 0.67. After excluding the non-crops pixels the mean value becomes -0.02 and the standard deviation 0.31.



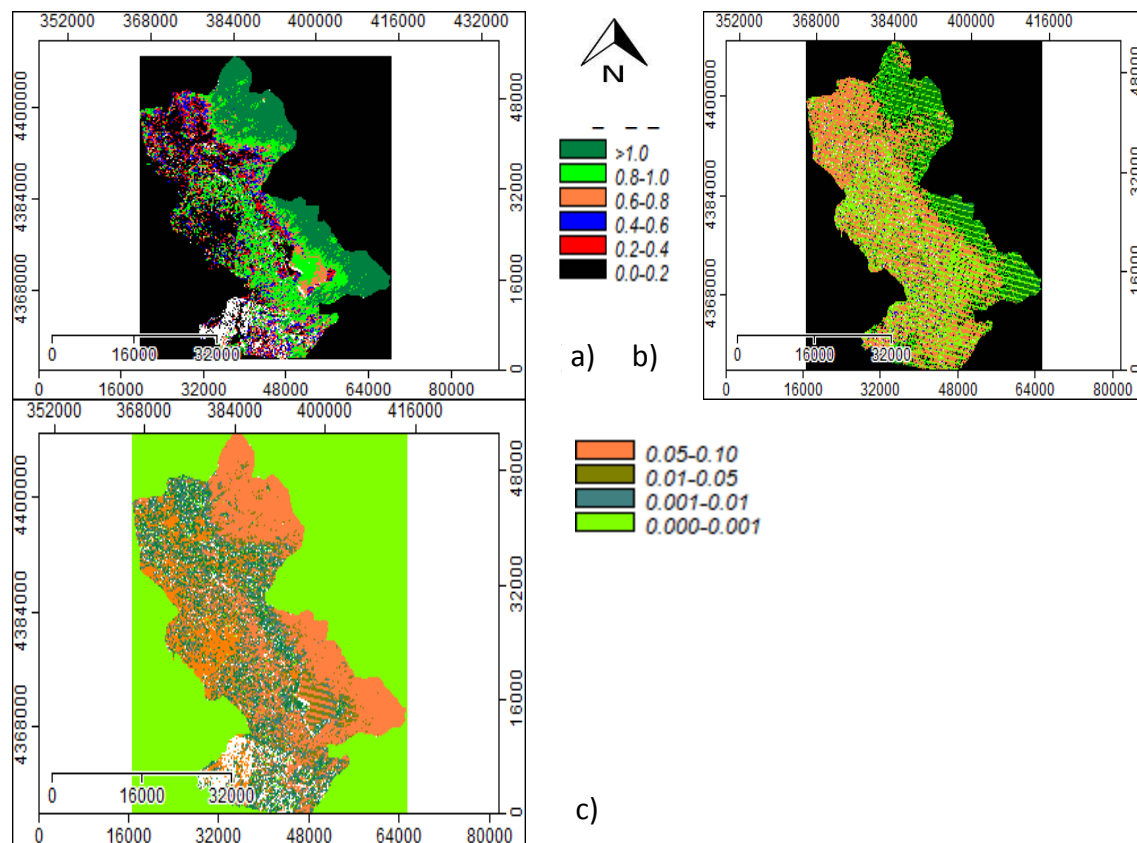


Figure 5.36. 24-6-2013: a) ET<sub>r</sub>F METRIC map, b) ET<sub>r</sub>F new proposed map, c) difference map.

#### 5.4.2 Landsat 7 imagery

A validation of the proposed methodology is attempted using the same base image and testing the ET<sub>r</sub>F map using Landsat 7 imagery for 3th of October 2012 which is the year where the model is based. A new Landsat based MODIS NDVI image is produced for that day following the same philosophy with Landsat 8 imagery, and then equation (5.5) is applied. The mean value of the difference map (Figure 5.37 (c)) between the METRIC based image (Figure 5.37 (a)) and the new ET<sub>r</sub>F image (Figure 5.37 (b)) is now 0.047, while the standard deviation is 0.37. After excluding the non-crops pixels the mean value becomes 0.006 and the standard deviation 0.11. The correlation coefficient



between the new  $ET_rF$  map and the METRIC one is  $R=0.72$  while  $R^2= 0.52$ . The results are very encouraging keeping in mind that almost 22% of the total pixels are lost due to the data gaps of Landsat 7 ETM+. Of course the accuracy is expected to be improved working with new improved satellite data sets.

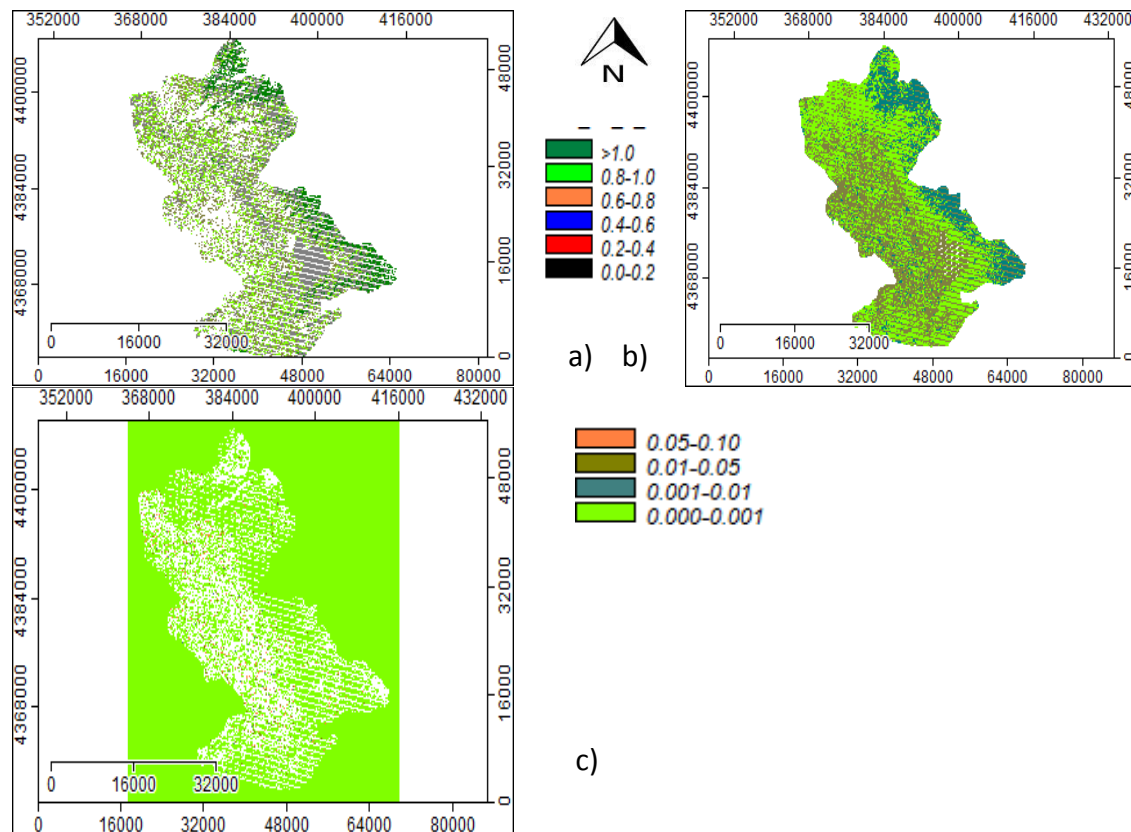


Figure 5.37. 3-10-2012: a)  $ET_rF$  METRIC map, b)  $ET_rF$  new proposed map, c) difference map.

#### 5.4.3 Estimation of daily crop water requirements using CropWat

After acquiring the new 30 m x 30 m  $ET_rF$  map the next step could be physically the computation of the new crop water requirements. A comparison between the METRIC based crop water requirements and the new ones is very important in order to assess the possible differences between them. For this reason CropWat model is utilized again

estimating daily crop water requirements. Landsat 8 imagery is used for validation (24/6/2013). This is the date when a more significant error of  $ET_{rF}$  is occurring according to the previous analysis. Another reason for the selection of the 24<sup>th</sup> of June is that zero values usually occurred in October at CropWat's outputs are avoided. Representative cotton, sugar beet, maize and alfalfa fields are utilized for the north, central and south groundwater zones. These zones are selected in order to achieve a good geographical representation of the watershed. In this situation there is no need to do the same for the other two surfaces zones described earlier, because the goal is only to validate the irrigation needs throughout the watershed and not to make a specific zone analysis. Finally,  $ET_{rF}$  ( $K_c$ ) values using classical METRIC methodology versus the new proposed methodology are collected and used as input for CropWat . The results are shown at the Table 5.16.

Table 5.16.  $ET_{rF}$  ( $K_c$ ) and crop irrigation requirement outputs for classical and proposed methodology.

24/6/2013	METRIC based $K_c$	Proposed $K_c$	CropWat's Crop Water Irrigation requirements (mm) - using METRIC based $K_c$	CropWat's Crop Water Irrigation requirements (mm) - using proposed $K_c$
<b>North Groundwater Zone</b>				
Cotton	0.69	0.72	3.55	3.76
Sugar beet	0.79	0.78	4.31	4.24
Maize	0.79	0.77	4.20	4.06
Alfalfa	0.48	0.48	2.05	2.05
<b>Central Groundwater Zone</b>				
Cotton	0.63	0.62	3.13	3.06
Sugar beet	0.75	0.73	4.03	3.89
Maize	0.75	0.77	3.92	4.06
Alfalfa	0.72	0.71	3.42	3.36
<b>South Groundwater</b>				

<b>Zone</b>				
Cotton	0.80	0.78	4.32	4.18
Sugar beet	0.72	0.74	3.82	3.96
Maize	0.77	0.75	4.06	3.92
Alfalfa	0.52	0.51	2.27	2.22

CropWat model is operated for each case, giving the estimated crop water requirements (in mm) as shown at the Table 5.16. Average values for the three related zones are taken then, giving Table 5.17 where the average crop water requirement for each crop is shown (in mm). The last column of Table 5.17 gives the % difference between the two estimations. It is obvious that the results are very satisfactory (less than 2% for each case). Cotton performs the best results, following by sugar beet, maize and alfalfa. Alfalfa performance can be justified to the big variations occurring to each field which is the result of the different farmers' regimes as it is already pointed out. In every case, considering the results, it is obvious that the accuracy of CropWat's crop water requirements after applying the proposed  $ET_rF$  values is very satisfactory.

Table 5.17. Average Crop Irrigation Requirement values (mm).

24/6/2013	METRIC based $K_c$	Proposed $K_c$	CropWat's Crop Water Irrigation requirements (mm) - using METRIC based $K_c$	CropWat's Crop Water Irrigation requirements (mm) - using proposed $K_c$	Crop Irrigation Requirements Difference (%)
Cotton			Average values		
	0.71	0.71	3.67	3.67	0
Sugar beet			Average values		
	0.75	0.75	4.05	4.03	0.49
Maize			Average values		
	0.77	0.76	4.06	4.01	1.23
Alfalfa			Average values		
	0.57	0.59	2.58	2.54	1.55

#### 5.4.4 CropWat sensitivity

A daily  $ET_rF$  is of course a very interesting challenge, but it is very useful to test the seasonal sensitivity of a crop irrigation model like CropWat to this approach. Of course CropWat is not too sensitive to a daily crop coefficient value but let's assume the worst case scenario (5.4.1) where every  $ET_rF$  ( $K_c$ ) value has a maximum error of  $\pm 0.02$  which is the average value of the difference, found when applying Landsat 8 imagery. Choosing cotton as an example for this analysis and assuming that the critical  $K_c$  values of cotton are 0.45, 1.05 and 0.60 respectively for the study area, when applying this kind of error, the irrigation water requirements are varying from 543.2 mm to 577 mm. More specifically, keeping the values 0.45, 1.05 and 0.60, the output of the model returns 560.1 mm, and then when setting the values to 0.47, 1.07 and 0.62 the model returns 577 mm of water. Similarly, setting the values to 0.43, 1.03 and 0.58 the model returns 543.2 mm. The error is less than 3% in each case. Similarly, applying this kind of analysis to all zones and crops defined at chapter 5.5, and taking the average values for each crop, Table 5.18 is derived. The "lower value" column represents irrigation water requirement values after error of -0.02 is added to the already established  $K_c$  value. The "upper value" column represents irrigation water requirement values after error of +0.02 is added to the already established  $K_c$  value. The "average values" column represents average irrigation water requirement values for the study area for every crop. The last two columns represent the final crop water requirement error (%) when applying the maximum error of  $\pm 0.02$  of  $K_c$  values to CropWat model. "Lower values error (%)" column represents errors when adding -0.02 to each  $K_c$  value to every

case, while “Upper values error (%)” column represents errors when adding +0.02 to each  $K_c$  value to every case respectively.

Table 5.18. CropWat irrigation requirements sensitivity to  $K_c$  errors

Irrigation requirements	Lower value (mm)	Actual Values (mm)	Upper value (mm)	Lower value error (%)	Upper value error (%)
Cotton	489.6	508.7	519.8	3.8	2.2
Sugar beet	407.7	426.6	444.0	4.4	4.1
Maize	453.8	475.5	489.6	4.6	3.0
Alfalfa	391.9	411.3	430.5	4.7	4.7

The results from Table 5.18 show that the error is always less than 5% for all cases which is assumed as an acceptable result. The best results are found for cotton, while the worst are found for alfalfa. The different phenological stages of the latter is obvious the reason for this. The results also show that cotton behaviour is better than the other crops which is in total accordance with the previous analysis. This could be attributed to the greater influence of weather conditions than the respective effect of  $K_c$  values to cotton crops.



**CHAPTER 6°**

**CONCLUSIONS AND PERSPECTIVES**

## **6 Conclusions and perspectives**

### *6.1 Summary of methodology and results*

In the study, crop water requirements are estimated using FAO's CropWat model, using as an input crop coefficient values deriving from remote sensing imagery. Meteorological data are also used as an input for CropWat instead of default climatic mean monthly data. An integrated approach is then proposed in order to calculate and map Landsat based daily crop coefficient values with a 30 m x 30 m resolution by applying a downscaling technique of MODIS imagery. The methodology is tested and validated at Lake Karla watershed in Greece as a case study, giving satisfactory results.

Initially, METRIC methodology is applied in the study area. METRIC is a satellite based surface energy balance method which gives as an output instantaneous actual ET values together with  $ET_rF$  values which are the same as the well known crop coefficient values ( $K_c$ ). METRIC is based on SEBAL methodology which is initially applied and tested in Lake Karla watershed. SEBAL estimates of ET have, in general, larger errors under windy and warm conditions under conditions of advection. Lake Karla watershed is a typical example of these conditions. METRIC on the other hand takes advantage of calibration using weather-based reference ET. As a result, both calibration and extrapolation of instantaneous ET to 24-h and longer periods compensate for regional advection effects where ET can exceed daily net radiation. This is the reason why METRIC is chosen in this study.

Meteorological data input needed for the application of METRIC methodology are collected from the meteorological stations of CERETETH and University of Thessaly. Landsat 5, Landsat 7, and MODIS imagery are also used for the development of the models while Landsat 7 and 8 imagery are used for validation. Pre-processing and all

the remote sensing techniques are carefully undertaken applying the EGSA' 87 map conversion system which is the Greek official projection system. Special remote sensing and G.I.S. software packages are used for the interpretation and construction of the models needed for the application of METRIC. It is very important to consider the specific wavelengths of the bands used for the application of radiation, reflectance, albedo, surface temperature and all the other physical variables which are prerequisites for the application. Image geometric correction is undertaken using previous maps taken from the local authorities as well as measurements made through field visits at the study area. One of the most important skills acquired during the time of the study is the ability to select the appropriate two boundary pixels: the "hot" and the "cold" pixel. The first pixel is completely dry, while the other is assumed completely wet. The selection of these pixels determines the appropriate coefficients (i.e.  $a$  and  $b$  coefficients) which are the internal calibration of METRIC and is dependent on the user judgement and ability to identify them. Any inappropriate selection of these pixels in METRIC calculation is a major source of error. A very thorough analysis is made as a result for every image defining hot and cold pixels. A previous knowledge of the study area is a very important prerequisite for the study. This knowledge is acquired through a series of frequent visits to the watershed. After considering the study area, the most important parameter for the selection of the "hot" and the "cold" pixels is surface temperature ( $T_s$ ). Fortunately, the temperature difference ( $dT$ ) used in METRIC is not affected by errors at the estimation of surface temperature since  $dT$  is a relative value calculated from the values at the two extreme ("hot" and "cold") anchor pixels on the image. The second significant influential parameter for the estimation of these anchor pixels is the surface albedo which is affected by the resolution of the satellite sensor, because albedo is calculated from the reflectance values of visible-near infrared and short wave bands of satellite data, and it is finally user-independent (Mokhtari, *et al.*, 2013). The third significant parameter is the computation of NDVI which is used for the calculation of several parameters in the algorithm.

During the application and analysis of METRIC a lot of blurry simplifications have been examined and corrected. The computation of Leaf Area Index (LAI) as a function of Vegetation Indices is reconstructed. SAVI index is defined again through a new



calibrated constant ( $L$ ), which is a result of a detailed analysis of a series of images. A lot of conditions throughout the same image are analyzed. The analysis reveals the influence of soil condition to SAVI index, where,  $L$  constant must be the value which tends to reduce the impact of soil wetness on the vegetation index. A new  $L$  value is developed and used at this dissertation for the Lake Karla watershed. Monin-Obukhov based iteration is also a very significant stage of the procedure because instability is a very frequent phenomenon at the area. Iterations are performed for all the study cases.

Land use classification and mapping is another tool used in this study. The classification is used for many reasons at this study. The first reason is that is very important for the assessment of momentum roughness length ( $z_{om}$ ) used for the estimation of sensible heat flux ( $H$ ) at METRIC. The second reason is that a land use classification is needed for the assessment of crop fields at the study area. This is very significant for the estimation of crop water requirements for the crops. Land use classification is also used for the estimation of the total crop area of the region and making masks deriving specific vectors which are used for the further processing when applying the methodology (subset, subtraction, etc.). Land use classification is undertaken using Landsat imagery while utilizing a handheld portable G.P.S. apparatus which is also used for verification purposes. Supervised classification is utilized for processing and maximum likelihood is chosen as the mathematical rule. Maximum likelihood is a statistical approach assuming multivariate normal distributions of pixels within classes. A pixel is then assigned to a class on the basis of its probability of belonging to a class. Finally, each pixel is assigned to the class having the highest probability of membership. Accuracy assessment of the performed classification is undertaken with success.

CropWat by the Land and Water Development Division of FAO is the tool used for the estimation of crop water requirements. The calculation of crop water requirements is one of the basic functions of CropWat, allowing the development of recommendations for improved irrigation practices, as well as planning of irrigation schedules. ET-retrieval algorithms for ET and  $ET_r$  mapping are very crucial for the application of CropWat at this dissertation. Having distributed crop coefficient values with a 30 m x

30 m spatial resolution for every crop, and every stage (initial, development, mid-season and late-season) is a very important development for CropWat 's computations. It is very important also, to mention that CropWat model in this study has been applied utilizing the actual meteorological data of 2007 and 2012 instead of the default mean monthly climatic data.

Field spectroscopy is another special tool used for the measurement of radiance, irradiance and reflectance in the field. The resulted spectral behavior of ground targets in the natural environment is used for the monitoring of their suitability over time. GER 1500 field spectro-radiometer is used in this study, which is a high performance instrument covering the ultraviolet, visible and near-infrared wavelengths from 350 nm to 1050 nm. The instrument makes a very rapid scanning, acquiring spectra in milliseconds. Using GER 1500, it is possible to calculate surface reflectance values and to convert these values into the reflectance of Landsat ETM+ bands 1, 2, 3 and 4. In other words, it is possible to convert the initial reflectance values of the 512 bands of GER 1500 (e.g. 449.81, 451.48, 453.15 nm) into reflectance for every integer value using interpolation, and then to apply relative spectral response (RSR) functions in order to filter these values. This filtering results to the matching of the reflectance values with each ETM+ band. The computation of the average within the limits of every ETM+ band obtains the equivalent in-band reflectance values. Having the equivalent in-band reflectance values, it is easy then to compute vegetation indices keeping the usual remote sensing methodology. An analysis of various vegetation indices (SAVI, EVI, EVI2, NDVI) in the study area reveals that NDVI is the most appropriate index for further processing. After acquiring accurate spectral reflectances values and computing NDVI values for the main crops of the study, it is then possible to find relationships between them and the crop coefficient values. The new ground-based NDVI values have now the capability to feature physical and crop characteristics more precisely and to incorporate them into the crop coefficient's relationship, without a previous land-use classification.

ET<sub>r</sub>F vs VI relationships are well established in remote sensing science, but there are many differences to the derived equations depended to the region which these

relationships have to be applied. This study suggests that a new relationship should be applied, taking into account the prevailing local weather, soil, and vegetation conditions. Field spectroscopy introduces a perfect opportunity to incorporate all these local conditions to the local  $ET_rF$  vs VI relationships. Tens of measurements are taken place during the growing season of 2012, and average values over each crop are utilized to finally estimate the local  $ET_rF$  vs VI relationship for the Lake Karla watershed.

One of the main problems arising when working with satellite imagery is to combine the perfect temporal and spatial resolution in order to achieve the best results according to each application. At this study MODIS imagery has been utilized producing ET and  $ET_rF$  products, but the spatial resolution is very poor compared to the results using Landsat imagery. The opposite happens when comparing the poor temporal resolution of Landsat based ET and  $ET_rF$  products with MODIS based products. For this reason, a downscaling procedure is developed in order to overcome the problems related to the poor temporal resolution of Landsat, combining the finest temporal resolution of MODIS. An important assumption for the application of the downscaling procedure is that the fine-scale variability inside a MODIS pixel remains the same from the first to the second Landsat image acquisition. Validation of the methodology is performed by comparing the initial METRIC-based crop coefficient map with the new computed one and the two maps are in good agreement. This is the reason why this downscaling methodology is finally combined with the already defined  $ET_rF$  vs VI relationships. NDVI is chosen as the appropriate VI in order to perform the internal downscaling procedure which has been described, resulting in a 30 m x 30 m daily vegetation product which now is incorporated to the already established  $ET_rF$  vs NDVI relationship.

Application of this relationship to the downscaled daily 30 m x 30 m NDVI map gives finally a new  $ET_rF$  product which is one of the prevailing innovation elements of the dissertation. Validation is performed with the already computed  $ET_rF$  map produced by METRIC. This agreement is not obtained by a pixel-by-pixel comparison, since that could put into question the total METRIC theory and this is not the scope of this study. Instead, the difference of the predicted minus the METRIC computed one is produced.

Finally, CropWat validates the good agreement between the proposed methodology and classic METRIC one, since the crop irrigation requirements values are almost the same for both cases.

In conclusion, combination of Landsat TM and ETM+ sensors, together with MODIS imagery is proved to be very successful. NDVI values derived from three different sources (GER 1500, ETM+ and MODIS) is maybe on a first thought difficult to combine, but since NDVI is defined as the ratio of Red and NIR bands, it tends to self-calibrate atmospheric impact (Agapiou *et al.*, 2011), so this issue has been overcome. Downscaling as a result gives a new high quality spatiotemporal product which is very promising for the future. Field spectroscopy is applied after the acquisition of an additional set of reflectance measurements without the use of satellite remote sensing imagery. The two sources are combined then giving new VI products which can be very well correlated with crop coefficient values. Finally, daily distributed crop coefficient values with a 30 m x 30 m spatial resolution for every crop, and every stage are derived and inserted to CropWat for the crop irrigation requirements estimation.

## 6.2 *Dissertation Innovative Elements*

Application of Remote Sensing based Surface Energy Balance is applied for the first time in Lake Karla watershed, central Greece. Analysis and mapping of actual evapotranspiration and crop coefficient is operated for monthly and daily basis through METRIC model. A descriptive analysis of this methodology reveals many blurry simplifications which traditionally have been applied to the methodology. The computation of Leaf Area Index (LAI) as well as Vegetation Indices (e.g SAVI and NDVI) is operated again on a new basis. For example SAVI vegetation index is defined again through a new calibrated constant (L). This constant is a result of a detailed analysis of a series of soil locations or conditions. This analysis reveals the influence of soil condition to SAVI index, where, L value must be the value which tends to reduce the impact of soil wetness on the vegetation index.

The combination of Landsat TM and ETM+ sensors, together with MODIS imagery is proved to be very successful. Downscaling as a result gives a new high quality spatiotemporal product which is promising for future use. Field spectroscopy is applied through the acquisition of an additional set of reflectance measurements without the use of satellite remote sensing imagery. Of course the two sources, (the satellite estimation and the field measurements) are combined then giving new vegetation indices (VI) products which can be very well correlated with crop coefficient values. This is where an integrated approach is proposed, computing daily crop coefficients with a 30 m x 30 m spatial resolution and incorporating them into CropWat model for the final computation of irrigation water needs. FAO's CropWat model has now a new challenge for the computation of water needs for the study area. Climatic data are replaced with actual meteorological data, and new crop conditions are incorporated after acquiring the new crop coefficient values and insert them manually. This methodology of course can be applied, at least, to other watersheds with similar soil and climate characteristics.

### 6.3 *Limitations*

One of the weakness elements of the whole procedure is that there is not an opportunity to validate the results with real ET or crop water requirement measurements. The reason is that there is an absence of a reliable established measurement network in the area. For this reason, an internal validation is performed instead. Initially, values of actual evapotranspiration produced by METRIC methodology are checked against the theoretical Penman-Monteith methodology. The procedure is performed at the regions close to the available meteorological stations of the study area giving satisfactory results. Then, the whole proposed methodology is tested by comparing CropWat outputs inserting  $K_c$  values derived from classical METRIC and the proposed methodology respectively. The final errors, assuming that the classical METRIC methodology is totally correct, are less than 2% of the computed crop water requirements, and this is a very satisfactory result for the whole validation of the proposed methodology. Finally, a sensitivity analysis of the possible generated errors of

CropWat model is checked against the possible error of the crop coefficients input. This analysis is based on the worst error scenario recorded from the described relative analysis. The final errors are found to be less than 5% of the computed crop water requirements.

Another important constraint to the methodology is the existence of different time scales of the sensors. Field measurements require only sunshine and availability of the sensor. It also requires availability of the personnel conducting the measurements which is a very important factor due to time-schedule difficulties. On the other hand MODIS and Landsat imagery is available only on a daily or bi-weekly basis respectively, which is a technical constraint. Weather conditions are also an important parameter which can reduce the utility of the images. Interpolation maybe is a solution but is not always the best because in many cases specific weather and soil conditions can not be sufficiently represented to the resulting product. This could be a very significant source of error to the whole methodology.

#### *6.4 Future Recommendations*

New challenges will arise applying this methodology to Landsat 8 and/or SPOT imagery from the beginning (and not only for validation). Landsat 8 for example includes additional bands, that differ from Landsat 7 but the most important is that is a new satellite, providing quality imagery without problems related with the gaps usually found on Landsat 7 SLC-off. Additionally Landsat 8's Operational Land Imager (OLI) and Thermal Infrared Sensor (TIRS) sensors provide improved signal-to-noise (SNR) radiometric performance quantized over a 12-bit dynamic range. This translates into 4096 potential grey levels in an image compared with only 256 grey levels in previous 8-bit instruments. Improved signal to noise performance will enable improved characterization of land cover state and condition which will be a very important improvement when applying to the described methodologies. Additionally, the enrichment of the meteorological stations network of the study area will provide a better tool for the estimation of local weather conditions. New meteorological data will

improve the accuracy of the computation of reference ET which is a prerequisite for the proposed methodology and as a result the accuracy of the entire METRIC application. The region will be divided into sub-regions and METRIC methodology will be applied separately for each sub-region with unique “cold” and “hot” pixels contributing to a more precise interpretation of the local soil and vegetation conditions prevailing in the region. This could result to a better final ET and  $ET_rF$  product which will lead to a more accurate correlation between  $ET_rF$  and NDVI, contributing to the final accuracy of the proposed methodology.

It is very important to state that it is very desirable to apply the proposed methodology to new regions of interest, having the same Mediterranean climatological conditions or not. Differences related to local conditions could be identified and analysed. Validation of the methodology applied to several different types of regions can establish a very useful tool for the estimation of crop water requirements worldwide.

As a final recommendation should be a creative cooperation between water scientists and space agencies resulting to the development of new sensors which will be adapted to the effective monitoring of water resources. The development of these sensors would lead to a wider development of remote sensing applications in the field of hydrology contributing crucially to water resources management and sustainable development practices.





**CHAPTER 7°**

**PUBLICATIONS RELATED WITH THE DISSERTATION**

## **7 Publications related with this dissertation**

During the period of preparation of this dissertation there was an opportunity to participate to a series of Greek and International Conferences and publications, which are chronologically presented:

- M. Spiliotopoulos, A. Loukas and L. Vasiliades, 2008. Actual evapotranspiration estimation from satellite-based surface energy balance model in Thessaly, Greece. European Geosciences Union, General Assembly 2008, Vienna, Austria, 13 - 18 April 2008.
- M. Spiliotopoulos, H. Michalopoulou and A. Loukas, 2009. Comparison of ground based and satellite derived regional actual evapotranspiration estimation for continental Greece. 6th EGU, General Assembly, Vienna, Austria, 19 - 24 April 2009, Geophysical Research Abstracts, Vol. 11, 2009 EGU2009-12585, EGU General Assembly 2009.
- M. Spiliotopoulos, A. Loukas, L. Vasiliades, 2009. Actual evapotranspiration estimation from satellite-based surface energy balance model in Thessaly, Greece. Proceedings of the common conference between Greek Committee for Water Resources Management and Hellenic Hydrotechnical Association: «Total water resources management under climate change conditions», Volos, 27-30 May 2009 (p.p. 789-796).
- M. Spiliotopoulos, A. Karioti, A. Loukas και N. Mylopoulos, 2012. Land use study for Karla lake watershed with the use of Remote Sensing. First Thessaly Environmental Conference pp. 813-818 (In Greek).
- M. Spiliotopoulos, A. Loukas, and H. Michalopoulou, 2013. Contribution to the study of regional actual evapotranspiration with the use of surface energy balance and remote sensing for central Greece. Advances in Meteorology,

Climatology and Atmospheric Physics, Eds Helmis, Costas G.; Nastos, Panagiotis. Springer Atmospheric Sciences 2013, 2013, XXX, 1278 p.

- M. Spiliotopoulos, N. Adaktylou , A. Loukas , H. Michalopoulou, N. Mylopoulos, L. Toullos, 2013. A spatial downscaling procedure of MODIS derived actual evapotranspiration using Landsat images at central Greece. Proceedings of SPIE The International Society for Optical Engineering 8795 , art. no. 879508.
- L. Toullos, G. Stancalie, P., P. Nejedlik and M. Spiliotopoulos, 2013. Sources of remote sensing data used for estimating variables in environmental change studies in agriculture. Proceedings of the International Scientific Conference "Environmental changes and adaptational strategies" Skalica, Slovakia, on 9th - 11th, September, 2013.
- G. Stancalie, A. Nertana, L. Toullos, M. Spiliotopoulos, 2014. Potential of using satellite based vegetation indices and biophysical variables for the assessment of the water footprint of crops. Proc. SPIE 9229, Second International Conference on Remote Sensing and Geoinformation of the Environment (RSCy2014), 92290K (August 12, 2014); doi:10.1117/12.2066392;http://dx.doi.org/10.1117/12.2066392.
- M. Spiliotopoulos, A. Loukas, N. Mylopoulos, L. Toullos, G. Stancalie, 2014. Investigation of spatial relationships between crop coefficients and specific ground based vegetation indices for Karla watershed, Greece. Proc. SPIE9229, Second International Conference on Remote Sensing and Geoinformation of the Environment (RSCy2014), 92290J (August 12, 2014); doi:10.1117/12.2066095; http://dx.doi.org/10.1117/12.2066095.
- Loukas, J. Tzabiras, M. Spiliotopoulos, N. Mylopoulos, 2014. Development of a district information system for water management planning and strategic decision making. Second International Conference on Remote Sensing and Geoinformation of Environment in Paphos, Cyprus, April 7-10, 2014 (pending).
- M. Romanguera, L. Toullos, G. Stancalie, M. Spiliotopoulos, P. Struzik, E. Calleja, 2014. Identification of the key variables that can be estimated using remote sensing data and needed for Water Footprint (WF) assessment. Proc. SPIE 9229, Second International Conference on Remote Sensing and Geoinformation of the

Environment (RSCy2014), 922912 (August 12, 2014); doi:10.1117/12.2066120;http://dx.doi.org/10.1117/12.2066120.

- M. Spiliotopoulos, N. Holden, A. Loukas, 2014. Leaf Area Index for the estimation of Actual Evapotranspiration using the Surface Energy Balance and Remote Sensing SEBAL (model) for central Ireland. 2014 ASABE and CSBE | SCSAB Annual International Meeting, July 13 – 16, 2014. Montreal, Quebec Canada.
- M. Spiliotopoulos, and A. Loukas, 2014. An alternative methodology for the estimation of daily crop coefficients using NDVI relationships derived from in-situ observations. European Journal of Remote Sensing (submitted).



## References

- Agapiou, A., Hadjimitsis, G.D., Georgopoulos, A., Sarris, A., Alexakis, D.D., 2012. Towards an archaeological index: identification of the spectral regions of stress vegetation due to buried archaeological remains. In: Ioannides, M., et al. (Eds.), *Lecture Notes of Computer Science*. Springer, Heidelberg, pp. 129e138. EuroMed 2012, 7616.
- Agapiou, A., Hadjimitsis, D.G., Papoutsas, C., Alexakis, D.D., Papadavid, G., 2011. The Importance of accounting for atmospheric effects in the application of NDVI and interpretation of satellite imagery supporting archaeological research: The case studies of Palaepaphos and Nea Paphos sites in Cyprus. *Remote Sensing*, 3 (12), pp. 2605-2629.
- Agapiou, A., Papadavid, G., Hadjimitsis, D., 2009, Surface reflectance retrieval from Landsat TM/ETM+ images for monitoring irrigation demand in Cyprus, 29th EARSeL Symposium, Chania, Crete, DOI: 10.3233/978-1-60750-494-8-166.
- Ahmad, M.D., Biggs, T., Turrall, H., and Scott, C.A., 2006. Application of SEBAL approach and MODIS time-series to map vegetation water use patterns in the data scarce Krishna river basin of India. *Water Science and Technology*, Vol. 53 ,10, pp.83-90.
- Alexandridis T.K., Chemin, Y., Cherif, I., Tsakoumis, G., Galanis, G., Arampatzis, G., Zalidis, G.C., Silleos, N.G., Stavrinos, E., 2008. Improving spatial resolution of agricultural water use estimation using ALOS AVNIR-2 imagery. In: *Proc. ALOS Principal Investigators Symposium 2008*, 3-7 November, Rhodes, Greece, 8 pp.
- Allen, R.G. 2001. Prediction of regional ET for the Tampa Bay, Florida watershed using SEBAL. personal communication.
- Allen, R.G., 2000. REF-ET: Reference Evapotranspiration Calculation Software for FAO and ASCE Standardized Equations. University of Idaho [www.kimberly.uidaho.edu/ref-et/](http://www.kimberly.uidaho.edu/ref-et/), (2000).

Allen, R.G., L.S. Pereira, D. Raes, D., and M. Smith. 1998. Crop evapotranspiration, guidelines for computing crop water requirements. FAO Irrig. and Drain. Paper 56, Food and Agric. Orgn. of the United Nations, Rome, Italy. 300 pp.

Allen, R.G.; Clemmens, A.J.; Burt, C.M.; Solomon, K.; O'Halloran, T., 2005. Prediction accuracy for project wide evapotranspiration using crop coefficients and reference evapotranspiration. J. Irrig. Drain. Eng., 131, 24–36.

Allen, R.G., Tasumi, M., and Trezza, R., 2007a. Satellite-based energy balance for mapping evapotranspiration with internalized calibration (METRIC): Model. ASCE J. Irrig. Drain. Eng. 133(4): 380-394.

Allen, R.G., Tasumi, M., Morse, A., Trezza, R., Wright, J.L., Bastiaanssen, W., Kramber, W., Lorite, I. And Robinson, C.W., 2007b. Satellite-based Energy Balance for Mapping Evapotranspiration with Internalized Calibration (METRIC) – applications. Journal of Irrigation and Drainage Engineering, 133, 395-406 .

Allen, R.G., M., Robison, C.W., Garcia, M., Trezza, R., Tasumi, M., and Kjaersgaard, J., 2010. ET<sub>F</sub> vs NDVI Relationships for Southern Idaho for Rapid Estimation of Evapotranspiration. Report to Idaho Department of Water Resources (IDWR), <http://www.idwr.idaho.gov/>.

Allen, R., Irmak, A., Trezza, R., Hendrickx, J.M.H., Bastiaanssen, W., Kjaersgaard, J., 2011. Satellite-based ET estimation in agriculture using SEBAL and METRIC. Hydrological Processes Volume 25, Issue 26, 30 December 2011, pp. 4011-4027.

Al-Ahmadi F.S., Hames A.S., 2009. Comparison of Four Classification Methods to Extract Land Use and Land Cover from Raw Satellite Images for Some Remote Arid Areas, Kingdom of Saudi Arabia. Journal of King Abdulaziz University, Earth Sciences 20 (1), pp. 167-191.

Ananiadis, C.I., 1956. Limnological study of Lake Karla. Bull.Inst. Océanogr. 1083:1-19.

Anderson, J.R., Hardy, E.E., Roach, J.T. and Witmer, R.E., 1976. A land use and land cover classification system for use with remote sensor data. U.S. Geological Survey Professional Paper, No. 964, USGS, Washington, D.C.

Artigas, F.J., Yang, J.S., March 2006. Spectral Discrimination of Marsh Vegetation Types in the New Jersey Meadowlands, USA. *Wetlands*, 26(1), 271-277. MDOC 2006-008.

ASCE-EWRI, 2005. The ASCE Standardized Reference Evapotranspiration Equation Environmental and Water Resources Institute of the ASCE, Report by the Task Committee on Standardization of Reference Evapotranspiration. <http://www.kimberly.uidaho.edu/water/asceewri/ascestdetmain2005.pdf>

Asner, G.P., Wessman, C.A., Bateson, C.A., Privette, J.L., 2000. Impact of Tissue, Canopy, and Landscape Factors on the Hyperspectral Reflectance Variability of Arid Ecosystems, *Remote Sensing of Environment*, 74(1), 69-84.

Bastiaanssen WGM, 2000. SEBAL-based sensible and latent heat fluxes in the irrigated Gediz Basin, Turkey. *Journal of Hydrology* 229:87-100.

Bastiaanssen, WGM, Menenti, M, Feddes, RA, Holtslag, AAM, 1998a. A remote sensing surface energy balance algorithm for land (SEBAL): 1. Formulation. *J. Hydrology*, 212-213: 198-212.

Bastiaanssen, WGM, Pelgrum, H, Wang, J, Ma, Y, Moreno J, Roerink, GJ, van der Wal T, 1998b. The Surface Energy Balance Algorithm for Land (SEBAL): Part 2 validation, *J. Hydrology*, 212-213: 213-229.

Bastiaanssen W.G.M., Noordman E.J.M., Pelgrum, H., Davids, G., Thoreson, B.P., Allen, R.G., 2005. SEBAL Model with Remotely Sensed Data to Improve Water Resources Management under Actual Field Conditions. *ASCE J. of Irrigation and Drainage Engineering*, 131: 85-93.

Batra, N., Islam, S., Venturini, V., Bisht, G., Jiang, L., 2006. Estimation and comparison of evapotranspiration from MODIS and AVHRR sensors for clear sky days over the Southern Great Plains. *Remote Sensing of Environment*. 103, 1 -15.

Bausch, W. C., and Neale, C. M. U., 1989. Spectral Inputs Improve Corn Crop Coefficients and Irrigation Scheduling. *Transactions of the ASAE*, 32(6):1901-1908.

Benedetti, R., & Rossinni, P., 1993. On the use of NDVI profiles as a tool for agricultural statistics: The case study of wheat yield estimate and forecast in Emilia Romagna. *Remote Sens. Environ.*, 45, 311–326.

Bhandari, S. , Phinn, S. , Gill, T., 2006. Preparing Landsat Image Time Series (LITS) for monitoring changes in vegetation phenology in Queensland, Australia. *Remote Sensing Vol. 4, Issue 6, June 2012*, pp. 1856-1886.

Bierkens, M.F.P., Finke, P.A. and Willigen, D.E., 2000. Upscaling and downscaling methods for environmental research. Wageningen University and Research Centre, Kluwer Academic Publishers.

Bisht, G., Venturini, V., Islam, S., Jiang L., 2005. Estimation of the net radiation using MODIS (Moderate Resolution Imaging Spectroradiometer) data for clear sky days. *Remote Sens. Environ.* 97, 52-67.

Blaney, H. F. and Criddle, W. D., 1950. Determining water requirements in irrigated areas from climatological and irrigation data. USDA, SCS, SCS-TP96, 48pp.

Blanta A., N.R. Dalezios, A. Maliara and N. Spyropoulos, 2011. Monitoring cotton crop evapotranspiration based on satellite data. *Proceedings, 5th HAICTA International Conference on Information Systems in Sustainable Agriculture, Food and Environment, 8-11 September, 2011, Skiathos, Greece, Volume I*, 1-12.



Boegh, E.; Soegaard, H.; Hanan, N.; Kabat, O.; Lesch, L., 1998. A remote sensing study of the NDVI-Ts relationship and the transpiration from sparse vegetation in the Sahel based on high resolution data. *Remote Sens. Environ.* 1998, 69, 224–240.

Bouchet, R. J., 1963. Evapotranspiration réelle et potentielle, signification climatique. *Proc. IASH General Assembly*, Vol. 62, International Association of Science and Hydrology, 134–142.

Bruce, C. M. and Hilbert, D. W., 2006. Pre-processing methodology for Application to Landsat TM/ETM+ Imagery of the Wet Tropics. Research report, no. 44; Cairns, Qld. : Rainforest CRC. Research report (Cooperative Research Centre for Tropical Rainforest Ecology and Management (Australia)), no. 44.

Brutsaert, W., 1982. *Evaporation into the Atmosphere, Theory, History, and Applications*, D. Reidel, Boston, MA, pp 299.

Brutsaert, W.H. & Sugita, M. 1992. Application of self-preservation in the Diurnal evolution of the surface energy budget to determine daily evaporation. *Journal of Geophysical Research* 97(D17): 18377–18382.

Burba, G.G., Verma, S.B., Kim, J., 1999. Surface energy fluxes of *Phragmites australis* in a prairie wetland. *Agricultural and Forest Meteorology*, 94, 31-51.

Byun, K., Liaqat, U.W., Choi, M., 2014. Dual-model approaches for evapotranspiration analyses over homo- and heterogeneous land surface conditions. *Agricultural and Forest Meteorology* Volume 197, 15 October 2014, Pages 169-187.

Caprio, J.M., 1974. The solar thermal unit concept in problems related to plant development and potential evapotranspiration. *Phenology and Seasonality Modeling* (H. Leith, ed.), Springer-Verlag, New York, pp. 353-364.

Carlson, T.N., Capehart, W.J., Gillies, R.r., 1995. A new look at the simplified method for remote sensing of daily evaporation. *Remote Sensing of Environment*. 54, 161-167.

Cartalis, K., and Feidas, C., 2006. Principles and applications of Remote Sensing. Giourdas Publications. ISBN 9603875201 (In Greek).

Chamoglou, M., Papadimitriou D., Kagalou, I, 2014. Key-Descriptors for the Functioning of a Mediterranean Reservoir: The case of the New Lake Karla-Greece. *Environ. Process. Springer*. 1: pp. 127-135.

Chavez, J.L., Neale, C.M.U., Hipps., L.E., Prueger. J.H., and Kustas, W.P., 2005. Comparing aircraft-based remotely sensed energy balance fluxes with eddy covariance tower data using heat flux source area functions. *Journal of Hydrometeorology*, AMS 6(6): 923-940.

Chebouni, A., Lo Seen, D., Njoku, E.G., and Monteny, B., 1996. Examination of the difference between radiative and aerodynamic surface temperatures over sparsely vegetated surfaces. *Remote sensing of Environment* 58(2): 176-186.

Choudhury, B.J., Ahmed, N.U., Idso, S.B., Reginato, R.J. and Daughtry, C.S.T., 1994. Relations between evaporation coefficients and vegetation indices studied by model simulations. *Remote Sens. Environ*. 50: 1-17.

Cleugh, H.A., Leuning, R., Mu, Q., 2007. Running, S.W. Regional evaporation estimates from flux tower and MODIS satellite data. *Remote Sens. Environ*. 106, 285-304.

Coll, C., Caselles, V., Sobrino, J.A., and Valor, E., 1994. On the atmospheric dependence of the split-window equation for land surface temperature. *International Journal of Remote sensing*, Vol. 15, pp. 105-122.

Congalton, R. and K. Green. 2009. Assessing the Accuracy of Remotely Sensed Data: Principles and Practices. 2nd Edition. CRC/Taylor & Francis, Boca Raton, FL 183p. - See more at: <http://www.nre.unh.edu/faculty/congalton#sthash.y2eZ5jxt.dpuf>.

Costandinidis, D, 1978. Hydrodynamique d'un systeme aquifere heterogene, Hydrogeologie de la Thessalie. Orientale. Dissertation, University of Grenoble (in French).

Crago, R.D. 1996. Comparison of the evaporative fraction and the Priestley–Taylor  $\alpha$  for parameterizing daytime evaporation. Water Resources Research 32(5): 1403–1409.

Crago, R., Friedl, M., Kustas, W., and Wang, Y., 2004. Investigation of aerodynamic and radiometric land surface temperatures. NASA Sci. Tech. Aerospace Reports (STAR) 42(1). Available at: [www.sti.nasa.gov/Pubs/star/starhtml](http://www.sti.nasa.gov/Pubs/star/starhtml).

D'Urso, G. Simulation and management of on-demand irrigation systems, PhD Thesis, Netherlands. Wageningen University, 2001.

D'Urso, G., Calera B., A., 2006. Operative approaches to determinate crop water requirements from Earth Observation data: Methodologies and Applications. Earth observation for vegetation monitoring and water management. Conference Proceedings, Naples, 9-10, Nov., 2005. 852, 14-25.

Dalezios, N.R., Loukas, A., and Bampzelis, D., 2002. Spatial Variability of Reference Evapotranspiration in Greece. Physics and Chem. of the Earth, 27(23-24), 1031-1038.

Dalezios, N.R., Mplanta, A., Domenikiotis, C., 2011. Remotely Sensed Cotton Evapotranspiration for Irrigation Water Management in Vulnerable Agriculture of Central Greece. JITAG. Journal of Information Technology Agriculture. Vol. 4, No 1,1-14.

Dalezios, N.R. and Spyropoulos, N.V., 2015: Remote Sensing in Drought Quantification and Assessment. Book chapter in Vol.3 of Handbook of Drought and Water Scarcity, published by Taylor and Francis (in press).

DeBruin H.A.R., and Keijman, J.K., 1979. The Priestley-Taylor evaporation model applied to a large shallow lake in the Netherlands, *Journal of Applied Meteorology*, 18, 898-903.

DeFries, R. and Belward, A. S., 2000. Global and regional land cover characterization from satellite data; an introduction to the Special Issue. *Int.J.Remote Sensing*, 2000, vol.21, no. 6&7, 1083-1092.

Delikaroglou. D., 2008. The Hellenic Positioning System (HEPOS) and its foreseeable implications on the Spatial Data Infrastructure in Greece. *Tech. Chron. Sci. J. TCG I* (1-2): 95–103.

Diak, G.R., Rabin, R.M., Gallo, K.P., Neale, C.M., 1995. Regional-scale comparisons of NDVI, soil moisture indices from surface and microwave data and surface energy budgets evaluated from satellite and in-situ data. *Remote Sensing Reviews*. 12, 355-382.

Dodouras, S., Lyratzaki, I. and Papayannis, T., 2014. Lake Karla Walking Guide. Mediterranean Institute for Nature and Anthropos (MED-INA), Athens, Greece.

Domenikiotis, C., Spiliotopoulos, M., Tsiros, E., and Dalezios, N.R., 2004. Early Cotton Yield Assessment by The use of the NOAA/AVHRR derived drought Vegetation Condition Index in Greece, *International Journal of Remote Sensing*, Volume 25, Number 14, pp 2807 - 2819.

Domenikiotis, C., Spiliotopoulos, M., Tsiros, E., and Dalezios, N.R, 2004. Early cotton production assessment in Greece based on the combination of the drought vegetation

condition index (VCI) and Bhalme and Mooley drought index (BMDI), *International Journal of Remote Sensing*, Volume 25, Number 23, pp 5373–5388.

Domenikiotis, C., Tsiros, E., Spiliotopoulos, M., Dalezios, N.R., 2004. Use of NOAA/AVHRR-based Vegetation Condition Index (VCI) and Temperature Condition Index (TCI) for drought monitoring in Thessaly, Greece. *Proceedings of EWRA Symposium - Water Resources Management: Risks and Challenges for the 21st Century*, Izmir, Turkey, 2-4 September 2004 (Edited by: N.B. Harmancioglu, O.Fistikoglu, Y. Dalkilic and A. Gul), pp 769-782.

Domenikiotis, C., Spiliotopoulos, M., Tsiros, E., and Dalezios, N.R., 2005. Remotely sensed estimation of annual cotton production under different environmental conditions in Central Greece, *Physics and Chemistry of the Earth*, Volume 30, Issues 1-3, pp. 45-52.

Du, J., Song, K., Wang, Z., Zhang, B., Liu, D., 2013. Evapotranspiration Estimation Based on MODIS Products and Surface Energy Balance Algorithms for Land (SEBAL) Model in Sanjiang Plain, Northeast China. *Chin. Geogra. Sci.* 2013 Vol. 23 No. 1 pp. 73–91. doi: 10.1007/s11769-013-0587-8

Duchemin, B., Hadria, R., Erraki, S., Boulet, G., Maisongrande, P., Chehbouni, A., Escadafal, R., Ezzahar, J., Hoedjes, J. C. B., Kharrou, M. H., Khabba, S., Mougenot, B., Olioso, A., Rodriguez, J.-C., and Simonneaux, V., 2006. Monitoring wheat phenology and irrigation in Central Morocco: On the use of relationships between evapotranspiration, crops coefficients, leaf area index and remotely-sensed vegetation indices. *Agricultural Water Management* 79(1):1-27.

Duffie, J.A., & Beckman, W.A., 1980. *Solar Engineering of Thermal Processes*, John Wiley & Sons, New York.

Europe's Environment. The Dobris Assessment, 1995. EEA (European Environment Agency).

FAO, 1977. Guidelines for predicting crop water requirements by J. Doorenbos & W.O. Pruitt. FAO Irrigation and Drainage Paper No. 24. Rome.

FAO, 1979. Yield response to water by J. Doorenbos & A. Kassam. FAO Irrigation and Drainage Paper No. 33. Rome.

FAO, 1992. CROPWAT, a computer program for irrigation planning and management by M. Smith. FAO Irrigation and Drainage Paper No. 26. Rome.

FAO 1993. CLIMWAT for CROPWAT, a climatic database for irrigation planning and management by M. Smith. FAO Irrigation and Drainage Paper No. 49. Rome.

FAO, 1998. Crop evapotranspiration by R. Allen, LA. Pereira, D. Raes & M. Smith. FAO Irrigation and Drainage Paper No. 56. FAO, Rome.

Fleming, D.J., 2006. Effect of Relative Spectral Response on Multi-Spectral Measurements and NDVI from different Remote Sensing Systems. PhD Thesis. University of Maryland, USA.

Gamon, J.A.; Field, C.B.; Goulden, M.; Griffn, K.; Hartley, A.; Joel, G.; Penuelas, J.; Valentini, R., 1995. Relationships between NDVI, canopy structure and photosynthesis in three Californian vegetation types. *Ecol. Appl.*, 5, 28–41.

Giannopoulos D., 2010. Temporal land use mapping for Nafplio, Argolis using multispectral remote sensing data. Msc Thesis. Agriculture University of Athens (In Greek).

Gleick, P.H., 1993. Water in Crisis: A Guide to the World's Freshwater Resources. Oxford University Press.

Glenn, E. P., Neale, C. M. U., Hunsaker, D. J., and Nagler, P. L., 2011. Vegetation index-based crop coefficients to estimate evapotranspiration by remote sensing in agricultural and natural ecosystems. *Hydrological Processes*, 25, pp. 4050–4062.

Gnardelli ,T., 2004. Biodiversity in Greece and the role of Natura 2000 Network. Hellenic Court of Audit.

Goward, S., Cruickshanks, G.D., Hope, A., 1985. Observed relation between thermal emission and reflected spectral radiance of a complex vegetated landscape. *Remote Sensing of Environment*, 18, 137-146.

Gowda, P.H., Chávez, J.L., Colaizzi, P.D., Evett, S.R., Howell, T.A., Tolk, J.A., 2007. Remote sensing based energy balance algorithms for mapping ET: Current status and future challenges. *Transactions of the ASABE*, 50 (5), pp. 1639-1644.

Greek Ministry of Environment, Regional Planning and Public Works, 1999. Lake Karla's Restoration: Environmental Technical Report, Cost Benefit Study and Support Studies. Athens, Greece: Greek Ministry of Environment, Regional Planning and Public Works (In Greek).

Gulik, T.V.D., and Nyvall, J., 2001. Crop coefficients for use in irrigation scheduling. Water Conservation Factsheet No. 577.100-5. Ministry of Agriculture, British Columbia, Canada. <http://www.agf.gov.bc.ca/resmgmt/publist/500Series/577100-5.pdf>

Hargreaves, G.H. 1974. Estimation of potential and crop evapotranspiration. *Transactionsofthe ASAE* 17(4):701-704.

Hendrickx, J.M.H. and Hong, S.H., 2005. Mapping sensible and latent heat fluxes in arid areas using optical imagery. *Proceedings of SPIE*, 5811, 169-170.

Hong H., Hendrickx J., and Borchers B., 2012. Down scaling of SEBAL derived evapotranspiration maps from MODIS (250) to Landsat (30 m) scales. *International Journal of Remote Sensing*, Vol. 32, 6457-6477.

Huete, A., Didan, K., Miura, T., Rodriguez, E.P., Gao, X., Ferreira, L.G., 2002. Overview of the radiometric and biophysical performance of the MODIS vegetation indices. *Remote Sens. Environ.* 2002, 83, 195-213.

Hubbard, K.G., Sivakumar, M.V.K., 2000. Eds. *Automated Weather Stations for Applications in Agriculture and Water Resources Management: Current Use and Future Perspectives*. In *Proceedings of an International Workshop*, Lincoln, NE, USA, 6–10 March 2000.

Huete, A.; Justice, C.O.; Van Leeuwen, W. MODIS Vegetation Index (MOD13): Algorithm Theoretical Basis Document; 2011. Available online: [http://modis.gsfc.nasa.gov/data/atbd/atbd\\_mod13.pdf](http://modis.gsfc.nasa.gov/data/atbd/atbd_mod13.pdf) (accessed on 8 February 2011).

Hunsaker, D. J., Pinter, P. J., Jr., Barnes, E. M., and Kimball, B. A., 2003. Estimating cotton evapotranspiration crop coefficients with a multispectral vegetation index. *Irrig. Sci.*, 22(2), 95–104.

Hunsaker, D.J., Pinter, P.J., Jr., Kimball, B.A., 2005. Wheat basal crop coefficients determined by normalized difference vegetation index. *Irrig. Sci.*, 24, 1–14.

Hydromentor, 2014. Development of an integrated system for monitoring and managing the quantity and quality of water resources in rural catchments under climate change. Application in the basin of Lake Karla Greek: 3.1 Land use report. Greek Ministry of Education.

Idso, S.B., Reginato, R.J., and Jackson, R.D., 1977. An equation for potential evaporation from soil, water and crop surfaces adaptable to use by remote sensing. *Geophys. Res. Letters* 4: 17, 187-188.



Irmak, S., 2001. Estimating Crop Evapotranspiration from Reference Evapotranspiration and Crop Coefficients, University of Nebraska-Lincoln Extension, USA.

Irmak, A., Kamble, B., 2009. Evapotranspiration data assimilation with genetic algorithms and SWAP model for on-demand irrigation. *Irrig. Sci.* 28, 101–112.

Irmak, S., 2010. Nebraska water and energy flux measurement, modeling, and research network (NEBFLUX). *Trans. ASABE* 2010, 53, 1097–1115.

Irmak, A., Ratcliffe, I., Ranade, P., Hubbard, K., Singh, R.K., Kamble, B., Kjaersgaard, J., 2011. Estimation of land surface evapotranspiration with a satellite remote sensing procedure. *Great Plains Res.* 2011, 21, 73–88.

Irmak, I., 2012. *Evapotranspiration - Remote Sensing and Modeling*. ISBN 978-953-307-808-3, 526 pages, Publisher: InTech, DOI: 10.5772/725.

Jackson, R.D., Idso, S.B., Reginato, R.J., Pinter, P.J., 1981. Canopy temperature as a crop water stress indicator. *Water Resources Res.*, 17, 1133-1138.

Jayanthi, H.; Neale, C.M.U.; Wright, J.L., 2000. Seasonal Evapotranspiration Estimation Using Canopy Reflectance: A Case Study Involving Pink Beans. In *Proceedings of Remote Sensing and Hydrology*, Santa Fe, NM, USA, 2–7 April 2000; pp. 302–305.

Jensen, M.E. and Haise, H.R., 1963. Estimating evapotranspiration from solar radiation. *J. Irrig. Dir. ASCE* 89Q 15-41.

Jensen, M.E., Burman, R.D., Allen, R.G., 1990. Eds. *Evapotranspiration and Irrigation Water Requirements*. ASCE Manuals and Reports on Engineering Practices No. 70., Am. Soc. Civil Engrs., New York, NY, 360 p.

Jiang, L. and Islam, S., 1999. A methodology for estimation of surface evapotranspiration over large areas using remote sensing observations. *Geophys. Res. Lett.* 26, 2773-2776.

Jiang, Z., Huete, A., Didan, K., and Miura, T., 2008. Development of a Two-Band Enhanced Vegetation Index without a Blue Band. *Remote Sensing of Environment* 112: 3833–45.

Jonch-Clausen, T., Fugl, J., 2001. Firming up the conceptual basis of integrated water resources management. *International Journal of Water Resources Development* 17 (4), pp. 501-510.

Ju, J. , Roy, D.P., 2008. The availability of cloud-free Landsat ETM+ data over the conterminous United States and globally *Remote Sensing of Environment* Vol. 112, Issue 3, 18 March 2008, pp. 1196-1211.

Justice, C.O. , Townshend, J.R.G., Vermote, E.F., Masuoka, E., Wolfe, R.E, Saleous, N., Roy, D.P., Morisette, J.T., 2002. An overview of MODIS Land data processing and product status. *Remote Sensing of Environment* Vol. 83, Issue 1-2, pp. 3-15.

Kalavrouziotis, I.K., Sakellariou-Makrantonaki, M.S., Vagenas, I.N. , Lemesios, I., 2006. Assessment of water requirements of crops for the reuse of municipal wastewaters from the wastewater treatment plant at Patras, Greece. *International Journal of Environment and Pollution*. Volume 28, Issue 3-4, 2006, p.p. 485-495.

Kalma, J.D., McVicar, T.R., McCabe, M.F., 2008. Estimating land surface evaporation: A review of methods using remotely sensed surface temperature data *Surveys in Geophysics* 29 (4-5) , pp. 421-469.

Kamble, B., Irmak, A., 2008. Assimilating Remote Sensing-Based ET into SWAP Model for Improved Estimation of Hydrological Predictions. In *Proceeding of the 2008 IEEE International Geoscience and Remote Sensing Symposium*, Boston, MA, USA, 7–11 July

2008; Volume 3, doi: 10.1109/IGARSS.2008.4779530.

Kamble, B., Kilic, A., and Hubbard, K., 2013. Estimating crop coefficients using remote sensing-based vegetation index. *Remote Sensing*. Vol. 5, Issue 4, pp. 1588-1602.

Kanellou, E., C. Domenikiotis and N.R. Dalezios, 2006. Spatially Distributed Potential Evapotranspiration based on NOAA/ AVHRR Satellite Data and GIS, International Conference on: Information Systems in Sustainable Agriculture, Agroenvironment and Food Technology, 20-23 September 2006, Volos, Greece, 831-838.

Karioti K., 2013. Land use and water needs mapping for Lake Karla watershed. MSc Thesis. University of Thessaly, Greece. (In Greek).

Kaufman, Y.J., Sendra, C., 1988. Algorithm for automatic atmospheric corrections to visible and near- IR satellite imagery. *International Journal of Remote Sensing*. Vol. 9, Issue 8, 1988, pp. 1357-1381.

Kerkides, P., Michalopoulou, H., Papaioannou G., Pollatou R., 1996. Water balance estimates over Greece. *Agricultural Water Management*. Vol. 32, pp. 85-104.

Khalaf, Adla, Jamil, 2010. Spatial and Temporal Distribution of Groundwater Recharge in the West Bank Using Remote Sensing and GIS Techniques, Durham theses, Durham University. Available at Durham E-Theses Online: <http://etheses.dur.ac.uk/442/>

Kokkinos, K., P. Sidiropoulos, L. Vasiliades, A. Loukas, N. Mylopoulos, and A. Liakopoulos, 2009. Integrated Modelling of Surface Water and Groundwater Through OpenMI: The Case of Lake Karla Watershed. *HydroEco 2009 – 2nd International Multidisciplinary Conference on Hydrology and Ecology “Ecosystems Interfacing with Groundwater and Surface Water”*, 20-23 April 2009, Vienna, Austria.

Kondoh, A., 1994. Comparison of the evapotranspiration in Monsoon Asia estimated from different methods, J. of Japanese Assoc. of Hydrol. Sci., 24, 1 1-30 (in Japanese with English abstract).

Kustas, W.P., and Daughtry, C.S.T., 1990. Estimation of the soil heat flux/net radiation ratio from multispectral data. Agric. Forest Meteorology 49(3): 205-223.

Kustas, W.P., and Norman, J.M., 1996. Use of remote sensing for evapotranspiration monitoring over land surfaces. Hydrol. Sci, J. 41(4): 495-516.

Kustas, W.P., Li F, Jackson, T.J., Prueger, J.H., MacPherson, J.I., Wolde, M., 2004. Effects of remote sensing pixel resolution on modeled energy flux variability of croplands in Iowa. Remote Sens Environ 92:535–547.

Lapidou, C., Kakoulidis, I., Loukas, A., 2011. Ecosystem simulation modeling of nitrogen dynamics in the restored lake Karla in Greece. Desalination and Water Treatment. Vol. 33, Issue 1-3, pp. 61-67.

Li, Z.-L., Tang, R., Wan, Z., Bi, Y., Zhou, C., Tang, B., Yan, G., (...), Zhang, X. A, 2009. A review of current methodologies for regional Evapotranspiration estimation from remotely sensed data. Sensors, 9 (5), pp. 3801-3853.

Liakatas A, and Anadranistakis, M, 1992. Derived meteorological parameters: Evapotranspiration, Hydroscope: Creation of a National Databank for Hydrological and Meteorological Information, Contractor: Department of Water Resources, Hydraulic and Maritime Engineering – National Technical University of Athens, Report 5/4, Hellenic National Meteorological Service, Athens, December 1992, 31 pages.

Liakatas A., and Anadranistakis, M., 1992. Secondary Meteorological Parameters: Evapotranspiration. Hydroskopio, Stride Hellas Programme. Development of a National Data Bank for Hydrological and Meteorological Information, Athens (In Greek).

Liang, S., 2004. Quantitative Remote Sensing of Land Surfaces. John Wiley and Sons, Inc.

Lillesand, T.M. and Kiefer, R.W., 2000. Remote Sensing and Digital Image Interpretation, Wiley, New York, 724 p.

Linacre, E.T., 1977. A simple formula for estimating evaporation rates in various climates, using temperature data alone. *Agricultural Meteorology* 18:409-424.

Loheide II, S.P., and Gorelick, S.M., 2005. A local-scale high-resolution evapotranspiration mapping algorithm (ETMA) with hydroecological applications at riparian meadow restoration sites. *Remote Sensing of Environment* 98(2-3): 182-200.

Loukas, A., N. Mylopoulos, K. Kokkinos, P. Sidiropoulos, L. Vasiliades and A. Liakopoulos, 2008. The effect of spatial discretization in integrated modeling of surface and groundwater hydrology through OpenMI. *International Interdisciplinary Conference on Predictions for Hydrology, Ecology and Water Resources Management – Using Data and Models to Benefit Society*, Prague, Czech Republic, 2008.

Loukas, A., Mylopoulos, N., Vasiliades, L., 2007. A modeling system for the evaluation of water resources management strategies in Thessaly, Greece. *Water Resources Management* 21 (10), 1673-1702.

Loukas, A., L. Vasiliades, C. Domenikiotis and N.R. Dalezios, 2004. Water Balance of Forested Mountainous Watersheds Using Satellite Derived Actual Evapotranspiration. *Remote Sensing 2004*, International Society for Optical Engineering (SPIE), Barcelona, 8-12 September 2004, 5232, 456-466.

Loukas, A., L. Vasiliades, C. Domenikiotis and N.R. Dalezios, 2006. Regional Estimation of NDVI-Derived Actual Evapotranspiration for Water Balance Modeling” *International Symposium “GIS and Remote Sensing: Environmental Applications”*, Volos, 7-9

November 2003, pp 277-286.

Loukas, A., L. Vasiliades, C. Domenikiotis, and N.R. Dalezios, 2005. Basin-wide Actual Evapotranspiration Estimation Using NOAA/AVHRR Satellite Data. *Physics and Chemistry of the Earth*, Vol. 30, 1-3, pp. 69-79.

Luo, Y., Trishchenko, A.P., Khlopenkov, K.V., 2008. Developing clear- sky, cloud and cloud shadow mask for producing clear-sky composites at 250-meter spatial resolution for the seven MODIS land bands over Canada and North America. *Remote Sens Environ* 112:4167–4185.

Mahairas, A.E., 1995. Final Study of the Karla Reservoir and Associated Works, Vol. 1. Technical Review, Greek Ministry of the Environment, Athens, in Greek.

Makkink, G.F., 1957. Testing the Penman formula by means of lysimeters. *Journal of the Institution of Water Engineers* 11(3):277-288.

Manevski, K., Manakos, I., Petropoulos, G.P., Kalaitzidis, C., 2011. Discrimination of common Mediterranean plant species using field Spectroradiometry. *International Journal of Applied Earth Observation and Geoinformation* 13, 922–933.

Marica A., & Cuculeanu, V., 1999. Uses of a decision support system for agricultural management under different climate conditions, Abstracts Volume of the 4th European Conference on Applications of Meteorology (ECAM99), Norrköping, Sweden, 13-17 September. p. 135.

McCloy, K.R., 2010. Development and Evaluation of Phenological Change Indices Derived from Time Series of Image Data, *Remote Sensing*, 2, 2442-2473.

McMahon, T. A., Peel, M. C., Lowe, L., Srikanthan, R. ,and McVicar T. R., 2013. Estimating actual, potential, reference crop and pan evaporation using standard

meteorological data: a pragmatic synthesis. *Hydrol. Earth Syst. Sci.*, 17, 1331–1363, 2013. doi:10.5194/hess-17-1331-2013.

Mendicino G., and Senatore A., 2012. The Role of Evapotranspiration in the Framework of Water Resource Management and Planning Under Shortage Conditions. DOI: 10.5772/19171.

Menenti, M., and Choudhury, 1993. Parameterization of Land Surface evapotranspiration using a location dependent potential evapotranspiration and surface temperature range. In *Proc. Exchange Processes at the Land Surface for a Range of Space and Time Scales*, 561-568. Bolle et al., eds. IAHS Publication 212. International Association of Hydrological Sciences.

Menenti, M., Azzali, S., and D'Urso, G., 1996. Remote sensing , GIS and hydrological modelling for irrigation management. In: *Sustainability of Irrigated Agriculture* (ed. By L. S. Pereira et al.), 453-472. Kluwer Academic Publishes, The Netherlands.

Menzel, L., E. Teichert and Weiß, M., 2007. Climate change impact on the water resources of the semi-arid Jordan region. In: M. Heinonen, Ed.: *Proc. 3rd International Conference on Climate and Water*, Helsinki, 320-325.

Michalopoulou, H. and Papaioannou, G., 1991. Reference crop evapotranspiration over Greece. *Agricultural Water Management*, 20, 209-221.

Migdakos, E., and Gemtos, T., 1998. Relationship between growing degree days and phenological stages of cotton growth in Greece—a case study of Karditsa prefecture. *Proceedings of the International Symposium on Applied Agrometeorology and Agroclimatology*, 24–26 April 1996, Volos, Greece, edited by N. R. Dalezios (Luxembourg: Office for Official Publications of the European Communities), pp. 425–430.

Milton, E. J., Rollin, E.M., Emery, D.R., 1995. Advances in field spectroscopy, Advances in Environmental Remote Sensing (ed. F.M. Danson and S.E. Plummer), John Wiley & Sons, Chichester.

Milton, E. J., 1987. Principles of field spectroscopy, International Journal of Remote Sensing, 8, 1807-1827.

Mimikou M., 2005. Water resources in Greece : Present And Future. Global NEST Journal, Vol 7, No 3, pp 313-322.

Ministry of the Environment, Planning and Public Works / Public Works Secretariat – Directorate of Land Reclamation Works, 2009. Presentation: Restoration of Lake Karla. Mitsakaki, C., Agatza-Balodimou, A.M., Papazissi, K., July 2006. Geodetic reference frames transformations. Survey Review 38 (301): 608–618.

Mitsakaki, C., Agatza-Balodimou, A.M., Papazissi, K., July 2006. Geodetic reference frames transformations. Survey Review 38 (301): 608–618.

Mkhwanazi M.M., and Cavez, J.L., 2013. Mapping evapotranspiration with the remote sensing ET algorithms METRIC and SEBAL under advective and non-advective conditions: accuracy determination with weighing lysimeters. Hydrology Days 2013, Colorado State University, U.S.A.

MODIS Reprojection Tool (MRT) Manual, 2011. Release 4.1. Land Processes DAAC USGS Earth Resources Observation and Science (EROS) Center.

Mokhtari, M.H., Ahmad., B., Hoveidi, H., Busu, I., 2013. Sensitivity analysis of METRIC – Based Evapotranspiration Algorithm. Int. J. Environ. Res., 7(2):407-422.

Monin, AS, Obukhov AM, 1954. Basic laws of turbulent mixing in the surface layer of the atmosphere. Tr. Akad. Nauk SSSR Geofiz. Inst 24: 163–187.



Monteith, J. L. , 1981. Evaporation and surface temperature. Quarterly Journal of the Royal Meteorological Society, 107, 1–27.

Monteith, J. L., 1965: Evaporation and Environment. - Symp. Soc. Expl. Biol. 19, 205-234.

Moran, M.S., Clarke, T.R., Inoue, Y., Vidal, A., 1994. Estimating crop water deficit using the relationship between surface-air temperature and spectral vegetation index. Remote Sensing of Environment, 49, 246-363.

Moran, M.S., Rahman, A.F., Washburne, J.C. and Kustas, W.P., 1996. Combining the Penman-Monteith equation with measurements of surface temperature and reflectance to estimate evaporation rates of semiarid grassland. Agricultural and Forest Meteorology, 80, 87-109.

Morton, F. I., 1965: Potential evaporation and river basin evaporation. ASCE J. Hydraul. Div., 102 (HY3), 275–291.

Moustaka, E, Mylopoulos, N., Loukas, A., 2002. Assessment of the restored Lake Karla operation under different hydrological and water demand scenarios. Protection and Restoration of the Environment: 2002, July 1 –July 5; Skiathos, Greece: 207-215.

Muramatsu, K., Furumi, S., Fujiwara, N., Hayashi, A., Daigo, M. and Ochiai, F., 2000. 'Pattern decomposition method in the albedo space for Landsat TM and MSS data analysis', International Journal of Remote Sensing, 21:1, 99 - 119.

Mylopoulos, N., Sidiropoulos, P., 2008. Groundwater management under hydrogeologic uncertainty in an overexploited aquifer, 33rd International Geological Congress, Oslo, Norway.

Neale, C.M.U., Bausch, W.C., and Heerman., D. F., 1989. Development of reflectance-based crop coefficients for corn. Transactions of the ASAE, 32(6): 1891-1899.

O'Connell, J., Connolly, J., Vermote, E.F., Holden N.M., 2013. Radiometric normalization for change detection in peatlands: a modified temporal invariant cluster approach, *International Journal of Remote Sensing*. Vol. 34, Issue 8.

Olioso A, Chauki H, Courault D, Wigneron J.P., 1999. Estimation of Evapotranspiration and Photosynthesis by Assimilation of Remote Sensing Data into SVAT Models. *Remote Sensing of Environment*. 68:341–356.

Otazu, X., and Arbiol, R., 2000. Land use map production by fusion of multispectral classification of Landsat images and texture analysis of high resolution images. *International archives of Photogrammetry and Remote Sensing*, Vol. XXXIII, Supplement B7. Amsterdam, the Netherlands.

Ozdogan, M., Woodcock, C.E., Salvucci, G.D., Demir, H., 2006. Changes in summer irrigated crop area and water use in Southeastern Turkey from 1993 to 2002: Implications for current and future water resources. *Journal of Hydrometeorology* 7 (2) , pp. 235-251.

Papadavid, G, 2012. Estimating evapotranspiration for annual crops in Cyprus using remote sensing. Phd Thesis, Department of Civil Engineering and Geomatics, Cyprus University of Technology, Lemesos, Cyprus.

Papadavid, G., Hadjimitsis, D., Michaelides, S., Nisantzi, A., 2011. Crop evapotranspiration estimation using remote sensing and the existing network of meteorological stations in Cyprus. *Advances in Geosciences* 30, pp. 39-44.

Papadavid, G., Hadjimitsis, D.G., Toullos, L., Michaelides, S., 2013. A Modified SEBAL Modeling Approach for Estimating Crop Evapotranspiration in Semi-arid Conditions. *Water Resources Management* 27 (9), pp. 3493-3506.

Papadavid, G., Perdikou, S., Hadjimitsis, M., Hadjimitsis, D., 2012. Remote sensing applications for planning irrigation management. The use of SEBAL methodology for

estimating crop evapotranspiration in Cyprus. *Environmental and Climate Technologies* 9 (1), pp. 17-21.

Papadimitriou, T., Katsiapi, M., Kormas, K.A., Moustaka-Gouni, M., Kagalou, I., 2013. Artificially-born "killer" lake: Phytoplankton based water quality and microcystin affected fish in a reconstructed lake. *Science of the Total Environment*. Volume 452-453, 1 May 2013, pp. 116-124.

Papazafiriou, Z., 1999. Water demand of crops. Thessaloniki, Greece. Ziti Publishing (In Greek).

Paul, G. , Gowda, P.H., Vara Prasad, P.V., Howell, T.A., Aiken, R.M., Neale, C.M.U., 2014. Investigating the influence of roughness length for heat transport (zoh) on the performance of SEBAL in semi-arid irrigated and dryland agricultural systems. *Journal of Hydrology*. Volume 509, 13 February 2014, Pages 231-234.

Patil, B.M., Desai, C.G., Umrikar, B.N., 2012. Image classification tool for Land Use / Land cover analysis: A Comparative Study Of Maximum Likelihood and Minimum Distance Method. *International Journal of Geology, Earth and Environmental Sciences* ISSN: 2277-2081 (Online) An Online International Journal Available at <http://www.cibtech.org/jgee.htm> 2012 Vol. 2 (3) September - December, pp.189-196.

Paulson, C.A., 1970. The mathematical representation of wind speed and temperature profiles in the unstable atmospheric surface layer. . *Appl. Meteorol.* 9:857-861.

Penman, H.L., 1948. Natural evaporation from open water, bare soil, and grass. *Proceedings of the Royal Society of London A* 193:120-146.

Penman, H.L., 1963. *Vegetation and Hydrology*. Tech. Comm. No. 53, Commonwealth Bureau of Soils, Harpenden, England.

Priestley, C.H.B, and Taylor, R.J., 1972. On the assessment of surface heat flux and evaporation using large-scale parameters. *Monthly Weather Review* 100(2):81-92.

Psomas, A., Kneubühler, M., Huber, S., Itten, K., Zimmermann, N.E., 2005. Hyperspectral remote sensing for estimating aboveground biomass and for exploring species richness patterns of grassland habitats. *International Journal of Remote Sensing* Vol. 32, No. 24, 20 December 2011, 9007–9031.

Raupach, M.R., Thom A.S., 1981. Turbulence in and above Plant Canopies. *Annual Review of Fluid Mechanics* 13, 97-129.

Rentzelou, A., De Jong, T. M., 2012. An example of civil engineering taking ecology into account. Scientific Report. Delft University of Technology.

Rivas-Martinez, S., 1995. Bases para una nueva clasificacion bioclimatica de la Tierra. *Folia Botanica Matritensis* 16.

Romero, M.G. 2004. Daily Evapotranspiration Estimation by Means of Evaporative Fraction and Reference Evapotranspiration Fraction. Draft of Ph.D. Dissertation Submitted to Utah State University, Logan, UT, USA, 175p.

Roerink, G.J., Su, B., and Menenti, M., 2000. S-SEBI: A simple Remote Sensing Algorithm to estimate the surface energy balance. *Physics and Chemistry of the Earth, Part B*, 25 (2): 147-157.

Romaguera, M., Toullos, L., Stancalie, Gh., Nertan, A., Spiliotopoulos, M., Struzik, P., Calleja, E.J., and Papadavid, G., 2014. Identification of the key variables that can be estimated using remote sensing data and needed for Water Footprint (WF) assessment. *Proc. SPIE 9229, Second International Conference on Remote Sensing and Geoinformation of the Environment (RSCy2014)*, 922912 (August 12, 2014); <http://dx.doi.org/10.1117/12.2066120>.

Rouskas G., 2001. The return of Karla. Athens, Private Publishing, ISBN: 9789608536333.

Roy, D.P., Wulder, M.A., Loveland, T.R., Woodcock, C.E., Allen, R.G., Anderson, M.C., Helder, D., Irons, J.R., Johnson, D.M., Kennedy, R., Scambos, T.A., Schaaf, C.B., Schott, J.R., Sheng, Y., Vermote, E.F., Belward, A.S., Bindschadler, R., Cohen, W.B. Gao, F., Hipple, J.D., Hostert, P., Huntington, J., Justice, C.O., Kilic, A., Kovalskyy, V., Lee, Z.P., Lymburner, L., Masek, J.G., McCorkel, J., Shuai, Y., Trezza, R., Vogelmann, J., Wynne, R.H., Zhu, Z., 2014. Landsat-8: Science and product vision for terrestrial global change research. *Remote Sensing of Environment* 145. pp. 154–172.

Rubio, E., Colin, J., D'Urso, G., R. Trezza, R. Allen, A. Calera, J. González, A. Jochum, M. Menenti, M. Tasumi, Kelly, C., Vuolo, F., 2006. Golden day comparison of methods to retrieve  $K_c$ -NDVI,  $K_c$ -analytical, MSSEBS, METRIC). *AIP Conference Proceedings* 852, pp. 193-200.

Ruhoff, A.L., Adriano R. Paz, A., Collischonn, W., Aragao, L.E.O.C., Rocha, H.R., Malhi, Y.S., 2012. A MODIS-Based Energy Balance to Estimate Evapotranspiration for Clear-Sky Days in Brazilian Tropical Savannas. *Remote Sens.* 2012, 4, 703-725; doi:10.3390/rs4030703.

Ruhoff, A. L., Paz, A. R., Collischonn, W., Aragao, L. E.O.C., Rocha, H. R., Malhi, Y. S. A, 2012. MODIS-Based Energy Balance to Estimate Evapotranspiration for Clear-Sky Days in Brazilian Tropical Savannas. *Remote Sensing*, v. 4, p. 703-725.

Saxton, K.E., and Willey, P.H., 1986. The SPAW model for agricultural field and pond hydrologic simulation. P. 401-435. In V.P. Singh and D.K. Frevert (ed.) *Watershed models*. CRC press, Boca Raton, FL.

Schaaf, C.B., Gao, F., Strahler, A.H., Lucht, W., Li, X.W., Tsang, T., Strugnell, N.C., Zhang, X.Y., Jin, Y.F., Muller, J.P., Lewis, P., Barnsley, M., Hobson, P., Disney, M., Roberts, G., Dunderdale, M., Doll, C., d'Entremont, R.P., Hu, B.X., Liang, S.L., Privette, J.L., Roy,

D., 2002. First Operational BRDF, Albedo and Nadir Reflectance Product from MODIS. Remote Sensing of Environment. Vol. 83, Issues 1–2, November 2002, Pages 135–148.

Schultz, G.A., 1997. Use of Remote Sensing data in a GIS environment for water resources management. Remote Sensing and Geographical Information Systems for Design and Operation of Water Resources Systems (Proceedings of Rabat Symposium S3, April 1997). IAHS Publ. no 242.

Sellers, P.J., 1985. Canopy reflectance, photosynthesis and transpiration. Int. J. Remote Sens., 6, pp. 1335–1372.

Shaykewich C.F., 1994. An appraisal of cereal crop phenology modelling, Canadian Journal of Plant Science, 329-341.

Shuttleworth, W.J., Gurney, R.J., Hsu, A.Y. & Ormsby, J.P. 1989. The Variation in Energy Partition at Surface Flux Sites. Proceedings of the IAHS Thrid International Assembly, Baltimore, MD, USA.

Shuttleworth, J., and Guerny, 1990. Evaporation. In: D.R. Maidment (Editor), Handbook of Hydrology. McGraw Hill, New York, 4.1 - 4.53.

Sidiropoulos, P., 2007. Στοχαστική Προσομοίωση του Υπόγειου Υδροφορέα της Λίμνης Κάρλας. Μεταπτυχιακή Εργασία Ειδίκευσης, Π.Μ.Σ. Τμήματος Πολιτικών Μηχανικών, Πανεπιστήμιο Θεσσαλίας, Βόλος (In Greek).

Sidiropoulos, P., A. Loukas, N. Mylopoulos, and L. Vasiliades, 2009. Integrated OpenMI modelling and management of lake Karla aquifer under climate change. EGU General Assembly, 19-24 April 2009, Vienna, Austria, Geophysical Research Abstracts, Vol. 11.

Sidiropoulos, P., Mylopoulos, N., Loukas, A., 2013. Optimal Management of an Overexploited Aquifer under Climate Change: The Lake Karla Case. Water Resources Management, Volume 27, 6, pp 1635-1649.

Silleos, N., Misopolinos, N., and Perakis, K., 1992. Relationships between remote sensing spectral indices and crops discrimination, *Geocarto International*, 7, (2), 41-51.

SIRRIMED, 2014. Sustainable Use of Irrigation Water in the Mediterranean Region. E.C. EFP7 Cooperation Theme "Food, Fisheries and Biotechnologies". Final Report. [www.sirrimed.org](http://www.sirrimed.org), 2014.

Slatyer, R.O. and McIlroy, I.C., 1961, *Practical Microclimatology*, CSIRO, Australia and UNESCO.

Smith M., 1992. CROPWAT - A computer program for irrigation planning and management. FAO Irrigation and drainage paper 46.

Solano R.; Didan, K.; Jacobson A.; Huete A. MODIS Vegetation Indices (MOD13) C5 User's Guide; 2010. Available online (accessed on 23 November 2010) <http://tbrs.arizona.edu/project/MODIS/UsersGuide.pdf>

Spiliotopoulos, M., Loukas, A. and Michalopoulou, H., 2013. Contribution to the Study of Regional Actual Evapotranspiration with the Use of Surface Energy Balance and Remote Sensing for Central Greece. *Advances in Meteorology, Climatology and Atmospheric Physics*, Springer, 309-315.

Spiliotopoulos, M., Adaktylou, N., Loukas, A., Michalopoulou, H., Mylopoulos, N., and L. Toullos, L., 2013. A spatial downscaling procedure of MODIS derived actual evapotranspiration using Landsat images at central Greece. *Proc. SPIE 8795*, First International Conference on Remote Sensing and Geoinformation of the Environment (RSCy2013), 879508 (August 5, 2013); <http://dx.doi.org/10.1117/12.2027536>.

Spiliotopoulos, M. Loukas, A., Mylopoulos, N., Toullos, L. and Stancalie, G., 2014. Investigation of spatial relationships between crop coefficients and specific ground based vegetation indices for Karla watershed, Greece. *Proc. SPIE9229*, Second

International Conference on Remote Sensing and Geoinformation of the Environment (RSCy2014), 92290J (August 12, 2014); <http://dx.doi.org/10.1117/12.2066095>.

Stancalie, Gh., Nertan, A. T.; Toullos, L. and Spiliotopoulos, M., 2014. Potential of using satellite based vegetation indices and biophysical variables for the assessment of the water footprint of crops. Proc. SPIE 9229, Second International Conference on Remote Sensing and Geoinformation of the Environment (RSCy2014), 92290K (August 12, 2014); <http://dx.doi.org/10.1117/12.2066392>.

Stanhill, G, 1961. A comparison of methods of calculating potential evapotranspiration from climatic data. Israel J. Agric. Res. 11Q 159-171.

Starks, P. J., Norman, J. M., Blad, B. L., Walter-Shea, E. A., and Walthall, C. L., 1991. Estimation of shortwave hemispherical reflectance (albedo) from bidirectionally reflected radiance data. Remote Sensing of Environment, 38(2), 123-134. [doi:10.1016/0034-4257(91)90074-G]

Stathakis, D., and Faraslis, I., 2014. Monitoring urban sprawl using simulated PROBA-V data. International Journal of Remote Sensing, 35 (7), pp. 2731-2743.

Su, Z., 2002. The surface energy balance system (SEBS) for estimation of turbulent fluxes. Hydrol. Earth Systems Sci., 6(1): 85-99.

Tang, R, Li, Z.L., Tang, B, 2010. An application of the Ts-VI triangle method with enhanced edges determination for evapotranspiration estimation from MODIS data in arid and semi-arid regions: Implementation and validation. Remote Sensing of Environment, 114, 540-551.

Tanner, C.B., 1967. Measurement of evapotranspiration. Irrigation of Agricultural Lands. (R.M. Happen, M.R. Haise and T.W. Enminster. Eds.). Am. Soc. Agron. Madison, Wisc., pp. 534-574.



Tasumi, M., Trezza, R., Allen, R. G., and Wright, J., 2005. Operational aspects of satellite-based energy balance models for irrigated crops in the semi-arid U.S. *Irrigation and Drainage systems*, 19: 355–376.

Tasumi, M., Allen, R. G., and Trezza, R. 2008. At-surface reflectance and albedo from satellite for operational calculation of land surface energy balance. *Journal of Hydrologic Engineering*, 13(2), 51-63. [doi:10.1061/(ASCE)1084-0699(2008)13:2(51)]

Thornthwaite, C. W., 1948. An approach toward a rational classification of climate. *Geographic Review* 38:55-94.

Timmermans, W.J., Kustas, W.P., Anderson, M.C., French, A.N., 2007. An intercomparison of the surface energy balance algorithm for land (SEBAL) and the two-source energy balance (TSEB) modeling schemes. *Remote Sens Environ* 108:369–384.

Torkil Jønch-Clausen, Korsgaard, L., Jensen, R.A., Jønch-Clausen, T., Rosbjerg, D., Schou, J.S., 2007. A service and value based approach to estimating environmental flows. *International Journal of River Basin Management*. Volume 6, Issue 3, 2008, pp. 257-266.

Toulios, L., and Silleos, N., 1994. Relationships between soil properties and soil spectral behavior. *Proceedings of the 5th Pan-Hellenic Soil Conference*, Xanthi 25-27 May . pp. 91-102 (In Greek).

Toulios, L., and Silleos, N., 1994. Diachronic study of crop spectral response in Central Greece. *Proceedings of the International Symposium on Spectral Sensing Research*, Vol. 2, 10-15 July 1994. San Diego, California, USA.

Toulios, L., Toulios, M., and Zerva, G., 1998. Spectral analysis for cotton growth monitoring. *World cotton research conference*, 2: New frontiers in cotton research. pp 534-539.

Townshend, J.R.G., and Justice, C.O., 2002. Towards operational monitoring of terrestrial systems by moderate-resolution remote sensing Remote Sensing of Environment 83 (1-2), pp. 351-359.

Trezza, R., Allen, R., 2003. Crop water requirements from a remote sensing model for the snake plain area in Idaho. *Geoensenzan*, Vol. 8, pp. 83-90.

Tsakiris, G., 1995. *Water resources: Engineering Hydrology*. Athens, Greece. Symmetry Pubishin (In Greek).

Tsirogiannis, I., Savvas, D., Katsoulas, N., Kittas, C., 2012. Evaluation of crop reflectance indices for greenhouse irrigation scheduling. *Acta Horticulturae* Volume 927, 28 February 2012, Pages 269-276.

Tsouni, A., Kontoes, C., Koutsogiannis, D., Elias, P., Mamassis, N., 2008. Estimation of actual evapotranspiration by remote sensing: Application in Thessaly plain, Greece. *Sensors* 8 (6), pp. 3586-3600.

Tsouni A., Koutsogiannis, D., Kontoes, C., Mamasis, N. and Elias, P., 2005. Estimation of actual epapotranspiration by remote sensing: Application in Thessaly plain, Greece. In: N.R. Dalezios and H. Dobesch (Editors), *Proceedings of the International Symposium on GIS and Remote Sensing: Environmental Applications*, Volos, Greece, 7-9 November 2003, pp. 261-275.

Tucker, C.J., 1979. Red and photographic infrared linear combinations for monitoring vegetation. *Remote Sens. Environ.*, 8, 127–150.

Turc, I., 1961. Evaluation des besoins en eau d'irrigation, evapotranspiration potentielle, *Ann, Agron.*, 12(1), 13-49.

Tuttle, E.M., Jensen, R.R., Formica V.A., and Gonser, R.A., 2006. Using remote sensing image texture to study habitat use patterns: a case study using the polymorphic white-

throated sparrow (*Zonotrichia albicollis*). *Global Ecology and Biogeography*, 15, 349–357.

Tzabiras, J., Spiliotopoulos, M, Kokkinos, K., Fafoutis, C., Sidiropoulos, P., 2014. A GIS based district information system for water resources management and planning. EGU General Assembly Conference Abstracts 16, 15446.

US Army Corps of Engineers (USACE), 2003. Remote Sensing, Engineering and design, Engineering Manual EM 1110-2-2907, 217 p.

U.S. Geological Survey “Band designations of Landsat satellites”, Ulivieri, C., Castronuovo, C., Francioni, M., and Cardillo, R., 1992. A split window algorithm for estimating land surface temperatures derived from satellites. Washington, D. C: Comm. on Space Programs and Research (COSPAR).

Van Bavel, C. H. M., 1966. Potential evapotranspiration: The combination concept and its experimental verification. *Water Resour. Res.* 2: 455-467.

Van den Hurk, B., 2001. Energy balance based surface flux estimation from satellite data, and its application for surface moisture assimilation. *Meteorol. Atmos. Phys.* 76, 43-52.

Venturini, V.; Islam, S., Rodriguez, L., 2008. Estimation of evaporative fraction and evapotranspiration from MODIS products using a complementary based model. *Remote Sens. Environ.* 112, 132-141.

Vasiliades, L., Loukas, A, Patsonas, G., 2009. Evaluation of a statistical downscaling procedure for the estimation of climate change impacts on droughts. *Natural Hazards and Earth System Science* 9 (3), pp. 879-894.

Vazquez, D.P., Olmo R.F.J., Arboledas, L.A., 1997. A comparative study of algorithms for estimating land surface temperature from AVHRR data. *Remote Sensing of Environment* 62, 215-222 (1997).

Vermote, E.F., Kotchenova, S.Y., Ray, J.P., 2010. MODIS Surface Reflectance User's Guide. Available online (accessed on 23 November 2010): [http://modis-sr.ltdri.org/products/MOD09\\_UserGuide\\_v1\\_2.pdf](http://modis-sr.ltdri.org/products/MOD09_UserGuide_v1_2.pdf).

Wan, Z. , 2010. MODIS Land Surface Temperature Products Users' Guide. Available online: [http://www.icess.ucsb.edu/modisMODIS\\_LST\\_products\\_Users\\_guide\\_C5.pdf](http://www.icess.ucsb.edu/modisMODIS_LST_products_Users_guide_C5.pdf) (accessed on 23 November 2010).

Wan, Z.; Li, Z.L., 2008. Radiance-based validation of the V5 MODIS land-surface temperature product. *Int. J. Remote Sens.* 29, 5373-5395.

Wan, Z.; Zhang, Y.; Zhang, Q.; Li, Z.L., 2004. Quality assessment and validation of the MODIS global land surface temperature. *Int. J. Remote Sens.*, 25, 261-274.

Wang L., Wang W., Dorsey J., Yang X., Guo B. and Shum H.Y., 2005, Real-time rendering of plant leaves, in *Proc. ACM SIGGRAPH 2005*, Los Angeles (USA), 31 July - 4 August 2005, pp. 167-174.

Waters, R., Allen, R., Bastiaanssen, W., 2002. SEBAL. Surface Energy Balance Algorithms for Land. Idaho Implementation. Advanced Training and Users Manual. Idaho, USA.

Webb, E.K., 1970. Profile relationships: the log-linear range, and extension to strong stability. *Quart. J. Roy. Meteorol. Soc.* 96:67-90.

Wonsook, H., Prasanna, H.G., Terry, A.H., 2012. A review of downscaling methods for remote sensing-based irrigation management: part I. *Irrig Sci.* DOI 10.1007/s00271-012-0331-7.

Woodcock, C.E., Allen, R., Anderson, M., Belward, A., Bindschadler, R., Cohen, W., Gao, F., Goward, S.N., Helder, D., Helmer, E., Nemani, R., Oreopoulos, L., Schott,

J., Thenkabail, P.S., Vermote, E.F., Vogelmann, J., Wulder, M.A., Wynne, R., 2008. Free access to landsat imagery Science. Vol. 320, Issue 5879, 23 May 2008, (letter) p. 1011.

Wriedt G., Van Der Velde M., Aloe A. and Bouraoui F., 2008. A European irrigation map for spatially distributed agricultural modelling. Agricultural Water Management. 96 (5), 771-789.

Wukelic, G.E., D.E. Gibbons, Martucci, L.M., Foote, H.P., 1989. Radiometric calibration of Landsat thematic mapper thermal band. Remote Sensing of Environment 28:339-347.

Yang R., and Friedl, M.A., 2003. Determination of Roughness Lengths for Heat and Momentum over Boreal Forests. Boundary-Layer Meteorology 107: 581–603, 2003.

Yang, F., White, M.A., Michaelis A.R., Ichii K., Hashimoto, H., Votava, P., Zhu, A.-X., Nemani, R.R., 2006. Prediction of continental-scale evapotranspiration by combining MODIS and meriFlux data through support vector machine. IEEE Trans Geosci Remote 44:3452–3461.

Zalidis G., Dimitriadis K., Chatzigiannakis S., 1995. The concept of the former lake Karla. Published by Goulandris Natural History Museum.

Zhang, X.C., Wu, J.W., Wu, H.Y., Li, Y., 2011. Simplified SEBAL method for estimating vast areal evapotranspiration with MODIS data. Water Science and Engineering, 2011, 4(1): 24-35. doi:10.3882/j.issn.1674-2370.2011.01.003.

Γ.Γ.Δ.Ε./Γ.Δ.Υ.Ε. ΔΙΕΥΘΥΝΣΗ ΕΓΓΕΙΟΒΕΛΤΙΩΤΙΚΩΝ ΕΡΓΩΝ (Δ7), 2006. Μελέτη έργων μεταφοράς και Διανομής νερού λίμνης Κάρλας Οριστική Μελέτη (έργα Α΄, Β΄ φάσης) (In Greek).

## Electronic data-bases

- CORINE 2000: Land cover map of the EU: <http://www.integrated-assessment.eu/node/838>.
- European Space Agency (ESA), <http://www.esa.int/>
- Exelis Visual Information Solutions, "Vegetation indices". Colorado, USA. <http://www.exelisvis.com> (2010).
- Global Water Partnership, <http://gwp.org>.
- [http://landsat.usgs.gov/band\\_designations\\_landsat\\_satellites.php](http://landsat.usgs.gov/band_designations_landsat_satellites.php)
- Institute for Research and Technology, Thessaly: <http://ireteth.certh.gr>
- Labsphere, New Hampshire, USA: <http://www.labsphere.com>
- National Aeronautics and Space Administration (NASA), 2013. MODIS specifications" <http://modis.gsfc.nasa.gov/about/specifications.php>.
- National Aeronautics and Space Administration. Aqua Project Science: <http://aqua.nasa.gov>.
- National Aeronautics and Space Administration. Aqua Project Science. Landsat Science: <http://landsat.gsfc.nasa.gov>.
- National Aeronautics and Space Administration. MODIS WEB: <http://modis.gsfc.nasa.gov/about>

- National Aeronautics and Space Administration. MODIS WEB:  
<http://modis.gsfc.nasa.gov/about/specifications.php>
- National Aeronautics and Space Administration. Terra, the EROS Flagship:  
<http://terra.nasa.gov>
- Saatchi, S. n.d. Projects in the Amazon Basin:  
[http://www-radar.jpl.nasa.gov/carbon/ab/ar\\_method.htm](http://www-radar.jpl.nasa.gov/carbon/ab/ar_method.htm).
- Spectra Vista Corporation: <http://www.spectravista.com/1500.html>
- Swiss Federal Institute of Technology, Zurich , 2014. Digital Library.  
<http://www.ifu.ethz.ch/hydrologie/>
- USGS GLOBAL Visualization Center EROS: <http://glovis.usgs.gov>.





# **ANNEX 1**

## **The CLC classification categories**



The CLC classification categories.

<b>GRID_</b>					
<b>CODE</b>	<b>CLC_CODE</b>	<b>LABEL1</b>	<b>LABEL2</b>	<b>LABEL3</b>	<b>RGB</b>
1	111	Artificial	Urban fabric	Continuous	230-000-077
		surfaces		urban fabric	
2	112	Artificial	Urban fabric	Discontinuous	255-000-000
		surfaces		urban fabric	
3	121	Artificial	Industrial,	Industrial or	204-077-242
		surfaces	commercial	commercial	
4	122	Artificial	and transport	Road and rail	204-000-000
		surfaces	units	networks and	
5	123	Artificial	Industrial,	associated	230-204-204
		surfaces	commercial	land	
6	124	Artificial	and transport	Port areas	230-204-230
		surfaces	units	Airports	
7	131	Artificial	Mine, dump	Mineral	166-000-204
		surfaces	and	extraction	
8	132	Artificial	construction	Dump sites	166-077-000
		surfaces	sites		

			sites		
			Mine, dump and construction sites	Construction sites	255-077-255
9	133	Artificial surfaces	Artificial, non- agricultural vegetated areas	Green urban areas	255-166-255
10	141	Artificial surfaces	Artificial, non- agricultural vegetated areas	Sport and leisure facilities	255-230-255
11	142	Artificial surfaces	Agricultural areas	Non-irrigated arable land	255-255-168
12	211	Agricultural areas	Agricultural areas	Permanently irrigated land	255-255-000
13	212	Agricultural areas	Agricultural areas	Rice fields	230-230-000
14	213	Agricultural areas	Permanent crops	Vineyards Fruit trees and berry plantations	230-128-000
15	221	Agricultural areas	Permanent crops	Olive groves	242-166-077
16	222	Agricultural areas	Permanent crops	Olive groves	230-166-000
17	223	Agricultural areas	Pastures	Pastures	230-230-077
18	231	Agricultural areas	Heterogeneous agricultural areas	Annual crops associated with	255-230-166
19	241	Agricultural areas			

				permanent crops	
			Heterogeneous	Complex	
		Agricultural	agricultural	cultivation	
20	242	areas	areas	patterns	255-230-077
				Land principally occupied by agriculture, with significant	
			Heterogeneous	areas of	
		Agricultural	agricultural	natural	
21	243	areas	areas	vegetation	230-204-077
			Heterogeneous		
		Agricultural	agricultural	Agro-forestry	
22	244	areas	areas	areas	242-204-166
		Forest and semi natural		Broad-leaved	
23	311	areas	Forests	forest	128-255-000
		Forest and semi natural		Coniferous	
24	312	areas	Forests	forest	000-166-000
		Forest and semi natural			
25	313	areas	Forests	Mixed forest	077-255-000
			Scrub and/or		
		Forest and semi natural	herbaceous	Natural	
26	321	areas	vegetation	grasslands	204-242-077
27	322	Forest and	associations	Moors and	166-255-128
			Scrub and/or		

		semi natural areas	herbaceous vegetation associations Scrub and/or Forest and semi natural areas	heathland     Sclerophyllous vegetation	
28	323		Scrub and/or Forest and semi natural areas		166-230-077
29	324		herbaceous vegetation associations	Transitional woodland- shrub	166-242-000
30	331		Open spaces with little or no vegetation	Beaches, dunes, sands	230-230-230
31	332		Open spaces with little or no vegetation	Bare rocks	204-204-204
32	333		Open spaces with little or no vegetation	Sparsely vegetated areas	204-255-204
33	334		Open spaces with little or no vegetation	Burnt areas	000-000-000
34	335		Open spaces with little or no vegetation	Glaciers and perpetual snow	166-230-204
35	411	Wetlands	Inland wetlands	Inland marshes	166-166-255
36	412	Wetlands	Inland wetlands	Peat bogs	077-077-255
37	421	Wetlands	Maritime	Salt marshes	204-204-255

---

			wetlands		
			Maritime		
38	422	Wetlands	wetlands	Salines	230-230-255
			Maritime		
39	423	Wetlands	wetlands	Intertidal flats	166-166-230
40	511	Water bodies	Inland waters	Water courses	000-204-242
41	512	Water bodies	Inland waters	Water bodies	128-242-230
				Coastal	
42	521	Water bodies	Marine waters	lagoons	000-255-166
43	522	Water bodies	Marine waters	Estuaries	166-255-230
44	523	Water bodies	Marine waters	Sea and ocean	230-242-255
48	999	NODATA	NODATA	NODATA	
				UNCLASSIFIED	
			UNCLASSIFIED	LAND	
49	990	UNCLASSIFIED	LAND SURFACE	SURFACE	
				UNCLASSIFIED	
			UNCLASSIFIED	WATER	
50	995	UNCLASSIFIED	WATER BODIES	BODIES	230-242-255
				UNCLASSIFIED	
			UNCLASSIFIED	WATER	
50	995	UNCLASSIFIED	WATER BODIES	BODIES	230-242-255

---





## **ANNEX 2**

### **Julian Day Calendar**



## Julian Day Calendar: Regular Years

Day	January	February	March	April	May	June
1	1	32	60	91	121	152
2	2	33	61	92	122	153
3	3	34	62	93	123	154
4	4	35	63	94	124	155
5	5	36	64	95	125	156
6	6	37	65	96	126	157
7	7	38	66	97	127	158
8	8	39	67	98	128	159
9	9	40	68	99	129	160
10	10	41	69	100	130	161
11	11	42	70	101	131	162
12	12	43	71	102	132	163
13	13	44	72	103	133	164
14	14	45	73	104	134	165
15	15	46	74	105	135	166
16	16	47	75	106	136	167
17	17	48	76	107	137	168
18	18	49	77	108	138	169
19	19	50	78	109	139	170
20	20	51	79	110	140	171
21	21	52	80	111	141	172
22	22	53	81	112	142	173
23	23	54	82	113	143	174
24	24	55	83	114	144	175
25	25	56	84	115	145	176
26	26	57	85	116	146	177
27	27	58	86	117	147	178
28	28	59	87	118	148	179
29	29		88	119	149	180

30	30	89	120	150	181
31	31	90		151	

Day	July	August	September	October	November	December
1	182	213	244	274	305	335
2	183	214	245	275	306	336
3	184	215	246	276	307	337
4	185	216	247	277	308	338
5	186	217	248	278	309	339
6	187	218	249	279	310	340
7	188	219	250	280	311	341
8	189	220	251	281	312	342
9	190	221	252	282	313	343
10	191	222	253	283	314	344
11	192	223	254	284	315	345
12	193	224	255	285	316	346
13	194	225	256	286	317	347
14	195	226	257	287	318	348
15	196	227	258	288	319	349
16	197	228	259	289	320	350
17	198	229	260	290	321	351
18	199	230	261	291	322	352
19	200	231	262	292	323	353
20	201	232	263	293	324	354
21	202	233	264	294	325	355
22	203	234	265	295	326	356
23	204	235	266	296	327	357
24	205	236	267	297	328	358
25	206	237	268	298	329	359
26	207	238	269	299	330	360

27	208	239	270	300	331	361
28	209	240	271	301	332	362
29	210	241	272	302	333	363
30	211	242	273	303	334	364
31	212	243		304		365

## Julian Day Calendar: Leap Years

Day	January	February	March	April	May	June
1	1	32	61	92	122	153
2	2	33	62	93	123	154
3	3	34	63	94	124	155
4	4	35	64	95	125	156
5	5	36	65	96	126	157
6	6	37	66	97	127	158
7	7	38	67	98	128	159
8	8	39	68	99	129	160
9	9	40	69	100	130	161
10	10	41	70	101	131	162
11	11	42	71	102	132	163
12	12	43	72	103	133	164
13	13	44	73	104	134	165
14	14	45	74	105	135	166
15	15	46	75	106	136	167
16	16	47	76	107	137	168
17	17	48	77	108	138	169
18	18	49	78	109	139	170
19	19	50	79	110	140	171
20	20	51	80	111	141	172
21	21	52	81	112	142	173
22	22	53	82	113	143	174
23	23	54	83	114	144	175

24	24	55	84	115	145	176
25	25	56	85	116	146	177
26	26	57	86	117	147	178
27	27	58	87	118	148	179
28	28	59	88	119	149	180
29	29	60	89	120	150	181
30	30		90	121	151	182
31	31		91		152	

Day	July	August	September	October	November	December
1	183	214	245	275	306	336
2	184	215	246	276	307	337
3	185	216	247	277	308	338
4	186	217	248	278	309	339
5	187	218	249	279	310	340
6	188	219	250	280	311	341
7	189	220	251	281	312	342
8	190	221	252	282	313	343
9	191	222	253	283	314	344
10	192	223	254	284	315	345
11	193	224	255	285	316	346
12	194	225	256	286	317	347
13	195	226	257	287	318	348
14	196	227	258	288	319	349
15	197	228	259	289	320	350
16	198	229	260	290	321	351
17	199	230	261	291	322	352
18	200	231	262	292	323	353
19	201	232	263	293	324	354
20	202	233	264	294	325	355

---

21	203	234	265	295	326	356
22	204	235	266	296	327	357
23	205	236	267	297	328	358
24	206	237	268	298	329	359
25	207	238	269	299	330	360
26	208	239	270	300	331	361
27	209	240	271	301	332	362
28	210	241	272	302	333	363
29	211	242	273	303	334	364
30	212	243	274	304	335	365
31	213	244		305		366

---





## **ANNEX 3**

### **The selection of hot and cold pixels**



### **The selection of hot and cold pixels.**

One of the basic assumptions of METRIC is the proposing of “cold” and “hot” pixels which are pixels representative of the area of interest. These pixels must be located in large and homogeneous areas. It is not easy to select hot and cold pixels, because a great knowledge of the study is required together with special remote sensing practices. The appropriate selection of hot and cold pixels is the most important action in METRIC methodology; otherwise, many errors are produced until the final product. A general assumption in METRIC is, that, climate conditions are uniform within the area of interest. For any reason that the weather conditions are changing within an area represented by an image, splitting of image may be the best solution. Different parts of the images have to be processed separately, with unique hot and cold pixels for each part (SEBAL, Idaho Implementation).

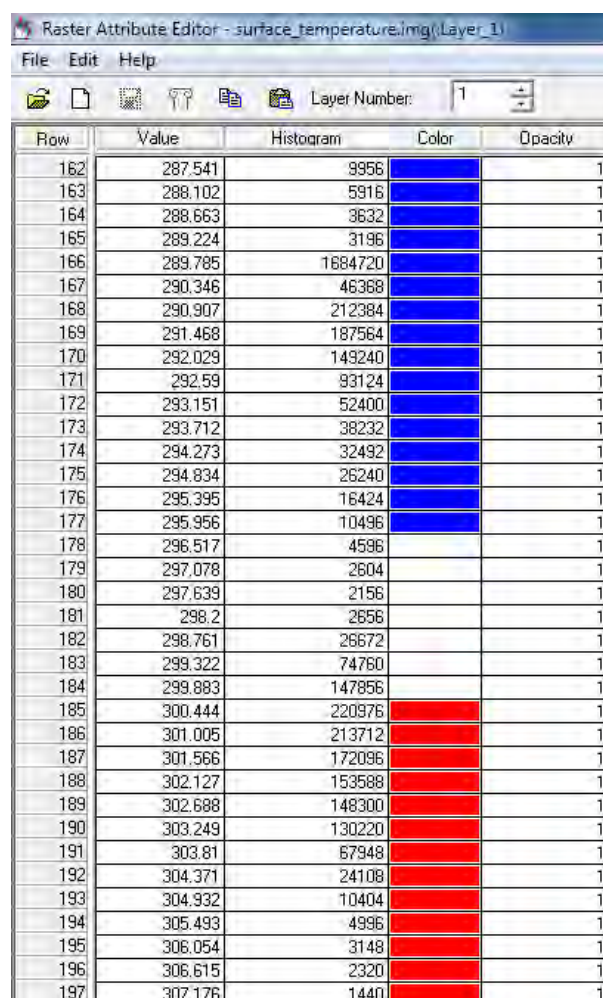
It is not easy to select hot and cold pixels with an automatic or software oriented way, because only the user really knows all these specified conditions prevailing in the study area. For the manual selection of hot and cold pixels previous outputs of METRIC methodology are needed. NDVI or LAI, albedo and surface temperature are usually recommended as a guide for the selection of those pixels. One very good practice is to give a pseudo color to LAI, albedo and temperature images for a better visualization of the prevailing differences (figure 1). Special attention must be given that both of these “anchor” pixels should be located in large and homogeneous areas that contain more than one band 6 pixel. The reason is obvious. Band 6 (thermal) pixel has a 60 m × 60 m spatial resolution for Landsat 7 and 120 m × 120 m for Landsat 5.

### **Selection of Cold Pixel**

Cold pixel can be defined as a wet, well-irrigated crop surface with full ground cover by vegetation. In other words it can be said that cold pixel is a very moist

terrain. In METRIC it is assumed that in the cold pixel all the energy is used for the evaporation of water and there is no sensible heat flux. A pixel with high values of LAI (or NDVI), low temperature and low albedo is a very good candidate to be selected as a “cold” pixel. It is very usual to select a water body as a cold pixel because all available energy is used to evaporate water there.

Figure 2 shows an example for a pixel with LAI=6, albedo=0.24 and T=290.92. The location of this pixel is recorded in order to be processed later.



Row	Value	Histogram	Color	Opacity
162	287.541	9956	Blue	1
163	288.102	5916	Blue	1
164	288.663	3632	Blue	1
165	289.224	3186	Blue	1
166	289.785	1684720	Blue	1
167	290.346	46368	Blue	1
168	290.907	212384	Blue	1
169	291.468	187564	Blue	1
170	292.029	149240	Blue	1
171	292.59	93124	Blue	1
172	293.151	52400	Blue	1
173	293.712	38232	Blue	1
174	294.273	32492	Blue	1
175	294.834	26240	Blue	1
176	295.395	16424	Blue	1
177	295.956	10496	Blue	1
178	296.517	4596	Blue	1
179	297.078	2604	Blue	1
180	297.639	2156	Blue	1
181	298.2	2656	Blue	1
182	298.761	26672	Blue	1
183	299.322	74760	Blue	1
184	299.883	147856	Blue	1
185	300.444	220976	Red	1
186	301.005	213712	Red	1
187	301.566	172096	Red	1
188	302.127	153588	Red	1
189	302.688	148300	Red	1
190	303.249	130220	Red	1
191	303.81	67948	Red	1
192	304.371	24108	Red	1
193	304.932	10404	Red	1
194	305.493	4996	Red	1
195	306.054	3148	Red	1
196	306.615	2320	Red	1
197	307.176	1440	Red	1

Figure 1. Attribute table: Surface Temperature (Landsat 5 TM, 15/8/2011)

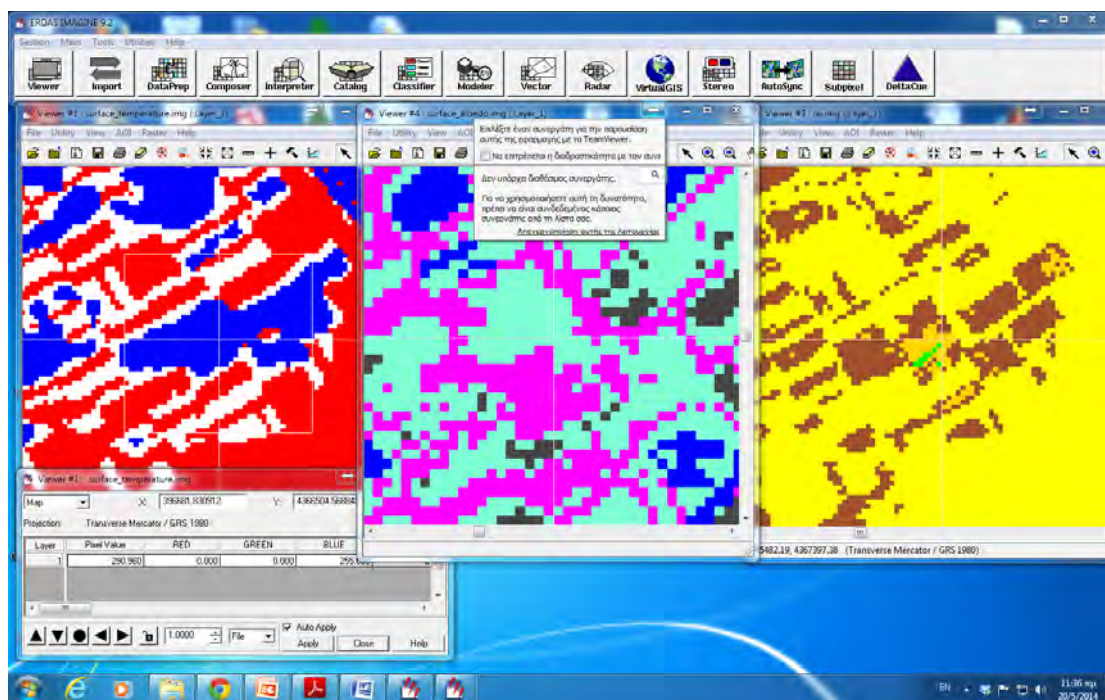


Figure 2. Colored images: Surface Temperature, Surface Albedo and LAI (Landsat 5 TM, 15/8/2011). The coordinates of the inquire cursor for the cold pixel candidate are  $x/y = 396681.8/ 4366504.6$  (EGSA 87)

### Selection of Hot Pixel

Cold pixel can be defined as a dry and bare agricultural field. In other words it can be said that hot pixel is a very dry terrain. In METRIC it is assumed that in the hot pixel all the energy is used for heating the surface, and there is no latent heat flux. A pixel with low values of LAI (or NDVI), high temperature and high albedo is a very good candidate to be selected as a “hot” pixel. Some examples for the selection of the appropriate “hot” pixel are given below (Table 1).

Table 1. Hot pixel candidates

Sample no	LAI	$T_s$	$\alpha$	Coordinates (EGSA 87)
1	0.06	311,96	0,20	388618/ 4364759
2	0,07	311.93	0,25	389071/



---

				4363421
3	0,133	311.24	0.28	393397/ 4370795

---

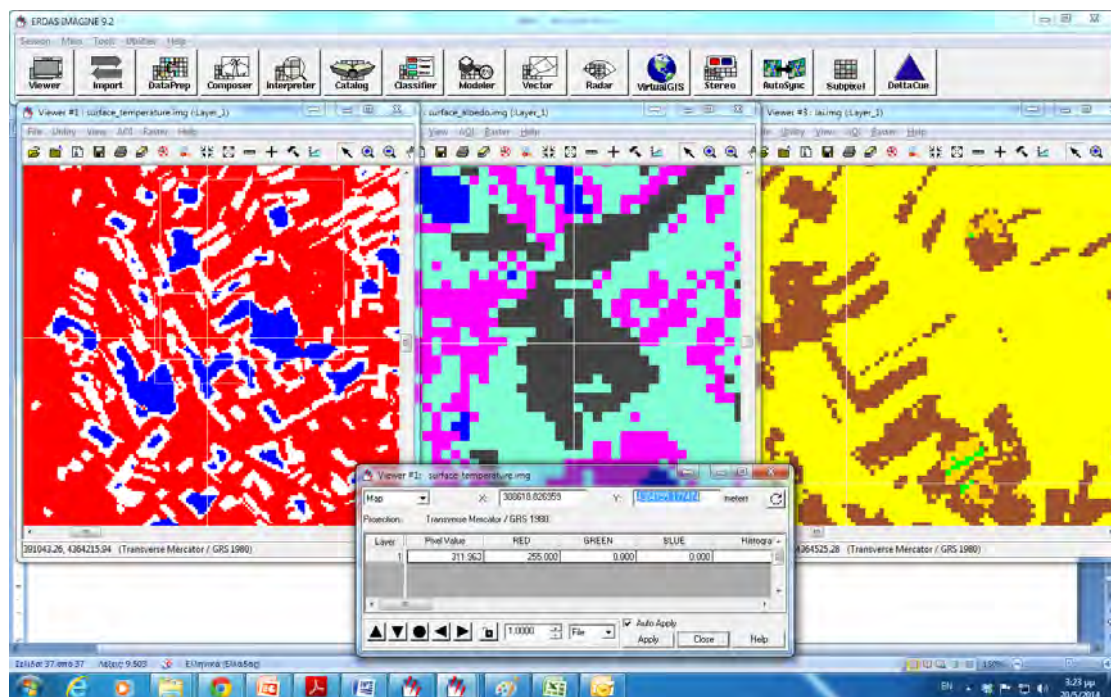


Figure 2. Hot pixel candidate no.1

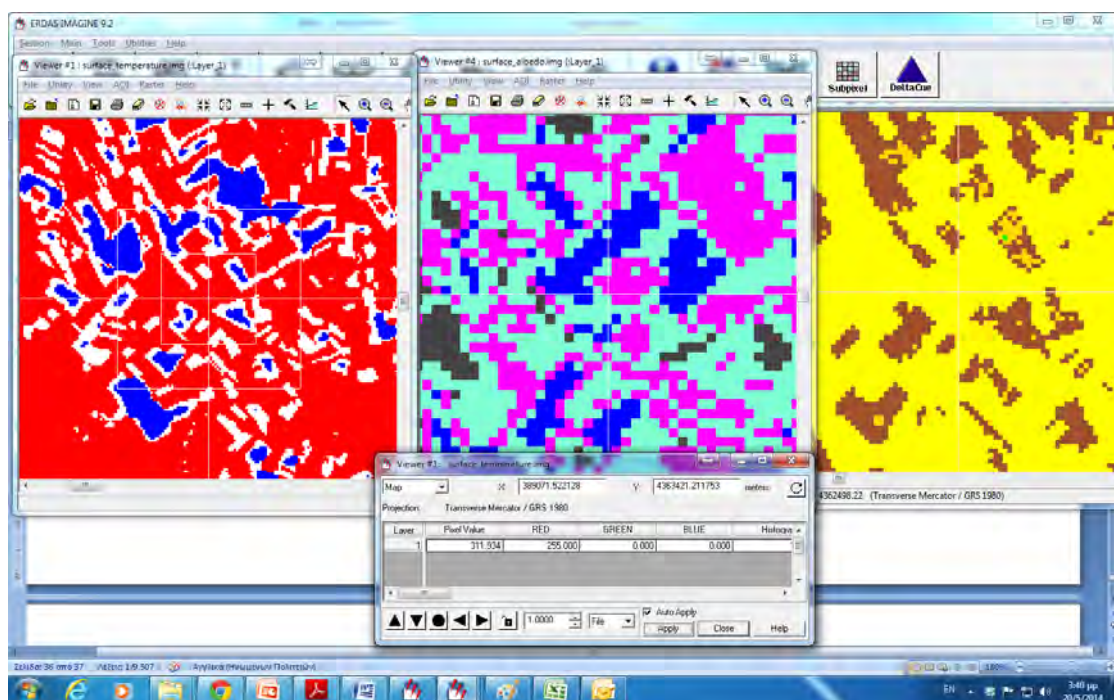


Figure 3. Hot pixel candidate no.2

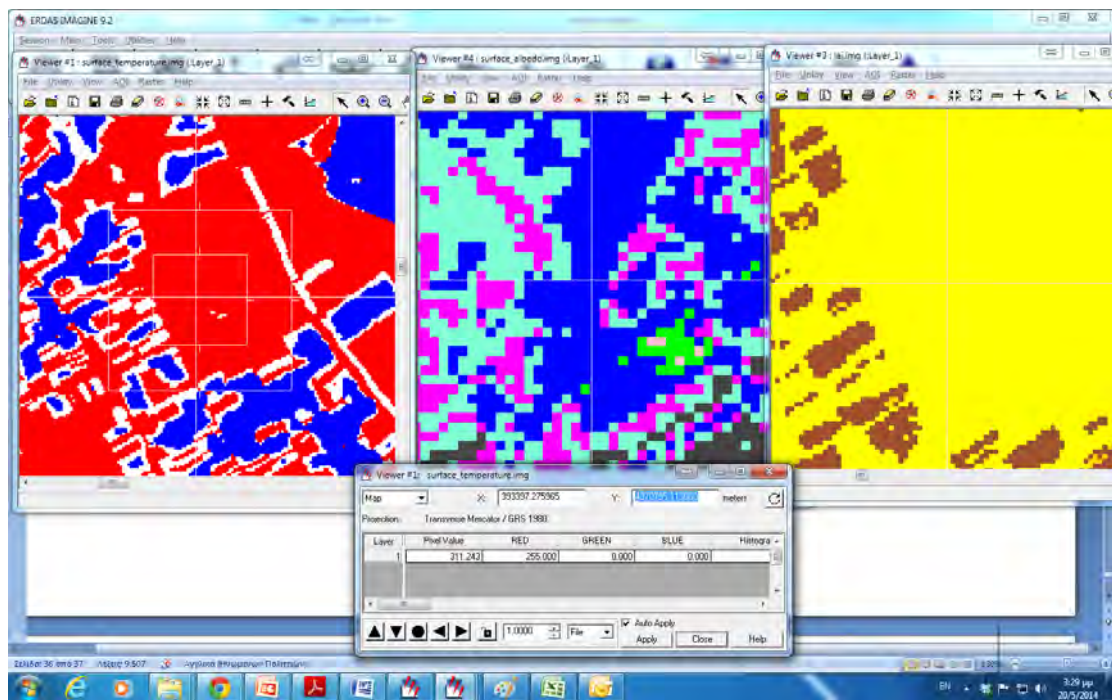


Figure 4. Hot pixel candidate no.3





## **ANNEX 4**

### **Instability**



## The first law of thermodynamics

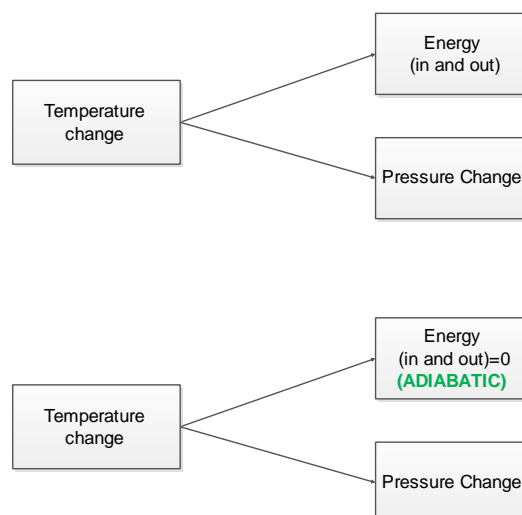
The defining characteristics of any given air mass are in general the temperature range, the pressure, and the moisture content. There are different air masses that are usually in motion following definite paths through the troposphere. These differences establish the weather systems acting at any particular time.

The internal energy or heat content  $Q$  of an air parcel subject to movement within the atmosphere may be changed, either by a change in temperature or by doing work on its surroundings. This can be stated by the simple formula:

$$Q = T + W$$

Where  $T$  is the temperature of the air mass, and  $W$  is the work.

It is well known that the expansion of the air mass reduces pressure, while contraction increases pressure. This can be explained thinking that when the parcel rises, its density decreases as the parcel expands doing work on its surroundings. On the other hand, an air mass downward is compressed and warmed increasing its density. When no energy added or removed in the air mass, then  $Q = 0$ , and this is called an adiabatic process. Assuming that the general rising or falling of the air is adiabatic, this fundamental property is a key when dealing with air masses.



### **Environmental Lapse Rate (ELR)**

There is a general assumption that an air parcel does not physically mix with its surroundings when rising. Of course the wind, turbulence etc. can disturb this equilibrium, but generally the parcel it is assumed to keep its thermodynamic behavior.

When heating causes an air mass to expand and rise into the atmosphere, then a heat loss of the air mass to its surroundings causes cool to the parcel. The resulting drop of the temperature is called the Lapse Rate. The Normal Lapse Rate of the troposphere is generally 6.5 °C., and this is also called the Environmental Lapse Rate (ELR). ELR is a function of the condition of the atmosphere. The parcel will continue to rise as well as the parcel is warmer than the surrounding air. In the case that the parcel enters air that is warmer it will start to sink.

The lifting of an air mass can be accomplished by:

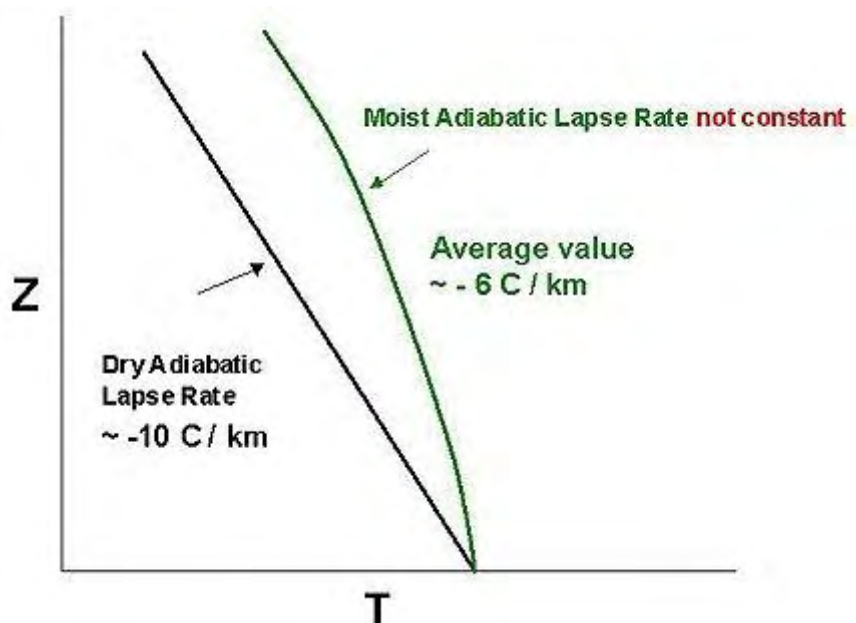
- Thermal convection
- Dynamic convergence
- Frontal collision
- Orographic uplift

A typical case found in this thesis is where the thermal convection is occurred caused from surface or lower atmosphere heating.

### **Dry and moist adiabatic lapse rate**

If the air has low moisture content for a defined temperature, its temperature decrease as it moves upwards can be determined by its Dry Adiabatic Lapse Rate (DALR). A typical DALR value is -10°C per kilometer upwards into the atmosphere. If, instead, the air is saturated, the moving can be defined by the Moist Adiabatic Lapse Rate (MLR). A typical MLR value may be - 6°C per km of rise. MLR is smaller than DALR due to the

release of latent heat. DALR tends to increase at a constant rate compared with the MLR which varies with altitude.

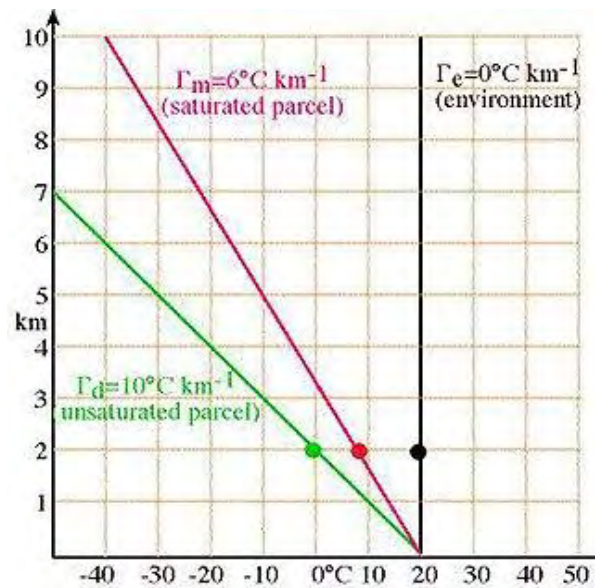


### The concepts of Air Stability and Instability.

Parcels of air rising through the lower atmosphere generally cool adiabatically. The future of this rise depends on the relationship between the temperature and density of the air parcel and the surrounding air. This can be thought of as the relationship between the ELR and the DALR/ MLR of the air parcel.

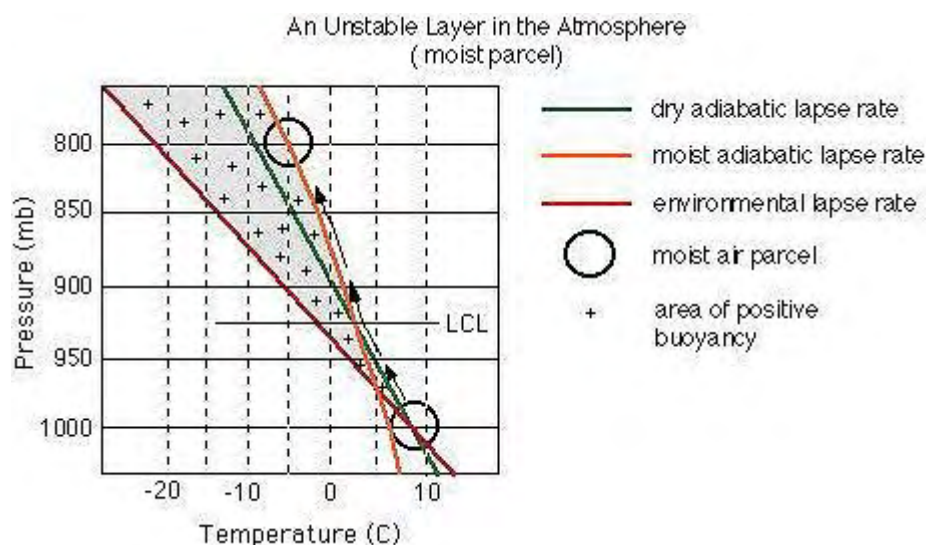
#### Stability:

Stability occurs when the ELR is less than the DALR. This means that the air parcel cools more rapidly than the surrounding air. In that way the air is cooler than the surrounding air and so it is colder, which means it is denser, and it will sink back down (in the case that there are no mountains forcing it to rise). In stable air, small changes in temperature with height are occurred and anticyclonic weather is prevailed.



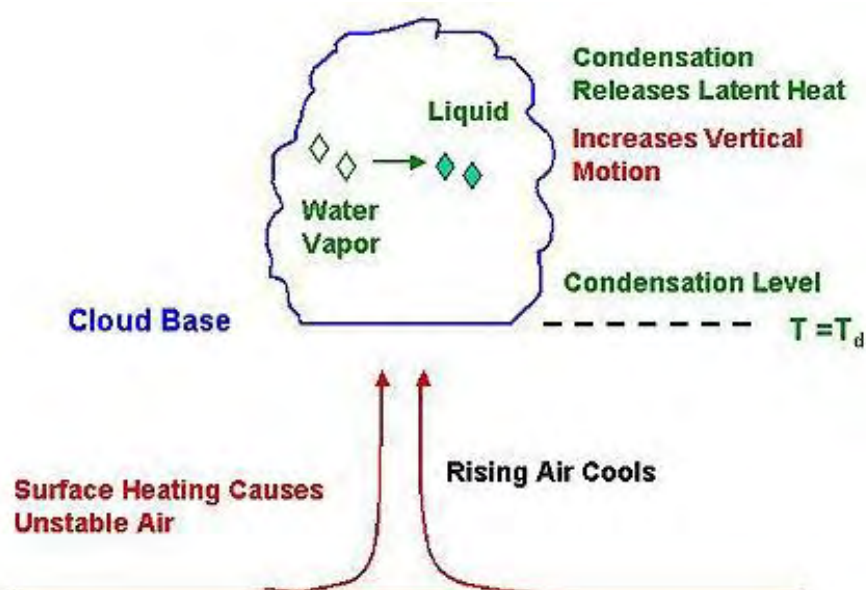
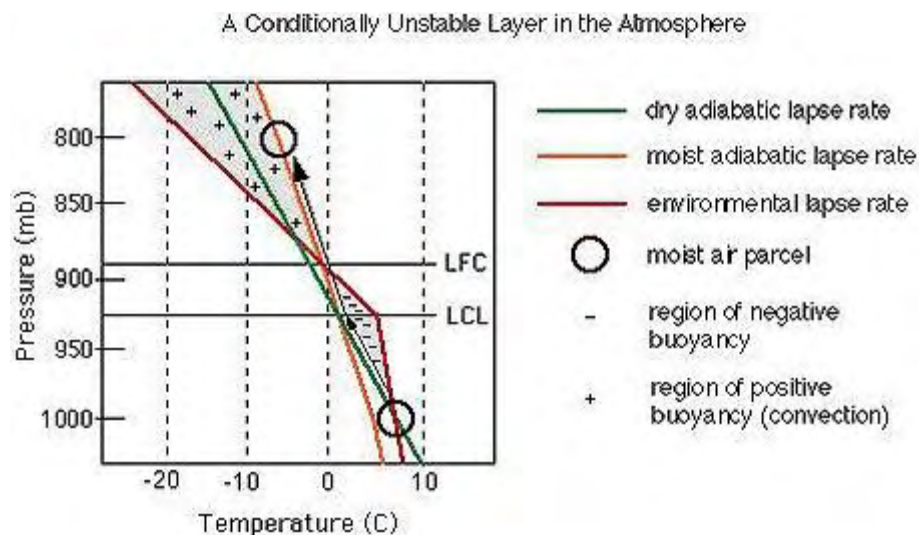
### Instability:

In the case of instability the ELR is greater than the DALR. It is also always greater than the MLR as MLR is always less than the DALR. In that way, the air parcel cools down more slowly with height from the ground than the surrounding air. This means that as the air parcel rises it becomes warmer and lighter than its surrounding air, forcing it to rise further. If the dew point is reached then latent heat is released as the vapor condenses, warming the parcel. The parcel then rises even more rapidly as the MLR is less even than the DALR before. During thermal convection the unstable air moves the air up rapidly causing cooling and convective clouds usually found in thunderstorms.



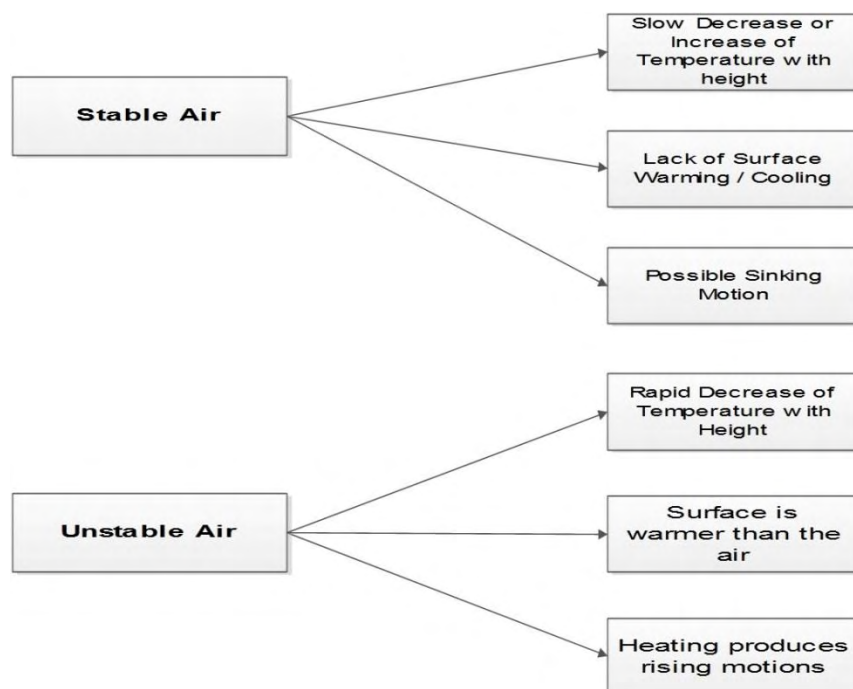
### Conditional Instability:

Conditional instability occurs when the ELR is less than the DALR but it is more than the MLR. In that way the rising air is stable in the lower layers of the atmosphere, but after a forcing power (a hill or a mountain) can be rise and cool below its dew point. In other words, after that the parcel will rise as it is unstable. Fine and sunny weather is expected in this kind of stability in areas below the condensation level, but cloudy and rainy in higher areas.



### General conditions:

Stability	$ELR < MLR < DALR$
Instability	$MLR < DALR < ELR$
Conditional Instability	$MLR < ELR < DALR$



### Neutral Atmosphere:

In a Neutral Atmosphere, the Dry and Environmental Lapse Rates are the same and the temperatures of both the parcel and its surrounding air are identical at some neutral layer. In other words, the air parcel and surrounding air are in thermal equilibrium having the same temperature. A parcel will rise cooling until it reaches this layer where the temperature balance occurs. This condition usually occurs through some external lifting force such as convergence or orographic rise.

In METRIC, a neutral atmospheric condition is initially assumed and a stability correction is later applied using the Monin-Obukhov length (L) as the indicator. Stability



conditions must be considered during the computation of sensible heat flux ( $H$ ) because they can affect the aerodynamic resistance to heat transport ( $r_{ah}$ ).

In places with positive sensible heat flux ( $H$ ), the change of temperature with elevation becomes smaller because the air mass is heated by the positive  $H$ . In this case, vertical air movement is easier and therefore aerodynamic resistance becomes smaller as  $H$  becomes higher. In general, air is in a neutral condition at a well-watered agricultural field at noon and in an unstable condition at a dry bare field at noon. The stable condition will most likely occur at night and sometimes in the afternoon in irrigated areas surrounded by desert land.

\*Information about this Annex is retrieved from the website of Federation of American scientists: <http://fas.org/> as well as from SEBAL Advanced Training and Users Manual (Waters *et al.*, 2002).